Title
Merging Galaxies and Dark Matter Halos

Author
Wetzel, Andrew Rodger

Publication Date
2010

Peer reviewed|Thesis/dissertation

Merging Galaxies and Dark Matter Halos

by

Andrew Rodger Wetzel

A dissertation submitted in partial satisfaction of the
requirements for the degree of
Doctor of Philosophy

in

Astrophysics

in the

Graduate Division
of the
University of California, Berkeley

Committee in charge:
Professor Martin White, Chair
Professor Bill Holzapfel
Professor Eliot Quataert

Spring 2010

Merging Galaxies and Dark Matter Halos

Abstract

Merging Galaxies and Dark Matter Halos

by

Andrew Rodger Wetzel
Doctor of Philosophy in Astrophysics

University of California, Berkeley

Professor Martin White, Chair

Mergers between distinct objects are a natural part of hierarchical structure formation. Mergers are also one of the most critical elements in the evolution of both galaxies and halos. I use high-resolution, cosmological volume simulations to explore galaxy and halo evolution and merging activity in a cosmological context, including environmental dependence, merger rates and dynamics, and how these processes in halos connect with those of galaxies.

I first explore halo merging and evolution, focusing on its interplay with large-scale environment. While halo spatial clustering has been thought to depend only on mass, I examine how spatial clustering depends on secondary parameters such as halo formation time, concentration, and recent merger history, a phenomenon known as "assembly bias". Next, I examine the extent to which close spatial pairs of objects can be used to predict mergers, finding limited utility to the pair-merger method arising from a competition between merger efficiency and completeness. I also explore the dependence of merging on environmental density, discovering that merging is less efficient in overdense environments. I then investigate how a massive galaxy/halo population at high redshift connects to a massive population of the same number density today, finding that scatter in mass growth and mergers between massive objects preclude a direct population mapping either forward or backward in time.

In the latter part of this work, I explore the dynamics and mergers of galaxies in groups and clusters. I first examine the orbital distributions of satellite halos/galaxies at the time of infall onto a more massive host halo, finding that satellite orbits become more radial and penetrate deeper at higher host halo mass and higher redshift. I then track the evolution of galaxies in groups directly, examining the merger rates of galaxies over time and finding that galaxy mergers do not simply trace halo mergers. I also examine the small-scale environments of galaxy mergers, discovering that recently merged galaxies exhibit enhanced small-scale spatial clustering for a short time after a merger. Finally, by using abundance matching to assign stellar mass to subhalos, I explore the importance of merging vs. disruption processes for satellite galaxy evolution. I rigorously test the connection of galaxies to subhalos by comparing simulations against observed galaxy spatial clustering, satellite fractions, and cluster satellite luminosity functions, finding agreement in all cases.

Contents

List of Figures

List of Tables

Acknowledgments

Thank you...

Dissertation committee, for insightful comments, criticisms, and encouragement.

Joanne, for being a gracious collaborator, mentor, and seminar wrangler.

Daniel, for your patient mentoring, collaborating, and introducing me to cosmology.

Alexia, for your collaboration and insight as an academic sibling.

Jeremy, for your welcome collaboration and scientific acumen.

Dexter, for making things that needed to happen happen.

Eric, for the many, many insightful conversations, about science and otherwise.

Occupants of Campbell 544, for five years of welcome sardonicism.

Mom and Dad, for fostering curiosity, encouraging learning, and unswerving support.

Erin and Suzy, for being role models in learning.

Whitney, for tolerating my silliness and making the last five years so delightful.

Berkeley, for endless amusement and rather good food.

National Science Foundation, for paying the bills.

Most importantly, Martin, for all the sarcasm, with a side of advising.

Chapter 1

Introduction

The Universe contains structure on all scales we can probe. A fundamental goal of astrophysical cosmology is to understand the origin and evolution of structure on the largest observable scales. Structure, in the form of density perturbations, was seeded via the amplification of quantum fluctuations during a period of accelerated expansion called inflation. Processed by the subsequent 14 Gyr of gravitational instability, these density perturbations have given rise to collapsed dark matter structures called halos. These dark matter halos provide the backdrop for the subsequent formation of all collapsed baryonic structures, including stars, galaxies, and galaxy clusters.

Our understanding of initial dark matter density fluctuations and how they propagate in a non-linear manner to the present day has progressed significantly in the last decade. However, the formation and evolution of galaxies remains one of the central unsolved questions in astrophysical cosmology. Observationally, we have passed a critical turning point as we now have the capacity to extract key physical results from large-scale galaxy surveys, spanning the faintest dwarf satellites around the Milky Way to the formation of the earliest massive galaxies. The challenge now is to connect the rich structure of the dark sector to the even richer observed structure of baryons by mapping galaxies to dark matter halos. Such a theoretical mapping is necessary not only for a comprehensive understanding of galaxy evolution in a cosmological context, but also to advance our understanding of cosmology and large-scale structure itself, since galaxies provide the observable tracers of dark structure.

One of the most critical, but poorly understood, elements in the evolution of both halos and galaxies is mergers. Mergers occur as gravitational attraction pulls two distinct objects together, and through dynamical relaxation they coalesce to a single resultant object. Mergers are responsible for a significant amount of the mass growth of halos and galaxies. Moreover, the violent merger process also transforms the structure of halos and galaxies. In particular, galaxy mergers are thought to play a pivotal role in the transformation of gas-rich spirals to gas-poor ellipticals (Toomre & Toomre 1972) while driving intense starbursts (Barnes & Hernquist 1991). Additionally, mergers between galaxy clusters can affect the dynamics of member galaxies as well as the temperature and morphology of the Intra-Cluster Medium (ICM; e.g., Rowley et al. 2004; Poole et al. 2007).

Beginning in the early 1990's (Carlberg 1990; Lacey & Cole 1993; Kauffmann & White 1993), much effort has gone into theoretical investigations of halo and galaxy mergers in a cosmological context. However, even today our understanding of mergers remains incomplete, largely because mergers are violent, highly non-linear processes not easily addressed by analytic techniques. Enormous progress has been made through the use of cosmological numerical simulations, which fully capture the non-linear processes of structure formation including mergers. However, as mergers are rare events, large-volume simulations are necessary for adequate statistics and to accurately represent structure on the largest scales, while high spatial resolution is necessary to accurately capture merger dynamics on galaxy scales. Only in the last five years has our computational capacity allowed sufficient dynamic range for both regimes.

Through the use of high-resolution, cosmological-volume N-body simulations, the aim of this work is to explore galaxy and halo mergers in a cosmological context and how the two relate to one another. How do galaxies map to dark matter (sub)halos? How does the merging process tie in with large- and small-scale environment? How readily do close pairs of objects merge? What are the cosmological dynamics of halos and galaxies during mergers? What is the cosmological evolution of the galaxy merger rate? How important are merging and disruption processes for the evolution of galaxies in groups? These topics constitute the scope of this work.

1.1 ΛCDM Cosmology

An understanding of the formation of *all* collapsed structures begins with a robust cosmological model for the contents, geometry, and expansion history of the Universe. This proceeds to a description of the growth of structure, which proceeds to an understanding of the evolution of dark matter halos and subhalos, which in turn proceeds to an understanding of how galaxies form and evolve within them.

A standard concordance model of cosmology has emerged within the last decade, in which the current contents of the Universe are dominated by two "dark" components not directly observable: dark energy (Λ), a highly uniform energy density with negative pressure which is causing the expansion of the Universe to accelerate, and Cold Dark Matter (CDM), a non-relativistic particle(s) which effectively interacts only via gravity and thus is collisionless. Only about 1/6 of the matter in the Universe is baryonic (and leptonic), and a cosmologically insignificant amount of the current contents are in the form of radiation.

The geometry and expansion history of the Universe are given by the field equations of General Relativity, once the contents of the Universe are specified. On sufficiently large scales, the Universe is both homogeneous and isotropic, an assumption known as the Cosmological Principle which has passed all current observational tests. Under the assumption of the Cosmological Principle and energy-momentum conservation, field equations of General

Relativity can be simplified to the Friedman equations (see e.g., Peacock 1999)

$$H^2 \equiv \left(\frac{\dot{a}}{a}\right)^2 = \frac{8\pi G}{3}\rho + \frac{\Lambda}{3} - \frac{k}{a^2} \tag{1.1}$$

$$\frac{\ddot{a}}{a} = -\frac{4\pi}{3}G(\rho + 3p)\,. \tag{1.2}$$

Here, $a(t)$ is the scale factor of the Universe at time t, ρ is the sum of energy densities of the contents of the Universe, Λ is the Cosmological Constant, k is the curvature of the Universe. p is the pressure of the contents of the Universe, which is often given by the equation of state $w \equiv p/\rho$. Dark matter is collisionless, having $w = 0$, radiation has $w = 1/3$, and dark energy, which is assumed henceforth to be a Cosmological Constant, has $w = -1$. Current observations indicate that the curvature of the Universe is zero to within a few percent (Komatsu et al. 2010), and so we will assume $k = 0$ in Eq. 1.1.

The quantity $H(z)$ is the Hubble Parameter which represents the expansion rate of the Universe. $H(z)$ is generally normalized to its current value, H_o, given by

$$H_o = 100\,h\ \mathrm{km\,s^{-1}} \tag{1.3}$$

where h is a dimensionless constant referred to as the Hubble Constant.

Given the three components of the contents of the Universe, we simplify Eq. 1.1 to

$$\left(\frac{\dot{a}}{a}\right) = H_o\left[\Omega_m(z) + \Omega_r(z) + \Omega_\Lambda(z)\right]^{\frac{1}{2}} \tag{1.4}$$

where

$$\Omega_i(z) = \frac{\rho_i(z)}{\rho_{\mathrm{crit}}(z)},\ i = m, r, \Lambda \tag{1.5}$$

represent the densities of matter, radiation, and dark energy scaled to the critical density, $\rho_{\mathrm{crit}}(z) = \frac{3H^2(z)}{8\pi G}$, the density needed to make the Universe flat (which is assumed). Ω_b, the contribution from specifically baryonic matter, is incorporated into Ω_m. Stress-energy conservation leads to matter density evolving as $\rho_m \propto (1+z)^3$ and radiation density evolving as $\rho_r \propto (1+z)^4$, and ρ_Λ is constant for vacuum energy given by a Cosmological Constant, as assumed here.

The Universe began nearly 14 billion years ago with an initial expansion moment known as the Big Bang. Shortly thereafter, a period of accelerated expansion, known as inflation, caused the size of the Universe to expand by at least $\sim e^{50}$, and in the process amplified primordial (quantum) density fluctuations to a macroscopic scale. During the first 100000 years, the energy density of the Universe was dominated by relativistic species, primarily photons and neutrinos, which contributed significant pressure and retarded the further growth of density perturbations. After about 100000 years, the energy density of the Universe transitioned to being dominated by matter, at which point significant formation of structure began through the process of gravitational collapse. However, the hot, ionized baryons remained

tightly coupled to the radiation field and were unable to further collapse. This continued until the Universe cooled sufficiently that the baryons combined to neutral species and decoupled from the radiation field, an event referred to as recombination. Thus, structure formation of both dark matter and baryons began in earnest around 300000 years after the Big Bang and has continued through the subsequent 13 Gyr of gravitational collapse.

1.2 Density Fluctuations & Spatial Clustering

Knowing the contents and expansion history of the Universe, the final ingredient to specify the evolution of structure is the initial spectrum of density perturbations produced during inflation. The density perturbation field, $\delta(\mathbf{x})$, characterizes the fractional deviation of density from the mean value. Generally, inflation is expected to produce density fluctuations described by a Gaussian distribution with zero mean, which is consistent with current observations (Slosar et al. 2008; Komatsu et al. 2010). These density fluctuations are not randomly distributed in space, but instead are spatially correlated with one another. This is quantified by the correlation function

$$\xi(r) \equiv \langle \delta(x)\delta(x+r) \rangle \tag{1.6}$$

where $\langle\rangle$ denotes the spatial average, and we have used the Cosmological Principle to reduce to a function a scalar separation, r. Alternately, we can characterize the density field by the power spectrum, $P(k)$, which is the Fourier transform of the correlation function, with $k = 2\pi/r$.

Inflation is generally thought to produce an initial power spectrum of fluctuations which can be well approximated by a power law

$$P(k) \propto k^{n_s} \tag{1.7}$$

with spectral index, n_s, close to the scale-invariant Harrison-Zel'dovich spectrum, $n_s = 1$. Since the growth of density perturbations is retarded during radiation domination, k modes which enter the horizon before matter-radiation equality experience only weak (logarithmic) growth with $a(t)$, while those modes which enter after matter-radiation equality grow linearly with $a(t)$. Thus, the power law nature of the spectrum is broken. This effect is quantified by the transfer function, $T(k)$, which relates the primordial matter power spectrum to that after matter-radiation equality

$$P(k) = T^2(k) P_{\rm primordial}(k)\,. \tag{1.8}$$

$T(k)$ is constant for low k and rolls over to nearly $T(k) \propto k^{-2}$ at high k, which causes a peak in $P(k)$ at $k \simeq 0.0145\,h\,{\rm Mpc}^{-1}$ or $r \simeq 430\,h^{-1}\,{\rm Mpc}$.

Parameter	Value	Error
$\Omega_{r,o}$	1.4×10^{-5}	-
$\Omega_{b,o}$	0.046	0.002
$\Omega_{m,o}$	0.27	0.02
$\Omega_{\Lambda,o}$	0.73	0.02
h	0.70	0.01
n_s	0.96	0.01
σ_8	0.81	0.02

Table 1.1: Current measured cosmological parameters, adapted from Komatsu et al. (2010).

1.3 Cosmological Parameters

As described above, expansion history of the Universe is governed by the density of matter, Ω_m, radiation, Ω_r, and dark energy, Ω_Λ. The expansion rate is normalized by its current value, set by the Hubble parameter, h. The initial density fluctuations are described by the matter power spectrum at the time of recombination, which is given by the slope of the primordial power spectrum, n_s, and its normalization, which is often expressed as σ_8, the variance of matter density within spheres of radius $8\,h^{-1}\,\mathrm{Mpc}$. Finally, the detailed shape of the matter power spectrum at high k is also influenced by baryon oscillations at the time of recombination, determined by Ω_b. These seven cosmological parameters, with the theoretical framework of General Relativity, provide a complete description of the gravitational growth of structure across the history of the Universe.

Table 1.1 lists the currently best-fit cosmological parameters, adapted from a compilation of observations analyzed in Komatsu et al. (2010). These values are derived from measurements of the CMB at $z \simeq 1100$ (Larson et al. 2010), Baryon Acoustic Oscillations (BAO) in nearby galaxy samples (Percival et al. 2009), and the Hubble Constant as determined via supernovae (Kowalski et al. 2008). These values (or values close to them) will be assumed hereafter.

1.4 Dark Matter Halos

1.4.1 Halo Collapse & Mass Function

We now turn to the formation, evolution, and structure of dark matter halos. As the linear density perturbations seeded by inflation are amplified through gravitational collapse, they form self-bound, non-linear conglomerations known as halos. Although halo formation is complex, being influenced by large-scale tidal fields and punctuated by violent mergers leading to halos with highly ellipsoidal geometry, a simple spherical collapse model provides a heuristic description of the halo formation process (see e.g., Peacock 1999).

Given a nearly uniform density Universe filled only with matter, Birkhoff's theorem states that the evolution of a spherical region depends only on the matter inside, allowing us to treat the region as an isolated universe. If the spherical region is sufficiently overdense, the gravitational self-attraction will overcome the initial expansion such that the spherical region will reach some maximum radius and then recollapse to a point. Following the evolution of this spherical region, turn-around occurs when the average density within the sphere is $\simeq 5.6\times$ that of the background. In reality, the subsequent collapse will not occur to a point, but random motions will maintain a finite size of the collapsed halo. This is given by the virial theorem for the equilibrium state, in which the kinetic energy K relates to the potential energy V by $V = -2K$. Since all energy is potential at turnaround, upon virialization the halo will be half of its maximum radius, or $8\times$ as dense. In the meantime, the expanding background Universe has become $4\times$ less dense, leading to a virialized halo which is $\simeq 178\times$ as dense as the background. This value is often rounded up (rather arbitrarily), leading to a common definition that a virialized halo has average density $\rho_{\rm halo} = 200\,\rho_{\rm crit}$.

The above spherical collapse formalism can also be used to compute the mass function of collapsed halos (Press & Schechter 1974; Bond et al. 1991). While the above model followed the full (non-linear) collapse process, the density threshold for collapse can also be related to the value it would have if we kept only the linear term in the overdensity expansion. This linear overdensity is clearly unphysical, since for $\delta \gtrsim 1$ the perturbative expansion is not valid. However, this exercise is useful in that it allows us to relate an overdensity in linear theory to a collapsed (non-linear) halo. If one keeps only linear terms in the overdensity expansion, then at the time the halo collapses to a point (which in reality it does not), its *linear* density contrast is $\delta \simeq 1.69$ (see e.g., Peacock 1999).

With this threshold, we then require only a measure for the strength of linear density fluctuations corresponding to a given mass scale, which in turn provides the likelihood that halos of that mass have collapsed. This is determined by the linear matter power spectrum, with which we compute the variance of the density field, $\sigma(M(r))$, smoothed on a mass scale $M = \frac{4\pi}{3}\rho_m r^3$. In the case of a matter-only Universe, the amplitude of the linear power spectrum, and hence the value of σ, grows simply as $(1+z)^{-1}$ (this growth slows as dark energy starts to dominate).

Put all together, this leads to a collapsed halo mass function

$$\frac{dn}{dM} = \sqrt{\frac{2}{\pi}}\frac{\rho_m}{M}\frac{\delta_c}{\sigma^2}\frac{d\sigma}{dM}\exp\left[-\frac{\delta_c^2}{2\sigma^2}\right] \tag{1.9}$$

where ρ_m is the matter density. Since a Gaussian density field leads to larger mass scales having weaker density fluctuations, the number of halos declines with mass. There is a critical mass scale, $M_*(z)$, at which the variance of the density field just crosses the threshold for collapse, that is, $\delta_c = \sigma(M_*)$. Physically, $M_*(z)$ represents the "typical" mass scale for halo collapse at a given redshift. Below $M_*(z)$, the superposition of halos collapsed from many past epochs leads to a halo mass function which falls off as $dn/dM \propto M^{-\alpha}$, with $\alpha \approx 1.8$. Above $M_*(z)$, halos have just recently formed, so the abundance of halos falls off

exponentially with mass because of the Gaussian nature of the density field (Bardeen et al. 1986). Note that, while Eq. 1.9 qualitatively matches the halo mass function as measured in simulation (Sheth & Tormen 1999; Jenkins et al. 2001; Warren et al. 2006; Tinker et al. 2008a), it is not quantitatively accurate to more than $\sim 50\%$. Indeed, the non-linear nature of halo formation has inhibited *any* existing purely analytic model from correctly predicting this basic statistic.

1.4.2 Halo Bias

Next, we turn to the large-scale spatial distribution of dark matter halos. This is usually quantified by the halo correlation function, which is an extension of Eq. 1.6 to discrete objects. Specifically, the halo correlation function, $\xi_{hh}(r)$, represent the excess probability beyond random of finding halo pairs at a given separation

$$P(r) = 4\pi r^2 \Delta r n \left[1 + \xi_{hh}(r)\right] \tag{1.10}$$

where n is the total number density of halos and Δr is a small radial bin width.

Since halos form *only* in overdense regions, they do not represent a random sampling of the density field, but instead are biased to preferentially high density regions, an effect known as "halo bias" (Kaiser 1984; Davis et al. 1985). The halo bias parameter, b, is often defined via the ratio of the halo correlation function to that of the underlying matter

$$b^2 \equiv \frac{\xi_{hh}(r)}{\xi_{mm}(r)} \,. \tag{1.11}$$

Since the most massive halos can form only in the most dense environments, the halo bias increases with mass, scaling as the (negative) derivative of the halo mass function (see Fig. 2.1). The most massive halos ($M > M_*$) are more biased than the underlying matter ($b > 1$), while low mass halos ($M < M_*$) are anti-biased ($b < 1$). Large-scale halo bias ($\gtrsim 5\,h^{-1}\,\mathrm{Mpc}$) is therefore a calculable prediction of cosmological models (Kaiser 1984; Bardeen et al. 1986; Mo & White 1996; Sheth & Tormen 1999), though since one must first define a halo to measure its clustering, analytic models of halo bias are limited in the same sense as the mass function. Moreover, standard models have assumed that the bias of a halo depends only on its mass, but Chapters 2 and 3 explore how halo spatial clustering also depends on secondary parameters, such as concentration and formation history.

1.4.3 Halo Structure

While the halo mass function and bias can be partially understood though analytic models, the internal structure of dark matter halos has proved more elusive to simple analytic explanations. This difficulty is largely because halos are highly non-linear, aspherical objects, experiencing growth through violent mergers, and so halo structure represent a regime where simple perturbation techniques fail. Perhaps surprisingly then, the structure of dark matter

halos as measured in simulations is highly regular. A halo's (spherically averaged) radial density profile follows the simple relation

$$\rho \propto \left(\frac{r}{r_s}\right)^{-1} \left(1 + \frac{r}{r_s}\right)^{-2} \tag{1.12}$$

known as the NFW profile (Navarro et al. 1997). Physically, the scale radius, r_s represents the transition from a shallow r^{-1} inner profile to a steeper r^{-3} outer profile. Heuristically, the inner profile arises during the rapid accretion phase of early halo formation, while the outer profile arises from more gradual recent accretion. There is ongoing debate whether a halo profile is better fit by a three parameter Einasto profile (e.g., Navarro et al. 2010), but these two profiles differ significantly only in the very inner region where, in reality, baryonic physics strongly changes either profile.

A halo's physical extent is given by its virial radius, $R_{\rm vir}$, which is often defined as the radius within which the mean density is $200\times$ the background critical density, R_{200} (though sometimes the convention of $200\times$ the background *matter* density is used instead, which leads to significantly higher halo masses at low redshifts where $\Omega_m < \Omega_{\rm total}$). The ratio of the NFW scale radius to the virial radius is a measure of the concentration of the density profile, and so this ratio is called the concentration parameter

$$c \equiv \frac{r_s}{R_{\rm vir}}\,, \tag{1.13}$$

though just as varying conventions exist for a halo's virial radius, so too for concentration. While there is considerably scatter in halo concentration at fixed mass, more massive halos are less concentrated on average (Bullock et al. 2001). Heuristically, a halo's concentration is a reflection of its assembly history, with halos that form earlier (when the Universe is denser) being more concentrated (e.g., Zhao et al. 2009).

1.4.4 Halo Mergers

In the framework of hierarchical structure formation, halos first form as small objects and grow more massive over time. However, the mechanisms of halo growth and evolution are not as simple as the monolithic spherical collapse model outlined above. Instead, a significant amount of halo growth occurs via merging with smaller, virialized halos. Thus, it is critical to have a cosmological understanding of the frequency of merging, the environments in which mergers take place, and what impact mergers have on the substructure within halos.

Since merging is (typically) a two-body interaction, mergers are sometimes postulated to occur preferentially in higher density environments (e.g., Furlanetto & Kamionkowski 2006). If true, this might imply that recently merged halos should exhibit stronger spatial clustering than all halos at the same mass scale. Such an effect would not only change the standard model of large-scale structure, in which spatial clustering depends only on halo mass, but it would have important observational implications for the use of spatial clustering to infer

halo masses (which are difficult to measure directly), as is sometimes done with galaxies, galaxy clusters, and quasars (e.g., Cole & Kaiser 1989; Majumdar & Mohr 2003; Blain et al. 2004; Shen et al. 2007).

These questions regarding the interplay between mergers and large-scale structure are addressed in the first part of this thesis. Chapter 2 explores whether recently merged halos exhibit special spatial clustering properties beyond that determined by halo mass, while Chapter 3 explores more directly the efficiency of the halo merging process in different density environments. Additionally, since mergers and merger rates are difficult to observe directly, a common observational method has been to assume that close spatial pairs provide a good proxy for mergers, given some coalescence timescale (e.g., Patton et al. 2000; Bell et al. 2006). Chapter 3 also tests this assumption directly, examining both the efficiency and the completeness of the pair-merger method.

A primary goal of the field of galaxy evolution to understand the connection between galaxies observed at high redshift and those of the present day. A common method used in such studies is to rank objects in descending order by mass and connect a population above some number density threshold at high redshift to a population above the same number density threshold today. Chapter 4 explores how scatter in mass growth and merging activity affect how massive populations connect to one another across time by using massive halos as tracers for massive galaxies.

1.5 Galaxies

Dark matter halos provide the backdrop for the formation of more compact baryonic structures such as galaxies. Having an understanding of dark matter halo merging and evolution, the latter part of this thesis is devoted to exploring in detail the formation, structure, and dynamics of dark matter subhalos and their connection to the evolution of galaxies within groups and clusters. This is a challenging task, as the evolution of galaxies is even more complex than that of dark matter, involving gas dynamics, star formation, and various forms of feedback, which is why many facets of our understanding of galaxy evolution remain unresolved.

1.5.1 Subhalos & Galaxies

Beyond just driving halo mass growth, halo mergers govern the evolution of substructure within halos. When two halos merge, the smaller halo does not instantaneously dissolve into the larger one, but it retains its identity as an self-bound substructure halo, or subhalo, inside the larger host halo (Tormen et al. 1998; Klypin et al. 1999; Moore et al. 1999). After infall, a subhalo will continue to orbit within the host halo as dynamical friction slows its velocity and tidal fields cause its mass to be stripped from the outside-in. As a subhalo's orbital radius shrinks and mass stripping becomes more efficient in the host halo's dense central region, a subhalo will eventually lose sufficient mass that it is no longer identifiable, at which

point it has "disrupted". The combination of continuous subhalo infall and disruption leads to host halos having $10-20\%$ of their mass being contained within self-bound subhalos.

Galaxies form at the centers of dark matter halos as baryons cool and contract toward the minimum of a halo's potential well (White & Rees 1978; Blumenthal et al. 1986; Dubinski 1994; Mo et al. 1998). While galaxies form in isolated halos, as halos merge and smaller halos become subhalos of larger host halos, the galaxies in the smaller halos become satellite galaxies within the larger host halo. In this picture, a dark matter halo hosts a central galaxy at its core, which is the galaxy that originally formed within the halo, and it can host multiple more recently accreted satellite galaxies. Satellite galaxies exhibit rich orbital dynamics and are thought to experience accelerated evolution. For instance, satellite galaxies show evidence of color and/or morphological evolution as their gas is stripped and heated by the dense cluster environment (Butcher & Oemler 1984). Satellite galaxies also experience stellar mass loss from tidal stripping, contributing stars to a diffuse Intra-Cluster Light (ICL; e.g., Mihos et al. 2005; Gonzalez et al. 2007). Finally, most satellite galaxies are expected to eventually merge with the host halo's central galaxy (Ostriker & Tremaine 1975).

The efficiency and importance of all of these processes are governed by the orbital dynamics of satellites, which are set by the initial conditions upon accretion onto the larger host halo. Thus, Chapter 5 explores the orbital distributions of satellite halos at the time of infall, focusing specifically on satellite orbital parameters and their evolution with halo mass and redshift. This lays out the initial conditions of satellite galaxy evolution, and in subsequent chapters we follow the evolution of subhalos within host halos to explore galaxy merging and disruption processes directly.

1.5.2 Galaxy Mergers

Mergers represent perhaps the most important process which governs the evolution of galaxies. More than just providing a mechanism for galaxy mass growth, mergers are thought to be transformative processes that affect a galaxy's morphology, color, star formation, gas content, and central supermassive black hole (Toomre & Toomre 1972; Carlberg 1990; Barnes & Hernquist 1991). In the standard picture, the galaxies form as baryons cool and contract toward the minimum of a halo's potential well, which produces a gas-rich galaxy with flat, spiral structure (White & Rees 1978; Blumenthal et al. 1986; Dubinski 1994; Mo et al. 1998). Mergers between two gas-rich galaxies provide a mechanism for efficient energy and angular momentum dissipation of the gas, which leads to dense gas cores that trigger intense starbursts. The conversion of gas to stars, combined with various forms of feedback, largely exhaust and expel the remaining gas supply. The violent merger process also can change a galaxy's morphology, transforming a rotation-dominated spiral to a velocity dispersion-dominated elliptical.

The intense starbursts triggered during gas-rich mergers are thought to manifest themselves as various populations in the galaxy zoo, including Ultra-Luminous Infrared Galaxies (ULIRGs) at $z \lesssim 1$ as well as Lyman Break Galaxies (LBG), Lyman-alpha Emitters (LAE), and Sub-Millimeter Galaxies (SMG) at higher redshifts. Additionally, galaxy mergers are

expected to contribute to the growth of supermassive black holes, which produces Active Galactic Nuclei (AGN) and quasar activity. However, the details of how mergers trigger these observed galaxy populations and the extent to which they relate to one another remains unresolved. Within the last decade, we have accumulated statistically significant observational samples of such galaxy populations, including information on their counts over time and their spatial clustering properties (e.g., Steidel et al. 2003; Coppin et al. 2006; Gawiser et al. 2007; Shen et al. 2007; Tacconi et al. 2008; Yamauchi et al. 2008). Thus, from a theoretical perspective, it imperative to have precise cosmological predictions for galaxy merger rates and the spatial clustering properties of merger populations.

Galaxy merger rates have often been inferred from halo merger rates by assuming that the accreted satellite galaxies merges with its central galaxy on some dynamical infall time (e.g., Kauffmann et al. 1993). However, this simple approximation neglects many important processes, including differential mass evolution of central and satellite galaxies, satellites merging with other satellites, unbound satellite orbits, and satellite galaxy disruption before merging. In Chapter 6, we outline our numerical techniques for identifying and tracking subhalos in high-resolution, cosmological simulations, including building robust subhalo merger trees to track galaxy mergers. We use these subhalo merger trees to compare galaxy and halo merger rates and explore the importance of the above processes on the satellite population.

Just as halo mergers have been thought to occur in higher density environments with enhanced large-scale spatial clustering, galaxy mergers have been postulated to exhibit enhanced small-scale ($\lesssim 200\,h^{-1}\,\mathrm{kpc}$) spatial clustering. If true, then small-scale clustering measurements of a given galaxy population could be used as a direct test of the merger-driven nature of that population. Chapter 7 explores the small-scale clustering properties of galaxy mergers, with applications to high redshift quasars and starburst populations. Chapter 7 also explores more generally the environments of the galaxy mergers, including dependence on host halo mass and location within the host halo.

1.5.3 The Subhalo-Galaxy Connection

Because of the large dynamic range (high resolution and large volume) needed to fully examine galaxy evolution in a cosmological context, much of the theoretical work in this direction is based on dark matter N-body simulations. Such simulations can effectively capture the non-linear gravitational dynamics of dark matter, including mergers and environmental dependence, but since they lack baryonic physics, one needs a mapping between dark matter subhalos and galaxy mass in order to connect with observations.

Chapter 8 explores a direct, empirical mapping which assumes a monotonic relation between subhalo dark mass and galaxy stellar mass, populating subhalos such that one reproduces by construction the observed stellar mass function (Vale & Ostriker 2006; Conroy et al. 2006; Shankar et al. 2006). However, even with this well-defined mapping, it remains unclear what the fates of satellite galaxies are. In particular, how does the mass stripping and tidal disruption of the more diffuse subhalo map to that of its more compact galaxy? Most galaxy evolution models have assumed that all satellite galaxies remain intact and

eventually merge with their central galaxy. However, galaxy clusters are observed to contain an appreciable amount of stellar material in the form of diffuse ICL, stripped from satellite galaxies during infall (e.g., Mihos et al. 2005). Chapter 8 thus examines the interplay between satellite orbital dynamics and tidal mass stripping, with the goal of empirically relating subhalo mass loss to galaxy merging and disruption. We also use this framework to empirically constrain satellite galaxy lifetimes.

With these theoretical tools in place, Chapter 8 then proceed to rigorously test our mapping of galaxies to subhalos. We demonstrate the ability of our simulation plus galaxy mapping to correctly reproduce all large-scale structure measurements, including spatial clustering, satellite fractions, and galaxy cluster satellite luminosity functions. The success of this relatively simple model for how light traces mass offers a promising framework to further our understanding of both galaxy evolution and cosmology.

Chapter 2

The Clustering of Massive Halos

Abstract

The clustering properties of dark matter halos are a firm prediction of modern theories of structure formation. We use two large-volume, high-resolution N-body simulations to study how the correlation function of massive dark matter halos depends upon their mass, assembly history, and recent merger activity. We find that halos with the lowest concentrations are presently more clustered than those of higher concentration, the size of the effect increasing with halo mass, in agreement with trends found in studies of lower mass halos. The clustering dependence on other characterizations of the full mass accretion history appears weaker than the effect with concentration. Using the integrated correlation function, marked correlation functions, and a power-law fit to the correlation function, we find evidence that halos which have recently undergone a major merger or a large mass gain have slightly enhanced clustering relative to a random population with the same mass distribution.

2.1 Introduction

The pattern of clustering of objects on large scales is a calculable prediction of cosmological models and thus comprises one of the fundamental cosmological statistics. Within modern theories of structure formation, the clustering of rare, massive dark matter halos is enhanced relative to that of the general mass distribution (Kaiser 1984; Efstathiou et al. 1988; Cole & Kaiser 1989; Mo & White 1996; Sheth & Tormen 1999), an effect known as bias. The more massive the halo, the larger the bias. As a result, the mass of halos hosting a given population of objects is sometimes inferred by measuring their degree of clustering – allowing a statistical route to the notoriously difficult problem of measuring masses of cosmological objects (e.g., Cooray & Sheth 2002).

Since halos of a given mass can differ in their formation history and large-scale environ-

ment[1] , a natural question arises: do these details affect halo clustering? In currently viable scenarios for structure formation, objects grow either by accretion of smaller units or by major mergers with comparable-sized objects. The formation history of a halo can thus be characterized by its mass accumulation over time, such as when it reached half of its mass, had a mass jump in a short time, or last underwent a (major) merger.

Theoretically, the simplest descriptions of halo growth and clustering (Bond et al. 1991; Bower 1991; Lacey & Cole 1993, 1994; Kitayama & Suto 1996a,b) do not give a dependence upon halo formation history (White 1994; Sheth & Tormen 2004; Furlanetto & Kamionkowski 2006; Harker et al. 2006). To reprise these arguments: pick a random point in the universe and imagine filtering the density field around it on a sequence of successively smaller scales. The enclosed density executes a random walk, which in the usual prescription is taken to be uncorrelated from scale to scale. The formation of a halo of a given mass corresponds to the path passing a certain critical value of the density, δ_c, at a given scale. The bias of the halo is the "past" of its random walk and its history the "future" of the walk. All halos of the same mass at that time correspond to random walks crossing the same point, and thus have the same bias. (Note that the derivation, using sharp k-space filtering, does not match the way the prescription is usually applied, and this has been suggested by some of the above authors as a way to obtain history dependence. Introducing an environmental dependence through elliptical collapse, for example, will also give a history dependence.)

The lack of dependence on halo history in the simplest descriptions does not close the discussion, however. While these analytic methods work much better than might be expected given their starting assumptions, the Press-Schechter based approaches still suffer many known difficulties (e.g., Sheth & Pitman 1997; Benson et al. 2005). Other analytical ways of estimating the clustering of mergers have been explored. For example, Furlanetto & Kamionkowski (2006) defined a merger kernel (not calculable from first principles) and assumed that all peaks within a certain volume eventually merged. Such an ansatz implies that recently merged halos are more clustered for $M > M_*$ and less clustered for $M < M_*$, with some dependence upon predecessor mass ratios and redshifts. ($M_*(z)$ is the mass at which $\sigma(M, z)$, the variance of the linear power spectrum smoothed on scale M, equals the threshold for linear density collapse δ_c). Using close pairs as a proxy for recently merged halos, they found a similar enhancement of clustering for $M > M_*$ and reduction for $M < M_*$ in several (analytic) clustering models.

Simple analytic models cannot be expected to capture all of the complexities of halo formation in hierarchical models, and full numerical simulations are required to validate and calibrate the fits. Fortunately, numerical simulations are now able to produce samples with sufficient statistics to test for the dependence of clustering on formation history. Early work by Lemson & Kauffmann (1999) showed that the properties of dark matter halos, in particular formation times, are little affected by their large-scale environment if the entire population of objects is averaged over. They interpreted this as evidence against formation

[1]The large-scale environment of a halo refers to the density, smoothed on some scale larger than the halos, for example, $5 - 10\,h^{-1}\,\mathrm{Mpc}$.

history and environment affecting clustering. As emphasized by Sheth & Tormen (2004), however, this finding — plus the well known fact that the typical mass of halos depends on local density — implies that the clustering of halos of the same mass must also depend on formation time. Using a marked correlation function, Sheth & Tormen (2004) found that close pairs tend to have earlier formation times than more distant pairs, work which was extended and confirmed by Harker et al. (2006). Gao et al. (2005) found that later forming, low-mass halos are less clustered than typical halos of the same mass at the present; a possible explanation of this result was given by Wang et al. (2007a). Wechsler et al. (2006) found a similar dependence upon halo formation time, showing that the trend reversed for more massive halos and that the clustering depended on halo concentration. However, in order to probe to higher masses these authors assumed that the mass dependence was purely a function of the mass in units of the non-linear mass, then used earlier outputs to probe to higher values of this ratio. It should be noted that scaling quantities by M/M_* gives a direct equality only if clustering is self-similar. Since $P(k)$ is not a power-law and $\Omega_m \neq 1$, a check of this approximation is crucial.

These formation time dependencies are based on (usually smooth) fits to the accretion history of the halo. However, halo assembly histories are often punctuated by large jumps from major mergers that have dramatic effects on the halos. Major mergers can be associated with a wide variety of phenomena, ranging from quasar activity (Kauffmann & Haehnelt 2000) and starbursts in galaxies (Mihos & Hernquist 1996) to radio halos and relics in galaxy clusters (see Sarazin 2005, for phenomena associated with galaxy cluster mergers). Major mergers of galaxy clusters are the most energetic events in the universe. It follows that major merger phenomena can either provide signals of interest or can cause noise in selection functions that depend upon a merger-affected observable. If recently merged halos cluster differently from the general population (merger bias), and this is unaccounted for, conclusions drawn about halos on the basis of their clustering would be suspect. The question of whether such merger bias exists remains unresolved, as previous work to identify a merger bias through N-body simulations and analytic methods yields mixed results (Gottlöber et al. 2002; Percival et al. 2003; Scannapieco & Thacker 2003; Furlanetto & Kamionkowski 2006).

In this chapter we consider the clustering of the most massive dark matter halos, measured from two large volume $(1.1\,h^{-1}\,\mathrm{Gpc})^3$ N-body simulations. We concentrate on massive halos, as most previous simulations did not have the volume to effectively probe this end of the mass function, and furthermore, for the largest mass halos the correspondence between theory and observation is particularly clean. We first examine the long-term growth history of halos, calculating the "assembly bias" as a function of growth history, extending previous results to higher masses. We then look to short-term history effects, measuring the "merger bias" as a function of recent major merger activity or large mass gain.

2.2 Simulations

To investigate the effects of formation history on clustering statistics we use two high-resolution N-body simulations performed with independent codes: the HOT code (Warren & Salmon 1993) and the TreePM code (White 2002). Both simulations evolved randomly generated, Gaussian initial conditions for 1024^3 particles of mass $10^{11}\,h^{-1}\,\mathrm{M}_\odot$ from $z = 34$ to the present, using the same ΛCDM cosmology ($\Omega_M = 0.3 = 1 - \Omega_\Lambda$, $\Omega_B = 0.046$, $h = 0.7$, $n = 1$ and $\sigma_8 = 0.9$) in a periodic cube of side $1.1\,h^{-1}\,\mathrm{Gpc}$. For the HOT simulation a Plummer law with softening $35\,h^{-1}\,\mathrm{kpc}$ (comoving) was used. The TreePM code used a spline softened force with the same Plummer equivalent softening. The TreePM data were dumped in steps of light crossings of $136\,h^{-1}\,\mathrm{Mpc}$ (comoving), producing 30 outputs from $z \approx 3$ to $z = 0$. The HOT data were dumped from $z \approx 1$ (lookback time of $5.3\,h^{-1}\,\mathrm{Gyr}$) to $z = 0$ in intervals of $0.7\,h^{-1}\,\mathrm{Gyr}$, with the last interval at $z = 0$ reduced to $0.4\,h^{-1}\,\mathrm{Gyr}$. The outputs before $z \approx 1$ had so few high mass halos that the statistics were not useful for the merger event calculations. For comparisons of how using light crossings vs. fixed time steps in Gyr changes merger ratios, see Cohn & White (2005). The TreePM simulations were used for the assembly histories and the HOT simulations for the merger bias calculations – though the results from the two simulations were consistent so either could have been used in principle.

For each output we generate two catalogs of halos via the Friends-of-Friends (FoF) algorithm (Davis et al. 1985), using linking lengths $b = 0.2$ and 0.15 in units of the mean inter-particle spacing. These groups correspond roughly to all particles above a density threshold $3/(2\pi b^3)$, thus both linking lengths enclose primarily virialized material. Henceforth halo masses are quoted as the sum of the particle masses within FoF halos, thus a given halo's $b = 0.15$ mass will be smaller than its $b = 0.2$ mass (see White 2001, for more discussion). We consider halos with mass $M > 5 \times 10^{13}\,h^{-1}\,\mathrm{M}_\odot$ (more than 500 particles); at $z = 0$ there are approximately $96,000$ such halos in each simulation for the $b = 0.15$ catalog and $120,000$ for the $b = 0.2$ catalog. The mass functions and merger statistics from the two simulations are consistent within Poisson scatter.

Given a child-parent relationship between halos at neighboring output times, construction of the merger tree is straightforward. Progenitors are defined as those halos at an earlier time which contributed at least half of their mass to a later (child) halo. Of the approximately 10^5 halos at $z = 0$ we find only 14 for which our simple method fails. In these cases a "fly-by" collision of two halos gives rise to a halo at $z = 0$ with no apparent progenitors. Excluding these halos does not change our results. For the TreePM run, we use all 30 outputs to construct the merger tree, which stored all of the halo information (mass, velocity dispersion, position, etc.) for each halo at each output. Each node of the tree pointed to a linked list of its progenitors at the earlier time, enabling a traversal of the tree to find mass accretion histories and mergers. The HOT run produced outputs for each time interval of child and parent halos.

2.3 Measuring Clustering

A basic measure of clustering is the two-point function, which in configuration space is the correlation function, $\xi(r)$. To compute $\xi(r)$ we use the method of Landy & Szalay (1993):

$$\xi(r) = \frac{\langle DD\rangle - 2\langle DR\rangle + \langle RR\rangle}{\langle RR\rangle} \tag{2.1}$$

where D and R are data and random catalogs, respectively, and the angle brackets refer to counts within a shell of small width having radius r. In computing $\langle DR\rangle$ and $\langle RR\rangle$ we use $10\times$ as many random as data points. To compute errors, we divide the simulation volume into 8 octants and compute $\xi(r)$ within each octant. Since we probe scales much smaller than the octants, we treat them as uncorrelated volumes, and we quote the mean $\xi(r)$ and error on the mean under this assumption. These errors tend to be ~ 1.4–2 times larger than the more approximate $\sqrt{N_{\rm pair}}$ error estimates used in some previous work.

Our goal is to test the dependence of the clustering of objects associated with some history dependent property. A relevant quantity for comparison is the (mass dependent) bias of the halos relative to the underlying dark matter, which we define as:

$$\xi(r) = b^2 \xi_{\rm dm}(r)\,. \tag{2.2}$$

Analytically, the large-scale bias is related to a derivative of the halo mass function (Efstathiou et al. 1988; Cole & Kaiser 1989; Mo & White 1996; Sheth & Tormen 1999). For the Sheth-Tormen form of the mass function one finds

$$b_{ST}(M_{180\rho_b}) = 1 + \frac{\nu'^2 - 1}{\delta_c} + \frac{0.6}{\delta_c\,(1+\nu'^{0.6})} \tag{2.3}$$

where $\nu' = 0.841\delta_c/\sigma(M_{180\rho_b})$ and $\delta_c = 1.686$. This has been improved upon using the Hubble volume simulations (Colberg et al. 2000; Hamana et al. 2001) — see also Seljak & Warren (2004) for discussion of the bias defined through $P(k)$ on similar scales. Hamana et al. (2001) used FoF halos with $b = 0.164$ and found

$$\begin{aligned} b(M,R,z) &= b_{ST}(M_{108},z) \\ &\times \left[1.0 + b_{ST}(M_{108},z)\sigma_R(R,z)\right]^{0.15}\,. \end{aligned} \tag{2.4}$$

The subscripts on the mass M indicate which overdensity threshold is being used to define the halo mass. We took $M = 0.93\,M_{108}$ and $M = 1.07\,M_{180b}$, calculating the conversion using the profile of Navarro et al. (1997) assuming a concentration $c = 5$. The change in conversion factor was less than a percent for the range of concentrations of interest. See White (2001) for more details, discussion and definitions.

We show the bias $b = \sqrt{\xi(r)/\xi_{\rm dm}(r)}$ at $r = 18\,h^{-1}\,$Mpc as a function of mass in Fig. 2.1. The bias for halos with $M > 5\times10^{13}\,h^{-1}\,{\rm M}_\odot$ changed less than 5% on scales $r \geq 15\,h^{-1}\,$Mpc. We include the two bias fits given above for $r = 18\,h^{-1}\,$Mpc at $z = 0$. The Hamana et al.

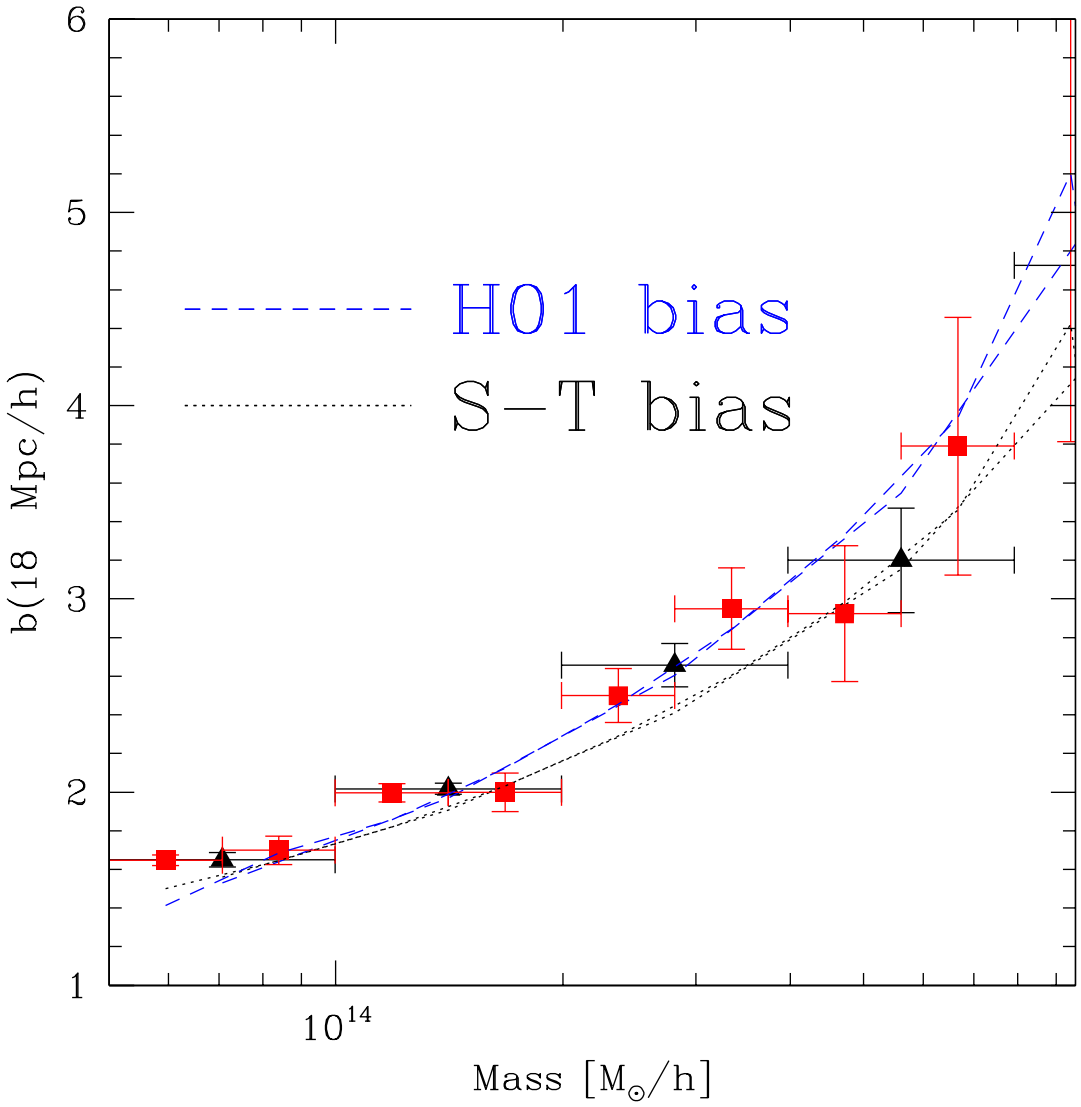

Figure 2.1: Bias, $b(r) = \sqrt{\xi(r)/\xi_{\rm dm}(r)}$, at $r = 18\,h^{-1}\,$Mpc for two different binnings in mass. Horizontal error bars on each point show the range of masses used. The bias was approximately scale-invariant in this mass regime from $15-30\,h^{-1}\,$Mpc. We show two fits to $b(M)$ proposed in the literature: that of Hamana et al. (2001) (dashed) and Sheth & Tormen (1999) (dotted), each plotted for both mass binnings.

(2001) fit was derived from a larger simulation volume; Fig. 2.1 is included to illustrate the mass dependence of the global bias, to provide a comparison context for the sizes of the additional biases of concern in this chapter. We now turn to estimates of bias effects due to the history of the halos.

2.4 Assembly Bias

We begin by considering parametrizations of the formation history of halos which emphasize the global properties, that is, those related to the halo mass growth over a long period of time. We consider three parametrizations of halo histories which have previously been used with lower mass halos: c, $a_{1/2}$, and a_f (Wechsler et al. 2006; Gao et al. 2005; Sheth & Tormen 2004). Using these parametrizations Sheth & Tormen (2004), Harker et al. (2006), Gao et al. (2005), Wechsler et al. (2006), and Croton et al. (2007) have shown that the clustering of halos of fixed mass is correlated with formation time, a result which has come to be termed "assembly bias". The effect is strongest for smaller halos, and this has been the focus of earlier work. For the extremely massive halos that we consider halo identification is simpler, as none of our halos are subhalos. However, since massive halos are rarer, the statistics are poor even for a simulation volume as large as ours.

The concentration, c, is a parameter in an NFW fit to a halo density profile (Navarro et al. 1997).[2] We perform a least squares fit of the NFW functional form to the radial mass distribution of all the particles in the FoF group, allowing c and M_{200} to vary simultaneously. This is in order to be similar to the procedure of Bullock et al. (2001) to allow ready comparison. The concentration is expected to correlate with the time by which most of the halo formed, with earlier forming halos are more concentrated (Navarro et al. 1996; Wechsler et al. 2002; Gao et al. 2004b). There is also a weak dependence of concentration on halo mass. We have tried to minimize this effect by dividing out the average concentration for each mass (calculated from the data) to get a "reduced" concentration, which is essentially uncorrelated with mass (correlation is less than 0.2%).

The second parameter encapsulating the formation history is $a_{1/2}$, the scale factor at which a halo accumulates half of its final mass. We find $a_{1/2}$ by linearly interpolating between the two bracketing times. Analytic properties of this definition have been studied in Sheth & Tormen (2004), and $a_{1/2}$ is often used as a proxy for formation epoch. The third parameter, a_f, the formation scale factor, is also a formation time proxy. It is defined through a fit to the halo mass accretion history (Wechsler et al. 2002):[3]

$$M(z) = M_0 \exp\left[-2a_f z\right] \tag{2.5}$$

where M_0 is the mass of the halo at $z = 0$. We calculate this from the history by doing a

[2] We follow NFW and take $c = r_{200}/r_s$; note that Wechsler et al. (2006) use $c_{\rm vir} = r_{\rm vir}/r_s$ where $r_{\rm vir} \simeq r_{100}$ for our cosmology. At $z = 0$, $c_{\rm vir} \simeq 1.25\,c$.

[3] Miller et al. (2006) present an analytic justification for this form based on extended Press-Schechter theory.

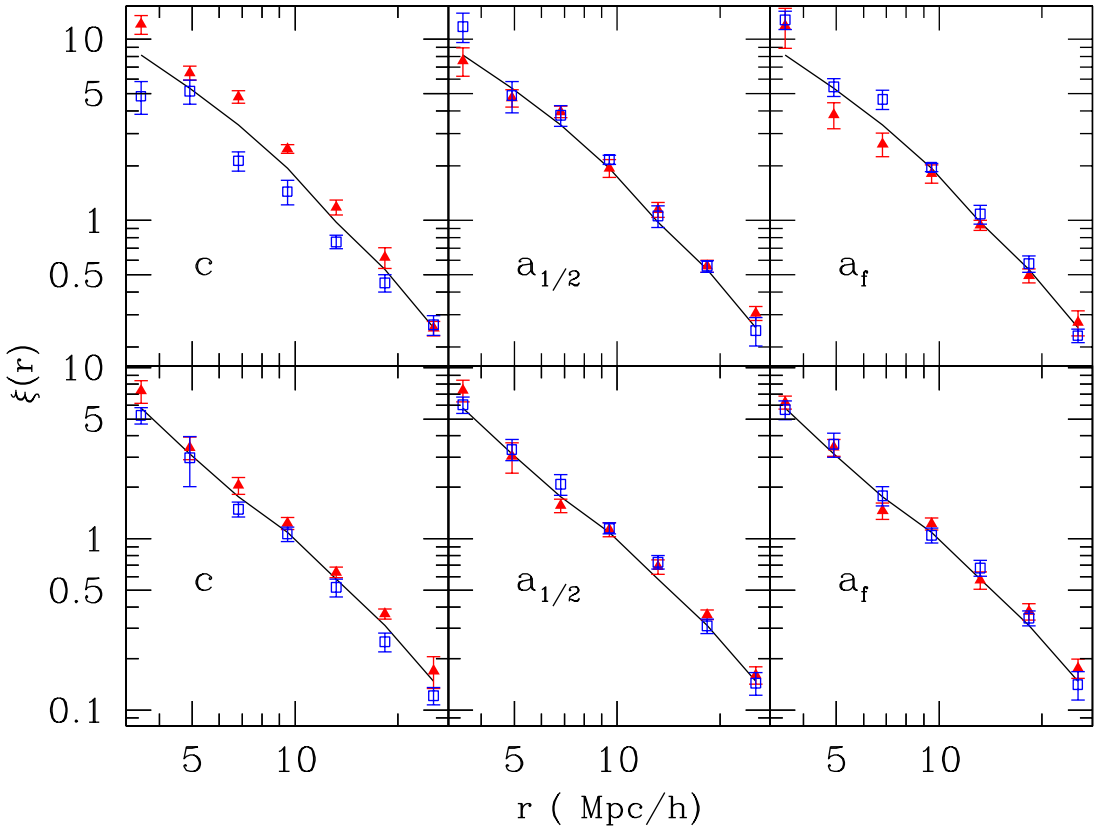

Figure 2.2: Correlation function of the lowest (filled triangles) and highest (open squares) quartiles of (reduced) concentration, c (left), half mass scale factor, $a_{1/2}$ (center) and formation scale factor, a_f (right). Solid curve is $\xi(r)$ for the full halo sample. **Top**: $10^{14}\,h^{-1}\,\mathrm{M}_\odot \leq M \leq 3\times10^{14}\,h^{-1}\,\mathrm{M}_\odot$. **Bottom**: $5\times10^{13}\,h^{-1}\,\mathrm{M}_\odot \leq M \leq 8\times10^{13}\,h^{-1}\,\mathrm{M}_\odot$. A clear signal is seen for concentration and formation scale factor for the more massive halos.

least squares fit of $\ln(M_i/M_0)$ against z_i for all the z_i steps. Although this form does not fit the mass accretion history of massive halos particularly well due to their frequent mergers, the fit is well defined and, as will be shown below, a_f nonetheless appears to be correlated with clustering.

The correlations[4] for many of the above parameters were presented in Cohn & White (2005). Some of these correlations have been compared in different combinations in Wechsler et al. (2002), Zhao et al. (2003a), Zhao et al. (2003b), Wechsler et al. (2006), and Croton et al. (2007). Except for Zhao et al. (2003b,a), these were for galaxy scale halos rather than galaxy cluster scale halos. The formation histories for low mass halos tend to be smoother and better fit to the form of Wechsler et al. (2006), since they undergo fewer mergers than high mass halos at late times. Wechsler et al. (2006) and Zhao et al. (2003a) give a formula for the concentration in terms of the formation time of Wechsler et al. (2002); our correlation coefficient is characterizing the scatter around any such correlation. For the current sample the strongest correlation (0.69) is between the formation redshift, $z_f = 1/a_f - 1$, and the half-mass redshift, $z_{1/2} = 1/a_{1/2} - 1$, consistent with the 0.70 found by Cohn & White (2005) with a sample about 1/7 the size. The formation redshift, z_f, and reduced concentration have a correlation of 0.53. The full concentration and $z_{1/2}$ (z_f) have a correlation of 0.56 (0.54). These correlations increase as the lower mass limit is decreased from $10^{14}\,h^{-1}\,\mathrm{M}_\odot$ to $5\times10^{13}\,h^{-1}\,\mathrm{M}_\odot$.

To highlight any effects of assembly bias we take the highest and lowest quartiles of the distribution of each of these three parametrization values and compare the resulting $\xi(r)$ to that of the full sample (similar to Wechsler et al. 2006). We show examples for $10^{14}\,h^{-1}\,\mathrm{M}_\odot < M < 3\times10^{14}\,h^{-1}\,\mathrm{M}_\odot$ and $5\times10^{13}\,h^{-1}\,\mathrm{M}_\odot < M < 8\times10^{13}\,h^{-1}\,\mathrm{M}_\odot$ in Fig. 2.2. For the higher mass halos we see a strong dependence of clustering on concentration. We see a similar, but noticeably smaller, dependence on a_f, indicating that more recently formed objects cluster more strongly. As all of the objects we consider have $M > M_*$, our results are in line with the expectation of Wechsler et al. (2006) and the theoretical model of Furlanetto & Kamionkowski (2006). Specifically, this confirms the result found by Wechsler et al. (2006) at $z = 0$, without needing to make the approximation that $b(c, M, z) = b(c, M/M_*(z))$.

The ratio of their correlation function at their top c quartile to the total sample for halos $\sim 10\,M_*$ was ~ 1.25. This is larger than our ratio, which doesn't reach 1.2 for any of the radii considered in Fig. 2.2, though it is well within our (and their) errors. This is mirrored for the lowest c quartile where our effect is similarly reduced but within the errors. We are using reduced concentration, while they divide each halo's concentration by the average concentration in its mass bin, $\tilde{c}_{\rm vir}$. For the lower mass sample a much weaker trend is seen (the ratios for the quartiles when selected on concentration barely reaches 10%), agreeing with the expectation that the signal decreases as $M \to M_*$. At fixed mass, the trend of b with c is consistent with the fit of Wechsler et al. (2006), but the trend is so weak relative to the noise that the result is of marginal significance.

Gao et al. (2005) and Harker et al. (2006) found bias for $M > M_*$ based on $z_{1/2}$,

[4]Defined as $(\langle ab\rangle - \langle a\rangle\langle b\rangle)/\sqrt{\langle(a-\langle a\rangle)^2\rangle\langle(b-\langle b\rangle)^2\rangle}$, see Lupton (e.g., 1993).

where both the lowest and highest quartiles of $z_{1/2}$ tended to be more clustered than the full sample. We see a hint of this as well, but the fluctuations are large. Croton et al. (2007) also found more dependence of clustering on $z_{1/2}$ (their formation time) than on concentration, once luminosity dependent bias was taken out. Note that their luminosity dependence might include some of the history measured by concentration or $z_{1/2}$ and their focus was on galaxies populating the halos rather than the halos themselves.

Note also that even though z_f and $z_{1/2}$ are correlated, the correlation is not strong enough so that bias in one implies bias in the other. The overlap of the upper and lower quartiles for these quantities for $M > 10^{14}\,h^{-1}\,\mathrm{M}_\odot$ is 62% and 54% respectively. As the rest of the clusters differ, the overall biases can be quite different, as seen in Fig. 2.2.

Another formation time related quantity, the redshift of last mass jump by 20% or more in a time step corresponding to the light crossing time of $136\,h^{-1}\,\mathrm{Mpc}$ comoving, had correlations with $z_{1/2}$ (0.70), z_f (0.61), and c (0.40). We found a small sign of bias in the correlation functions of its highest and lowest quartiles as well, leading us to expect a merger bias signal, as will be examined in §2.5.

In summary, we confirm and extend previous results to lower redshift and higher mass for concentration dependent bias. We see a smaller signal for formation time bias, and we see little (if any) signal for bias based on when halos reach half of their mass. Bias in concentration and half-mass redshift have been seen in previous work for smaller masses at higher redshift; our results show a smaller bias, but well within errors, at least for the concentration dependent bias.

2.5 Merger Bias

In the previous section we demonstrated the dependence of $\xi(r)$ upon halo formation history, characterized by an average property such as the "formation time". As halo assembly histories are punctuated by large jumps from major mergers, we can also ask whether the clustering of recently merged halos differs from that of the general population.

Although the concept of a major merger is intuitively easy to understand, there is no standard definition in the literature of "merger" or "major merger" (these terms will be used interchangeably henceforth). In simulations, where the progenitors can be tracked and masses measured, major mergers can be defined in terms of masses of the progenitors and the final halo. We define progenitors as those halos at an earlier time which contributed at least half of their mass to a later halo at the time of interest. The three most common ways to define a halo merger are: (1) the mass ratio of the two largest progenitors, $M_2/M_1 < 1$ (2) the same ratio, but using the contributing mass of the two most mass-contributing progenitors, and (3) M_f/M_i, the ratio of the current halo mass to the total mass of its largest progenitor at an earlier time. We also consider (4) M_f/M_1, the ratio of the current halo mass to the largest contributed mass. In our simulations the merger fraction per $0.7\,h^{-1}\,\mathrm{Gyr}$ with $M_2/M_1 > 0.3$ increases by more than a factor of 3 from $z = 0$ to 1.

One way to quantify how well the two body criteria (M_2, M_1 and M_f, M_i) describe

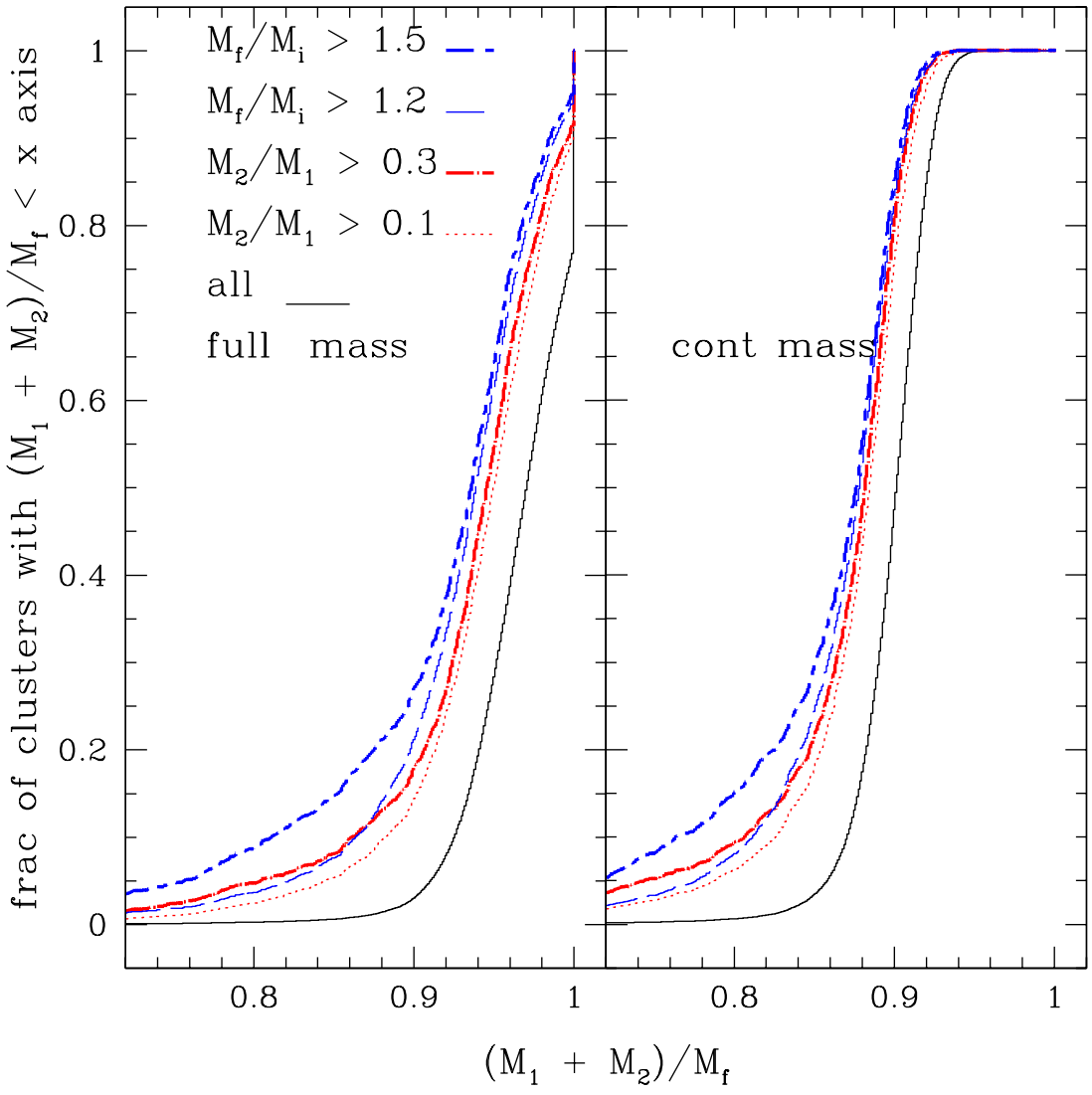

Figure 2.3: Cumulative distribution of merger $(M_1 + M_2)/M_f$ for different subsamples of our $b = 0.15$ halos at $z = 0$. Looking back $0.4\,h^{-1}\,\mathrm{Gyr}$ the subsamples are defined by $M_f/M_i > 1.5$, 1.2 or $M_2/M_1 > 0.3$, 0.1. Curves are in the same order, top to bottom, with the lowest curve being the full sample. **Left**: M_1, M_2 are the full masses of the two largest progenitors. **Right**: M_1, M_2 refer to the contributing mass.

the halo growth is to consider the ratio $(M_1 + M_2)/M_f$. This ratio is 1 for a halo formed only from its two largest predecessors: a two body merger with no other accretion. It is lowered by accretion or multi-body mergers. Fig. 2.3 shows the cumulative distribution of $(M_1 + M_2)/M_f$ for halos with $M > 10^{14}\,h^{-1}\,\mathrm{M}_\odot$ satisfying a variety of merger criteria. We considered both cases where M_1 and M_2 are the full and contributing progenitor masses. As can be seen on the right, for all halos with $M > 10^{14}\,h^{-1}\,\mathrm{M}_\odot$ at $z = 0$, considering mass gains within the last $0.4\,h^{-1}\,\mathrm{Gyr}$, at least 5% of the final halo mass is not from the two largest contributors. As the merger criteria is hardened (the merger is more "major"), the two largest progenitors contribute less and less of the final mass. As can be seen on the left, the same amount of mass as found in the two largest progenitors makes up the entire mass of the final halo in ∼25% of the full sample of halos. Lengthening the time step or looking to higher redshift also increases the fraction of halos getting their mass from halos other than the two largest progenitors. For simplicity, our subsequent analysis uses only the two body criteria to define mergers, so the accuracy of this assumption as examined above should be kept in mind.

Previous work to identify a merger bias through N-body simulations and analytic methods gives a mixed picture. Gottlöber et al. (2002) found a clustering bias for recently ($\Delta t = 0.5$ Gyr) merged objects with $M_f/M_i > 1.25$ and $M \leq M_*$ at $z = 0$. These authors, however, did not try to match the mass distribution of the comparison sample to that of the merged halos — a problem since mergers occur more often for more massive halos, and the bias is known to increase with halo mass. To isolate the effects due to merging, the comparison sample needs to have the same mass distribution as the merged sample, and most subsequent work has ensured this. Percival et al. (2003) found no bias between the correlation functions of recently merged ($\Delta t = 10^8$ yr, $M_2/M_1 > 0.3$) and general samples at $z = 2$ for halos with $M \sim M_*$, $25M_*$, and $150M_*$. Scannapieco & Thacker (2003) confirmed Percival et al.'s results for major mergers in a $z = 3$ sample for a smaller range of masses, but surprisingly found an enhancement of clustering for halos with recent ($\Delta t = 5 \times 10^7$, 10^8 yr) large total mass gain, $M_f/M_i > 1.20$. That is, they find a bias when selecting halos with a recent large mass gains, but not when selecting on recently merged halos' parent masses. Their signal was weak due to limited statistics.

That the previous literature is inconclusive is to be expected, given that the effects of merger history upon clustering are small, and extremely difficult to measure numerically. We expect the largest signal when $M \gg M_*$, but this is where the number density of objects is smallest. In addition, the most extreme mergers are the rarest, increasing the shot-noise in the measurement of $\xi(r)$. If we include more common events, the "merged" and "comparison" samples become more similar, washing out the signal of interest. At higher redshift, the merger rate increases, thus the merged and comparison samples have more overlap unless the merger ratio is increased, leading to worse statistics. To try to overcome these statistical effects, we use our large samples of simulated halos to search for a merger, or temporal, bias.

To define a recent major merger requires both a choice of threshold for one of the merger ratios and a choice of time interval. As we expect the halo crossing time to be $\sim 0.7\,h^{-1}\,\mathrm{Gyr}$

(e.g., Tasitsiomi et al. 2004a; Gottlöber et al. 2001; Rowley et al. 2004), we expect that outputs at this separation or shorter are small enough to catch recently merged halos while they are still unrelaxed. That is, a recent merger might be expected to correspond to a dynamically disturbed halo.

We consider the four merger criteria mentioned above, as well as a wide range of samples and merger definitions. We used 9 different time intervals from $z \approx 1$ to $z = 0$ as given in §2.2. We considered 4 different thresholds for both M_2/M_1 and M_f/M_i using both total and contributing mass of the progenitors: $M_2/M_1 > 0.1, 0.2, 0.3, 0.5$ and $M_f/M_i > 1.2, 1.3, 1.5, 2.0$. Furthermore, we used two minimum masses, $5 \times 10^{13}\, h^{-1}\,\mathrm{M}_\odot$, $10^{14}\, h^{-1}\,\mathrm{M}_\odot$, and two FoF linking lengths, $b = 0.15, 0.2$. Combinations of each of these criteria resulted in over 700 different pairs of "merged" and "comparison" samples. Although this data set is rich, systematic trends are difficult to identify. This is in part because considering more major mergers simultaneously increases the noise because of lower numbers of events.

Evidence of bias is slight in the binned $\xi(r)$. We used three methods to try to isolate the signal: the marked correlation function, the integrated correlation function, and a likelihood fit to a power law for the correlation function. The clustering and merger criteria influence these three quantities in distinct ways. We now describe each method and corresponding results in turn.

2.5.1 Marked correlation function

One problem with computing merger effects in terms of $\xi(r)$ is that, to compute the difference in clustering of merged and random samples, one must define a Boolean merger criterion — a halo is either in the merged sample or not. As halo histories are complex, a more nuanced measure of merger clustering is useful, and this can be provided by using the marked correlation function (Beisbart & Kerscher 2000; Beisbart et al. 2002; Gottlöber et al. 2002; Sheth & Tormen 2004; Harker et al. 2006; Sheth et al. 2005). Each of N objects gets assigned a mark, m_i, for $i = 1, \ldots, N$. Denoting the separation of the pair (i, j) by $r_{i,j}$, the marked correlation function, $M(r)$, is defined by

$$M(r) = \sum_{ij} \frac{m_i m_j}{n(r)\bar{m}^2} \tag{2.6}$$

where the sum is over all pairs of objects (i, j) with separation $r_{ij} = r$, $n(r)$ is the number of pairs, and the mean mark, $\bar{m}$, is calculated over all objects in the sample. The marked correlation function "divides" out the clustering of the average sample, and thus a difference in clustering is detected for $M(r) \neq 1$.

We consider five marks: M_2/M_1 (for both total and contributed masses), M_f/M_i, M_f/M_1 (where M_1 is contributed mass) and $\frac{1}{2}(1 + M_2/M_1)$. The last case had a smaller range of marks, and thus tests sensitivity to extreme events. The results for this mark were similar to the others, suggesting that we are not dominated by outliers. Halos are chosen with mass in a narrow range, $M_{\rm min} < M < \sqrt{2}M_{\rm min}$, to minimize the previously mentioned

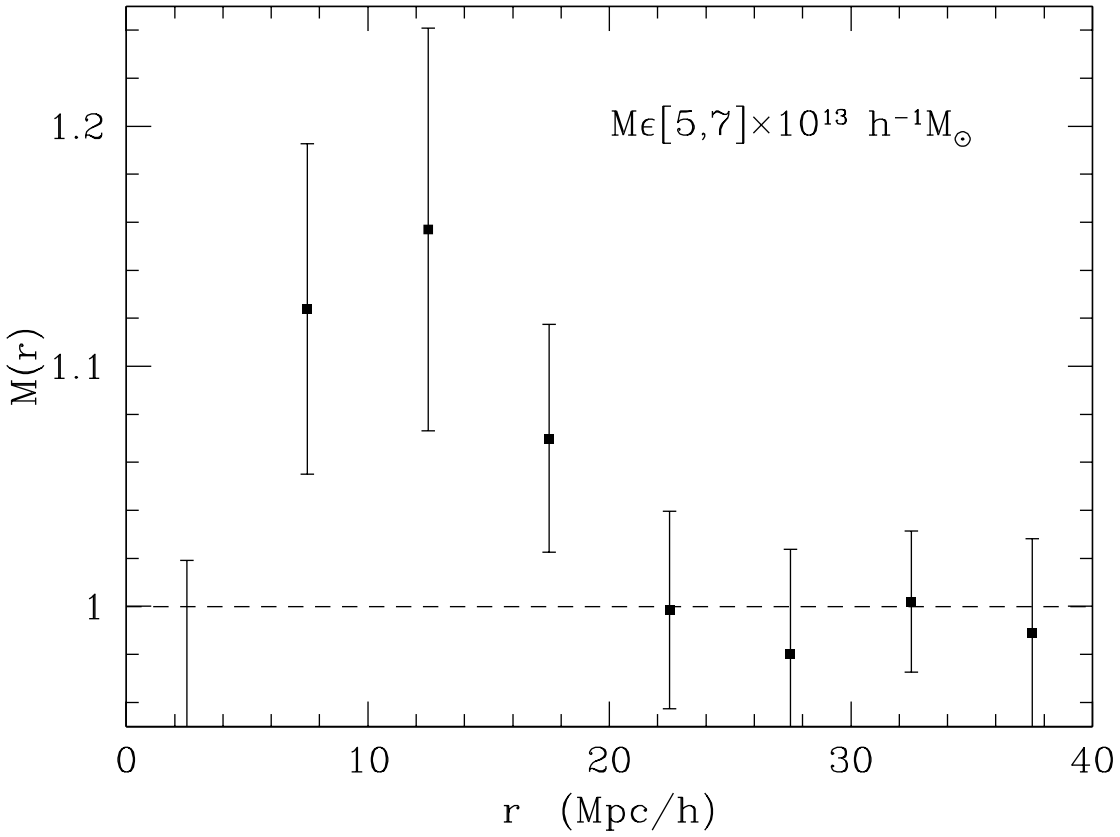

Figure 2.4: Marked correlation function for halos in the range 5–7 $\times 10^{13}\,h^{-1}\,\mathrm{M}_\odot$ at $z = 0$. The mark is the maximum progenitor mass ratio, M_2/M_1, within the last $1\,h^{-1}\,\mathrm{Gyr}$. Error bars come from dividing the sample into 8 octants.

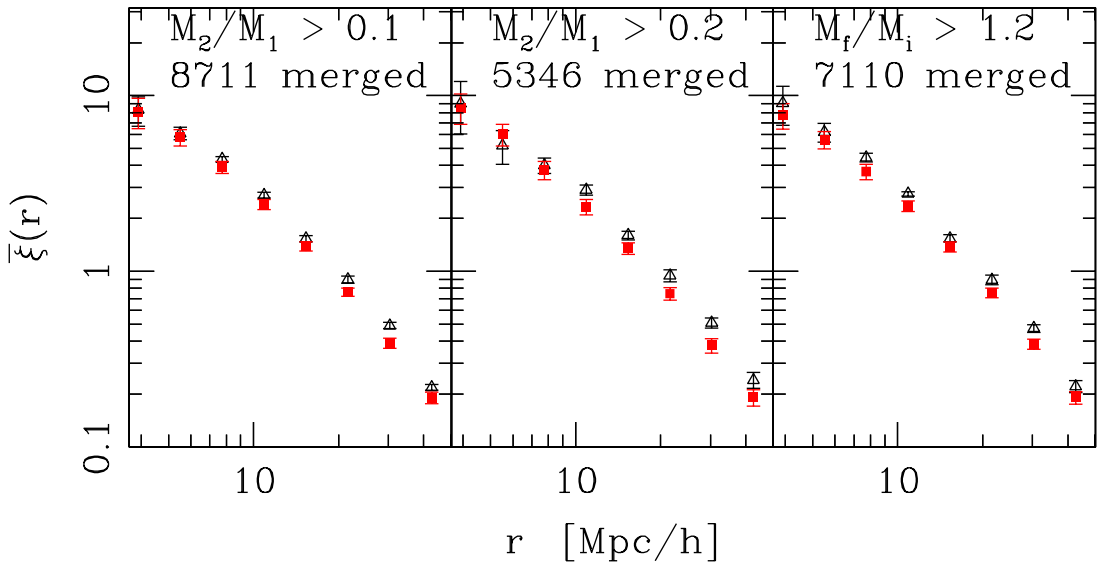

Figure 2.5: Integrated correlation function, $\bar{\xi}(r)$, of recently (within $0.4\,h^{-1}\,\mathrm{Gyr}$) merged halos (triangles) and a comparison sample of the same mass (squares) for $M_2/M_1 > 0.1$ (left), $M_2/M_1 > 0.2$ (middle), and $M_f/M_i > 1.2$ (right), where M_1, M_2 are the full masses of the progenitor halos, for halos in our $b = 0.15$ catalog at $z = 0$. The number of halos that merged out of the 96319 total halos with $M > 5 \times 10^{13}\,h^{-1}\,\mathrm{M}_\odot$ is shown at upper right in for each case. For these three examples, the differences between the two samples are largest at $30\,h^{-1}\,\mathrm{Mpc}$, with significance 3.1σ (left), 2.7σ (middle), and 2.5σ (right).

bias due to merged halos being more massive. The global bias changes less than a percent over the mass ranges we consider.

In our combined sample of several output times and mass ranges, the largest signal comes from using as mark the maximum value of M_2/M_1 within Δt of the present, as shown in Fig. 2.4. As Δt was increased the signal went smoothly to zero. We find similar behavior for $M_2/(M_1+M_2)$, which suggests that any bias is contributed by the systems where $M_2 \ll M_1$. The signal is extremely weak for the other marks we considered. By stacking the signal across multiple output times (see §2.5.3 for details) we are able to find small, but statistically significant detections of excess power for the marks M_2/M_1, $M_2/(M_1 + M_2)$, and M_f/M_i, for halos near $5 \times 10^{13}\, h^{-1}\, \mathrm{M}_\odot$. At higher masses there is weak evidence for an effect, but the large error bars weaken the statistical significance.

As the marked correlation function approach finds only a weak signal, typically an enhanced clustering of order 5–10%, we also explore two indicators which characterize the correlations by fewer parameters: the integrated correlation function observed at a single scale and a likelihood fit to a power law correlation function.

2.5.2 Integrated correlation function

Given an object at some position, the integrated correlation function

$$\bar{\xi}(r) \equiv \frac{3}{r^3} \int_0^r x^2 \xi(x)\, dx \tag{2.7}$$

is the probability beyond random that a second object will be within a sphere of radius r. This quantity enhances any increased clustering at short distances, but gives error bars that are even more highly correlated than those of the correlation function, $\xi(r)$, itself. A typical result is shown in Fig. 2.5, where a significant signal can be seen. As in the previous section, we find a weak signal regardless of merger definition in our more than 700 samples. Considering all the samples and all the separations r, more than 2/3 of the time the difference $\bar{\xi}_{\mathrm{merge}}(r) - \bar{\xi}_{\mathrm{all}}(r)$ was positive.

This method separates the data into radial bins, requiring us to estimate the clustering at many locations. Since the errors on the binned correlation points are highly correlated, we reduced $\bar{\xi}(r)$ to a single measurement by fixing a preferred scale. The signal tends to be largest near $r = 20\, h^{-1}\,\mathrm{Mpc}$ (though the signal is largest at $r = 30\, h^{-1}\,\mathrm{Mpc}$ in the examples in Fig. 2.5), and so we compare $\bar{\xi}(r)$ of the merged and general samples at this radius. On average, when a 2σ signal is seen (5–15% of the time, depending on mass ratio, etc.), $\bar{\xi}(r)$ for the mergers is $\sim$20% higher than for the general sample, although in extreme cases the difference can be as large as a factor of 2 or 3. Due to the noisy statistics it was hard to identify any clear trends.

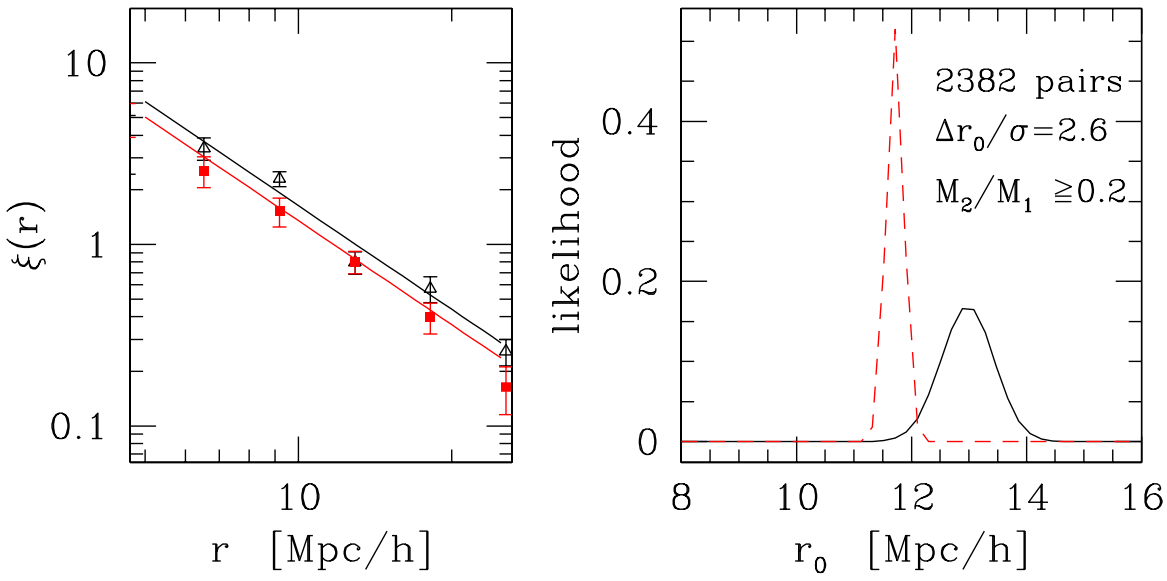

Figure 2.6: **Left**: Correlation function for a recently merged sample (triangles) and a comparison sample (squares) of the same mass. Lines indicate the best-fit $\gamma = 1.9$ power law model, fit directly to the cluster positions (not the binned $\xi(r)$). **Right**: Likelihood for the clustering amplitude, r_0, assuming a slope $\gamma = 1.9$ for the same samples at left. The sample is at $z = 0$, with a minimum mass of $5 \times 10^{13}\, h^{-1}\, \mathrm{M}_\odot$ ($b = 0.15$) and looking back $0.4\, h^{-1}$ Gyr. Mergers are tagged as having $M_2/M_1 \geq 0.2$, M_1, M_2 full progenitor masses.

2.5.3 Likelihood fit to r_0

The integrated correlation function sums all pairs within a spherical region. As an alternate approach, we approximate the correlation function as a power law over some range of radii, and we perform a likelihood fit to this power law correlation function:

$$\xi(r) = \left(\frac{r}{r_0}\right)^{-\gamma} \tag{2.8}$$

over the range of scales $(r_{\rm min}, r_{\rm max})$. This method incorporates information from many scales, so it is similar to the integrated correlation function, but it is combined with the expectation that the correlation function should be a power law and excises the center region. By using the positions of the halos directly in the fit to the likelihood, the errors differ from those in the integrated correlation function as well.

Assuming that the pair counts form a Poisson sample with mean proportional to $1+\xi(r)$, the likelihood L is (Croft et al. 1997; Stephens et al. 1997)

$$\begin{aligned} \ln L(r_0) &= -2\pi\,\bar{n}^2 \int_{r_{\rm min}}^{r_{\rm max}} r^2\ [1+\xi(r)]\ dr \\ &+ \sum_{i<j} \ln\left(\bar{n}^2 r_{i,j}^2\,[1+\xi(r_{i,j})]\right) + {\rm const} \end{aligned} \tag{2.9}$$

where the sum is over measured pairs i, j with separation $r_{i,j}$, and $\bar{n}$ is the measured average density.[5] , and $\xi(r)$ is given by Eq. 2.8. We fit over the range 5–25 h^{-1} Mpc, where the correlation function exhibits an approximately power law behavior. For the comparison sample we multiply the likelihoods for several different realizations in order to reduce the noise, and the we renormalize to unit area. A typical result, where a significant signal can be seen, is shown in Fig. 2.6, demonstrating both the power law fit and the maximum likelihood distribution. For the fits, r_0 was usually $\sim 10\,h^{-1}$ Mpc, within the range where the power law fit was being applied.

Across all of our samples, we find $\gamma \simeq 1.9 \pm 0.1$. To allow us to compare different samples more easily, we reduce the number of free parameters to one by holding $\gamma \equiv 1.9$. A typical example, demonstrating the ratio of the power law fit correlation functions of the merged and general sample, is shown in Fig. 2.7 as a function of lookback time. Since we fix $\gamma = 1.9$ for both the merged and general sample, the ratio $\xi_{\rm merge}/\xi_{\rm all}$ using Eq. 2.8 is scale-invariant within our fit range. While the enhanced clustering of the recently merged sample is small, it remains statistically significant. Typically, the merged sample shows an enhanced clustering of $5-10\%$ in the correlation function for the $0.7\,h^{-1}$ Gyr spacings, though we find no strong evidence of systematic bias evolution with redshift. Moreover, at $z = 0$, where the spacing is smaller ($0.4\,h^{-1}$ Gyr), we find a significantly enhanced $\xi(r)$ for the mergers, often $10-20\%$. Presumably, this increased clustering signal is caused by the

[5] We find that marginalizing or maximizing over $\bar{n}$ as a free parameter results in biased fits for several samples.

smaller time interval. Larger intervals encompass more mergers, leading to smaller errors, but also leading to a smaller signal, since mergers now encompass a more significant fraction of the comparison population. As mentioned above, looking at earlier times also makes the merged and comparison population overlap increase dramatically.

By averaging $\xi_{\rm merge}/\xi_{\rm all}$ across all of the $0.7\,h^{-1}$ Gyr spacings from $z \approx 1$ to $z = 0.04$, we are able to study the size of the merger bias simply as a function of merger ratio. Figure 2.8 shows the increase of $\xi_{\rm merge}/\xi_{\rm all}$ with M_2/M_1 (full mass) and M_f/M_i both for mergers within $0.4\,h^{-1}$ Gyr of the present and for the redshift-averaged $0.7\,h^{-1}$ Gyr spacings. The merger bias clearly increases with increasing merger ratio, with the smaller time step yielding stronger clustering as described above.

In summary, we find a weak bias in most cases for recent major mergers and recent large mass gains. While Percival et al. (2003) found no such merger bias, our signal is consistent with their upper limit of 20% on the bias effects of recent mergers. The work of Scannapieco & Thacker (2003) saw a small bias for large mass gains but noted that their statistics limited their ability to determine the significance. Our larger simulation volume allowed us to incorporate the effects of sample variance, which had been neglected in previous work. Sample variance increased the errors by 40% or more, which limited the significance of the signal. Nonetheless, we still found a small bias for *both* mergers and large mass gains.

2.6 Summary & Conclusion

The large-scale structure of the Universe is built upon a skeleton of clustered dark matter halos. For the past two decades we have known that rarer, more massive dark matter halos cluster more strongly than their lower mass counterparts. Halos of a fixed mass, however, can differ in their formation history and large-scale environment, and recent work on halos smaller than galaxy clusters has shown that this can lead to further changes in their clustering.

In this chapter we have used two large-volume, high-resolution N-body simulations to study the clustering of massive halos as a function of formation history. We confirmed earlier results that the lower concentration massive halos are more clustered than the population as a whole; extending these results to higher masses and lower redshifts than had been probed previously (Wechsler et al. 2006). (Previous work had looked at similar regimes of $M/M_*(z)$ but for smaller M and thus higher redshift; note again that exact scaling with $M/M_*(z)$ is not expected for non power law $P(k)$ and $\Omega_m \neq 1$.) Similarly, we confirmed the enhanced clustering of halos with later formation times, though the signal was not as strong as for concentration. The signal for bias based on a halo reaching half of its mass is weaker than that seen in Gao et al. (2005) (again at higher z) and not statistically significant in our case.

We also investigated whether recent merger activity affected the clustering of massive halos — a topic with a muddied history in the literature. While we found statistically significant ($> 2\sigma$) merger effects on clustering in many cases we considered, both for recent major mergers and large mass gain, in most cases this signal was weak: a 5–10% increase in

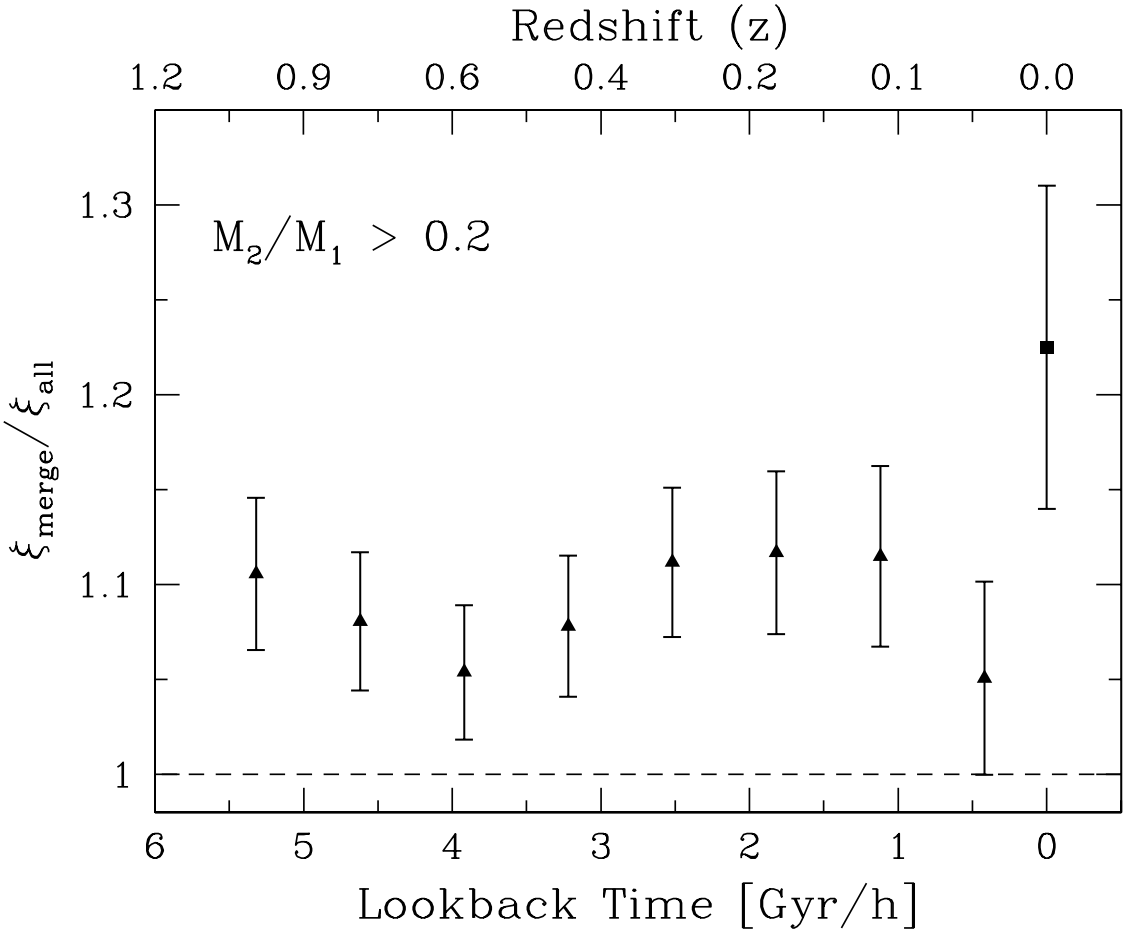

Figure 2.7: Ratio of the power law fit correlation functions for the merged and comparison samples, as a function of lookback time (redshift); $\Delta t = 0.7\,h^{-1}$ Gyr (triangles), $0.4\,h^{-1}$ Gyr (square). Mergers satisfy the criterion $M_2/M_1 > 0.2$, with M_2, M_1 total progenitor mass, for the $M > 5 \times 10^{13}\,h^{-1}\,\mathrm{M}_\odot$ halos in our $b = 0.15$ catalog. We find no evidence of systematic bias evolution with redshift. The enhanced clustering at $z = 0$ arises presumably from the shorter time interval used.

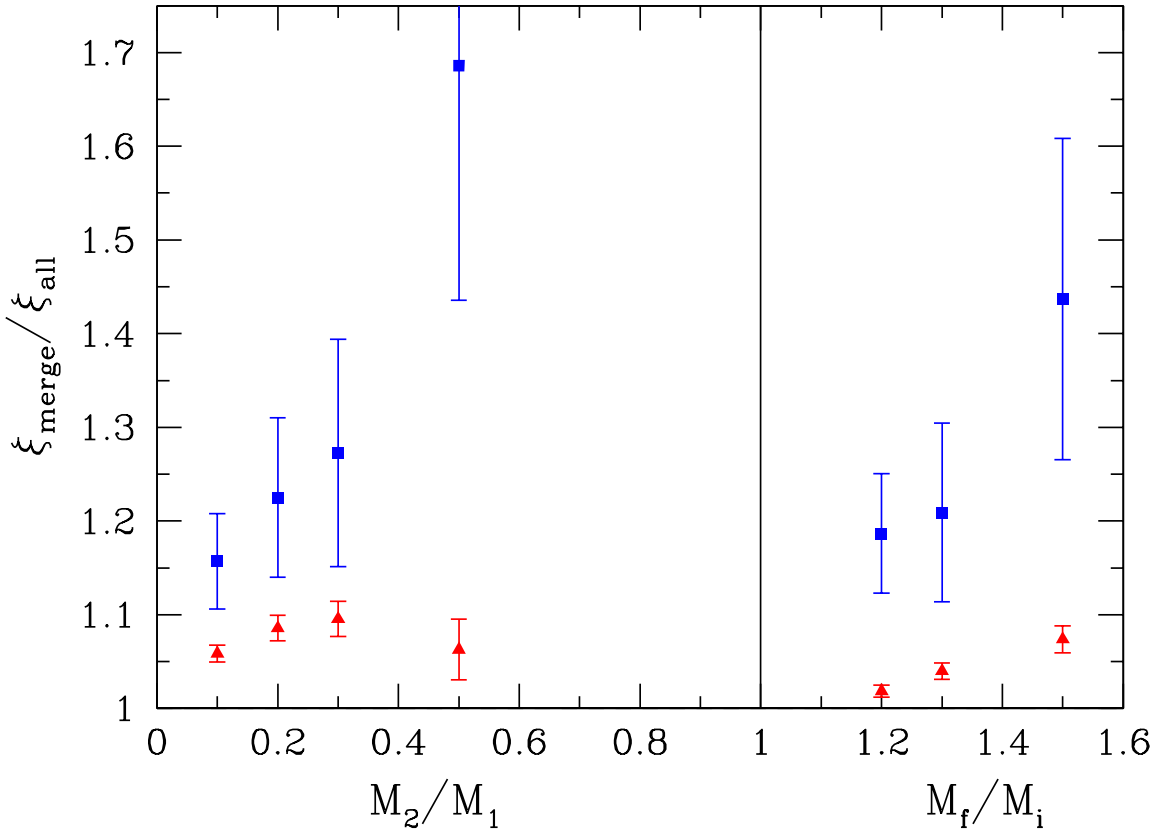

Figure 2.8: Ratio of the power law fit correlation functions for the merged and comparison samples as a function of merger ratio, M_2/M_1 (left points; full progenitor mass) and M_f/M_i (right points), for halos above $5 \times 10^{13}\, h^{-1}\, \mathrm{M}_\odot$ in our $b = 0.15$ catalog. Mergers are counted within $0.4\, h^{-1}\,$Gyr of $z = 0$ (squares) and an average across all $0.7\, h^{-1}\,$Gyr spacings from $z \approx 1$ to $z = 0.04$ (triangles). In both cases, merger bias increases with the severity of the merger.

bias. Our strongest signal came from using a likelihood fit of the correlation function to a power law, particularly for major mergers within $0.4\,h^{-1}\,\mathrm{Gyr}$ of the present, where we saw a typical merger bias of up to 20%. This bias signal is not necessarily at odds with the lack of signal in previous work, which looked for larger bias than that seen on average here.

Even with a $(1.1\,h^{-1}\,\mathrm{Gpc})^3$ volume, massive halos remain rare objects and small changes in their correlations are difficult to detect. We were plagued by the competing effects that increasing the severity of the merger (and hence underlying signal) decreases the number of pairs, worsening the statistics. General trends remain elusive, since changing various criteria (merger definition, minimum mass, time step) generally changed the number of halos involved, thus changing the errors. However, we did find that the strength of the merger bias typically increased with increasing merger ratio, that is, more major mergers are more strongly biased. Finally, we note that the correlations found between the last large (20%) mass gain and the different definitions of formation redshifts provide a connection between the assembly bias studied in §2.4 and the merger bias in §2.5. This bias is not expected from direct application of extended Press-Schechter theory, and it provides a phenomenon that a more precise analytic model of mergers should reproduce.

Chapter 3

Close Pairs as Proxies for Galaxy Cluster Mergers

Abstract

Galaxy cluster merger statistics are an important component in understanding the formation of large-scale structure. Cluster mergers are also potential sources of systematic error in the mass calibration of upcoming cluster surveys. Unfortunately, it is difficult to study merger properties and evolution directly because the identification of cluster mergers in observations is problematic. We use large N-body simulations to study the statistical properties of massive halo mergers, specifically investigating the utility of close halo pairs as proxies for mergers. We examine the relationship between pairs and mergers for a wide range of merger timescales, halo masses, and redshifts ($0 < z < 1$). We also quantify the utility of pairs in measuring merger bias. While pairs at very small separations will reliably merge, these constitute a small fraction of the total merger population. Thus, pairs do not provide a reliable direct proxy to the total merger population. We do find an intriguing universality in the relation between close pairs and mergers, which in principle could allow for an estimate of the statistical merger rate from the pair fraction within a scaled separation, but including the effects of redshift space distortions strongly degrades this relation. We find similar behavior for galaxy-mass halos, making our results applicable to field galaxy mergers at high redshift. We investigate how the halo merger rate can be statistically described by the halo mass function via the merger kernel (coagulation), finding an interesting environmental dependence of merging: halos within the mass resolution of our simulations merge less efficiently in overdense environments. Specifically, halo pairs with separations less than a few h^{-1} Mpc are more likely to merge in underdense environments; at larger separations, pairs are more likely to merge in overdense environments.

3.1 Introduction

Galaxy clusters are of great interest in cosmology as they are the largest and most recently formed structures in the cosmological hierarchy. The clustering and number density evolution of clusters are sensitive to both the growth function and the expansion history of the universe. Clusters contain a representative sample of baryons and dark matter and are thus also fascinating laboratories in which to study the influence of baryonic physics on the formation of large-scale structure, substructure, and its effect on the gravitational potential and dark matter halo shape. Statistical measures such as the mass function, the rate of structure growth, and the clustering of large structures, are fundamental predictions of cosmological models. Cluster observations are therefore expected to provide some of the most important constraints on fundamental cosmology and astrophysics (see Borgani 2006, for a recent review).

Cluster formation histories are frequently punctuated by large jumps in mass from major mergers (e.g., Cohn & White 2005). These mergers are one of the primary mechanisms for the buildup of mass in clusters and superclusters. In the standard paradigm (Kaiser 1984; Efstathiou et al. 1988; Cole & Kaiser 1989; Mo & White 1996; Sheth & Tormen 1999), observable properties such as the degree of spatial clustering depend *only* on the cluster mass. However, recent theoretical studies indicate that many cluster observables, such as spatial clustering, concentration, galaxy velocity dispersion, gas distribution and its attendant observables such as X-ray emissions and SZ decrement, depend on the cluster's formation time, mass accretion history, large scale environment (collectively referred to as "assembly bias"; Wechsler et al. 2002; Zhao et al. 2003b; Sheth & Tormen 2004; Gao et al. 2005; Wechsler et al. 2006; Croton et al. 2007; Harker et al. 2006; Wetzel et al. 2007; Gao & White 2007; Wang et al. 2007a; Jing et al. 2007; Hahn et al. 2008; Macciò et al. 2007; Sandvik et al. 2007). In addition, there is a dependence on recent merger history ("merger bias"; Scannapieco & Thacker 2003; Rowley et al. 2004; Furlanetto & Kamionkowski 2006; Wetzel et al. 2007; Poole et al. 2007; Jeltema et al. 2008; Hartley et al. 2008). Recent studies have claimed observational detection of assembly bias, though with mixed results (Berlind et al. 2006; Yang et al. 2006). Theory can predict cluster properties as a function of their mass, which is dominated by dark matter and thus cannot be directly measured. Since all methods of observing clusters are sensitive to the effects of assembly or merger bias, it is necessary to develop a more detailed understanding of the mechanisms of structure formation. Specifying a correlation function and mass function, and the evolution of these quantities, may not be sufficient to connect theory to observation. Understanding cluster merger properties is therefore crucial to utilize these objects as probes of cosmology.

We focus primarily on galaxy cluster mergers. Wetzel et al. (2007) used a large simulation volume to probe high-mass halos with good statistics. They found that halos of mass $M > 5 \times 10^{13}\,h^{-1}\,\mathrm{M}_{\odot}$ that have undergone a recent (within 1 Gyr or less) major merger or large mass gain exhibit an enhancement in their spatial clustering of up to $\sim$ 10–20% on scales of 5–25 h^{-1} Mpc compared with the entire halo population at the same mass. They noted that this merger bias persists for the redshift range $0 < z < 1$, and that the bias

increases with larger merger mass ratios or shorter merger timescales. If this merger bias remains unaccounted for, then mass-observable relations that connect theory with observation calibrated on the basis of clustering may be suspect.

Moreover, the gas properties of a recently merged halo cluster can be quite different from the general population. This can be mitigated by selecting "relaxed" halos (presumably those that have not had recent major mergers) when calibrating observables. However, the scaling relations from this selected sample may be biased with respect to that from the overall cluster population. In addition, if a merger accidentally entered the "clean" sample (for example, because it occurred along the line of sight), it could substantially bias the calibration, and hence the ensuing mass determination. It is thus important to predict the fraction of halos which have had recent merger activity. Observing cluster mergers as a function of redshift, studying the merger bias, and correlating mergers with other tracers of density and environment will also shed light on the nature of structure formation.

A number of authors (e.g., Patton et al. 1997, 2000, 2002; Infante et al. 2002; Lin et al. 2004a; De Propris et al. 2005, 2007; Conselice 2006; Bell et al. 2006; Masjedi et al. 2006) have studied the statistics of galaxy merging using close pairs as a proxy for mergers. In this work we extend those analyses to the cluster scale. It is important to quantify the conditions for which the pair proxy assumption is valid. Berrier et al. (2006) used simulations to examine the utility of galaxy pairs in measuring the redshift evolution of halo merger rates out to $z \approx 3$. They tracked the formation and evolution host halos of dark matter, as well as self-bound density peaks within host halos (subhalos), which includes both satellite objects and the central host halo itself. Using the assumption that galaxies are found at the centers of subhalos, they tracked *subhalo* mergers, finding that galaxy pair counts can probe the rates at which satellite galaxies merge with the central galaxy. These pairs can also constrain the galaxy Halo Occupation Distribution, the statistical number of galaxies found within a host halo of a given mass. However, galaxy pairs cannot be used to measure the merger rates of separate massive *host* halos.

The goal of this chapter is to investigate whether close spatial pairs of halo objects (galaxy clusters) can be used to observationally study the properties of mergers. Identifying a cluster merger in an observation is not straightforward because it relies principally on the object appearing morphologically "disturbed" (Rowley et al. 2004). Furthermore, it is difficult to estimate the completeness and the contamination of such an observed merger population. If close pairs prove to be a sufficient proxy for mergers, they would provide a clean tool to study merger statistics. We concentrate primarily on massive halos ($M > 5 \times 10^{13}\, h^{-1}\, \mathrm{M}_{\odot}$), corresponding to galaxy groups and clusters, in contrast to previous work which has focused on pairs as a proxy for galaxy mergers. However, our results also apply to any class of object that singly occupies a halo, particularly field galaxies at high redshift.

3.2 Simulations

Our study is conducted using two high-resolution N-body simulations of cold dark matter in a flat ΛCDM cosmology with parameter values $\Omega_m = 0.3$, $\Omega_b = 0.046$, $h = 0.7$, $n = 1$ and $\sigma_8 = 0.9$. Our simulations employ the HOT code (Warren & Salmon 1993) in a $(1.1\,h^{-1}\,\mathrm{Gpc})^3$ and a $(2.2\,h^{-1}\,\mathrm{Gpc})^3$ cube with periodic boundary conditions, using a Plummer softening length of $35\,h^{-1}\,\mathrm{kpc}$. Gaussian initial conditions were randomly generated for the 1024^3 particles of mass $10^{11}\,h^{-1}\,\mathrm{M}_\odot$ (smaller simulation) and $8 \times 10^{11}\,h^{-1}\,\mathrm{M}_\odot$ (larger simulation) at an initial redshift of $z = 34$. Simulation outputs were stored in intervals of 1 Gyr between redshifts $z \approx 1$ and $z = 0$, with the last interval of each simulation being shorter at ≈ 0.6 Gyr. All time intervals cited below represent the total time elapsed between two simulation outputs. Thus a merger timescale of $\Delta t = 1$ Gyr indicates that two separate halos have merged within 1 Gyr, an upper limit to the actual time of merger.

We generate a halo catalog for each output using the Friends-of-Friends (FoF) algorithm (Davis et al. 1985) with a linking length of $b = 0.15$ of the mean interparticle spacing. These groups correspond to a density threshold of $\sim 3/(2\pi b^3)$ and enclose primarily virialized material. In this work we will quote these FoF masses, which are about 20% smaller than the more commonly used FoF($b = 0.2$) masses (see White 2001, for more details). Since we are examining mergers, we use a smaller linking length to decrease contamination that arises from close neighboring halos being bridged by a narrow string of particles (although using a larger linking length of $b = 0.2$ changes our results by only a few percent, see Fig. 3.4). The halo catalogs of the smaller simulation include all halos of mass greater than $M \approx 5 \times 10^{12}\,h^{-1}\,\mathrm{M}_\odot$ (> 50 particles), though in our study we are concerned primarily with halos of mass $M > 5 \times 10^{13}\,h^{-1}\,\mathrm{M}_\odot$, of which there are around $75,000\,h^{-3}\mathrm{Gpc}^{-3}$ at $z = 0$. Our larger $(2.2\,h^{-1}\,\mathrm{Gpc})^3$ but less resolved simulation catalogs include all halos of mass $M > 4 \times 10^{13}\,h^{-1}\,\mathrm{M}_\odot$ (> 50 particles). We do not consider substructure within host halos.

Merger trees were constructed from the set of halo catalogs by specifying a parent-child relationship, where a "parent" is any halo that contributed mass to a halo at a later time (a "child"). We define a parent contributing more than half of its mass as a "progenitor". Under this restriction, a progenitor can never have more than one child. We define a merger as a child having more than one progenitor. In cases where we select on a child that had more than two progenitors, we apply the two body approximation by considering only the two progenitors that contributed the most mass to the child. Using instead the two most massive progenitors, as opposed to the two most mass-contributing progenitors, changes the progenitor identification in less than 1% of all mergers that we consider. In addition to this progenitor merger tree, a list of all contributing parents (not just progenitors) is stored for each child. This flexible storage of parent data allows us to study two body mergers, mergers with more than two progenitors, or mass accretion including all parents. However, when considering short timescales ($\lesssim 1$ Gyr), the two body criterion is a good approximation (see Chapter 2 for more details).

All errors cited are 1σ errors derived from dividing the simulations into 8 octants and

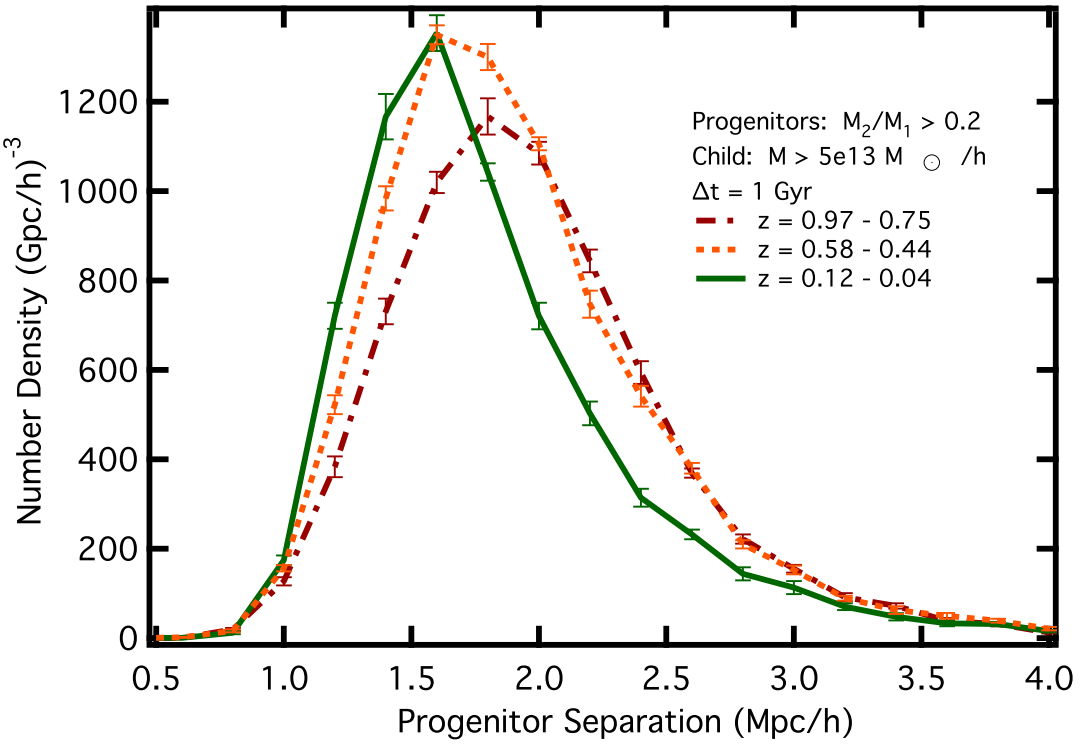

Figure 3.1: Number density of progenitor pairs as a function of (comoving) binned separation. We consider children with masses above $5 \times 10^{13}\, h^{-1}\, \mathrm{M}_{\odot}$ and restrict ourselves to cases where the two most mass-contributing progenitors have total mass ratios $M_2/M_1 > 0.2$ (major mergers). A fixed merger time interval of $\Delta t = 1$ Gyr is used for child halos at $z = 0.04$ (solid curve), $z = 0.44$ (dotted curve), $z = 0.75$ (dot-dashed curve).

computing the dispersion of the quantity of interest within each octant. Since we probe scales much smaller than the octants, we treat them as uncorrelated volumes.

3.3 Close Pairs as Predictors of Mergers

To examine whether close pairs of galaxy clusters form reliable predictors of mergers, we first extend the work of Chapter 2 on halo mergers, using the same simulation and halo catalogs (described in §3.2). We identify child halos of mass $M > 5 \times 10^{13}\, h^{-1}\, \mathrm{M}_{\odot}$ that are products of recent mergers with progenitor masses M_1 and M_2, where $M_2/M_1 > 0.2$ (major mergers). We explore the distribution of progenitor separations in Fig. 3.1, which shows the number density of progenitors as a function of binned progenitor separation. For time intervals of 1 Gyr, there is a characteristic comoving progenitor separation ($\sim 1.5\, h^{-1}\, \mathrm{Mpc}$) that does not evolve significantly with redshift. Without the influence of gravitational attraction,

halos with typical velocities of ~ 1000 km s^{-1} will travel 1 Mpc within 1 Gyr. Furthermore, the number density of mergers evolves only weakly with redshift. These factors suggest that close pairs might be a reasonable proxy for mergers.

These results represent a post-diction, where we know in advance which halos will merge. We now investigate whether close pairs of objects can reliably be used to *predict* mergers. The following subsections investigate how frequently pairs will merge as a function of pair mass, (comoving) separation, redshift, and merger time interval. We consider a given pair to have merged if both halos are progenitors of the same child at a later time-step. Since observations of galaxy clusters are generally limited by a threshold luminosity, we identify pairs of halos whose individual halo masses are above a given mass cut. We first examine the pair-merger hypothesis (that close pairs are merger proxies) for the best-case scenario in which halo positions and masses are known with complete accuracy, as in our simulations. This will provide a firm upper limit to the utility of pairs in predicting mergers. Then in §3.4 we consider observational complexities such as scatter in the halo mass, redshift space distortions, and redshift space errors, which significantly degrade the signal.

3.3.1 Pair Mergers at $z = 0$

First, we select halos at $z = 0.04$ and consider mergers to $z = 0$ ($\Delta t = 0.6$ Gyr). Figure 3.2 (top) shows the number density of pairs as a function of pair separation, $n_p(r)$, along with the number densities of pairs that merged, $n_m(r)$ (solid curves), and did not merge (dashed curves) within the time interval. The number density of pairs terminates at small separations because halos have finite radii (halo exclusion). The upper set of curves are halos of mass $M > 5 \times 10^{13}\, h^{-1}\, \mathrm{M}_\odot$ and the lower have $M > 10^{14}\, h^{-1} M_\odot$; the results are qualitatively similar. There is a limited range of separations larger than the halo exclusion limit in which the majority of pairs merge. Also plotted (center) are the same number densities, but as an integrated function of separation, demonstrating the relationship for pairs *within* the given separation r. In 0.6 Gyr at $z = 0$, massive halo pairs will only merge with certainty for separations $\lesssim 2\, h^{-1}$ Mpc.

Figure 3.2 (bottom) also shows the fraction of pairs that merge *within* the given separation, $n_m(< r)/n_p(< r)$ (falling curves). This fraction is the "efficiency" of the close-pair method in identifying merger candidates, since it shows the likelihood that a pair within the given separation will merge. It can also be thought of as a measure of contamination of the candidate sample, because its difference from 1 identifies the fraction pairs that do not merge. The rising curve shows the fraction of mergers over the *total* number density of mergers, $n_m(< r)/n_{\mathrm{m,tot}}$. This can be interpreted as the merger "completeness", as it shows the fraction of the total number of mergers found by identifying pairs within the given separation. Figure 3.2 confirms the intuitive result that because of greater accelerations, larger halos are able to merge from larger separations, which holds at all redshifts and time intervals (see Fig. 3.4).

If close pairs were ideal predictors of mergers, the rising and falling curves of Fig. 3.2 (bottom) would be step functions, crossing near a fraction (y-value) of 1 and demonstrating

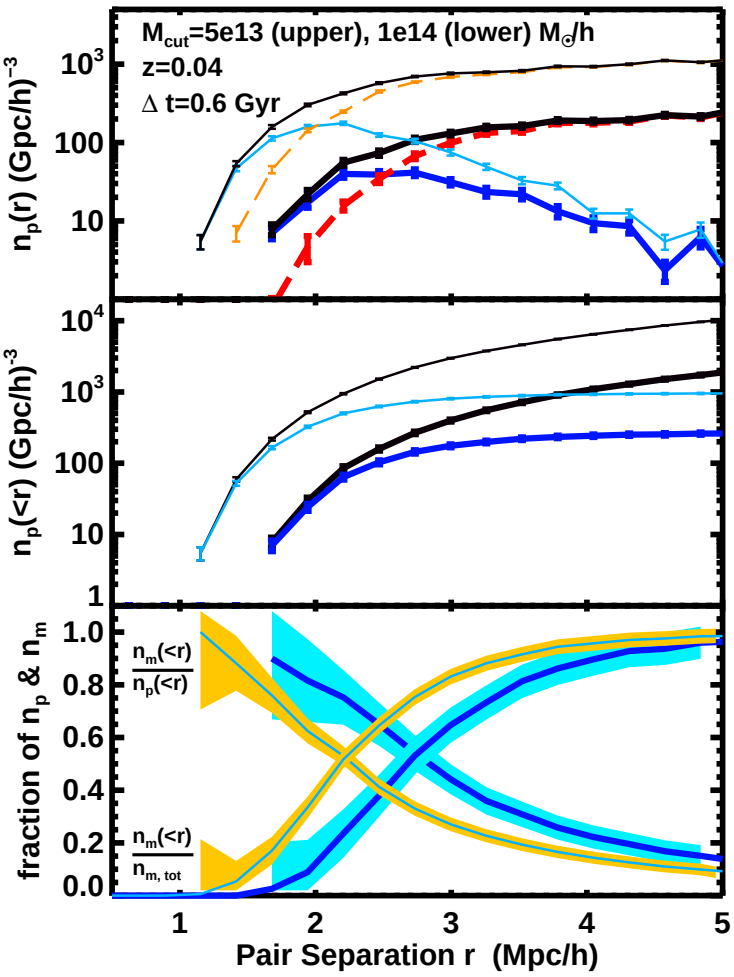

Figure 3.2: **Top**: Number density of pairs at $z = 0.04$ as a function of binned separation, $n_p(r)$ (black solid curve), the subset of these that merged in $\Delta t = 0.6$ Gyr, $n_m(r)$ (blue solid curve), the remainder that did not merge (red dashed curve). Upper curves (thin) are for pairs of mass $M > 5 \times 10^{13}\, h^{-1}\, \mathrm{M}_\odot$, and lower curves (thick) are for more massive pairs, $M > 10^{14}\, h^{-1}\, \mathrm{M}_\odot$. The intersection with the dashed curve shows the separation beyond which the majority of pairs do not merge, highlighting the limited range of separations for which merging is likely. **Middle**: Same, but integrated for all separations smaller than the abscissa. **Bottom**: Fraction of pairs separated by less than r that merged, $n_m(< r)/n_p(< r)$ (falling curves), indicating the efficiency of pairs as merger candidates, and the ratio of identified mergers to all mergers above the mass cut, $n_m(< r)/n_{\mathrm{m,tot}}$ (rising curves), indicating the completeness of the candidate sample. Error bars and shaded regions indicate the 1σ error of cosmic variance from dividing the simulation into octants.

a clear dichotomy between those pairs that merge and those that do not. However, because of dynamical effects halos do not simply accelerate toward one another; they merge with neighbors from a broad distribution of separations. Indeed, the effects of local environment can hinder the merging of close pairs that would ordinarily occur via non-linear two-body gravitational interaction (see §3.5 for more details).

The intersection of the efficiency and completeness curves represents an easily identifiable pair separation that compromises between maximizing completeness while minimizing contamination. At this intersection the fraction of pairs that merge, $n_m(< r)/n_p(< r)$, equals the fraction of total mergers, $n_m(< r)/n_{\rm m,tot}$, although the relevant populations are different. If this intersection occurs at a fraction close to 1, most pairs within the separation will merge, and those pairs will represent the majority of all mergers that occur in the time interval. However, if this fraction is low, pairs within the separation are not a representative indicator of mergers. Since the intersection of these two curves occurs at a fraction of ~ 0.5 for massive pair mergers within $\Delta t = 0.6$ Gyr at $z = 0$, we conclude that pairs at these redshifts and masses cannot be used to reliably predict mergers.

3.3.2 Redshift Dependence of Pair Mergers

We next examine whether the pair-merger hypothesis fares better at high redshift. We consider a longer merger timescale of $\Delta t = 1$ Gyr for massive halo pairs at $z \approx 1, 0.6$, and 0.1. Figure 3.3 (top) shows the pair merger fractions as a function of (comoving) separations. The pair merger efficiency (falling curves) increases significantly with redshift, while the merger completeness (rising curve) remains approximately invariant. For a given merger timescale, mergers come from pairs of essentially the same (comoving) separation, regardless of redshift (see Fig. 3.1). However, since gravitational interactions are governed by physical (not comoving) separations, Fig. 3.3 (bottom) shows the same merger fractions as a function of physical separation. The merger efficiency trend is reversed: pairs within a given physical separation are more likely to merge at low redshift, and mergers come from pairs of much larger physical separations at low redshift. The intersection of the efficiency and completeness curves occurs at a higher fraction at high redshift than at low redshift (75% vs. 60%), indicating that, for a fixed merger timescale, massive halo pairs provide a slightly better proxy for merger rates at higher redshift.

3.3.3 Mass & Linking Length Dependence of Pair Mergers

While it appears that cluster-mass halo pairs might provide a reasonable proxy for mergers at $z \approx 1$, we next examine whether these results are robust as a function of halo mass. Figure 3.4 (top) shows the pair merger fractions for halo masses down to $M > 5{\times}10^{12}\,h^{-1}\,{\rm M}_\odot$ at $z \approx 1$, where the pair separation is shown as a multiple of the minimum mass cut virial radius (r_{500}). Figure 3.4 (middle) shows the same but for higher halo masses and a shorter time interval at $z \approx 0$. While pairs of higher mass halos merge from larger physical pair separations, when scaled by the halo virial radius we find that the pair merger efficiency and

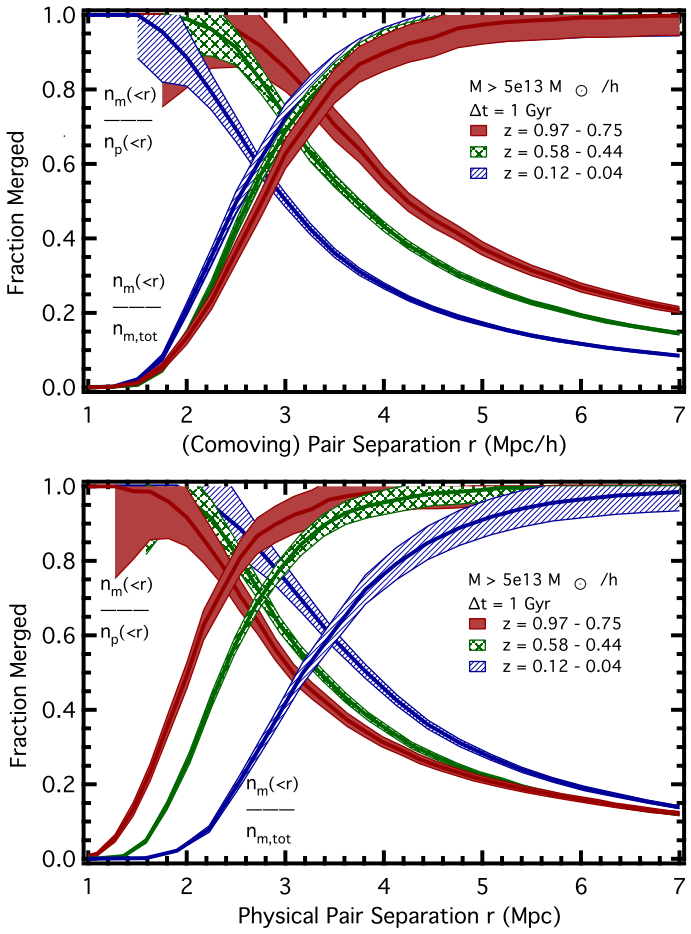

Figure 3.3: **Top**: Fraction of pairs separated by less than r that merged (falling curves), indicating efficiency, and the ratio of identified mergers to all mergers above the mass cut within $\Delta t = 1$ Gyr (rising curves), indicating completeness, for various redshifts. The total number density of such mergers is $458\,h^{-3}$ Gpc^{-3} ($z = 0.97 - 0.75$), $950\,h^{-3}$ Gpc^{-3} ($z = 0.58 - 0.44$), $1464\,h^{-3}$ Gpc^{-3} ($z = 0.12 - 0.04$). Note the approximate invariance of the total merger fraction (rising curve) with redshift. **Bottom**: Same, but as a function of physical separation. While pairs of a given comoving separation merge more frequently at high redshift, this trend reverses when considering physical separations.

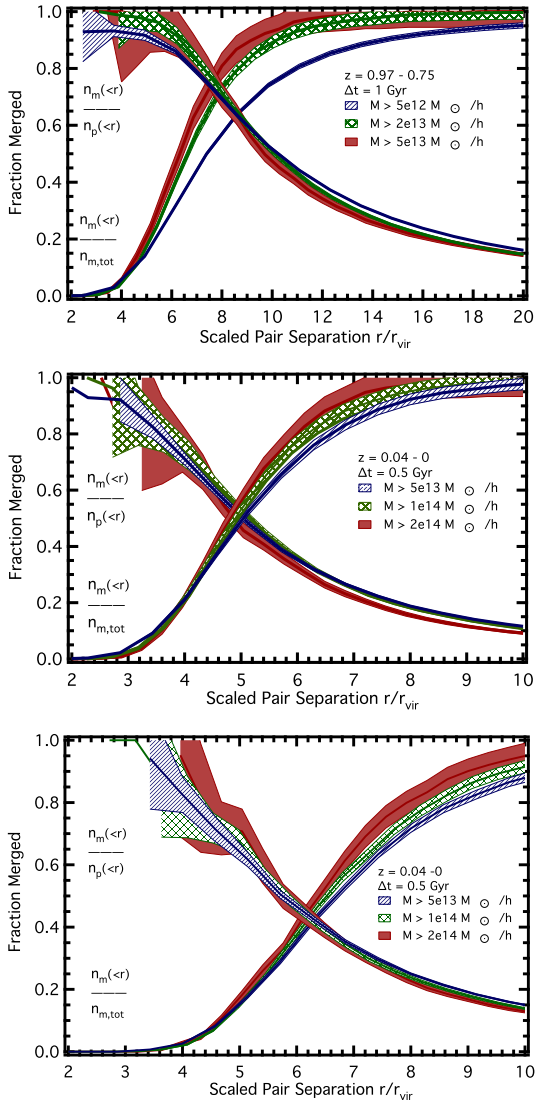

Figure 3.4: **Top**: Fraction of pairs separated by less than $r/r_{\rm vir}$ that merged (falling curves), indicating efficiency, and the ratio of identified mergers to all mergers above the mass cut within $\Delta t = 1$ Gyr (rising curves), indicating completeness, at $z \approx 1$ for various mass cuts. The total number density of such mergers is $45,750\,h^{-3}$ Gpc^{-3} ($M > 5\times10^{12}\,h^{-1}\,{\rm M}_\odot$), $3957\,h^{-3}$ Gpc^{-3} ($M > 2\times10^{13}\,h^{-1}\,{\rm M}_\odot$), $458\,h^{-3}$ Gpc^{-3} ($M > 5\times10^{13}\,h^{-1}\,{\rm M}_\odot$). **Middle**: Same, but for for higher mass halo pairs merging within $\Delta t = 0.5$ Gyr of $z = 0$ in the $(2.2\,h^{-1}\,{\rm Gpc})^3$ simulation. The total number density of such mergers is $1000\,h^{-3}$ Gpc^{-3} ($M > 5\times10^{13}\,h^{-1}\,{\rm M}_\odot$), $280\,h^{-3}$ Gpc^{-3} ($M > 1\times10^{14}\,h^{-1}\,{\rm M}_\odot$), $56\,h^{-3}$ Gpc^{-3} ($M > 2\times10^{14}\,h^{-1}\,{\rm M}_\odot$). **Bottom**: Same as middle, but for a linking length of $b = 0.20$. Masses and virial radii have been scaled to that of $b = 0.15$ for direct comparison.

completeness exhibit a nearly universal relation as a function of halo mass. This implies that any of our results in §3.3 for a given mass can be approximately scaled to those of another mass.

This universal merger relation also implies that the total merger fraction can be estimated by noticing that the following relation is satisfied at the crossing point of the curves: $(n_m(< r)/n_p(< r))/(n_m(< r)/n_{\rm m,tot}) = n_{\rm m,tot}/n_p(< r) = 1$. For example, from the middle panel of Fig. 3.4 we find that $n_{\rm m,tot} = n_p(< r)$ when evaluated at a scaled pair separation of $5r_{\rm vir}$. One can thus estimate the merger rate by counting pairs interior to $5r_{\rm vir}$. This is a potentially powerful result since it is approximately invariant for all mass-scales.[1] However, this radius is a function of the timescale considered, and is likely to depend on the cosmological parameters. Furthermore, although their number densities agree, the pair population within $5r_{\rm vir}$ does not directly correspond to the total merger population. This makes it impossible to use the pair population to directly study any other properties of mergers, for example, spatial clustering. Redshift space distortions will significantly undermine the utility of these results (see §3.4).

The only strong deviation from this nearly universal mass relation occurs for merger completeness of $5 \times 10^{12}\,h^{-1}\,{\rm M}_\odot$ halos (top), which results in an intersection of merger efficiency and completeness at a lower fraction (10–15% decrease) for lower-mass halos, a trend which we find does not depend strongly on redshift or merger timescale. The use of pairs as proxies for merger rates becomes increasingly unreliable as we approach massive galaxy-size halos, an important result for massive *galaxy* mergers at high-redshift, where galaxies are found primarily in distinct host halos.

These results augment those of Berrier et al. (2006), who found that the evolution of close galaxy pairs cannot be used to measure the host halo merger rate. Specifically, they found that the host halo merger rate evolves as $(1+z)^3$, while the number of close galaxy pairs evolves little with redshift. This arises because, at low redshift, the merger rate of host halos is low, but there are multiple galaxy pairs merging *within* massive host halos. At high redshift, the host halo merger rate is high, but the number density of halos massive enough to host more than one bright galaxy is low. Our results imply that even when considering major mergers of massive galaxies at high redshift, where each halo hosts a single bright galaxy, the close pair population will not reliably trace the merger population.

We have also compared two different linking lengths, to explore the dependence of our results on the FoF finder. In Fig. 3.4 (bottom), we show the results using a linking length of $b = 0.20$. Since changing the linking length changes the mass of a given halo, we have scaled the mass threshold for $b = 0.20$ to match the number densities of the $b = 0.15$ sample, thereby probing the same halo population. We have also scaled the halo separations by $r_{\rm vir} = r_{500}$. In the case of $b = 0.20$, the intersection of the efficiency and completeness curves is shifted outward by $\sim r_{\rm vir}$, which is not surprising since a halo found using $b = 0.20$ is expected to be $\sim 30\%$ larger than one found using $b = 0.15$. From the figure we see that changing the linking length results in a change of only a few percent in the merger fraction at

[1] We thank the referee for pointing out this universal behavior.

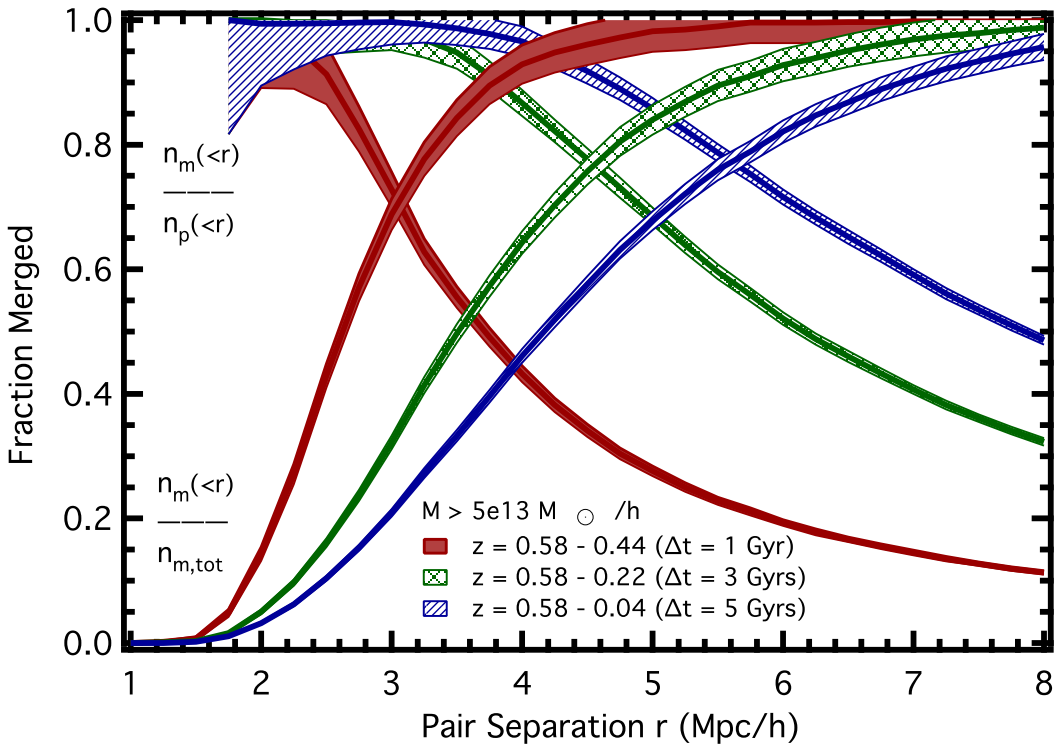

Figure 3.5: Faction of pairs separated by less than r that merged (falling curves), indicating efficiency, and the ratio of identified mergers to all mergers above the mass cut (rising curves), indicating completeness, for various merger timescales from $z = 0.58$. The total number density of such mergers is $950\,h^{-3}$ Gpc^{-3} ($z = 0.58-0.44$), $2755\,h^{-3}$ Gpc^{-3} ($z = 0.58-0.22$), $4282\,h^{-3}$ Gpc^{-3} ($z = 0.58 - 0.04$).

the intersection of the efficiency and completeness curves. Thus changing the linking length does not qualitatively alter any of our results. The weak dependence on the linking length suggests that for these mergers, the FoF procedure does not give rise to significant artificial bridging of nearby halos, and our results would not differ significantly from a similar analysis performed using a spherical overdensity halo finder (e.g., Lacey & Cole 1994).

3.3.4 Merger Timescale Dependence of Pair Mergers

Pair merging is also strongly dependent on the choice of merger timescale. Figure 3.5 shows that the merger efficiency (falling curves) increases with timescale, so pairs are more likely to merge when one considers longer time intervals. When considering mergers across 5 Gyr, a significant fraction (80%) of pairs with separations $< 5\,h^{-1}$ Mpc will merge. However, the merger completeness within a given separation (rising curves) decreases with

timescale, so one must consider pairs at larger separation to capture all mergers. Interestingly, the trade off between efficiency and completeness is only weakly dependent on the timescale, and we find similar results even for massive halo pairs at $z = 1$ merging to $z = 0$ ($\Delta t = 7.6$ Gyr). No matter which merger timescale are considered, the utility of pairs as proxies for mergers remains limited.

In all redshift, mass, and temporal regimes we consider, close halo pairs do not provide a robust predictor of overall merger rates. We conclude that, while pairs at small separations can reliably predict mergers, these constitute a small fraction of the total merger population. While our results could in principle be used to calibrate the merger fraction as a function of halo separation, close pairs do not provide a *self-consistent* probe of the merger population independent of our theoretical predictions (which are contingent upon having simulated the correct cosmology). *Thus, even in the best-case scenario of complete knowledge of mass and position, measurements of galaxy cluster pairs cannot be used to measure cluster merger rates. The same is true for any any class of object that singly occupies a halo, particularly in using field galaxy pairs at high redshift to probe galaxy mergers.*

3.4 Scatter in Mass, Redshift, & Redshift Space Distortions

The situation becomes more complicated when we consider redshift space distortions, redshift space errors, and scatter in the estimated mass of the halos. To identify the impact of imprecise determination of dark matter halo masses, we have recomputed several of the statistics of §3.3 after introducing an RMS scatter of $0.2\,M_{\rm cut}$, where $M_{\rm cut}$ is the threshold for detecting the pairs in the mock observation. The scatter in the mass causes some halos to fall out of the sample and others to enter it, resulting in a different population of halos near the threshold. Because the mass function is steep, many more low-mass halos enter the sample than high-mass halos leave it. Thus there are both more pairs to consider as merger candidates and more actual mergers between members of the observed sample. For example, if $M_{\rm cut} = 5 \times 10^{13}\,h^{-1}\,{\rm M}_\odot$, the number of pairs increases more than the number of mergers, resulting in a decrease in n_m/n_p of $\sim 5\%$ for pairs separated by $2 < r < 6\,h^{-1}\,{\rm Mpc}$ over $0.58 < z < 0.97$ ($\Delta t = 2$ Gyr). The effect is similar for other thresholds, redshifts, and intervals. Scatter in the mass has a more pronounced impact at high values of $M_{\rm cut}$ where the mass function is steeper. The trend with redshift is derivative of the evolution of the mass function: at a fixed value of $M_{\rm cut}$ there is more sensitivity to scatter at higher redshifts where the mass function steepens. There is not a significant trend with merger timescale Δt. The overall impact of imprecise mass measurements is to degrade the range in separation over which pairs might be considered useful proxies for mergers, but it is not a significant effect.

In contrast, redshift space distortions from Doppler shift due to the halo peculiar velocities $v_{\rm p}$ are catastrophic for the pair-merger hypothesis. When pairs are identified in redshift space, virtually none of them merge. In redshift space, the line of sight component is shifted

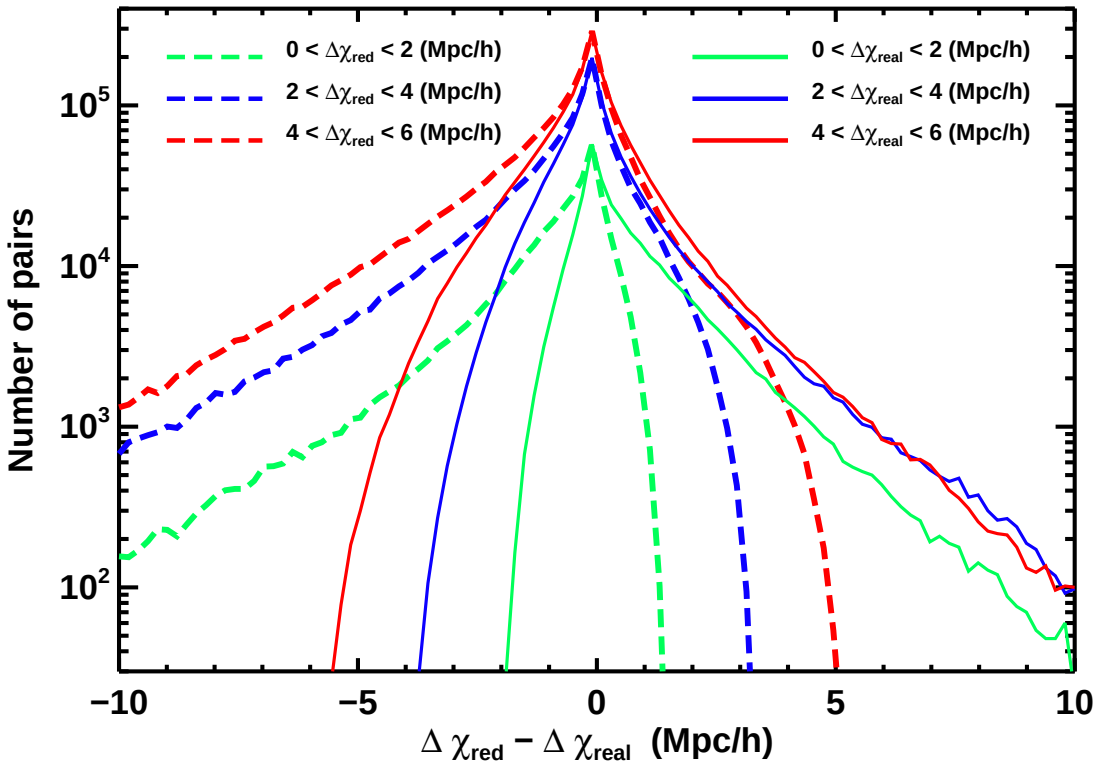

Figure 3.6: Histogram of the change in apparent separation because of redshift space distortions from halo peculiar velocities. Dashed curves indicate close pairs identified in redshift space (as in observation) and solid curves indicate pairs identified in real space. The region < 0 of the dashed curves indicate pairs that are artificially close in redshift space. The region > 0 of the solid curves indicate pairs that are artificially separated in redshift space.

relative to its real position by an amount

$$\Delta\chi_{||} = \int_z^{z+v_{\rm p}/c} \frac{c\,dz}{H(z)}\,. \tag{3.1}$$

For typical halo velocities in our simulation, this shift amounts to a few h^{-1} Mpc. Figure 3.6 illustrates that this distortion makes many close pairs appear to be highly separated and pairs that are highly separated to appear close. At redshift space separations less than $5\,h^{-1}$ Mpc, fewer than 5% of merger candidates actually merge in $\Delta t = 0.6$ Gyr at $z = 0$. Even at $z = 0.58$ where redshift space distortions are less severe, only $\sim 10\%$ of candidates merge over $\Delta t = 1$ Gyr. The situation improves modestly for longer time intervals, with $\sim 60\%$ of pairs merging over $\Delta t = 5.6$ Gyr, but this falls far short of the fraction in real space.

Figure 3.6 shows a histogram of the difference between a pair's separation in redshift

space (dashed line), as would be done in an observation, and its true separation in configuration space (solid curves) at $z = 0.04$. Merger candidates identified in real and redshift space are widely disjoint sets. The three sets of curves (colors) are bins of separation, as annotated. For the population of merger candidates identified in redshift space (dashed curves), the region greater than zero shows pairs for which the real separation was smaller than the measured separation, while the negative region shows pairs that appeared to be close in redshift space but were actually separated by several h^{-1} Mpc. The former set might be likely to merge, but the latter set is highly unlikely to do so. For the actual population of close pairs (solid curves), the region greater than zero shows pairs whose redshift space separations were greater than their real separations, and which were therefore likely removed from the sample of merger candidates. The reason for the asymmetry between the pair population that left the sample (solid, right side) and the population that entered the sample and replaced it (dashed, left side) is that pairs are most often found in overdense regions, toward which many other halos are streaming. The impact is that the pair population identified in redshift space is larger and has a broad distribution of physical separations; virtually none of the "merger candidates" we identified actually merge. This result is robust for all redshifts, merger intervals, and halo masses.

To a degree, this result also applies to the relationship between galaxy pairs and galaxy mergers. Observing galaxy pairs to study the merger rates of singly occupied host halos at high redshift will be similarly affected by redshift space distortions, as will using galaxy pairs to deduce the merger rates of multiply occupied host halos at lower redshift. However, the impact of redshift space distortions on using galaxy pairs to deduce the galaxy-galaxy merger rates within a single host halo may be less severe (Berrier et al. 2006). Inside a halo, galaxy mergers are predominately between a satellite galaxy and the central galaxy, and merger dynamics inside a host halo are influenced by dynamical friction, especially in group-mass halos and when the galaxy masses are comparable. Pair counts, even in redshift space, provide a rough proxy to the halo mass and will therefore correlate well with the merger rate within the halo.

The impact of redshift space errors is similar to that of redshift space distortions, except that, unlike with the velocities, the errors are not correlated with the high density regions. Redshift space errors that result in more than a few h^{-1} Mpc shift in the apparent position have a similar impact to redshift space distortions.

3.5 The Merger Kernel & the Density Dependence of Mergers

Since spatial information is a weak probe of halo merger statistics, we now turn to statistically describing the merger rate via the halo mass function. For any population of objects that are built up by binary mergers of smaller constituents, the rate at which the number of objects of a given mass changes can be described by the Smoluchowski coagulation equation, which has been applied to the evolution of dark matter halos (Silk & White 1978;

Cavaliere et al. 1992; Sheth & Pitman 1997; Benson et al. 2005). The abundance of halos at a given mass is increased through the creation of such halos by mergers of smaller halos, and decreased as these halos merge into more massive ones. The rate of change of the number density of halos of a given mass can then be determined by knowing the number density of halos at all masses via the mass function, and the proper merger kernel to relate the mass function to a merger rate. Historically, it has been difficult to study the coagulation of cluster-mass halos through simulation because these events are rare. However, with our large simulation volume the merger kernel can be computed in a statistically significant way.

We define the merger kernel $Q(m_1, m_2, z)$ as in Furlanetto & Kamionkowski (2006) (hereafter F&K), via the relation

$$Q(m_1, m_2, z) = \frac{n_m(m_1, m_2, z)}{n(m_1, z)\, n(m_2, z)\, \Delta t} \tag{3.2}$$

where $n_m(m_1, m_2, z)$ is the number density of mergers between parents of mass m_1 and m_2 in a time Δt, and $n(m, z)$ is the halo mass function. The quantity Q can be interpreted as the efficiency of merging for a pair of objects, such that the rate of mergers is a product of this efficiency with the densities of available parents. Note that in previous contexts the term efficiency refers to the ability of the close-pair technique to reliably identify merger candidates, whereas in this context the efficiency is the coefficient of the number densities when quantifying the merger rate. The time interval Δt should be sufficiently short that there is no significant evolution of the halo mass function. Satisfying this requirement drives down the number of mergers in a fixed volume, making statistically significant measurements difficult. However, with our large simulation volume we measure $Q(m_1, m_2, z = 0)$ on the interval $0 < z < 0.04$ ($\Delta t = 0.6$ Gyr) by classifying the two progenitors that contributed the most mass to each halo at $z = 0$ into ten logarithmically spaced mass bins in the range $10^{13} < h^{-1} M_\odot < 10^{15}$. The results are shown in Fig. 3.7

We find that Q follows the simple functional form

$$Q(m_1, m_2, z = 0) = A \left[\frac{m_1 + m_2}{h^{-1} M_\odot} \right]^B . \tag{3.3}$$

The best fit values for A and B, found using a linear least-squares fit to the data, are presented in Table 3.1 (bottom row). This functional form satisfies the formal requirement that the merger kernel be symmetric in its two arguments. For comparison, Benson et al. (2005) analytically found that $Q \propto (m_1 + m_2)$ when $P(k) \propto k^n$ with $n = 0$, which is approximately true in the trans-linear regime of cluster-mass halos.

3.5.1 Density Dependence of the Merger Kernel

Because the densities of the parent populations have been divided out, it is conceivable that the merger kernel Q is independent of the large-scale density field. Significant dependence on density would indicate that environmental effects other than the progenitor

δ_i	V $(h^{-1}$ Gpc$)^3$	A $(h^{-1}$ kpc$)^3$/Gyr	B	$\chi^2_{\rm red}$
-0.56	.47	$0.121 \pm 1.99 \times 10^{-3}$	0.88	1.00
-0.21	.33	$0.086 \pm 1.30 \times 10^{-3}$	0.88	1.55
0.20	.27	$0.072 \pm 9.98 \times 10^{-4}$	0.88	1.46
1.33	.21	$0.060 \pm 7.10 \times 10^{-4}$	0.88	1.41
0.0	1.28	$.088 \pm 2.23 \times 10^{-2}$	0.88 ± 0.008	3.09

Table 3.1: Best fit amplitude, A, and exponent, B, for the merger kernel $Q = A(m_1 + m_2)^B$, where $(m_1 + m_2)$ is the sum of the 2 progenitor masses. First four rows are the results for each of the 4 density subdivisions, while bottom row is the best fit for the entire simulation. The average density and total volume of each subdivision is listed at left, and the reduced χ^2 for each subdivision is listed at right.

densities, such as halo velocity distributions, halo impact parameters, and tidal fields, are at play in determining the merger rate. To investigate the dependence of Q on the large-scale density field we construct a coarse (64^3) density grid in our simulation and assign the dark matter particles to the nearest grid point, effectively smoothing the field on a scale of $\sim 17\,h^{-1}\,$Mpc. Each halo at $z = 0$ is also assigned to the coarse grid, and these halos are sorted in order of their large scale density environment and then divided into quartiles of density, with each quartile containing approximately the same number of halos. Using the coarse grid, we compute the total volume and overdensity of each quartile in the simulation, and these appear in the first two columns of Table 3.1. The mean overdensity of a quartile is defined as

$$\langle \delta_i \rangle = \frac{\langle \rho \rangle_i - \langle \rho \rangle}{\langle \rho \rangle} \qquad i = 1, 2, 3, 4 \tag{3.4}$$

where the angular brackets denote an average of the $\sim(17\,h^{-1}\,\mathrm{Mpc})^3$ cells of the coarse grid. The merger kernel Q is fit for each quartile to the form of Eq. 3.3, using the value of B determined from the entire simulation. The results are summarized in Table 3.1. The best fit values of A differ by several sigma, and the improvement in the reduced $\chi^2_{\rm red}$ statistic indicates that each of the individual density fits is a much better fit that a fit to the entire volume. This indicates that there is a clear trend in Q with the large-scale density field: as the density increases the efficiency of merging for a given system mass decreases. *Thus, the environmental effects in dense environments are hindering the merging process in comparison to less dense environments.*

Figure 3.7 shows Q in each of the four density environments plotted individually. The upper panel shows Q in the highest and lowest density quartiles, while the lower panel shows the results from the inner two quartiles. The solid line is the best fit model for the entire simulation, which is only a good approximation for environments close to the mean density. The yellow shaded region results from allowing A and B to deviate by their 1σ values. Figure 3.7 demonstrates clearly that a large component of the dispersion in the best fit to

the entire simulation originates in the density dependence of Q.

Figure 3.7 clearly indicates that merging is less efficient in high density environments than in low density environments, but we note that with regard to our fit there is an ambiguity as to whether this implies a lower normalization A or a shallower power law B. Given the rarity of these events at the high mass end and the limited dynamic range that is consequently driving the fit, there is large covariance between the fit values of A and B. We have performed the 2-parameter fit to Eq. 3.3 for each of the density quartiles individually and find that indeed A increases slightly with density (in contrast to the 1-parameter fit) while B decreases. Unfortunately, the formal errors in the parameters (from inversion of the covariance matrix) become so large that the four regions are statistically indistinguishable. However, the individual fits hint at an interesting possibility: if B decreases and A increases with density, then the merger efficiencies cross over as a function of system mass. Specifically, for lower total system masses ($m_1 + m_2$), merging becomes more efficient in high density environments. In our simulation, all four Q curves cross over in the mass range $10^{10}\,h^{-1}\,\mathrm{M}_\odot < (m_1 + m_2) < 10^{12}\,h^{-1}\,\mathrm{M}_\odot$, suggesting that galaxy scale mergers may be more efficient in denser environments. While this evidence is extrapolated from higher mass, the trend is potentially worth further investigation given that other halo properties, such as clustering as a function of concentration or formation time, reverse trend from $M > M_*$ to $M < M_*$ (Gao et al. 2005; Wechsler et al. 2006).[2]

We note that the merger kernel Q as computed in this section is not a direct cosmological observable. There is an observational counterpart to the merger kernel: the pair kernel, Q_p, computed using the number density of pairs with separations $r < r_{\Delta\mathrm{t}}$. The threshold separation is calibrated from simulations to any desired tolerance for completeness or contamination, but the result is insensitive to $r_{\Delta\mathrm{t}}$. In all cases, there are many more pairs than actual mergers, the amplitude A of Q_p is larger, and the power law B is shallower, both by several σ. It is infeasible to use pairs at any mass scale as a proxy to compute merger rates.

3.5.2 Density Dependence of Close Pair Mergers

The trend in the merger kernel is driven by the fact that the number of mergers grows more slowly with density than the parent mass functions. By studying changes in the relationship between close pairs and mergers in regions of differing local density, we can demonstrate that this is not universally true for all pair separations. We proceed in an analogous manner, smoothing over $\sim 17\,h^{-1}\,\mathrm{Mpc}$ and defining four density quartiles, each containing the same number of mergers. We consider pairs merging between $z = 0.12$ and $z = 0.04$ ($\Delta t = 1$ Gyr), though our results are insensitive to the time interval and redshift. Fig. 3.8 shows the results for pairs of halos above $5 \times 10^{12}\,h^{-1}\,\mathrm{M}_\odot$ (top) and $10^{14}\,h^{-1} M_\odot$ (bottom). The relationship between close pairs and mergers changes with the large-scale density. Pairs within a given separation are a less complete sample of merger candidates in

[2] $M_*(z)$ is the mass at which $\sigma(M, z)$, the variance of the linear power spectrum smoothed on scale M, equals the threshold for linear density collapse δ_c; $M_* \approx 7 \times 10^{12}\,h^{-1}\,\mathrm{M}_\odot$ at $z = 0$.

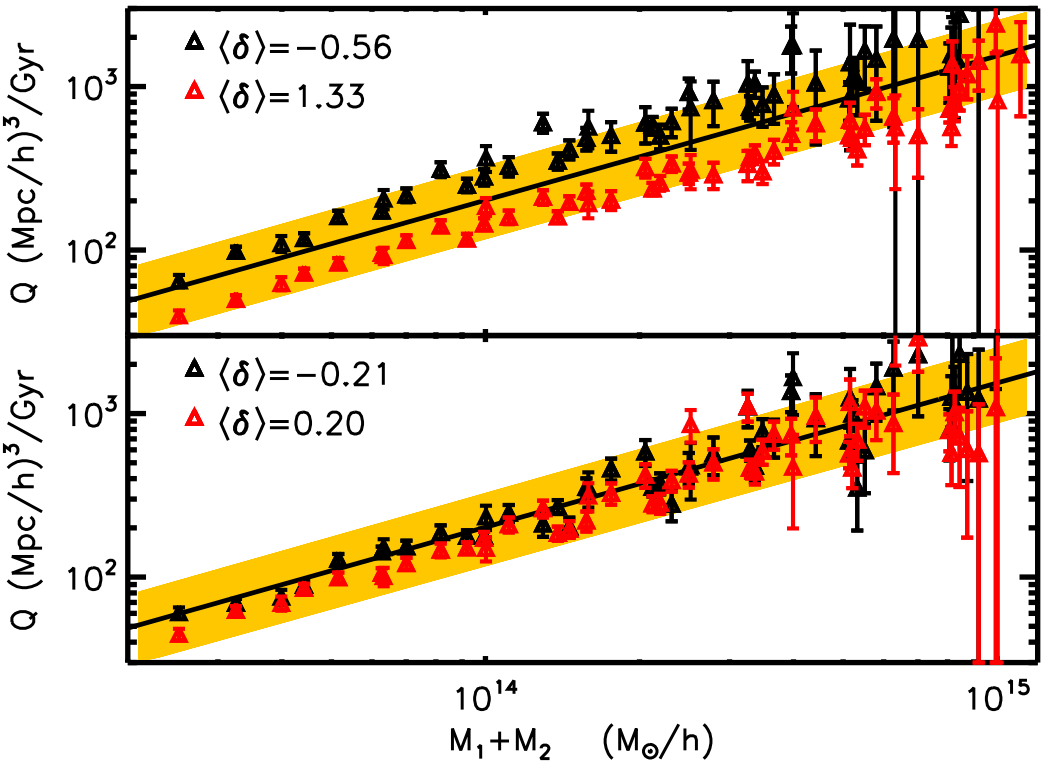

Figure 3.7: Merger kernel, Q, from the simulation for 10 logarithmic mass bins in progenitor masses, as a function of the sum of the progenitor masses. Solid line depicts the best fit of Eq. 3.3 to the whole simulation volume. Shaded region corresponds to the formal 1σ errors on the fit values of A and B. Top panel shows Q computed in the highest and lowest density quartiles and the bottom panel shows the quartiles closer to the mean density. The highest and lowest density regions differ in Q by several sigma, and the density dependence of Q is one of the main factors driving the dispersion in the fit to the whole simulation (shaded region).

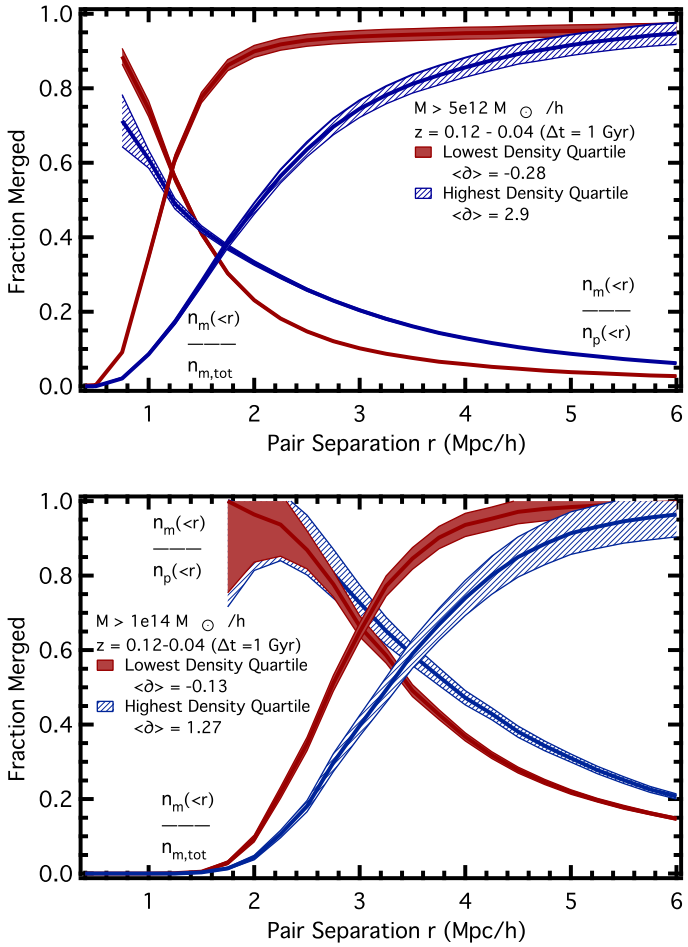

Figure 3.8: Fraction of the total number of pairs separated by less than r that merged (falling curves), indicating efficiency, and the fraction of all mergers in the simulation within $\Delta t = 1$ Gyr (rising curves), indicating completeness, for the highest and lowest density quartiles. Pairs are found at $z = 0.12$ for $M > 5 \times 10^{12}\, h^{-1}\, \mathrm{M}_{\odot}$ (top) and $M > 10^{14}\, h^{-1}\, \mathrm{M}_{\odot}$ (bottom).

overdense environments than in underdense regions (rising curves, top and bottom). Objects in overdense regions have higher velocities, which allow mergers to come from a broader range of progenitor separations and can extend the infall time of closer pairs by generating larger angular momenta.

Figure 3.8 also indicates that, at large separations, pairs are more efficient predictors of mergers in overdense regions than in underdense regions (falling curves) because higher velocities in overdense regions allow pairs from larger separations to merge. However, at small separations ($\lesssim 2\,h^{-1}\,\mathrm{Mpc}$), the relationship between pairs and mergers depends on the pair masses. Here, there are no high-mass ($\gtrsim 10^{14}\,h^{-1}\,\mathrm{M}_{\odot}$) halos because of halo exclusion, and pairs are more efficient predictors of mergers in *underdense* regions (top). This is likely because low-mass progenitors in overdense regions have large velocities and thus have longer infall times, resulting in large angular momenta that inhibit merging. In contrast, the smaller velocities in underdense regions enhance the probability that a very close pair will merge from simple gravitational attraction. High-mass halos have much stronger gravitational attractions and are thus less affected by the large-scale density field. Indeed, at small separations, massive halos are equally likely to merge in over- and underdense environments.

Finally, we note that the two methods we have presented to examine the density dependence of merging probe mergers in different ways. The merger kernel integrates over merger pair separations, thus considering mergers as a function of progenitor pair mass sum. Alternately, the close pair merger method selects only close halo pairs that are above a given mass cut, thus integrating over mass dependence and considering mergers as a function of pair separation. The merger kernel indicates that for all child halo masses in our simulation merging is more efficient in underdense environments. This is corroborated by Fig. 3.8 (top), which shows that for all halos in our simulation, pair merging is more likely in underdense environments for pairs within $1.5\,h^{-1}\,\mathrm{Mpc}$ separation. The accompanying merger completeness (rising) curves show that pairs within this separation constitute the majority of pair mergers in the given timescale. Figure 3.8 (bottom) shows that high-mass pairs are more likely to merge in overdense regions at all pair separations. However, since mergers between two halos both with $M > 10^{14}\,h^{-1}\,\mathrm{M}_{\odot}$ are extremely rare (as opposed to mergers between a high and low mass object), these contribute less to the merger kernel at a given child mass.

3.6 The Clustering of Close Pairs & Merger Bias

For two halos to merge, they must have been located in close physical proximity at an earlier time. Since closely spaced halos are more likely to be found in overdense regions, recently merged halos may exhibit enhanced spatial clustering. Moreover, if recently merged halos cluster differently from the general population ("merger bias") and this is unaccounted for, conclusions drawn about halos on the basis of their clustering could be compromised. For example, the use of cluster self-calibration to infer cluster masses (and in turn cosmological parameters) requires a precise knowledge of the clustering of clusters as a function of mass (Majumdar & Mohr 2003). A number of earlier studies have looked for such merger bias

(Gottlöber et al. 2002; Percival et al. 2003; Scannapieco & Thacker 2003; Wetzel et al. 2007), with mixed results.

Recently, Furlanetto & Kamionkowski (2006) developed an analytic model to predict the merger bias. Assuming that mergers correspond to closely spaced objects at an earlier time, they compare the clustering of close pairs to that of single objects, thus computing the pair bias as a proxy for merger bias. On scales much larger than the pair separations, they found an enhancement of clustering for pairs of mass $M > M_*$, implying that recently merged high-mass halos should exhibit a clustering bias. We now use F&K's framework to determine if the clustering of close halo pairs of mass $M \gg M_*$ provides an accurate proxy for the clustering of mergers.

Using simulations, Wetzel et al. (2007) found the most prominent merger bias ($\sim 20\%$) for major mergers ($M_2/M_1 > 0.3$) of high-mass halos ($M > 5 \times 10^{13}\,h^{-1}\,\mathrm{M}_\odot$) at $z = 0$ over $\Delta t = 0.6$ Gyr. We consider a similar mass and temporal regime. To improve our statistics we additionally use a simulation of eight times the volume previously used (see §3.2), which allows us to probe merger effects of more massive halos. We use a shorter timescale of $\Delta t = 0.5$ Gyr at $z = 0$ to define our merger interval to preserve the signal in the comparison population. Contrary to expectation, the merger bias *does not* increase with mass; it remains a 10–20% enhancement with similar statistical significance up to halos of mass $M > 4 \times 10^{14}\,h^{-1}\,\mathrm{M}_\odot$.

In computing the pair bias, F&K define "close" halo pairs by demanding that the probability of finding three or more halos in a sphere of a given radius is small compared to that of finding two. This is approximately equivalent to the restriction that the probability of finding two or more neighbors, $P(\geq 2)$, within a given separation from a halo is small compared to that of finding one, $P(1)$, which is what we will measure. For halos $M > 5 \times 10^{13}\,h^{-1}\,\mathrm{M}_\odot$ at $z \approx 0$, we find that $P(\geq 2)/P(1) \approx 0.1$ for a (comoving) sphere radius of $4\,h^{-1}\,\mathrm{Mpc}$. This separation restriction yields $\sim 6,800$ pairs per $(h^{-1}\ \mathrm{Gpc})^3$, out of $\sim 77,000$ halos per $(h^{-1}\ \mathrm{Gpc})^3$. While this is a sufficient number density of pairs for a robust correlation function measurement in our $(2.2\,h^{-1}\,\mathrm{Gpc})^3$ simulation volume, §3.3 demonstrated that close pairs do not reliably predict the merger population.

The analytical model of F&K predicts a significant merger bias in its application to the clustering of massive halos ($M \gg M_*$). For such objects, it predicts a correlation function of pairs $X_p(r)$ in terms of $\xi_h(r)$, the correlation function of individual halos:

$$X_p(r) = [1 + \xi_h(r)]^4 - 1\,. \tag{3.5}$$

This is computed on scales where the underlying matter fluctuations are linear, which at $z = 0$ corresponds to distances greater than $\sim 10\,h^{-1}\,\mathrm{Mpc}$. To compute the pair bias F&K use

$$b_p^2 \equiv \frac{X_p(r)}{\xi_h(r)}\,. \tag{3.6}$$

For a given halo mass, this can result in anomalously high pair biases. This is because the halo correlation function is implicitly a function of the halo mass; more massive halos are

more highly clustered. When computing the merger bias (or its proxy, the pair bias) the comparison population should be an ensemble of halos of the same characteristic mass as the child halo, not the parent halos. Otherwise, the merger bias becomes entangled with the effect that larger halos are more clustered. To adjust for this in the analytic model we note that $\xi_h(r, 2M) \approx 1.1\xi_h(r, M)$ near $M \sim 10^{14} M_\odot$. On scales $> 10\,h^{-1}\,\mathrm{Mpc}$, $\xi(r)$ is less than 1, so this leads to a pair bias of $b_p^2 \approx 3.6$. This pair bias is still significantly larger than the 10–20% merger bias seen in simulation for halos up to $M > 4 \times 10^{14}\,h^{-1}\,\mathrm{M}_\odot$.

As an alternative to an analytic approach, we next measure the clustering of close pairs in simulations to discover whether pair bias can predict merger bias. We consider pairs 0.5 Gyr prior to $z = 0$. To assign a unique position to a pair of neighboring halos, we impose a "couples" restriction, namely that each member of a pair is the other's nearest neighbor. This restriction remains robust for two body mergers, a good approximation for our time interval. Within the pair separations we consider ($< 2\,h^{-1}\,\mathrm{Mpc}$) couples constitute essentially all pairs. We select couples of halos above $5 \times 10^{13}\,h^{-1}\,\mathrm{M}_\odot$ at $z = 0.04$ and use their geometric centers to evaluate the couple correlation function. We use couples with separations less than $1.6\,h^{-1}\,\mathrm{Mpc}$, 80% of which correspond to mergers in our time interval (Fig. 3.4). To limit the effect of mass-dependence on the halo correlation function, we compare this correlation function with that obtained from single halos above $10^{14}\,h^{-1}\,\mathrm{M}_\odot$ at $z = 0$. While this ignores the effects of mass scatter in mergers, such effects remain small for this short timescale.

Figure 3.9 shows that with a $(2.2\,h^{-1}\,\mathrm{Gpc})^3$ simulation volume, no statistically significant pair bias is found. Such poor statistics arise because only a small fraction (15%) of total mergers are represented by couples at such close separations. Trying to increase statistics by considering couples at larger separations is undermined by the fact that the fraction of couples that merge is a steeply decreasing function of separation. As already mentioned, one cannot consider longer merger timescales, as this permits a larger fraction of the halo population to have undergone a major merger, thereby washing out the signal in the comparison population. We find similar results when looking at the pair bias for mass cuts from $M > 10^{13}\,h^{-1}\,\mathrm{M}_\odot$ to $M > 2 \times 10^{14}\,h^{-1}\,\mathrm{M}_\odot$, and thus we conclude that *pair bias cannot be used to reliably predict merger bias observationally, in simulation, or through current analytic treatment.*

3.7 Summary & Conclusion

Cluster merger statistics may provide insight into the nature of hierarchical structure formation and the mechanisms by which the largest coherent objects in the universe form. We use large-volume, high-resolution N-body simulations to investigate the utility of close spatial pairs of galaxy clusters as proxies for cluster mergers. We characterize merger statistics through the merger kernel, and examine the density dependence of merger efficiency. We highlight our conclusions as follows:

- Close pairs of galaxy clusters at very small separations ($< 1 - 2\,h^{-1}\,\mathrm{Mpc}$) can be used

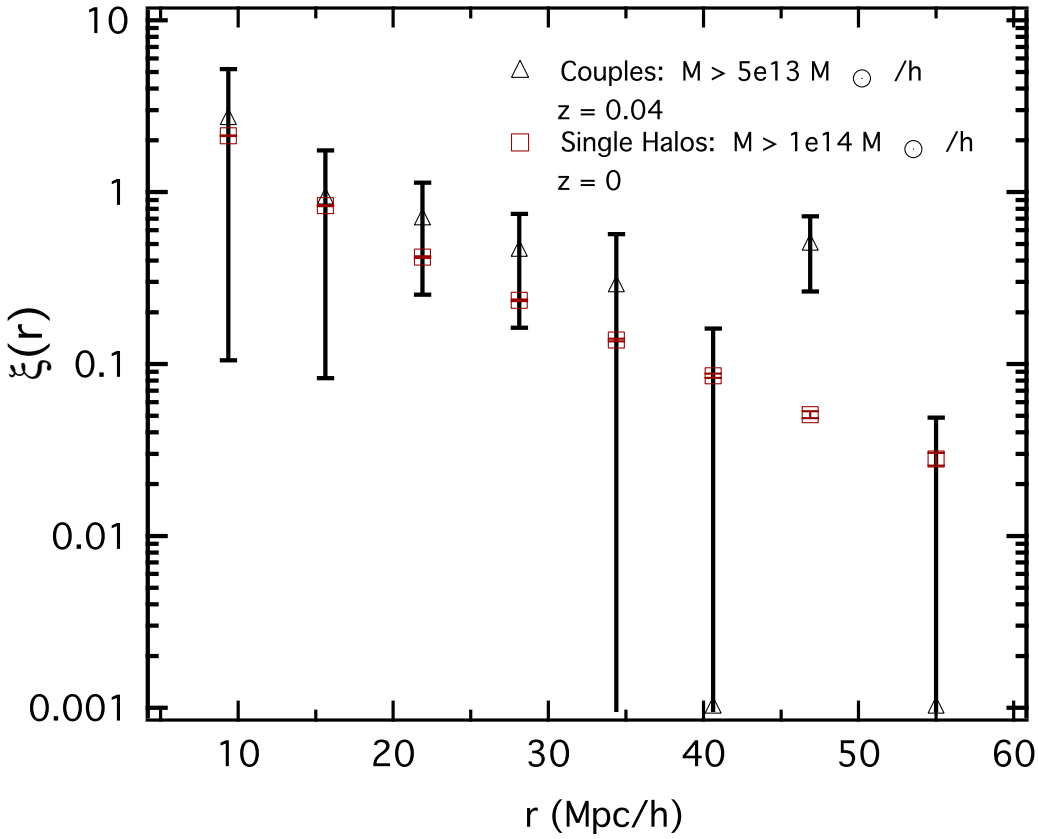

Figure 3.9: Correlation function of couples (triangles) at $z = 0.04$ compared with that of single halos (squares) at $z = 0$. Mass cuts are chosen so that the single halos are approximately the same mass as the child products of the couples. While enhanced signal is seen at $47\,h^{-1}\,\mathrm{Mpc}$, this is mitigated by the adjacent points which are both negative.

to reliably predict mergers. However, since these constitute a small fraction of the total merger population, close pairs are not a reliable proxy for cluster merger rates. We quantify this by measuring the efficiency and completeness of merger candidates identified via close pairs as a function of separation and find that their intersection typically occurs at a low merger fraction (0.5–0.6).

- We find that close pairs are even poorer proxies for mergers between massive galaxy-sized halos. This indicates that galaxy pairs will not provide a reliable proxy for galaxy merger rates at high redshift, where most galaxies reside in distinct halos.

- We note that the failure of close pairs as proxies for mergers indicates that determination of merger rates from spatial statistics, such as the correlation function, cannot be trusted outside the physical size of a single halo.

- We examine the mass, redshift, and timescale dependence of pair mergers, finding that the pair-merger hypothesis (that close pairs are proxies for mergers) at a given comoving separation is most accurate at high redshift, high mass, and over long merger timescales. In our best scenarios, the intersection of merger efficiency and completeness is at $\sim 75\%$, that is, 75% of pairs within a given separation merge, and these constitute 75% of all mergers. We also find a nearly universal relation for pair merger efficiency and completeness for different mass halos. This relation begins to break down as we approach massive galaxy-size halos, and is compromised by redshift space distortions.

- Redshift space distortions have a devastating impact on detecting close galaxy cluster pairs in surveys; nearly all of the merger candidates identified in redshift space do not merge. Although an extrapolation, we expect these results to be robust for galaxy-size halos at high redshift.

- We present the first fit from simulation to the merger kernel—a means to describe halo merger rates via the halo mass function (coagulation).

- The merger kernel exhibits dependence on local ($\sim 17\,h^{-1}\,\mathrm{Mpc}$) density. Specifically, halo merging in our high-mass regime is more efficient in underdense regions.

- Pairs at large separations ($\gtrsim 3\,h^{-1}\,\mathrm{Mpc}$) are more likely to merge in overdense regions. For pairs at small separations, low-mass halos are more likely to merge in underdense regions, while high-mass halos exhibit no environmental dependence.

- We sought to use cluster pairs to measure the merger bias by using the pair bias as a proxy for merger bias. We extended the treatment of previous analytic work to include the fact that mergers result in mass gain; when computing the bias of recently merged halos, the comparison population should be a set of halos of the same mass as the children, instead of the parents. Close spatial pairs that reliably merge are too rare to produce a statistically significant measure of merger bias, even in a $(2.2\,h^{-1}\,\mathrm{Gpc})^3$ simulation volume.

In conclusion, we have shown that close spatial pairs of galaxy clusters are of limited value as a probe of overall cluster merger rates. We have determined the merger kernel for halo coagulation for the first time from simulations, finding that a statistical description of halo mergers is of more promise. Further work is needed to extend our parametrization of the merger kernel to lower masses and higher redshifts, and to explore whether the environmental dependence of the merger rate persists in these regimes.

Chapter 4

Connecting Populations of Fixed Number Density across Cosmic Time

Abstract

Using a large-volume N-body simulation, we explore the mass evolution of halos to examine the extent to which the most massive population at high redshift maps to the most massive population at low redshift. We find that, for a sufficiently large sample, the most massive objects at high redshift evolve into the most massive objects at present day. However, the n most massive objects at high redshift do not comprise a complete set of main progenitors of the n most massive objects today. As a result, the n most massive objects today did not simply evolve from the n most massive objects at high redshift. For small samples (the very most massive objects), the mapping between populations at high and low redshift is poor either forward or backward in time. This behavior is driven by scatter in mass growth and mergers between the most massive objects.

4.1 Introduction

A primary goal of the field of galaxy evolution to understand the connection between galaxies observed at high redshift and those of the present day. A common method used in such studies is to rank objects in descending order by mass and connect a population above some number density threshold at high redshift to a population above the same number density threshold today (e.g., Blain et al. 2004; Bezanson et al. 2009). The assumption behind any number density-based method is that the (comoving) number density of a set of massive objects is preserved across cosmic time, such that one population evolved into/from the other. However, this method of relating populations ignores possible scatter in mass growth by assuming that, for example, the most massive object at high redshift becomes the most massive object today (and vice versa). Furthermore, this method ignores the possibility

that massive objects merge over time by assuming that n objects at high redshift evolve into n objects today.

The aim of this brief chapter is to examine the evolution of massive galaxies/halos over cosmic time, focusing on the degree to which one can map a population at high redshift to one at low redshift. Specifically, given n most massive objects at some z, do they evolve into the n most massive objects at $z = 0$? Conversely, given n most massive objects at $z = 0$, were they among the n most massive objects at some higher z? Furthermore, do the populations form a complete set in both directions? If all of these are true, it enables a trivial connection between populations across time. However, the extent to which they are not true invalidates any simple number density-based population mapping.

We focus on the most massive halos since these correspond to the galaxies that are most readily observable at high redshift. We examine populations at $z = 0$ and their connection with populations at higher z, particularly at $z = 2.5$ which is the peak epoch of galaxy star formation (Lilly et al. 1996; Madau et al. 1996; Hopkins & Beacom 2006) and hence the redshift of considerable interest for current high redshift galaxy observations (e.g., Steidel et al. 2003; Gawiser et al. 2007; Tacconi et al. 2008; Bezanson et al. 2009).

4.2 Methods

A theoretical understanding of the growth and evolution of the most massive galaxies requires a simulation of substantial volume which provides adequate counts of rare, massive objects and can probe a range of assembly and merger histories with correct large-scale structure. Thus, we use a dissipationless N-body simulation with 1500^3 particles in a $720\,h^{-1}\,\mathrm{Mpc}$ periodic cube ($3.7 \times 10^8\,h^{-3}\,\mathrm{Mpc}^3$ volume), which resolves halos down to $10^{11.4}\,h^{-1}\,\mathrm{M}_\odot$ (32 particles). Halos are found using the Friends-of-Friends (FoF) algorithm (Davis et al. 1985) with a linking length of $b = 0.168$ times the mean inter-particle spacing. Merger trees are constructed from the set of halo catalogs by specifying a parent-child relationship. To be a "parent", a halo must contribute more than half of its mass to a "child" halo at the next simulation output. Thus, a parent halo can never have more than one child, but a child can have an arbitrary number of parents. In relating halos at low redshift to their main progenitor at high redshift, we walk the merger trees back using the single most massive parent halo at each output. See Chapter 8 for more details on the simulation and the construction of halo merger trees.

As emphasized in Chapters 6, 7, 8, galaxies are expected to be in one-to-one correspondence with dark matter subhalos. However, simulations with sufficient resolution to robustly track subhalos are necessarily of limited volume. Here, we focus only on the most massive galaxies, which are almost entirely centrals and so correspond well with dark matter halos (see Fig. 8.12 in Chapter 8). Thus, here we use a lower resolution simulation which resolves only dark matter halos (and not subhalos), but which probes sufficiently large volume to correctly reproduce the high mass end of the mass function. Additionally, while halo mergers do not immediately lead to galaxy mergers, the dynamical infall times for massive satellites

are short (see Eq. 8.2 in Chapter 8), so the approximation that halo mergers quickly lead to galaxy mergers is good for these populations.

4.3 Scatter in Mass Evolution

We begin by examining the relationship between the masses of the most massive halos at $z = 0$ and their progenitors at $z = 2.5$, as well as the masses of the most massive halos at $z = 2.5$ and their descendants at $z = 0$. In general, halos only grow in mass over time, but there is considerable scatter in the mass growth rate at fixed mass (e.g., McBride et al. 2009). Figure 4.1 shows the relation between halo masses at $z = 0$ and 2.5, going both backward (top) and forward (bottom) in time. Linear fits to the log-normal mean relation yield

$$\log\{m(z = 2.5)\} = 4.26 + 0.59 \log\{m(z = 0)\} \tag{4.1}$$

with an average scatter of 0.36 dex, and

$$\log\{m(z = 0)\} = 3.04 + 0.85 \log\{m(z = 2.5)\} \tag{4.2}$$

with scatter decreasing with halo mass (average of 0.33 dex), where $m = M/(h^{-1}M_{\odot})$. Note that these fits do not change appreciably if we use instead the median mass relation.

As demonstrated by the nature of the scatter at low halo mass, there is a fundamental difference between considering forward (bottom) and backward (top) evolution. In particular, the increased scatter at low halo mass for forward evolution is driven by mergers between massive objects from $z = 2.5$ to 0, since any massive halos at $z = 2.5$ that merge with each other will map to the same descendant mass at $z = 0$. By contrast, a halo at $z = 0$ will only map to its single most massive progenitor at $z = 2.5$. This difference also explains why the slopes for going backward and forward in time are not simply inverses of each other, as would to true if there were a simple, monotonic mapping between mass at $z = 2.5$ and 0. Furthermore, even in the case of backward evolution, where there is a one-to-one mapping between halos, the scatter in mass is still substantial, being a factor of 2. These results suggest inherent difficultly in mapping both forward and backward in time between massive populations.

4.4 Connecting Populations of Fixed Number Density

We now turn to exploring how scatter in mass evolution and merging affects the conservation of object counts and their mass rank ordering over time. Specifically, we aim to answer whether the n most massive objects at z end up in the n most massive objects at $z = 0$, and whether the n most massive objects at $z = 0$ were among the n most massive objects at some higher z.

To address these questions, we rank order the halo population in descending order by mass at each simulation output, and we select the most massive halos above some number

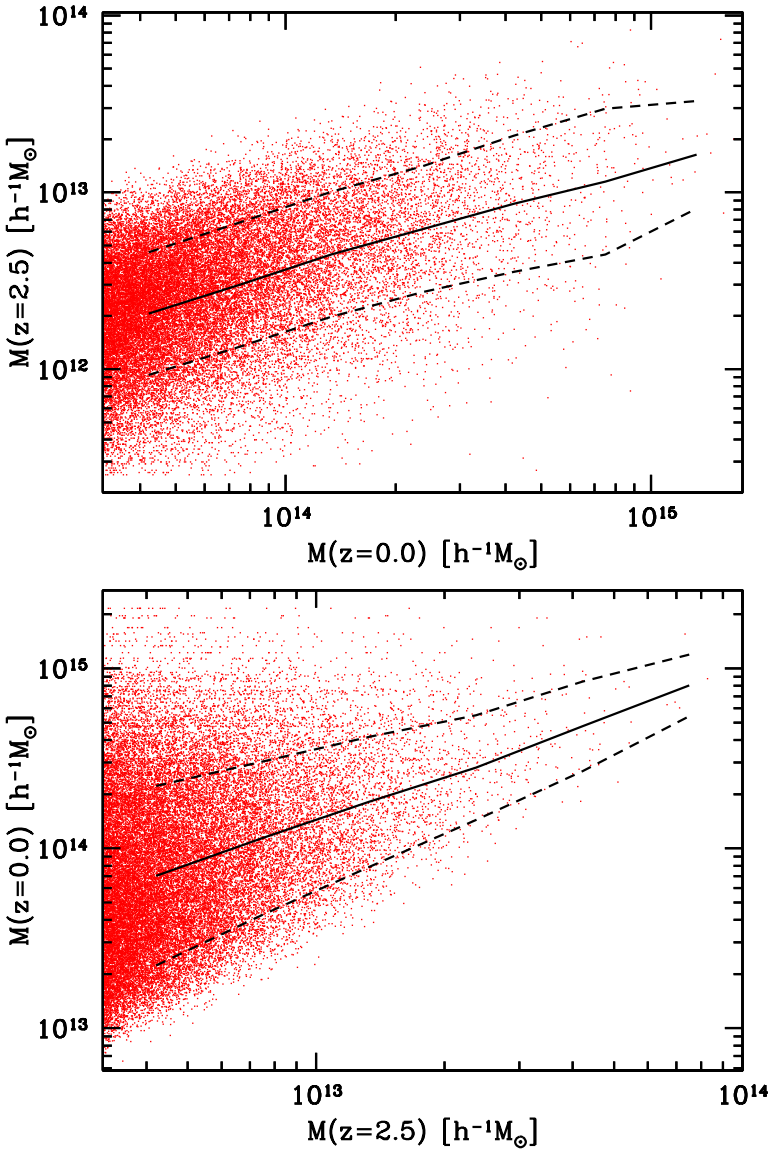

Figure 4.1: Relation between halo masses at $z = 0$ and 2.5, with logarithmic mean (solid curves) and log-normal scatter (dashed curves). **Top**: Mass that a halo had at $z = 2.5$ as a function its mass at $z = 0$. The logarithmic slope of the relation is 0.59 with an average log-normal scatter of 0.26 dex. **Bottom**: Mass that a halo will have at $z = 0$ as a function of its mass at $z = 2.5$. The logarithmic slope of the relation is 0.85 with an average log-normal scatter of 0.33 dex.

density threshold, n, at each redshift. At a given z ($z = 0$), we walk the halo merger trees forward (backward) in time, and we determine what fraction of the descendant (progenitor) halos at a lower (higher) redshift will be (were) a member of the set of most massive halos above the same number density threshold at $z = 0$ (z). Figure 4.2 shows the results for both evolution forward and backward in time between $z = 2.5$ and 0, as a function of threshold number density, n. For reference, $n = 10^{-5}\,h^3\,\mathrm{Mpc}^{-3}$ corresponds to $M > 10^{13.0}\,h^{-1}\,\mathrm{M}_\odot$ halos at $z = 2.5$ and $M > 10^{14.2}\,h^{-1}\,\mathrm{M}_\odot$ halos at $z = 0$.

Considering first forward evolution (solid curve), Fig. 4.2 shows that sufficiently rare (massive) halos at $z = 2.5$ do not evolve into similarly rare halos at $z = 0$. For example, of the $n = 10^{-6}\,h^3\,\mathrm{Mpc}^{-3}$ most massive halos at $z = 2.5$, only 35% end up in the $n = 10^{-6}\,h^3\,\mathrm{Mpc}^{-3}$ most massive halos at $z = 0$. However, when considering a sufficiently large sample, most halos do end up as part of a similar number density threshold population at $z = 0$, with $> 90\%$ for $n > 3 \times 10^{-4}\,h^3\,\mathrm{Mpc}^{-3}$.

Considering instead backward evolution (dashed curve), Fig. 4.2 shows that the fraction of very rare halos at $z = 0$ that descended from a similarly rare population at $z = 2.5$ is somewhat lower than what it was for forward evolution. However, in going to high number density the fraction never exceeds 45%. Thus, for *any* mass-ordered population of objects at $z = 0$, it is never true (to better than a factor of 2) that they descended from the most massive halos above the same number density threshold at $z = 2.5$.

What causes the number density dependence to this redshift mapping, and what sets the difference between forward and backward evolution? The difference between forward and backward evolution is driven primarily by massive halos merging over time. While all of the n most massive halos at $z = 0$ descended from unique halos at $z = 2.5$, the dotted curve in Fig. 4.2 shows the fraction of the n most massive halos at $z = 2.5$ which evolved into unique descendants, that is, did not merge with another more massive halo. This fraction goes to unity for the very most massive (rare) halos. Even though such massive halos have a strong correlation function, their number densities are sufficiently small that the average of number of similarly massive neighbors within $\sim 10\,h^{-1}\,\mathrm{Mpc}$ is still small enough to prohibit merging. However, a population with higher number density (lower mass) is more likely to undergo mergers with other massive objects in the sample, leading to fewer unique descendants at $z = 0$. For example, the $n = 8 \times 10^{-4}\,h^3\,\mathrm{Mpc}^{-3}$ most massive halos at $z = 2.5$ evolve into a population at $z = 0$ that is only half as large.

The trend of an increasing fraction of objects remaining the most massive with increasing threshold number density is driven primarily by scatter in mass growth. At the high mass end of the mass function, $n(> M)$ falls of exponentially, meaning that $M(< n)$ is nearly flat. Thus, scatter in mass growth affects population rank ordering more readily for more massive (rare) objects. However, the increased merger fraction at higher number density does affect this trend as well. Even if a halo experiences low mass growth and scatters out of the most massive population after some time, if a more massive halo which remained in the sample merges onto another one, this opens a new "slot" above the number density threshold and thus increases the probability that the low mass growth halo would be re-included. The rarest halos are not much affected by this merging process, but more common halos are.

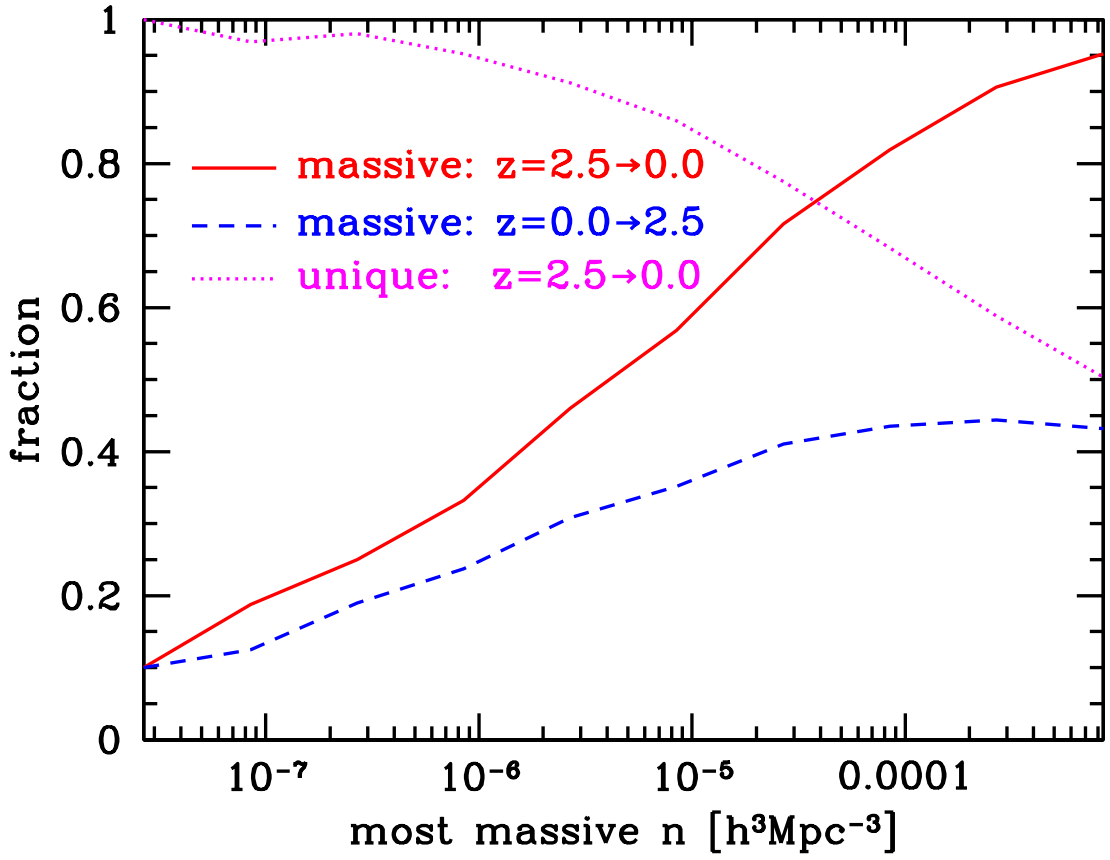

Figure 4.2: Fraction of the most massive halos that remain the most massive between $z = 0$ and $z = 2.5$ as a function of threshold number density, n. Solid curve shows the fraction of the n most massive halos at $z = 2.5$ that end up in the n most massive halos at $z = 0$, while dashed curve shows the fraction of the n most massive halos at $z = 0$ that descended from the n most massive halos at $z = 2.5$. Dotted curve shows the fraction of the n most massive halos at $z = 2.5$ that remain unique (do not merge with a more massive halo in the sample) by $z = 0$. Note that $n = 10^{-5}\,h^3\,\mathrm{Mpc}^{-3}$ corresponds to $M < 10^{13.0}\,h^{-1}\,\mathrm{M}_\odot$ halos at $z = 2.5$ and $M > 10^{14.2}\,h^{-1}\,\mathrm{M}_\odot$ halos at $z = 0$.

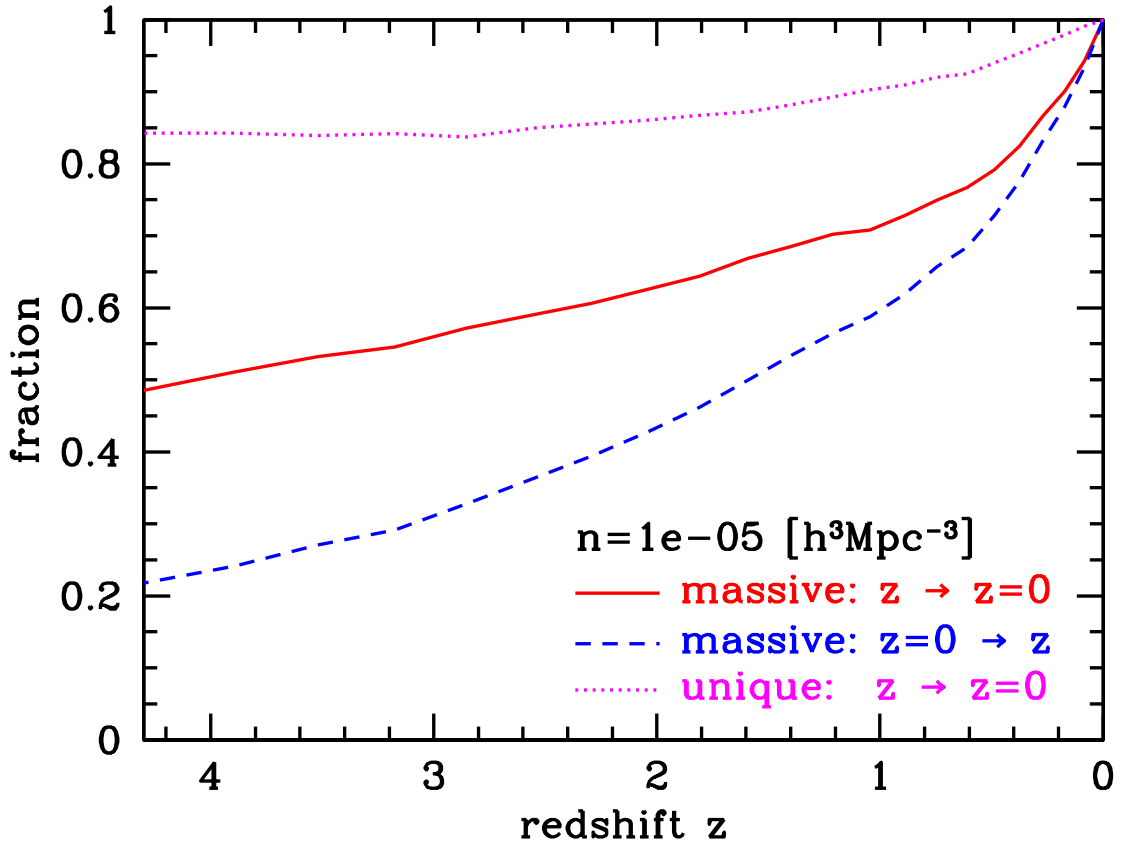

Figure 4.3: Fraction of the most massive halos that remain the most massive between $z = 0$ and z as a function of z, for a fixed number density threshold, n. Solid curve shows the fraction of the n most massive halos at z that end up in the n most massive halos at $z = 0$, while dashed curve shows the fraction of the n most massive halos at $z = 0$ that descended from the n most massive halos at z. Dotted curve shows the fraction of the n most massive halos at z that remain unique (do not merge with a more massive halo in the sample) by $z = 0$.

Figure 4.2 thus demonstrates that, in considering forward evolution (from high to low redshift), there is a fundamental competition between the likelihood that population remains the most massive and the likelihood that the population conserves number density. A very rare (massive) sample conserves number density well, but few of those objects end up as similarly rare at low redshift. Selecting a larger population at high redshift leads to less scatter in overall rank ordering, but this leads to a larger fraction of mergers and violation of conserved number density.

Finally, we examine how these trends vary with redshift interval. Figure 4.3 shows the results for both backward (solid) and forward (dashed) evolution, as in Fig. 4.2, but for fixed number density ($n = 10^{-5}\,h^3\,\mathrm{Mpc}^{-3}$) as a function of z. The ability to connect a population either backward or forward in time degenerates for a larger redshift interval, with less than 50% of the most massive halos at $z = 4$ becoming the most massive halos today, and less than 25% of the most massive halos today descending from the most massive ones at $z = 4$. Interestingly, the fraction of halos at a given z which evolve into unique halos (do no merge onto a more massive halo in the sample) at $z = 0$ (dotted curve) varies only weakly with z and remains constant beyond $z \approx 2.5$. Thus, the continued decline in the solid and dashed curves with z arises from the increased scatter in mass growth across larger cosmic time.

4.5 Summary & Discussion

In this brief chapter, we used a large-volume N-body simulation to explore the evolution of the most massive halos. We tested the extent to which one can connect populations across redshift by using a fixed number density threshold, both for forward evolution (whether the n most massive objects at z end up in the n most massive objects at $z = 0$) and for backward evolution (whether the n most massive objects at $z = 0$ were among the n most massive objects at some higher z). For forward evolution, using a sufficiently low number density threshold leads to a population mapping that well preserves number density (is "one-to-one") but does not preserve rank ordering (is not "onto"). As one increases the number density threshold, the mapping better preserves rank ordering but does not preserve number density. For backward evolution, the mapping always preserves number density but never preserves rank ordering to better than a factor of two. The extent to which forward evolution preserves number density evolves weakly with redshift interval, but the extent to which mapping in both directions preserves rank ordering degenerates strongly with redshift interval.

Our results do not negate the *qualitative* trend that massive galaxies at high redshift evolve into massive galaxies today, or that massive galaxies today evolved from massive galaxies at high redshift. Rather, our results demonstrate that scatter in mass growth and merging mean that one cannot *quantitatively* select the most massive objects above some number density threshold at a given z and assume they evolved into a population above the same number density threshold at $z = 0$ (and vice versa). For example, if one wants to understand galaxy evolution mechanisms by comparing the properties of a massive galaxy population of $n = 10^{-6}\,h^3\,\mathrm{Mpc}^{-3}$ at $z = 2.5$ against a population at $z = 0$, one must consider

a galaxy sample $\sim 3\times$ larger at $z = 0$ to capture the full scatter of mass growth. Similarly, one must consider an at least $2\times$ larger galaxy population at $z = 2.5$ to provide a complete picture of the main progenitors of massive galaxies at $z = 0$. While one can mitigate these effects of mass evolution scatter by considering larger samples, the larger samples are also more susceptible to merging with one another: the assumption of no cross-merging is rather poor for samples larger than $n = 10^{-5}\,h^3\,\mathrm{Mpc}^{-3}$.

While we expect these results based on the evolution massive halos to provide a good approximation for the evolution of massive galaxies, future work will involve examining similar trends in simulations which directly resolve subhalos/galaxies.

Chapter 5

On the Orbits of Infalling Satellite Halos

Abstract

The orbital properties of infalling satellite halos set the initial conditions which control the subsequent evolution of subhalos and the galaxies that they host, with implications for mass stripping, star formation quenching, and merging. Using a high-resolution, cosmological N-body simulation, I examine the orbital parameters of satellite halos as they merge with larger host halos, focusing primarily on orbital circularity and pericenter. I explore in detail how these orbital parameters depend on mass and redshift. Satellite orbits become more radial and plunge deeper into their host halo at higher host halo mass, but they do not significantly depend on satellite halo mass. Additionally, satellite orbits become more radial and plunge deeper into their host halos at higher redshift. I also examine satellite velocities, finding that most satellites infall with less specific angular momentum than their host halo but are 'hotter' than the host virial circular velocity. I discuss the implications of these results to the processes of galaxy formation and evolution, and I provide fitting formulas to the mass and redshift dependence of satellite orbital circularity and pericenter.

5.1 Introduction

In hierarchical structure formation, dark matter halos grow via accretion of both diffuse matter and virialized satellite halos. Beyond driving just halo mass growth, the nature of satellite accretion governs the subsequent evolution of both the satellite and host halos (hereon, 'satellite' and 'host' refer to the lower and higher mass halo, respectively, during a merger). Since galaxies form at the centers of dark matter halos (White & Rees 1978; Blumenthal et al. 1986; Dubinski 1994; Mo et al. 1998), the dynamics of infalling satellite halos will also influence the evolution of the accompanying galaxy populations.

After infall, a satellite halo can survive as a substructure halo (subhalo) of a larger host halo (Tormen et al. 1998; Klypin et al. 1999; Moore et al. 1999). As it orbits, a subhalo continues to host a (satellite) galaxy until it tidally disrupts or merges with the host halo's central galaxy[1] (e.g., Springel et al. 2001; Kravtsov et al. 2004a; Zentner et al. 2005; Conroy et al. 2006; Natarajan et al. 2009; Wetzel & White 2010). A satellite galaxy's survival timescale depends on its orbital parameters at the time of accretion, with galaxies on highly circular orbits surviving longer than those that rapidly plunge toward halo center.

Satellite orbits therefore influence the nature of galaxy mergers and the galaxy merger rate. Galaxy mergers are expected to drive morphological evolution (Toomre & Toomre 1972; Hausman & Ostriker 1978; White 1978; Barnes & Hernquist 1996), and the properties of the post-merger galaxy depend on the relative dynamics of the galaxies during the merger (Boylan-Kolchin et al. 2005; Cox et al. 2006; Hopkins et al. 2008c). It is thus necessary to understand the cosmological predictions for how close satellite galaxies come to the central galaxy during first pericentric passage and the relative velocities distributions when they merge.

After infall, satellites also can experience mass loss from tidal stripping, tidal heating, and disk shocking (e.g., Ostriker et al. 1972; Gnedin et al. 1999; Dekel et al. 2003; Taylor & Babul 2004; D'Onghia et al. 2010). Satellite galaxies are also thought to experience truncated star formation and/or morphological evolution, arising from ram-pressure stripping, adiabatic heating (strangulation), harassment, and/or tidal shock heating (e.g., Gunn & Gott 1972; Moore et al. 1998; Abadi et al. 1999; McCarthy et al. 2008). Resonant stripping processes may also drive the evolution of dwarf spheroidals around the Milky Way (D'Onghia et al. 2009). The efficiency of all of these processes depends critically on the details of satellite galaxy orbits.

Many semi-analytic models of satellite galaxy/subhalo evolution contain prescriptions for dynamical friction survival times and tidal stripping (see Baugh 2006, for a recent review). A number of authors have provided detailed fits to satellite survival times that depend on a satellite's circularity parameter at infall (Boylan-Kolchin et al. 2008; Jiang et al. 2008). All these models require proper initial conditions of satellite orbits as a function of both halo mass and redshift to be an accurate depiction of galaxy evolution in a cosmological context.

Several authors have examined the orbital parameters of infalling satellite halos in simulations (Tormen 1997; Vitvitska et al. 2002; Benson 2005; Wang et al. 2005; Zentner et al. 2005; Khochfar & Burkert 2006). However, most work has focused on orbits only at $z \sim 0$, and limited statistics and dynamic ranges have inhibited a robust investigation into possible mass and redshift dependence. The nature of large-scale structure formation suggests that the behavior of satellite accretion depends on halo mass and redshift. Triaxial collapse models of halo formation predict that more massive halos form from more spherical regions, with accreting matter containing less specific angular momentum (Zel'Dovich 1970; Bardeen et al. 1986; Eisenstein & Loeb 1995; Sheth et al. 2001). This is reflected in the nature of

[1] Additionally, $\sim 10\%$ of satellite galaxies merge with another satellite within the host halo (Angulo et al. 2008; Wetzel et al. 2009a,b).

the cosmic web, in which low-mass halos reside primarily within filaments while high-mass halos reside at the intersection of several filaments (Bond et al. 1996). In this picture, matter infall onto massive halos occurs via narrow filaments (Colberg et al. 1999; Aubert et al. 2004; Faltenbacher et al. 2005) and is more radial than matter infall onto low-mass halos, which are comparable in size to their local filament and thus experience more isotropic infall.

The nature of mass accretion may also vary with redshift, with implications for the formation of the earliest galaxies. For instance, hydrodynamic simulations suggest that galaxy formation at $z \gtrsim 2$ proceeds through highly radial flows of cold gas that penetrate deep into the host halo (Kereš et al. 2005; Dekel et al. 2009), behavior not observed in the local Universe. While these radial flows are influenced by complex gas dynamics, since dark matter dominates the mass of infalling matter, this trend implies that matter accretion onto massive halos at high redshift may be significantly more radial than at low redshift.

In this chapter, we use a high-resolution N-body simulation of cosmological volume to examine the orbits of satellite halos at the time of infall onto larger host halos. In addition to exploring the distributions of satellite orbital parameters, we also examine how the nature of satellite accretion varies with halo mass and redshift. The combination of high resolution and large volume allows us to study the nature of accretion from dwarf galaxy masses ($10^{10}\,h^{-1}\,\mathrm{M}_\odot$) to massive galaxy clusters ($10^{15}\,h^{-1}\,\mathrm{M}_\odot$) with good statistics from $z = 0$ to 5.

5.2 Methods

5.2.1 Simulations & Halo Tracking

To find and track halos, we employ a dissipationless N-body simulation using the TreePM code of White (2002). This simulation uses ΛCDM cosmology ($\Omega_\mathrm{m} = 0.25$, $\Omega_\Lambda = 0.75$, $h = 0.72$, $n = 0.97$ and $\sigma_8 = 0.8$) in agreement with a wide array of observations (Dunkley et al. 2009; Kowalski et al. 2008; Vikhlinin et al. 2009; Percival et al. 2009). For high mass and force resolution, the simulation evolves 1500^3 particles in a 200 Mpc cube, with a particle mass of $1.64 \times 10^8\,h^{-1}\,\mathrm{M}_\odot$ and a Plummer equivalent smoothing of 3 kpc. Initial conditions are generated using second-order Lagrangian Perturbation Theory at $z = 250$ where the RMS is 20% of the mean inter-particle spacing. 45 outputs are stored evenly in $\ln(a)$ from $z = 10$ to 0, with an output time spacing of $\sim 650\,\mathrm{Myr}$ at $z = 0$. Note that this is the same simulation as was used in Chapter 8.

Halos are found using the Friends-of-Friends (FoF) algorithm (Davis et al. 1985) with a linking length of $b = 0.168$ times the mean inter-particle spacing.[2] We keep all groups that have more than 60 particles, corresponding to $10^{10}\,h^{-1}\,\mathrm{M}_\odot$. This resolution level ensures that FoF halo masses are accurate to within 10% (Warren et al. 2006). Merger trees are constructed from the set of halo catalogs by specifying a parent-child relationship. To be

[2]The longer linking length of $b = 0.2$ is often used, but it is more susceptible to joining together distinct, unbound structures.

a 'parent', a halo must contribute more than half of its mass to a 'child' halo at the next simulation output. Thus, a parent halo can never have more than one child. A mergers is identified as a child halo with more than one parent.

5.2.2 Ejected Halos & Re-mergers

Once a satellite halo has fallen into a larger halo, it can retain its identity as a bound subhalo. In some cases a subhalo can become ejected from its host halo after infall, either from being on an initially unbound orbit or from a scattering event within the host halo. Up to 50% of all satellite halos within $2-3\,R_{\rm vir}$ of a host halo are a recently ejected population, particularly at low satellite halo mass (since subhalos experience severe mass stripping as they pass through a host halo) and for satellites with highly eccentric orbits (Gill et al. 2005; Ludlow et al. 2009; Wang et al. 2009). Including these re-merging satellite halos would bias the orbital distribution results because doing so would double count a single satellite halo across redshift and artificially enhance the population of highly elliptical orbits. Thus, we define infall as the first time a halo merges with a more massive halo, and we use this event to compute satellite orbits, discarding subsequent re-mergers. An exception is made if a satellite halo has more than doubled its mass since becoming ejected, since in this case a new halo is considered to have formed.

5.2.3 Calculating Orbits

To calculate the orbital parameters of satellite halos at infall onto more massive host halos, we use the simulation halo merger trees to find halos which are about to merge, that is, become joined within an isodensity contour by the FoF algorithm. We then compute the orbital parameters using halo masses, positions, and velocities in the output prior to merging. Positions and velocities are those of the halo's most bound particle, which is expected to correspond to a hosted galaxy. Velocities are calculated using physical coordinates, including Hubble flow.

With these halo properties, we calculate orbital parameters by treating the two halos as isolated point particles in the reduced mass frame (the limitations of this approximation are discussed below). Given satellite mass $M_{\rm sat}$ and host halo mass $M_{\rm host}$, with reduced mass $\mu = M_{\rm sat}M_{\rm host}/\left(M_{\rm sat}+M_{\rm host}\right)$, satellite separation $\mathbf{r} = \mathbf{r}_{\rm host}-\mathbf{r}_{\rm sat}$ and velocity $\dot{\mathbf{r}} = \dot{\mathbf{r}}_{\rm host}-\dot{\mathbf{r}}_{\rm sat}$, the orbital energy is

$$E = \frac{1}{2}\mu\dot{r}^2 - \frac{GM_{\rm sat}M_{\rm host}}{r} \tag{5.1}$$

and the angular momentum is

$$L = \mu\mathbf{r}\times\dot{\mathbf{r}}. \tag{5.2}$$

With these, we compute the orbital eccentricity,

$$e = \sqrt{1+\frac{2EL^2}{\left(GM_{\rm sat}M_{\rm host}\right)^2\mu}} \tag{5.3}$$

pericentric distance (from host halo center),

$$r_{\rm peri} = \frac{L^2}{(1+e)GM_{\rm sat}M_{\rm host}\mu} \tag{5.4}$$

and apocentric distance

$$r_{\rm apo} = \frac{L^2}{(1-e)GM_{\rm sat}M_{\rm host}\mu}. \tag{5.5}$$

Orbital circularity is defined as the ratio of the orbit angular momentum to that of the circular orbit with the same energy and can also be related to eccentricity

$$\eta = \frac{j(E)}{j_c(E)} = \sqrt{1-e^2}. \tag{5.6}$$

In the point particle two-body approximation, the above quantities are all conserved throughout the orbit, so they do not depend on the separation of the satellite from the host halo. Two of the above quantities (for example, circularity plus pericenter) are sufficient to uniquely describe an orbit. An alternate description can be given by the satellite's radial, $V_{\rm r}$, plus tangential, V_θ, velocity. Since these quantities vary throughout the orbit, they need to be defined at a given radius, in this case, at the host halo virial radius. To do this, we use the conservation of orbital energy and angular momentum to evolve the velocities from the satellite's measured location to where its center crosses the host halo virial radius, $R_{\rm vir}$, which is derived from the halo FoF mass and concentration assuming a spherical NFW (Navarro et al. 1996) density profile.

Hereon, all satellite halo distances and velocities are scaled to the host halo virial radius and virial circular velocity, $V_{\rm vir} = \sqrt{GM_{\rm vir}/R_{\rm vir}}$.

5.2.4 Calculating Orbital Distributions

The aim of this work is to examine the orbital parameter distributions of satellite halos as they first pass through the virial radius of a larger host halo. However, because of the finite time spacing of simulation outputs, satellite halos are identified at a variety of distances from the host halo virial radius prior to merging. This presents some difficulty in directly measuring orbital parameter distributions, since satellite halos can experience mass loss (or growth), dynamical friction, and tidal forces, all of which alter the orbital parameters as satellites traverse significant distances.

To circumvent this issue of finite time resolution, we estimate satellite orbital parameter distributions by selecting only satellite halos that are within a small separation of the host halo virial radius at the output prior to merging (as done by Vitvitska et al. 2002; Benson 2005; Wang et al. 2005). Specifically, we find satellite halos that are about to merge with a larger host halo and whose edge (given by its own virial radius) is in range $[1, 1+\Delta r]\, R_{\rm vir}$ of

the virial radius of the host halo.[3] We use $\Delta r = 0.25$, finding no significant difference using smaller values.

Since highly radial orbits spend less time within the given radial shell than highly circular ones, to properly estimate the overall orbital distributions one must scale the orbital counts by the crossing time within the shell. Specifically, we scale the counts by $\Delta t/t_{\rm cross}$, where Δt is the output time interval and $t_{\rm cross}$ is the orbital crossing time for a satellite halo edge to orbit from a separation of Δr to 0.[4]

Since this method of estimating satellite orbital distributions considers only satellites close to the location of interest, it is little-affected by mass stripping, dynamical friction, and tidal forces, and the error on the estimated orbital parameters is expected to be less than 10% (Benson 2005). There are, however, limitations to the point particle two-body approximation, which ignores multi-body interactions and halo ellipticities. Some satellites (up to 20% at $z = 0$) have their $r_{\rm peri}$ or $r_{\rm apo}$ within the radial selection shell, so these objects do not have a well-defined crossing time even though they do merge with the host halo in the next output. This population is dominated by satellites on highly circular orbits, such that $r_{\rm apo}$ is never beyond the outer radial shell. In weighting their counts for orbital distributions, these satellites are given a shell crossing time equal to the longest well-defined crossing time satellite in the given output, which amounts to a minimal weighting without discarding them. Additionally, some merging satellites are on formally unbound orbits, though this represents less than 2% of satellites regardless of mass or redshift.[5]

Finally, we have also examined how using $M_{\rm 200crit}$ instead of FoF mass influences the results.[6] We find that the averages of the orbital distributions from the two methods are within error, and thus the specific halo finding algorithm used does not significantly affect the results, in agreement with similar tests of Benson (2005).

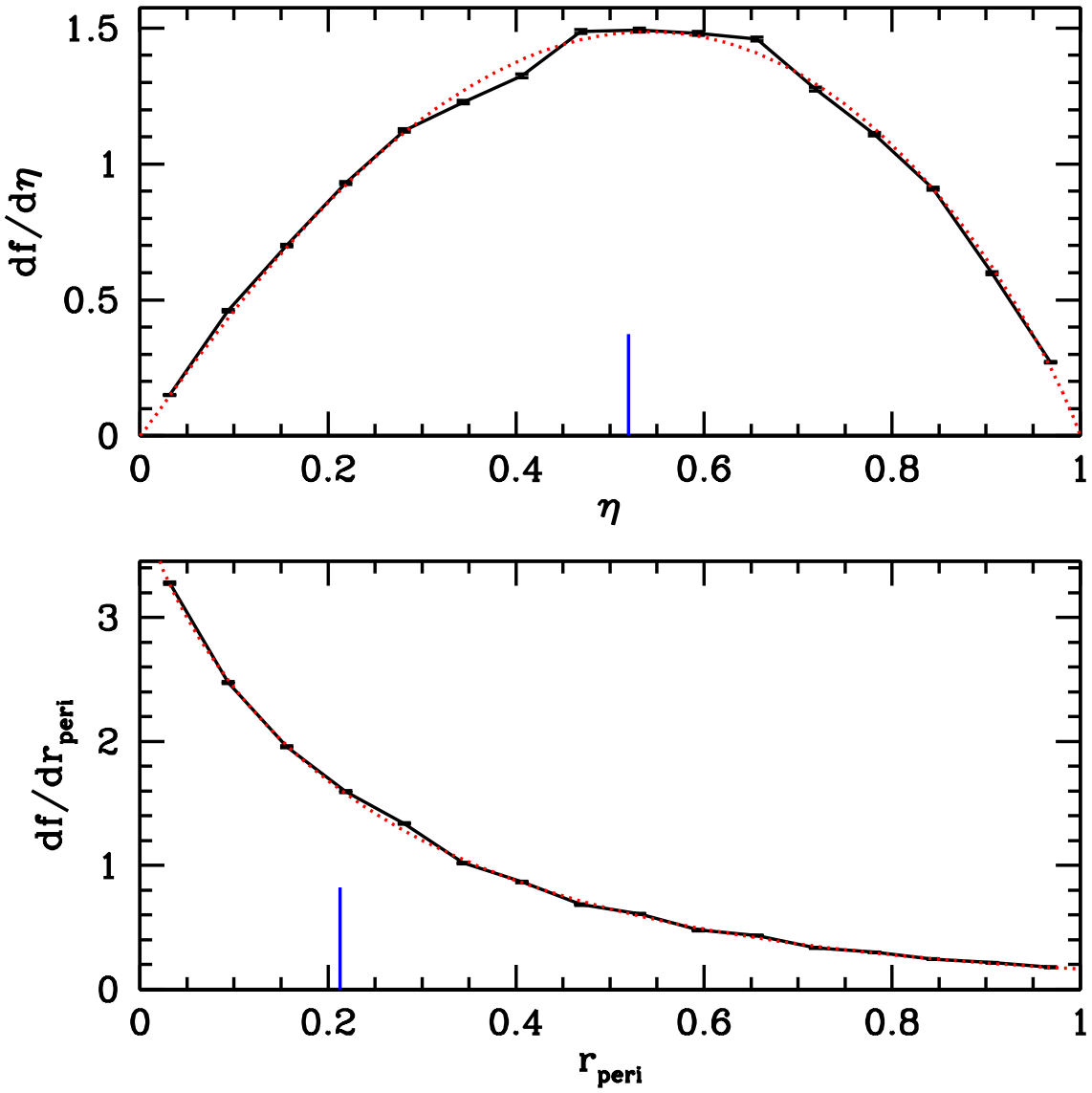

Figure 5.1: Distributions of circularity, η, and pericenter, $r_{\rm peri}$ (scaled to host halo virial radius), of infalling satellite halos at $z = 0$, for halos $> 10^{10}\,h^{-1}\,{\rm M}_\odot$. Errors bars indicate Poisson error in each bin. Vertical lines show average circularity and median pericenter. Dotted curves show fits to the distributions (Eqs. 5.7 and 5.8).

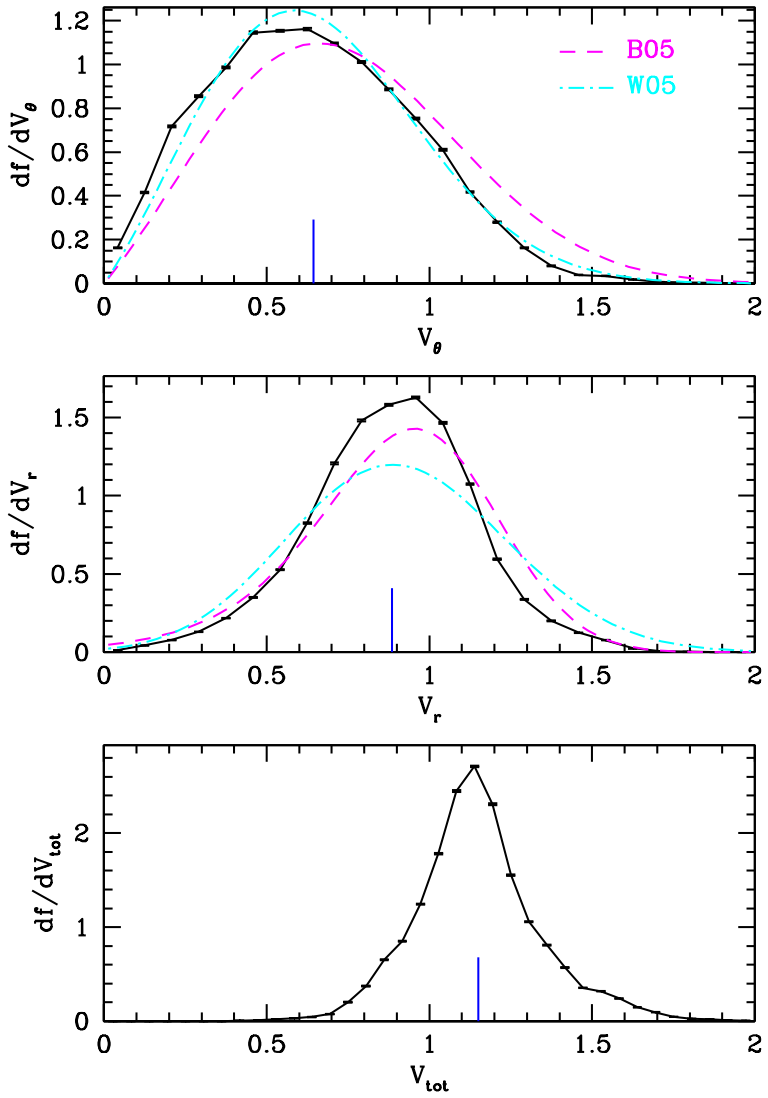

Figure 5.2: Distributions of tangential, V_θ, radial, V_r, and total, V_tot, velocity (scaled to host halo virial velocity) of infalling satellite halos at $z = 0$, for halos $> 10^{10}\,h^{-1}\,\mathrm{M}_\odot$. Vertical lines show average velocities. Dashed and dot-dashed curves show distributions from Benson (2005) and Wang et al. (2005).

5.3 Orbital Distributions at $z = 0$

We begin by examining the distributions of satellite orbital parameters for all infalling satellites at $z = 0$. Figure 5.1 shows the distribution of circularity and pericenter, scaled to the host halo virial radius, for all halos $> 10^{10}\,h^{-1}\,\mathrm{M}_{\odot}$. Circularity shows a broad distribution, peaking at $\eta = 0.52$ (which corresponds to an eccentricity of $e = 0.85$), in good agreement with earlier work (Tormen 1997; Zentner et al. 2005; Wang et al. 2005; Khochfar & Burkert 2006). Satellite orbits tend to be neither highly radial nor highly circular. Pericenter shows a distribution falling exponentially with radius, with a median value of $r_{\rm peri} = 0.21$ and falling to zero for $r_{\rm peri} > 1$. Most infalling satellites are on orbits taking them close to the center of the host halo.

While an orbit can be fully classified by its circularity and pericenter, another such combination is radial and tangential velocity as measured at the host halo virial radius. Figure 5.2 (top and middle) shows these satellite velocity distributions, scaled to the host halo virial velocity. Since the velocities are computed at the host halo virial radius, the tangential velocity is equivalent to the satellite specific angular momentum: $L/L_{\rm vir} = V_\theta/V_{\rm vir}$. Most satellites infall with less specific angular momentum than the virial value of the host halo, with an average $V_\theta = 0.64$. By contrast, the satellite radial velocity is typically comparable to the host halo virial velocity, with an average $V_{\rm r} = 0.89$. Taken together, these imply that most satellites are infalling 'hotter' than their host halo. Figure 5.2 (bottom) demonstrates this more explicitly, showing the satellite total velocity distribution, again scaled to the host halo virial velocity. On average, satellites are infalling with $\sim 15\%$ higher velocity than the matter within the host halo.

To compare with previous work, Fig. 5.2 also shows fits to the velocity distributions at $z = 0$ of Benson (2005) and Wang et al. (2005), which represent a Gaussian distribution for radial velocity and approximately a two-dimensional Maxwell-Boltzmann distribution for tangential velocity. While the radial velocity distribution seen here exhibits a somewhat narrower profile, the distributions show overall broad agreement, particularly in the averages

[3]We use the location of the satellite edge since the FoF algorithm merges the halos when the satellite edge is at the host halo $R_{\rm vir}$.

[4]This correction for crossing time was employed by Benson (2005) and Wang et al. (2005) but was neglected in Vitvitska et al. (2002).

[5]Another method to estimate satellite orbital parameter distributions is to consider all satellite halos which are about to merge, regardless of their distance from the host halo in the output prior to merging, as done by Khochfar & Burkert (2006). However, they find that in order to select systems which conserve energy and angular momentum, they are restricted to 'isolated' merger systems which do not change in total mass by more than 10% between outputs. Indeed, we find that using all satellites which are about to merge yields as high as 15% of orbits being formally unbound, since satellite halos on highly eccentric orbits, which are more likely to be found at large radii in the output prior to merging, become significantly more bound prior crossing the host halo virial radius. We find that while using this alternate method yields quantitatively different orbital distributions, it yields qualitatively similar results regarding the orbital distribution shapes and their mass and redshift dependence.

[6]The relation of FoF($b = 0.168$) mass to spherical overdensity (200crit) mass depends on halo concentration and redshift, though for the regimes considered here they are within $\sim 15\%$.

and peak locations. Some of the differences may be attributed to previous works using somewhat different cosmology and that Wang et al. (2005) selected satellite *subhalos* (halos which may have already merged) within a radial shell. More importantly, the previous works examined satellite orbits at a higher mass regime, and as will be explored in the next section, satellite orbital distributions depend on halo mass.

Finally, the above tangential velocity distribution explains why pericenter exhibits an exponential distribution. At fixed mass ratio, $r_{\rm peri} \propto V_\theta^2/(1+e)$ (Eq. 5.4). Since eccentricity is essentially limited to $0 < e < 1$, the $r_{\rm peri}$ distribution is dominated by the V_θ^2 term. V_θ is described by a two-dimensional Maxwell-Boltzmann distribution, $P(V_\theta) \sim V_\theta {\rm e}^{-(V_\theta - V_o)^2}$, so under transformation, the distribution of V_θ^2, and hence $r_{\rm peri}$, is exponential.

5.4 Mass Dependence

We next explore how satellite orbital distributions depend on halo mass at $z = 0$. We first examine the dependence on host halo mass by selecting satellite halos in the mass range $10^{10.0-10.5}\,h^{-1}\,{\rm M}_\odot$, and we use the large dynamic range of the simulation to explore the dependence across four decades in halo mass.

Figure 5.3 shows the distribution of circularity and pericenter, as in Fig. 5.1, but for two host halo mass ranges. The distributions clearly change shape, being skewed to both lower circularity and lower pericenter for more massive host halos, which drives the average/median of the distributions (vertical lines) down.

Figure 5.4 demonstrates more explicitly the dependence of average circularity and median pericenter on host halo mass. Circularity shows no dependence up to $\sim 3\times10^{12}\,h^{-1}\,{\rm M}_\odot$, but above this mass satellite orbits become less circular with increasing host halo mass, with average circularity dropping nearly 20% across the mass range. Interestingly, the turnover corresponds to the value of M_*, the characteristic halo mass scale of collapse, at $z = 0$.[7] Median pericenter decreases more strongly with host halo mass, falling by more than a factor of 2 across the mass range and showing no rollover at low mass. Overall, satellite orbits are both more radial and plunge deeper into their host halo at higher host halo mass.

Similarly, Fig. 5.5 (top and middle) shows the host halo mass dependence of satellite average tangential and radial velocity. Both velocity components remain below the host halo virial velocity at all mass scales. Tangential velocity monotonically declines with host halo mass, falling by 30%, implying that at higher halo masses, satellite accretion contributes angular momentum less efficiently. Radial velocity declines rapidly with host halo mass up to $\sim 3\times10^{12}\,h^{-1}\,{\rm M}_\odot$, beyond which it remains nearly flat.

These trends explain the host halo mass dependence of circularity and pericenter. Below $\sim 3\times10^{12}\,h^{-1}\,{\rm M}_\odot$, both V_θ and $V_{\rm r}$ decline with host halo mass, giving rise to constant circularity. At fixed circularity (eccentricity) and $M_{\rm sat}$, $r_{\rm peri}/R_{\rm vir} \propto V_\theta^2/M_{\rm host}^{4/3}$ (Eq. 5.4), so

[7] More specifically, $M_*(z)$ is the mass at which $\sigma(M,z)$, the variance of the linear power spectrum at redshift z smoothed on scale M, equals the threshold for linear density collapse, $\delta_c = 1.69$.

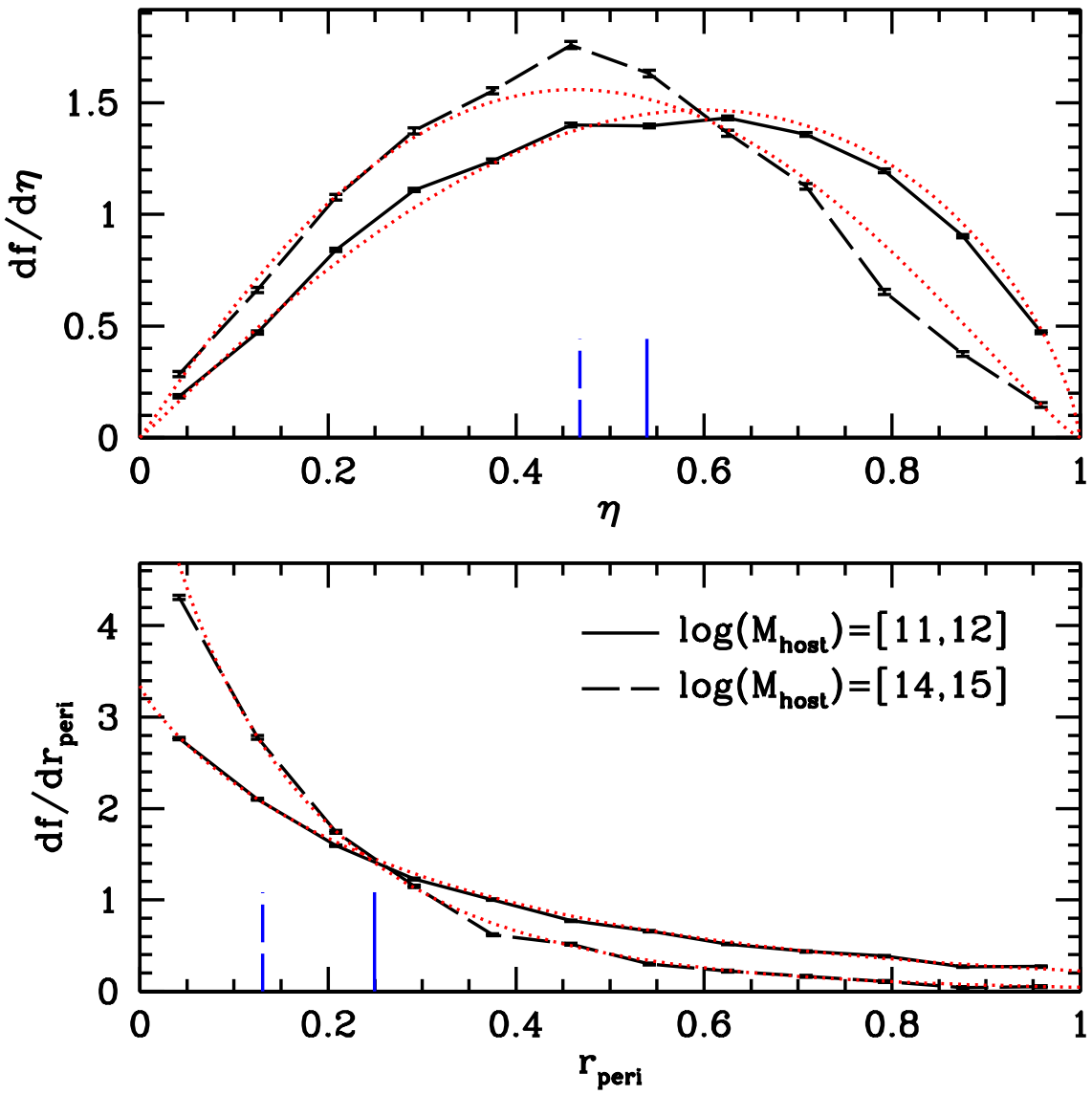

Figure 5.3: Distributions of circularity and pericenter at $z = 0$, for satellite halos of mass $10^{10.0-10.5}\,h^{-1}\,\mathrm{M}_\odot$ and host halos in two mass ranges. Vertical lines show average circularity and median pericenter. Dotted curves show fits to the distributions (Eqs. 5.7 and 5.8). Satellite orbital distribution shapes depend on host halo mass.

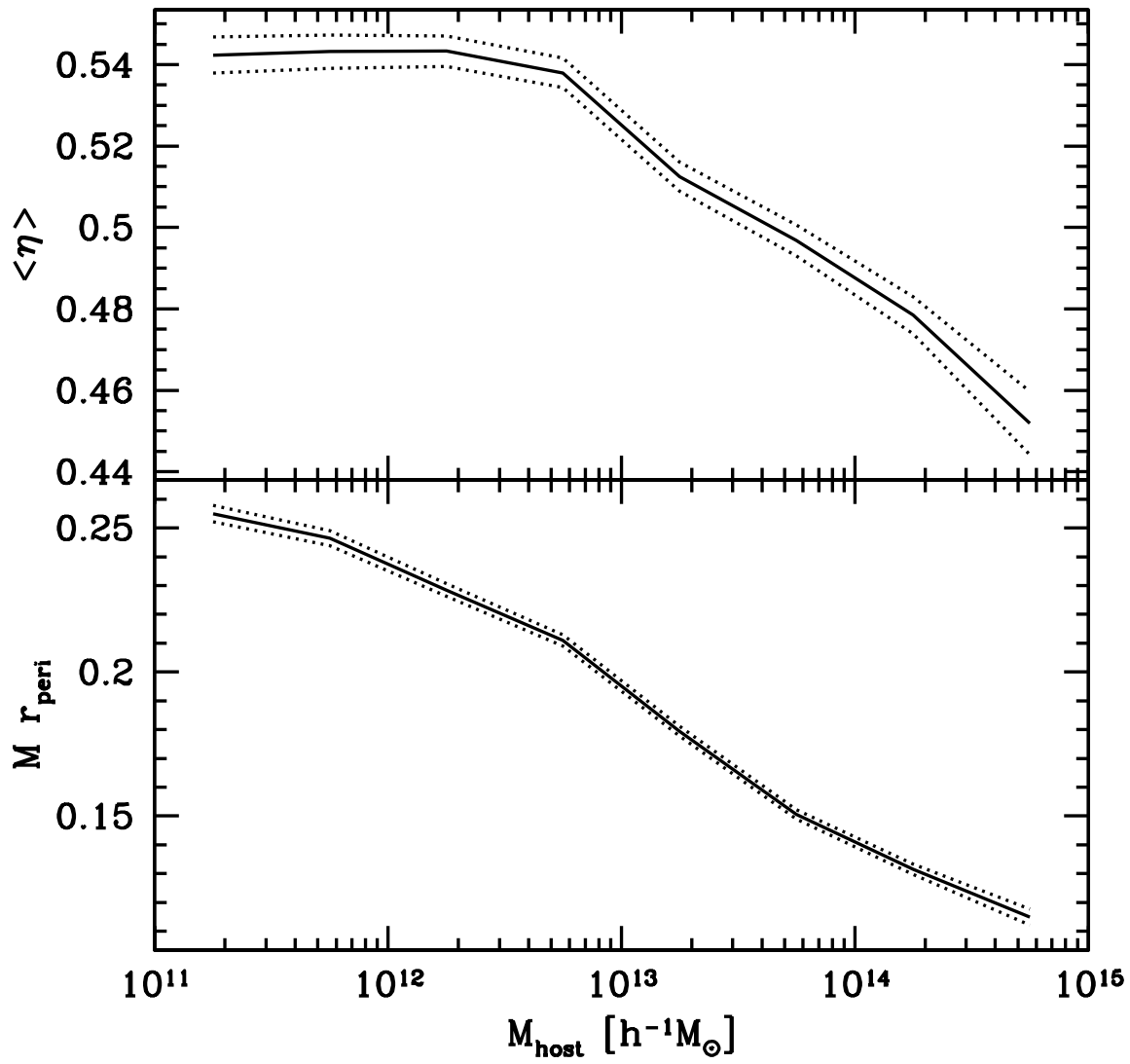

Figure 5.4: Dependence of satellite average circularity and median pericenter on host halo mass at $z = 0$, for satellite halos of mass $10^{10.0-10.5}\,h^{-1}\,\mathrm{M}_\odot$. Dotted curves show standard errors of the mean/median. Satellite orbits are both more radial and plunge deeper at higher host halo mass.

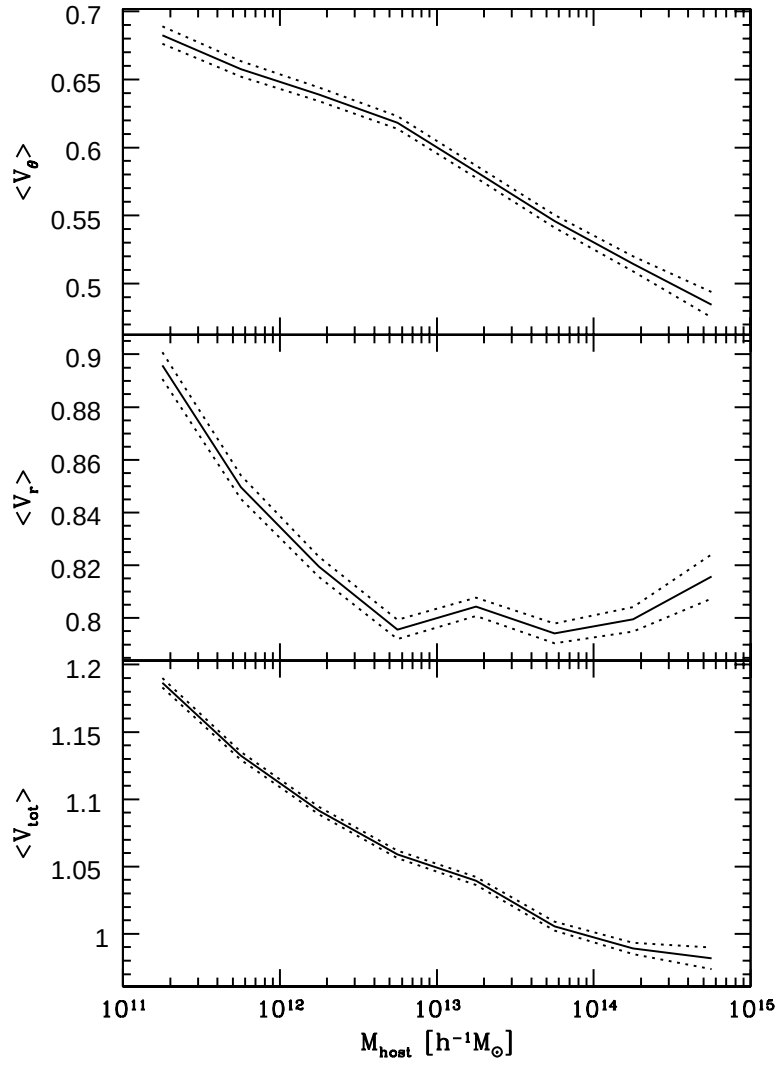

Figure 5.5: Dependence of satellite average tangential, radial, and total velocity on host halo mass at $z = 0$, for satellite halos of mass $10^{10.0-10.5}\,h^{-1}\,\mathrm{M}_{\odot}$. The degree to which satellite infall velocities are biased relative to their host halos depends on host halo mass.

$r_{\rm peri}$ continues to decline rapidly with mass. Above $\sim 3 \times 10^{12}\,h^{-1}\,{\rm M}_\odot$, declining V_θ and constant $V_{\rm r}$ cause both circularity and pericenter to decline with mass.

Additionally, Fig. 5.5 (bottom) shows the host halo mass dependence of satellite average total velocity. While satellite infall is usually 'hotter' than the host halo virial velocity, the magnitude of this effect decreases with host halo mass, falling by 20% over the mass range. Interestingly, this leads to a crossover such that satellites infalling onto halos $> 10^{14}\,h^{-1}\,{\rm M}_\odot$ are instead on average 'colder' than the host halo.

The above results clearly demonstrate that satellite orbital parameters depend on host halo mass. Alternately, Fig. 5.6 explores whether circularity and pericenter depend on satellite halo mass, for host halos of fixed mass $10^{14-15}\,h^{-1}\,{\rm M}_\odot$. While Fig. 5.6 suggests a possible drop in circularity and pericenter for very massive satellites, the large scatter across satellite halo mass does not lead to any clear, systematic trends. Moreover, we find no clear trends with satellite mass for *any* orbital parameters, including varying host halo mass or redshift. Thus, we conclude that the nature of satellite infall is controlled by host halo mass and is little affected by satellite mass. This supports the physical picture that orbital dynamics are governed by the most massive halo within a region, and that less massive satellites effectively act as massless tracers of the potential field.

5.5 Redshift Evolution

We now turn to explore the dependence of satellite orbital parameters on redshift. Since the halo mass function declines significantly with redshift, examining the mergers of all halos above the resolution limit ($> 10^{10}\,h^{-1}\,{\rm M}_\odot$) would convolve any redshift dependence together with the mass dependence of the previous section. So to isolate redshift trends, we examine halos in a fixed mass range: host halos of mass $10^{12.0-12.5}\,h^{-1}\,{\rm M}_\odot$ (corresponding to M_* halos at $z = 0$) and satellite halos of mass $10^{10-11}\,h^{-1}\,{\rm M}_\odot$.

Figure 5.7 shows the distribution of circularity and pericenter at three redshifts. Similar to the dependence on host halo mass in Fig. 5.3, the distributions are skewed to both lower circularity and lower pericenter at higher redshift. Figure 5.8 demonstrates more explicitly the dependence of average circularity and median pericenter on redshift. Average circularity falls nearly 30% from $z = 0$ to 5, while pericenter falls more rapidly to less than half of its $z = 0$ value. Overall, satellite orbits become more radial and plunge deeper into their host halos with increasing redshift.

Figure 5.9 also shows the redshift evolution of satellite velocities. Tangential velocity declines with redshift, implying that satellite accretion less efficiently contributes angular momentum growth at higher redshift. Conversely, radial velocity increases with redshift, approaching the host halo virial value at $z \approx 5$. Interestingly, the contrasting evolutionary trends of radial and tangential velocity lead to no significant evolution in total velocity. At all redshifts, satellite infall remains 'hotter' than the host halo virial velocity.

What drives the redshift evolution of satellite orbits? One possibility is that redshift dependence is simply a manifestation of the trends with mass from the previous section.

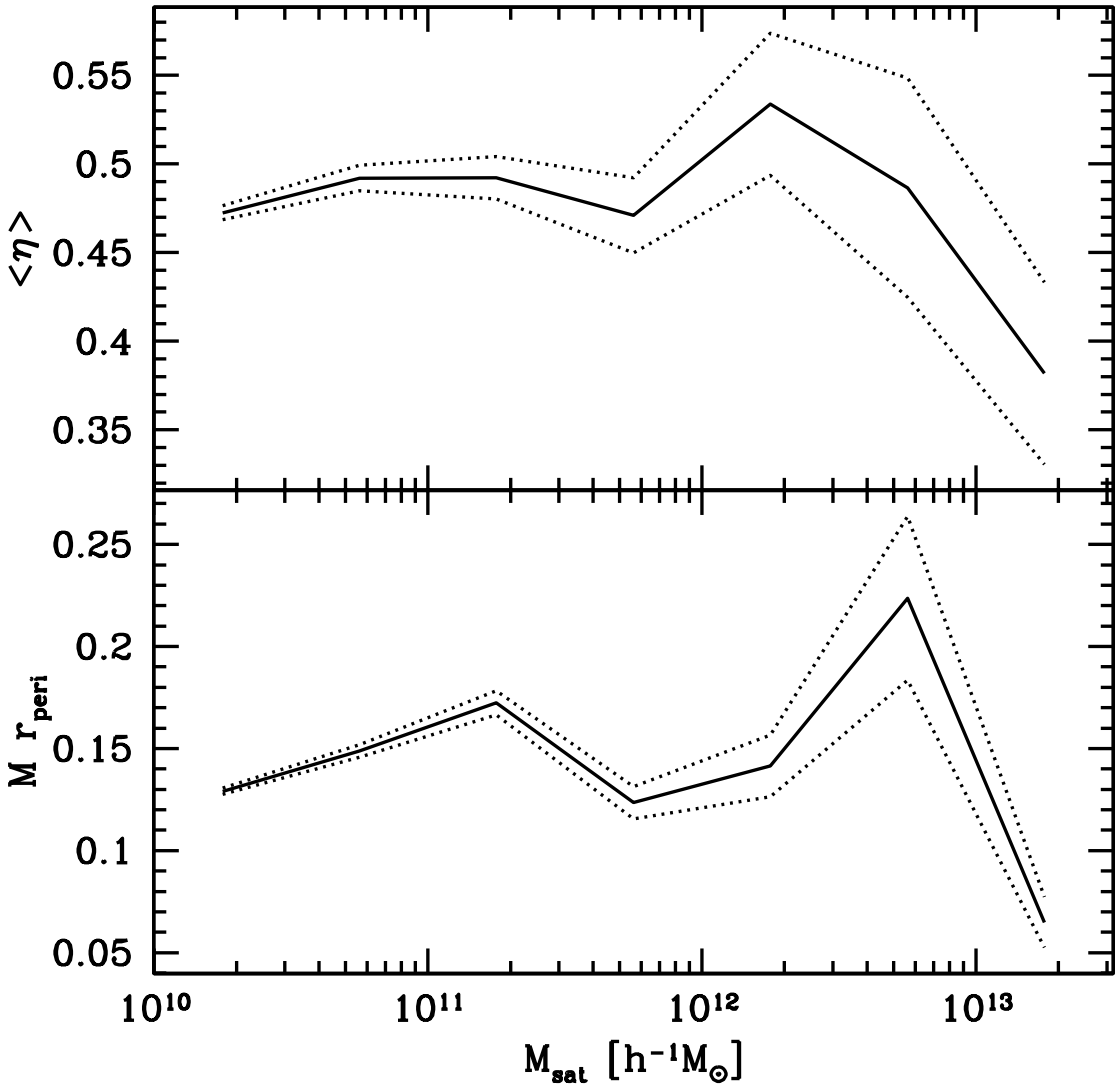

Figure 5.6: Dependence of satellite average circularity and median pericenter on satellite halo mass at $z = 0$, for host halos of mass $10^{14-15}\,h^{-1}\,\mathrm{M}_{\odot}$. No significant, systematic dependence on satellite mass is found at any mass scale or redshift.

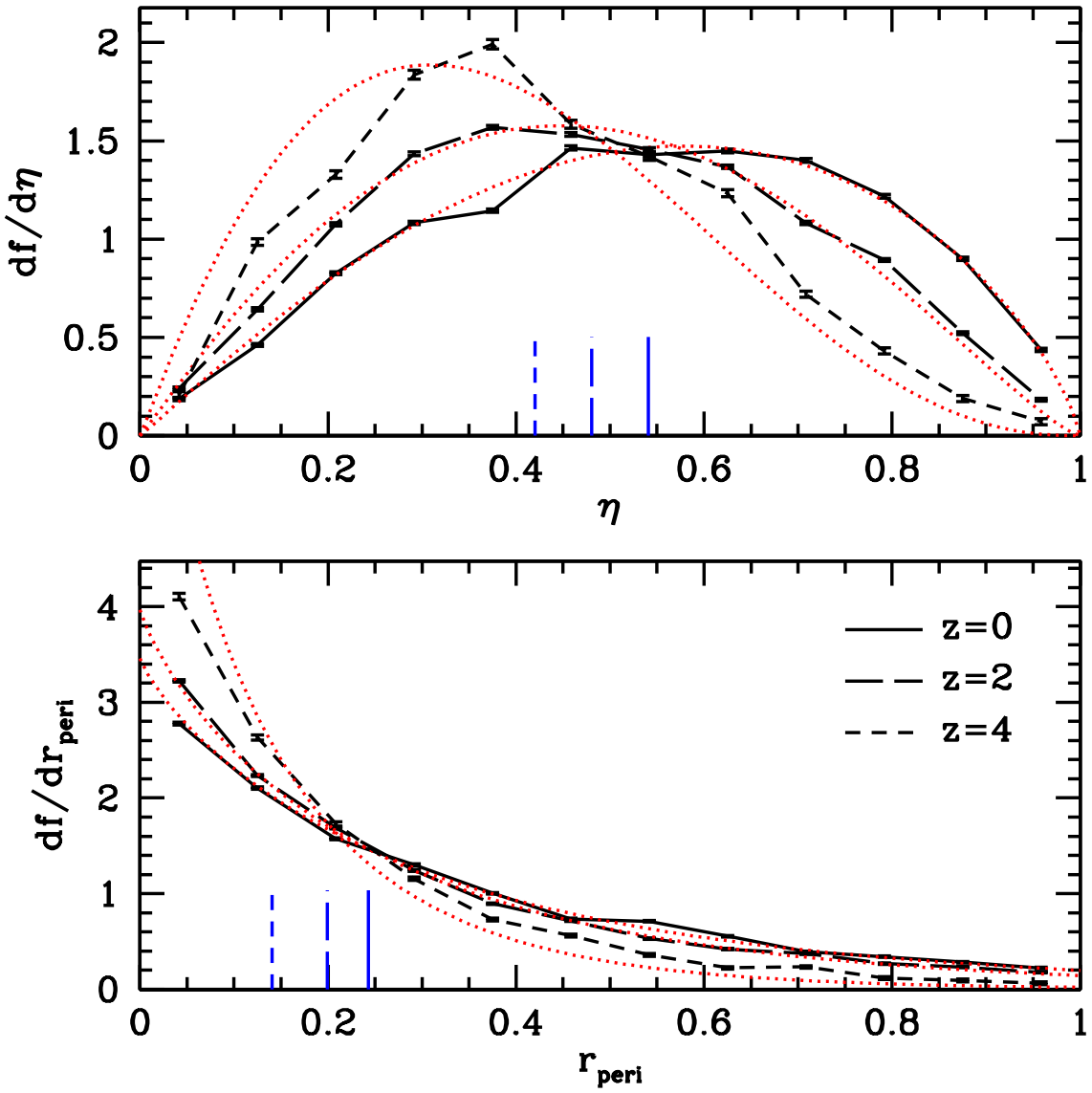

Figure 5.7: Distributions of circularity and pericenter at different redshifts, for host halos of mass $10^{12.0-12.5}\,h^{-1}\,\mathrm{M}_\odot$ and satellite halos of mass $10^{10-11}\,h^{-1}\,\mathrm{M}_\odot$. Dotted curves show fits to the distributions (Eqs. 5.7 and 5.8). Satellite orbital distribution shapes depend on redshift.

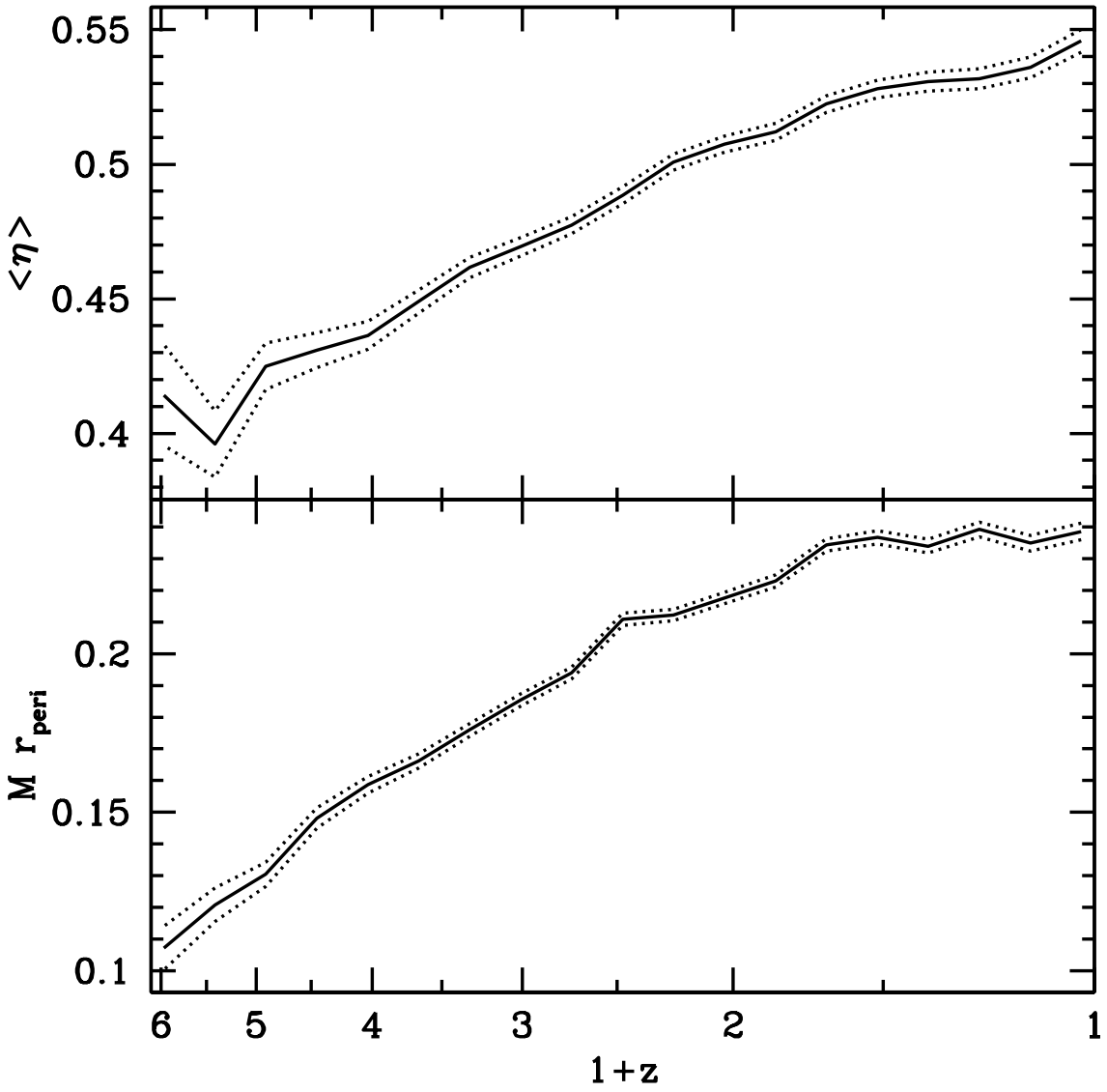

Figure 5.8: Dependence of satellite average circularity and median pericenter on redshift, for host halos of mass $10^{12.0-12.5}\,h^{-1}\,\mathrm{M}_\odot$ and satellite halos of mass $10^{10-11}\,h^{-1}\,\mathrm{M}_\odot$. Satellite orbits are both more radial and plunge deeper at higher redshift.

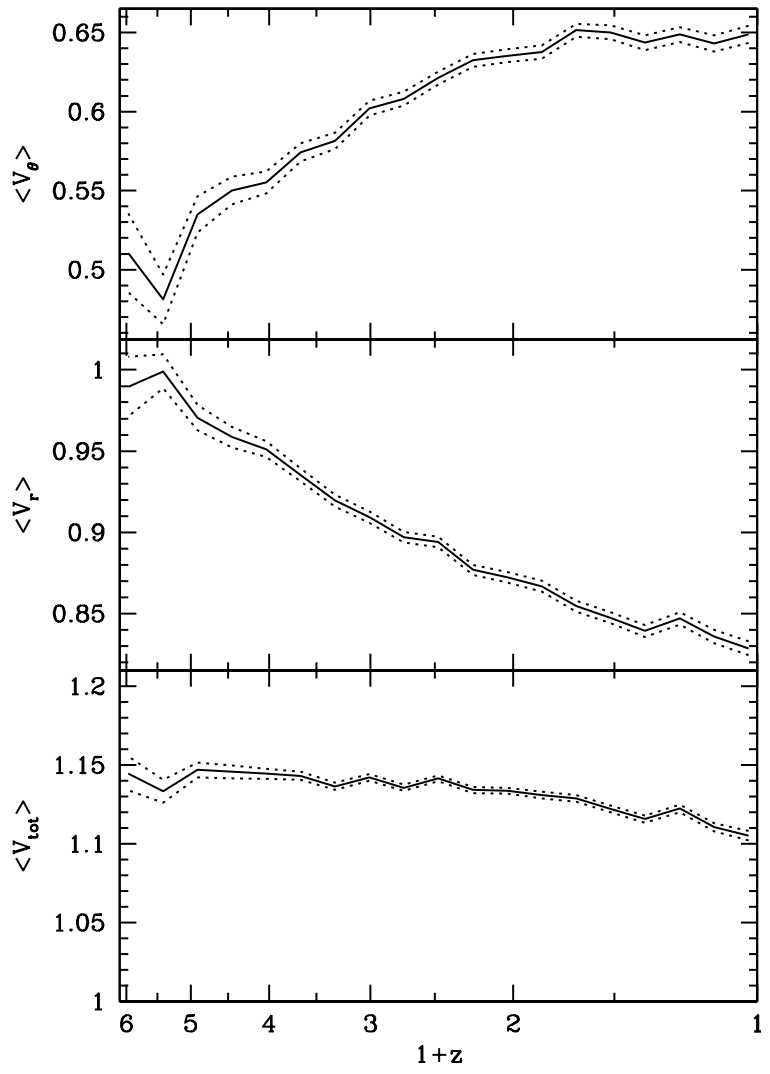

Figure 5.9: Dependence of satellite average tangential, radial, and total velocity on redshift, for host halos of mass $10^{12.0-12.5}\,h^{-1}\,\mathrm{M}_{\odot}$ and satellite halos of mass $10^{10-11}\,h^{-1}\,\mathrm{M}_{\odot}$. Tangential velocity declines with redshift, while radial velocity increases, leading to nearly constant total velocity.

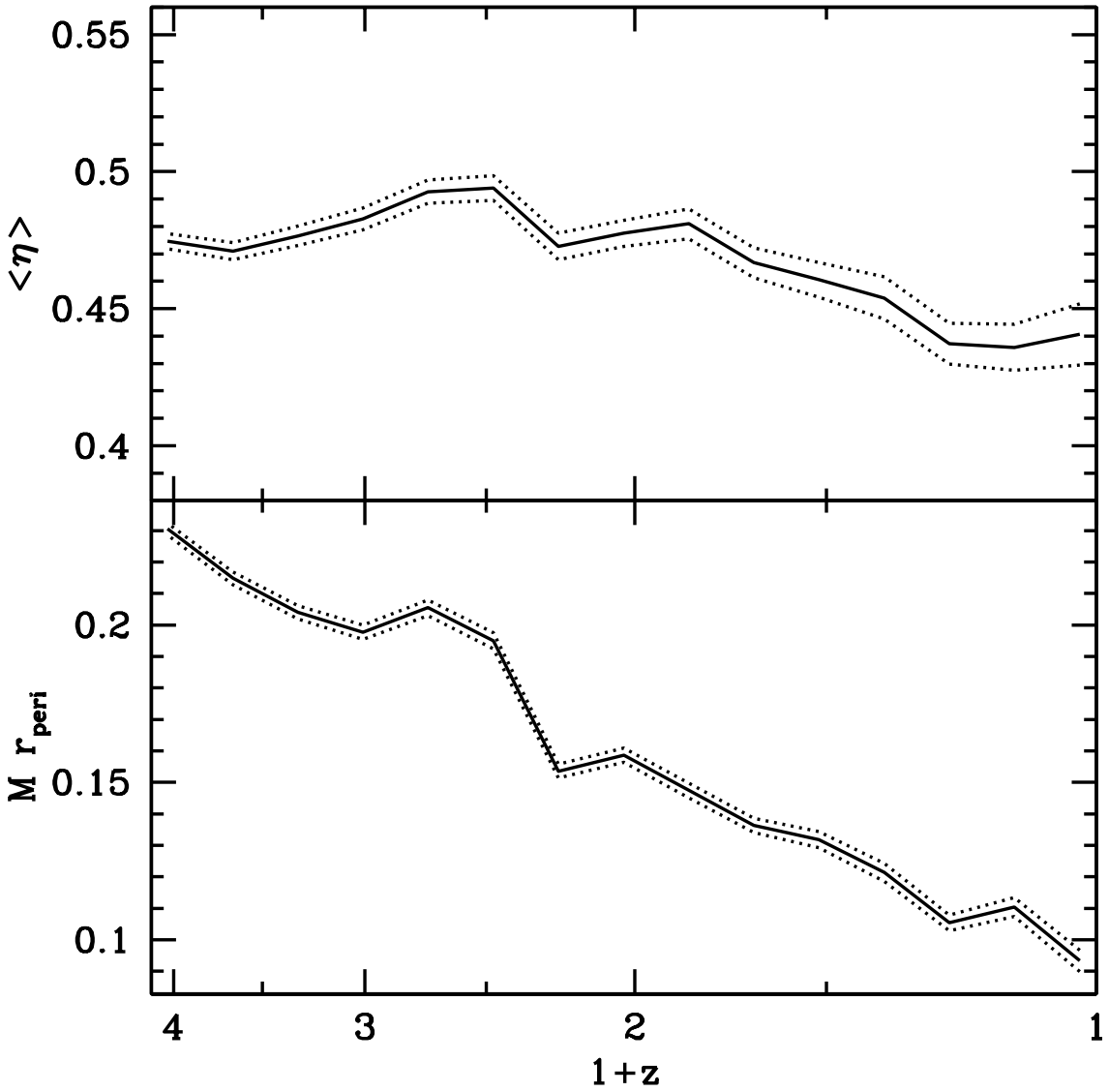

Figure 5.10: Same as Fig. 5.8, but for host halos of mass $270\,M_*(z)$ ($10^{14.75}\,h^{-1}\,\mathrm{M}_\odot$ at $z = 0$ down to $10^{10.3}\,h^{-1}\,\mathrm{M}_\odot$ at $z = 3$) and satellite halos of mass $10^{10.0-10.3}\,h^{-1}\,\mathrm{M}_\odot$. When scaled by $M_*(z)$, circularity remains nearly constant while pericenter increases significantly.

	α_i	β_i	γ_i	$g_i(z)$
C_0	3.38	0.567	0.152	1
C_1	0.242	2.36	0.108	1
R_0	3.14	0.152	0.410	$(1+z)^{-4}$
R_1	0.450	−0.395	0.109	$(1+z)^{-4}$

Table 5.1: Fit parameters for C_i, R_i, given by Eq. 5.9, for use in circularity (Eq. 5.7) and pericenter (Eq. 5.8) distributions.

Analytical triaxial collapse models of halo formation (Bardeen et al. 1986; Eisenstein & Loeb 1995; Sheth et al. 2001) predict a self-similarity in the nature of matter infall with redshift at fixed $M/M_*(z)$, since it is at M_* that halos transition from being located along filaments to being at the intersection of several filaments. In this picture, the above redshift dependence is driven by probing higher $M_{\rm host}/M_*(z)$ at higher z.

To investigate this, we select host halos of mass $M_{\rm host}/M_*(z) = 270$ at each redshift (corresponding to $10^{14.75}\,h^{-1}\,{\rm M}_\odot$ at $z = 0$ down to $10^{10.3}\,h^{-1}\,{\rm M}_\odot$ at $z = 3$) and satellite halos in the range $10^{10.0-10.3}\,h^{-1}\,{\rm M}_\odot$. Figure 5.10 (top) shows that satellite infall onto host halos of constant $M_{\rm host}/M_*(z)$ indeed exhibits nearly constant circularity. However, pericenter (bottom) is not constant but instead increases with redshift by a factor of 2 (opposite to the trend at fixed mass). Furthermore, at fixed $M_{\rm host}/M_*(z)$ we find a significant increase in radial, tangential, and total velocity with redshift. Thus, while the redshift evolution of satellite infall can be partially understood simply as a manifestation of mass dependence, intrinsic redshift dependence does exist.

5.6 Fits to Orbital Distributions

We now seek to provide analytical fits to the orbital distributions of the two parameters of primary interest, circularity and pericenter. The results of the previous sections show that the shapes of these orbital distributions depend sensitively on both mass and redshift. However, Fig. 5.10 shows that, at fixed $M_{\rm host}/M_*(z)$, circularity remains nearly constant with redshift. Figure 5.11 (top) demonstrates this more explicitly, showing that the overall circularity distribution remains approximately universal at fixed $M_{\rm host}/M_*(z)$. However, the distribution of pericenter is neither redshift-invariant at fixed $M_{\rm host}$ (Fig. 5.7) nor at fixed $M_{\rm host}/M_*(z)$ (Fig. 5.11).

The orbital distributions of satellite circularity, η, and pericenter, $r_{\rm peri}$, are given to good approximation across mass ($10^{10-15}\,h^{-1}\,{\rm M}_\odot$) and redshift ($z = 0 - 5$) by the following simple functional forms

$$\frac{{\rm d}f}{{\rm d}\eta} = C_0(M_{\rm host}, z)\eta^{1.05}(1-\eta)^{C_1(M_{\rm host},z)} \tag{5.7}$$

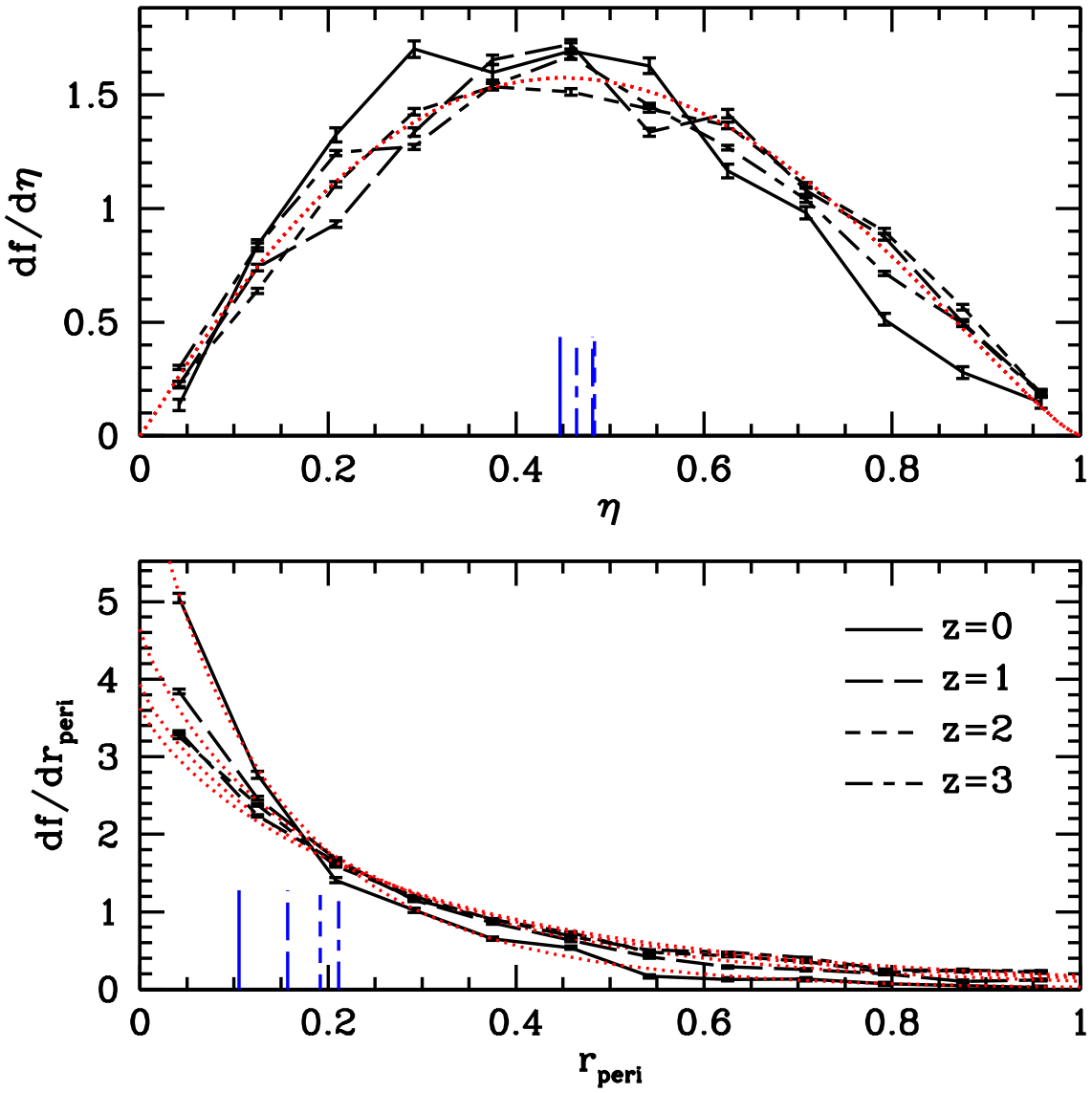

Figure 5.11: Distributions of circularity and pericenter at different redshifts, for host halos of mass $270\,M_*(z)$ and satellite halos of mass $10^{10.0-10.3}\,h^{-1}\,\mathrm{M}_\odot$. Dotted curves show fits to the distributions (Eqs. 5.7 and 5.8). The circularity distribution is nearly universal for host halos of fixed $M_{\rm host}/M_*(z)$.

$$\frac{\mathrm{d}f}{\mathrm{d}r_{\rm peri}} = R_0(M_{\rm host}, z)\exp\left\{-[r_{\rm peri}/R_1(M_{\rm host}, z)]^{0.85}\right\}. \quad (5.8)$$

Parameters $C_i(M_{\rm host}, z)$ and $R_i(M_{\rm host}, z)$ describe the mass and redshift dependence and take a similar functional form

$$C_i, R_i = \alpha_i \left(1 + \beta_i \left[g_i(z)\frac{M_{\rm host}}{M_*(z)}\right]^{\gamma_i}\right) \quad (5.9)$$

where the values for $\alpha_i, \beta_i, \gamma_i$ and the function $g_i(z)$ are given in Table 5.1. Since the circularity distribution is nearly constant when scaled by $M_{\rm host}/M_*(z)$, $g_i(z) = 1$ for C_i. While the pericenter distribution does not exhibit such redshift invariance, the scaling $g_i(z)M_{\rm host}/M_*(z)$ with $g_i(z) = (1+z)^{-4}$ for R_i fully encapsulates the redshift dependence.

Since parameters $C_0(M_{\rm host}, z)$ and $R_0(M_{\rm host}, z)$ are merely normalizations for probability distributions, their mass and redshift dependencies are implicitly given by those of $C_1(M_{\rm host}, z)$ and $R_1(M_{\rm host}, z)$. We include fits to their mass and redshift dependencies for completeness.

Finally, given the assumed cosmology the evolution of $M_*(z)$ is approximated to within 5% up to $z = 7$ by

$$\log\left[M_*(z)/\,h^{-1}\,\mathrm{M}_\odot\right] = 12.42 - 1.56z + 0.038z^2. \quad (5.10)$$

The orbital distribution fits given by Eqs. 5.7 and 5.8 provide a good description of both the mass and redshift dependence of satellite orbits. The accuracy of these fits is demonstrated explicitly in Figs. 5.1, 5.3, 5.7, and 5.11.

Note that while we do not examine in detail correlations between the circularity and pericenter distributions, some correlation is expected (with more circular orbits tending to have larger pericenters) though with significant scatter (Tormen 1997; Gill et al. 2004; Benson 2005; Khochfar & Burkert 2006).

5.7 Summary & Discussion

We use a high-resolution N-body simulation of cosmological volume to track the mergers of halos from dwarf galaxy masses ($10^{10}\,h^{-1}\,\mathrm{M}_\odot$) to massive galaxy clusters ($10^{15}\,h^{-1}\,\mathrm{M}_\odot$) across a large redshift range ($z = 0$ to 5). We explore the orbital parameters of satellite halos at infall, when they cross within the virial radius of a larger host halo. The main results are as follows:

- Satellite orbital parameters exhibit broad distributions. For all resolved halos at $z = 0$, the average values of the distributions are: circularity $\eta = 0.52$, (median) pericenter $r_{\rm peri}/R_{\rm vir} = 0.21$, tangential velocity $V_\theta/V_{\rm vir} = 0.64$, radial velocity $V_{\rm r}/V_{\rm vir} = 0.89$, and total velocity $V_{\rm tot}/V_{\rm vir} = 1.15$.

- Satellite orbits are more radial and plunge deeper into their host halos at higher host halo mass, but orbits are not significantly affected by satellite halo mass.

- Infalling satellites are typically 'hotter' than the host halo virial velocity, except onto the most massive host halos where satellite are slightly 'colder'.
- At fixed halo mass, satellite orbits become more radial and plunge deeper into their host halos at higher redshift.
- The satellite circularity distribution exhibits almost no redshift evolution for host halos of fixed $M_{\rm host}/M_*(z)$, implying that redshift dependence of circularity at fixed mass is simply derivative of varying $M/M_*(z)$. However, pericenter exhibits significant increase with redshift at fixed $M_{\rm host}/M_*$.

As explored in S5.3, the orbital distributions we find at $z = 0$ when stacking halos of all masses agree well with those of previous work. However, previous results of possible mass and/or redshift dependence of satellite orbits are mixed. Benson (2005) found evidence that satellite orbits become more radial at higher halo mass scales but was unable to quantify this further, while Vitvitska et al. (2002) and Wang et al. (2005) saw no such halo mass dependence over a limited mass range. By contrast, Vitvitska et al. (2002) found that satellite angular momentum decreases with increasing satellite mass to host halo mass ratio, while Wang et al. (2005) and Khochfar & Burkert (2006) found no dependence on mass ratio, though again over a limited mass ratio range. Finally, the results of Benson (2005) suggest trends with redshift while those of Vitvitska et al. (2002) do not. In most cases, previous work has been limited in terms of merger statistics (in some cases, examining infall onto a handful of halos) and dynamical range (unable to explore both $M \gg M_*$ and $M \ll M_*$). The results here demonstrate clear dependence of satellite orbits on host halo mass and redshift and no significant evidence for dependence on satellite mass. This is broadly consistent with the predictions of analytical triaxial collapse models (Bardeen et al. 1986; Eisenstein & Loeb 1995; Sheth et al. 2001), in which more massive halos arise from a more spherical Lagrangian volume with less angular momentum. We emphasize that the existence of mass and redshift dependence implies that fits to orbital distributions based on stacking halos of all masses at $z \sim 0$ (e.g., Benson 2005; Zentner et al. 2005; Wang et al. 2005) are not universally accurate.

The mass and redshift trends seen here have implications for various aspects of galaxy formation and evolution. For example, recent work suggests that galaxy formation at $z \gtrsim 2$ proceeds through narrow streams of cold gas (Kereš et al. 2005; Dekel et al. 2009), fundamentally different behavior than seen in the local Universe. Dekel & Birnboim (2006) argued that this difference arises in part because massive ($\sim 10^{12}\,h^{-1}\,{\rm M}_\odot$) halos at high redshift form at the intersection of narrow filaments, while at low redshift such halos are more likely embedded within a filament and experience wide-angle inflow. Our results on the redshift evolution of satellite accretion qualitatively support this picture, but it is not clear that the evolution seen here is strong enough to imply a fundamental change the nature of accretion at $z \sim 2.5$, when most orbital parameters differ from their $z = 0$ values by $\sim 20\%$. This suggests that the above results are driven more strongly by evolving gas physics than by the nature of mass accretion.

Our results also have clear implications for satellite galaxy evolution within groups. Environmental effects such as ram-pressure stripping of gas and tidal stripping of stars are expected to occur primarily at orbital pericenter (e.g., Dekel et al. 2003; Taylor & Babul 2004; McCarthy et al. 2008). Beyond their dependence on evolving gas physics, our results suggest that satellite galaxy quenching and morphological evolution proceed more efficiently and rapidly at higher group masses and higher redshift.

While this work focuses on the orbital parameters of satellite halos at the time of infall, it is not immediately clear how well these orbital distributions and their mass and redshift dependencies persist to satellite populations well after infall, as the orbits become affected by triaxial halo potentials, dynamical friction, and tidal stripping. There has been some work in this direction on satellite subhalo orbits within host halos (Gill et al. 2004; Reed et al. 2005; Sales et al. 2007), which found orbital parameter distributions similar to those here (for example, $\eta \sim 0.5$). Furthermore, Faltenbacher (2009) recently found that the orbits of satellite subhalos within host halos at $z = 0$ are more radially biased in more massive host halos. These suggest that the results here do remain valid well after infall.

Moreover, there is possible observational evidence in support of the trends seen here. Herbert-Fort et al. (2008) examined the orbital velocities of galaxies in local galaxy clusters, finding highly asymmetric velocity distributions consistent with satellites largely retaining their infalling orbits. Promisingly, Biviano & Poggianti (2009) examined satellite galaxy orbits in galaxy clusters from $z = 0$ to $z = 0.8$ and found evidence that satellite orbits are indeed less isotropic (more radial) at higher redshift.

Finally, the results on satellite velocities also have implications for relating satellite dynamics to those of the overall group. At lower host halo masses, satellite velocities become significantly 'hotter' than than the host halo, implying a possible systematic biasing in using satellite velocity dispersions to infer halo masses (Faltenbacher 2009, found a similar trend with mass for the velocity bias of satellite subhalos within host halos). Future work will involve a more detailed analysis of satellite velocity bias and its mass and redshift dependence.

Chapter 6

Galaxy Merger Rates, Counts, & Types

Abstract

Galaxies are believed to be in one-to-one correspondence with simulated dark matter subhalos. We use high-resolution N-body simulations of cosmological volumes to calculate the statistical properties of subhalo (galaxy) major mergers at high redshift ($z = 0.6 - 5$). We measure the evolution of the galaxy merger rate, finding that it is much shallower than the merger rate of dark matter host halos at $z > 2.5$, but roughly parallels that of halos at $z < 1.6$. We also track the detailed merger histories of individual galaxies and measure the likelihood of multiple mergers per halo or subhalo. We examine satellite merger statistics in detail: $15\% - 35\%$ of all recently merged galaxies are satellites and satellites are twice as likely as centrals to have had a recent major merger. Finally, we show how the differing evolution of the merger rates of halos and galaxies leads to the evolution of the average satellite occupation per halo, noting that for a fixed halo mass, the satellite halo occupation peaks at $z \sim 2.5$.

6.1 Introduction

Mergers are key in the hierarchical growth of structure, and major galaxy mergers (referred to as mergers henceforth) are thought to play a crucial role in galaxy evolution. Specifically, they are expected to trigger quasar activity (Carlberg 1990), starbursts (e.g., Barnes & Hernquist 1991; Noguchi 1991), and morphological changes (e.g., Toomre & Toomre 1972), and they are thought to be related to Lyman Break Galaxies (LBG), Sub-Millimeter Galaxies (SMG), and Ultra-Luminous Infrared Galaxies (ULIRG) (see reviews by Giavalisco 2002; Blain et al. 2002; Sanders & Mirabel 1996, respectively). Observational samples of such objects at $z \gtrsim 1$ are now becoming large enough to allow for statistical analyses of

their counts (e.g., Steidel et al. 2003; Ouchi et al. 2004; Coppin et al. 2006; Yoshida et al. 2006; Gawiser et al. 2007; McLure et al. 2008; Patton & Atfield 2008; Tacconi et al. 2008; Yamauchi et al. 2008).

Understanding galaxy mergers and their connection to these observables requires comparison with theoretical predictions. In simulations, galaxies are identified with subhalos, the substructures of dark matter halos (e.g. Ghigna et al. 1998; Moore et al. 1999; Klypin et al. 1999; Ghigna et al. 2000).[1] Simulations are now becoming sufficiently high in resolution and large in volume to provide statistically significant samples (e.g. De Lucia et al. 2004; Diemand et al. 2004; Gao et al. 2004b; Reed et al. 2005). This high mass and force resolution is necessary to track bound subhalos throughout their orbit in the host halo and avoid artificial numerical disruption. This is particularly important for tracking the orbits of galaxies, which are expected to reside in the dense inner core of subhalos and to be more stable to mass stripping than dark matter because of dissipative gas dynamics. The correspondence of galaxies with subhalos has been successful in reproducing galaxy counts and clustering in a wide array of measurements (e.g., Springel et al. 2001, 2005b; Zentner et al. 2005; Bower et al. 2006; Conroy et al. 2006; Vale & Ostriker 2006; Wang et al. 2006; Wetzel & White 2010). Henceforth, we will use the term galaxy and subhalo interchangeably.

A subhalo forms when two halos collide and a remnant of the smaller halo persists within the larger final halo. Thus, subhalo merger rates are sometimes inferred from halo merger rates[2] or subhalo distributions, using a dynamical friction model to estimate the infall time of satellite galaxies to their halo's central galaxy (several of these methods are compared in Hopkins et al. 2008b). However, a detailed understanding of galaxy mergers requires a sufficiently high-resolution simulation that can track the evolution and coalescence of subhalos directly.

Here we use high-resolution dark matter simulations to examine subhalo merger rates, counts, and types, their mass and redshift dependence, and their relation to their host halos. Under the assumption that galaxies populate the centers of dark matter subhalo potential wells, our subhalos are expected to harbor massive galaxies ($L \gtrsim L_*$). Although our subhalo mass assignment is motivated by semi-analytic arguments, our results are independent of any specific semi-analytic modeling prescription.

Previous work on subhalo mergers includes both dark matter only simulations (Kolatt et al. 2000; Springel et al. 2001; De Lucia et al. 2004; Taylor & Babul 2005; Berrier et al. 2006; Wang & Kauffmann 2008; Mateus 2008) and hydrodynamic simulations (Murali et al. 2002; Tormen et al. 2004; Maller et al. 2006; Thacker et al. 2006; Simha et al. 2009). Many of these earlier studies concern subhalo mergers within a single object (such as the Milky Way or a galaxy cluster), others use lower resolution. We use simulations of significant volume (100

[1] A subhalo can comprise an entire halo if there are no other subhalos within the halo, see §6.2.

[2] Halo merger counts and rates have been studied in a vast literature, both estimated analytically (e.g., Kauffmann & White 1993; Lacey & Cole 1993; Percival & Miller 1999; Benson et al. 2005; Zhang et al. 2008) and measured in simulations (e.g., Lacey & Cole 1994; Tormen 1998; Somerville et al. 2000; Cohn et al. 2001; Gottlöber et al. 2001; Cohn & White 2005; Li et al. 2007; Cohn & White 2008; Fakhouri & Ma 2008; Stewart et al. 2008).

and $250\,h^{-1}\,$Mpc cubes) and with high spatial and temporal resolution. In addition, many previous works focus on subhalo mass loss and survival rate, while our main interest here is the population of resulting merged subhalos itself (most similar to the works of Maller et al. 2006; Guo & White 2008; Simha et al. 2009; Angulo et al. 2008). We characterize subhalo merger properties in detail, including satellite mergers, at high redshift ($z = 0.6 - 5$) during the peak of merger activity. We also investigate the satellite halo occupation (number of satellites per halo), and its evolution as shaped by the relative merger rates of subhalos and halos. The satellite halo occupation is a key element in the halo model (Seljak 2000; Peacock & Smith 2000; Berlind & Weinberg 2002; Cooray & Sheth 2002), a framework which describes large-scale structure in terms of host dark matter halos.

6.2 Numerical Techniques

6.2.1 Simulations

We use two dissipationless N-body simulations of 800^3 and 1024^3 particles in a periodic cube with side lengths $100\,h^{-1}\,$Mpc and $250\,h^{-1}\,$Mpc, respectively. For our ΛCDM cosmology, $\Omega_m = 0.25$, $\Omega_\Lambda = 0.75$, $h = 0.72$, $n = 0.97$ and $\sigma_8 = 0.8$, in agreement with a wide array of observations (Smoot et al. 1992; Tegmark et al. 2006; Reichardt et al. 2009; Dunkley et al. 2009), this results in particle masses of $1.4 \times 10^8\,h^{-1}\,\mathrm{M}_\odot$ ($1.1 \times 10^9\,h^{-1}\,\mathrm{M}_\odot$) and a Plummer equivalent smoothing of $4\,h^{-1}\,$kpc ($9\,h^{-1}\,$kpc) for the smaller (larger) simulation. The initial conditions were generated at $z = 200$ using the Zel'dovich approximation applied to a regular Cartesian grid of particles and then evolved using the *TreePM* code described in White (2002) (for a comparison with other codes see Heitmann et al. 2008; Evrard et al. 2008). Outputs were spaced every 50 Myr (~ 100 Myr) for the smaller (larger) simulation, from $z \sim 5$ to 2.5. Additional outputs from the smaller simulation were retained at lower redshift, spaced every ~ 200 Myr down to $z = 0.6$, below which we no longer fairly sample a cosmological volume. For mergers, we restrict these later outputs to $z < 1.6$ based on convergence tests of the merger rates (we lack sufficient output time resolution in the intervening redshifts to properly catch all mergers; see end of §6.3.1 for more). Our redshift range of $z = 0.6 - 5$ allows us to examine subhalos across 7 Gyr of evolution.

To find the subhalos from the phase space data we first generate a catalog of halos using the Friends-of-Friends (FoF) algorithm (Davis et al. 1985) with a linking length of $b = 0.168$ times the mean inter-particle spacing. This partitions the particles into equivalence classes by linking together all particles separated by less than b, with a density of roughly $\rho > 3/(2\pi b^3) \simeq 100$ times the background density. The longer linking length of $b = 0.2$ is often used. However, this linking length is more susceptible to joining together distinct, unbound structures and assigning a halo that transiently passes by another as a subhalo. Thus, we use a more conservative linking length, which for a given halo at our mass and redshift regime yields a $\sim 15\%$ lower mass than $b = 0.2$.[3] We keep all FoF groups with more

[3]Many Millennium subhalo studies use Spherical Overdensity (SO) halos based on an FoF(0.2) catalogue,

than 32 particles, and we refer to these groups as "(host) halos". Halo masses quoted below are these FoF masses.

When two halos merge, the smaller halo can retain its identity as a "subhalo" inside the larger host halo. We identify subhalos (and sometimes subhalos within subhalos) using a new implementation of the *Subfind* algorithm (Springel et al. 2001). We take subhalos to be gravitationally self-bound aggregations of particles bounded by a density saddle point. After experimentation with different techniques we find this method gives a good match to what would be selected "by eye" as subhalos. We use a spline kernel with 16 neighbors to estimate the density and keep all subhalos with more than 20 particles. The subhalo that contains the most mass in the halo is defined as the central subhalo, all other subhalos in the same halo are satellites.[4] The central subhalo is also assigned all matter within the halo not assigned to the satellite subhalos. The position of a subhalo is given by the location of its most bound particle, and the center of a host halo is defined by the center of its central subhalo. For each subhalo we store a number of additional properties including the bound mass, velocity dispersion, peak circular velocity, total potential energy, and velocity.

Figure 6.1 (top) shows the projected image of a sample halo of mass $2.2 \times 10^{12}\, h^{-1}\, \mathrm{M}_{\odot}$, which hosts 12 satellite subhalos, at $z = 2.6$ in the $100\, h^{-1}\,$Mpc simulation. (At this redshift in our simulations there are approximately 200 halos per $(100\, h^{-1}\,\mathrm{Mpc})^3$ above this mass.) Halos at this mass and redshift regime are dynamically active and often highly aspherical, with mean axial ratio (ratio of smallest-to-largest semi-major axes) of ~ 0.5, and recently merged halos have even more discrepant axial ratios (Allgood et al. 2006). Figure 6.1 also shows how a halo's densest region (figure center), center of mass, and substructure distribution can all be offset from one another. Because of these asymmetries, satellite subhalos sometimes extend well beyond r_{200c}, which we will call the halo virial radius.[5]

6.2.2 Subhalo Tracking

We identify, for each subhalo, a unique "child" at a later time, using subhalo tracking similar to Springel et al. (2005b); Faltenbacher et al. (2005); Allgood (2005); Harker et al. (2006). We detail our method to illustrate the subtleties which arise and to allow comparison with other work.

We track histories over four consecutive simulation outputs at a time because nearby subhalos can be difficult to distinguish and can "disappear" for a few outputs until their

in part to take out the extra structure joined by the larger linking length. Neto et al. (2007) compares the FoF(0.2) halo centers and those for the SO halos used to define the corresponding subhalo populations. More generally, White (2001) compares different mass definitions in detail, and Cohn & White (2008) discusses the relation of FoF(0.2), FoF(0.168), SO(180) and Sheth-Tormen (Sheth & Tormen 1999, based on $b = 0.2$) masses at high redshift.

[4] In most cases, the central subhalo in *Subfind* is built around the most bound and most dense particle in the group. However, this is not always the case.

[5] The halo virial radius, r_{200c} (the radius within which the average density is $200\times$ the critical density), is calculated from the FoF ($b = 0.168$) mass by first converting to M_{200c} assuming a spherical NFW (Navarro et al. 1996) density profile, and then taking $M_{200c} = 200 \frac{4\pi}{3} \rho_c r_{200c}^3$.

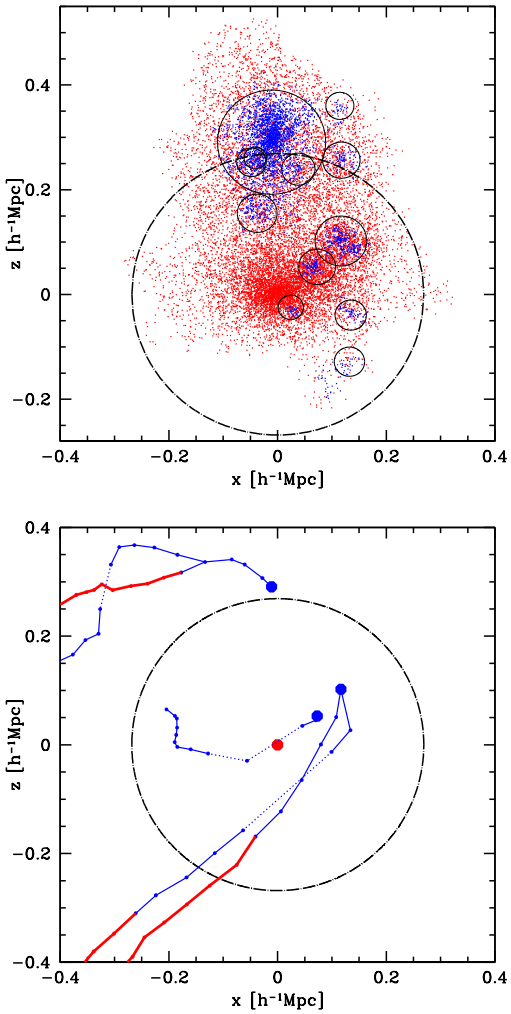

Figure 6.1: **Top**: Projected image of a halo of mass $2.2 \times 10^{12}\, h^{-1}\, \mathrm{M}_{\odot}$ at $z = 2.6$ which hosts 12 satellite subhalos. Particles assigned to the central subhalo are red, while those assigned to satellite subhalos are blue. Dot-dashed circle shows the halo's virial radius (r_{200c}), derived from its mass assuming a spherical NFW density profile, while the solid circles highlight the satellite subhalos and scale in radius with their mass. The central subhalo has bound mass of $1.8 \times 10^{12}\, h^{-1}\, \mathrm{M}_{\odot}$, so nearly 20% of the halo's mass lies in satellite subhalos. **Bottom**: Tracking histories of massive satellite subhalos in the above halo. Large dots show the positions of satellite subhalo centers at $z = 2.6$ for subhalos that had a mass $> 10^{11}\, h^{-1}\, \mathrm{M}_{\odot}$ when they fell into the halo. Small dots show their positions (relative to that of the halo center) at each output (spaced 50 Myr) back 800 Myr. Thin blue curves show subhalo trajectories when they are satellites while thick red curves show when they are centrals (before falling into the halo). Dotted curves indicate when the parent-child assignment has skipped an output (during a fly-by near another subhalo).

orbits separate them again. For each subhalo with mass M_1 at scale factor a_1, its child subhalo at a later time (scale factor a_2 and mass M_2) is that which maximizes

$$\alpha = f\left(M_1, M_2\right) \ln^{-1}\left(\frac{a_2}{a_1}\right) \sum_{i \in 2} \phi_{1i}^2 \tag{6.1}$$

where

$$f\left(M_1, M_2\right) = \begin{cases} 1 - \frac{|M_1 - M_2|}{M_1 + M_2} & M_1 < M_2 \\ 1 & M_1 \geq M_2 \end{cases} \tag{6.2}$$

and where ϕ_{1i} is the potential of particle i computed using all of the particles in subhalo 1, and the sum is over those of the 20 most bound particles in the progenitor that also lie in the candidate child. We track using only the 20 most bound particles since our ultimate interest is in galaxies, which we expect to reside in the highly bound, central region of the subhalo (20 is the minimum particle count for our subhalos). We do not use all the progenitor particles because summing over all of the particles in the progenitor that also lie in the child candidate leads to instances of parent-child assignment in which the child subhalo does not contain the most bound particles of its parent. We also found that weighting by ϕ^2 gave better results than weighting by ϕ, but higher powers of ϕ did not perform appreciably better than ϕ^2. Finally, we weight against large mass gains with a mass weighting factor so that smaller subhalos passing through larger ones and emerging later on the other side are correctly assigned as fly-by's and not mergers. We find $\sim 95\%$ of subhalos have a child in the next time step, with $\sim 4\%$ percent skipping one or more output times and $\sim 1\%$ having no identifiable child.

Figure 6.1 (bottom) shows the tracking histories of the most massive subhalos within the halo shown in Fig. 6.1 (top), for subhalos that had a mass $> 10^{11}\, h^{-1}\, \mathrm{M}_\odot$ when they fell into the halo. The upper-most subhalo was a separate halo ($M = 1.3 \times 10^{12}\, h^{-1}\, \mathrm{M}_\odot$) hosting its own massive satellite subhalo. It then fell into the main halo and then both (now satellite) subhalos merged with each other. The right-most subhalo is an example of two separate halos falling into the main halo, becoming satellites, and subsequently merging with each other. Finally, the track through the center shows a single subhalo falling towards the central subhalo. Instead of merging with the central, it passes through as a fly-by.

All of these tracks show instances where the parent-child assignment algorithm has skipped an output (dotted curves) as one subhalo passes through another and re-emerges on the other side. Note also that, while the dot-dashed circle shows the halo virial radius (at the last output), the locations of the transitions of central to satellite subhalos during infall show that the spherical virial radius is only a rough approximation.

As a halo falls into a larger host halo and becomes a satellite subhalo, mass loss from tidal stripping can be extreme (90% or more) as the satellite subhalo orbits towards the center of its host halo. Figure 6.2 shows the evolution from infall of a long-lived satellite with infall mass $M_{\rm inf} = 6 \times 10^{11}\, h^{-1}\, \mathrm{M}_\odot$ and maximum circular velocity at infall of $V_{\rm c,inf} = 258\ \mathrm{km\,s^{-1}}$. Mass and maximum circular velocity ($V_{\rm c,max}^3$) are stripped by $\sim 90\%$ by the time the satellite first reaches pericenter. After pericentric passage, a satellite can also gain

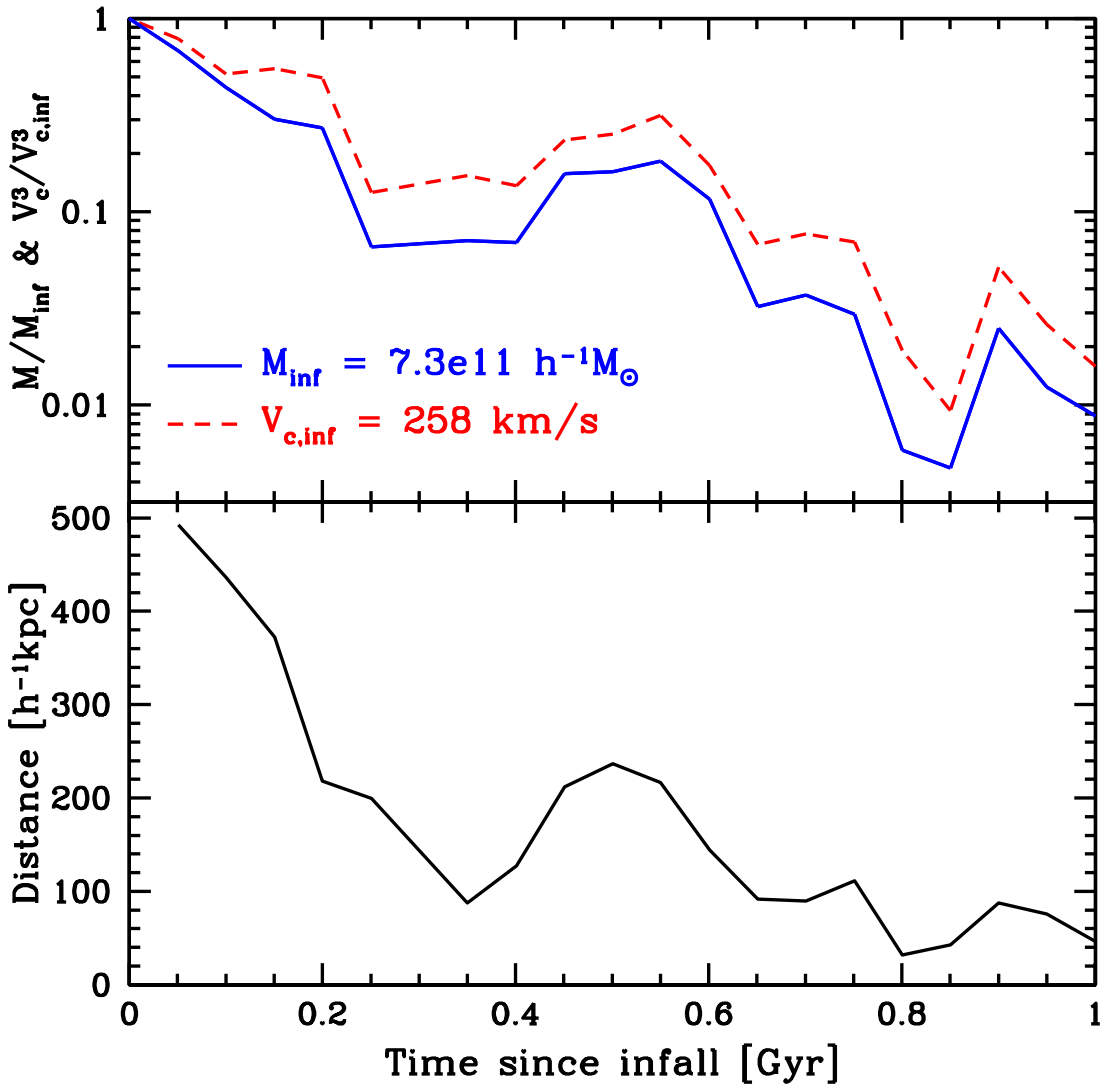

Figure 6.2: **Top**: Evolution of mass (solid curve) and circular velocity (dashed curve) as a function of time since infall for a satellite that fell into a halo of mass $8 \times 10^{12}\, h^{-1}\, \mathrm{M}_{\odot}$ at $z = 3.7$. **Bottom**: Radial distance of satellite from center of host halo. Mass and circular velocity exhibit correlations with radial distance, such as mass gain as the satellite recedes from the center of its host halo. This satellite experienced no major merger activity throughout its history.

mass and circular velocity as it moves away from the dense center of its host halo. This is shown in Fig. 6.2 where mass and circular velocity strongly correlate with radial distance throughout the orbit. This is partially an effect of our subhalo finder: the density contrast of a subhalo, which defines its physical extent and hence its mass, drops as it moves to a region of higher background density.[6] However, this is also driven by a physical effect: as a satellite approaches the dense center of its host halo, it will be compressed by tidal shocks in response to the rapidly increasing potential (see Fig. 12 of Diemand et al. 2007; Gnedin & Ostriker 1997; Dekel et al. 2003).

Since a central subhalo is defined as the most massive subhalo, a satellite subhalo can become a central (and vice versa), which we refer to as a "switch".[7] We find that $\sim 4\%$ of all centrals at any output become satellites within the same halo in the next output, and of these a third immediately return to being centrals in the following output. Switches are twice as common during a merger event, either when two satellites merge, or when a satellite merges with the central, forming a less dense object and allowing another satellite to bind more mass to itself. When a satellite switches to a central and back to a satellite, the original satellite can be mistakenly assigned as a direct parent of the final satellite (and thus the central is assigned no parent) since our child assignment weights against large mass gains (which occurs when a satellite becomes a central). We fix these distinct cases by hand.

These switches highlight the fact that the distinction between a central and satellite subhalo is often not clear-cut: at this redshift and mass regime massive halos undergo rapid merger activity and thus often are highly disturbed and aspherical, with no well-defined single peak that represents the center of the halo profile.

6.2.3 Subhalo Mass Assignment

Since we use subhalos as proxies for galaxies, we track subhalo mass that is expected to correlate with galaxy stellar mass. Galaxies form at halo centers as baryons cool and adiabatically contract toward the minimum of the halo's potential well, which leads to a correlation between halo mass and galaxy stellar mass (White & Rees 1978; Blumenthal et al. 1986; Dubinski 1994; Mo et al. 1998). When a halo falls into a larger halo and becomes a satellite subhalo, its outskirts are severely stripped as discussed above, but its galaxy's stellar mass would be little influenced as the galactic radius is typically $\sim 10\%$ that of the subhalo radius. This motivates assigning to subhalos their mass at infall, $M_{\rm inf}$, which is expected to correlate with galactic stellar mass throughout the subhalo's lifetime. The subhalo infall mass function has been successful at reproducing the observed galaxy luminosity function and clustering at low redshifts (Vale & Ostriker 2006; Wang et al. 2006; Yang et al. 2009). Maximum circular velocity at infall, $V_{\rm c,inf}$, has also been successfully

[6] A fly-by, when a subhalo passes through and is temporarily indistinguishable from a larger subhalo, is an extreme case of this.

[7] In more detail, a switch occurs when the density peak of a satellite (above the background) contains more mass than is within the central subhalo's radius at the position of the satellite.

matched to some observations (Conroy et al. 2006; Berrier et al. 2006). Below, we show the relation between $M_{\rm inf}$ and $V_{\rm c,inf}$ and its redshift evolution.

Our prescription for assigning $M_{\rm inf}$ to subhalos is as follows. When a halo falls into another and its central subhalo becomes a satellite subhalo, the satellite is assigned $M_{\rm inf}$ as the subhalo mass of its (central) parent.[8] If a satellite merges with another satellite, the resultant child subhalo is assigned the sum of its parents' $M_{\rm inf}$. Since the central subhalo contains the densest region of a halo, inter-halo gas is expected to accrete onto it, so we define $M_{\rm inf}$ for a central subhalo as its current self-bound subhalo mass, which is typically $\sim 90\%$ of its host halo's mass.[9] However, since a central subhalo can switch to being a satellite, while a satellite switches to being a central (all within a single host halo), we require an additional rule because using the above simple assignment of $M_{\rm inf}$ to centrals would lead to a central and satellite in a halo each having the halo's current bound mass. Thus, we assign a central to have $M_{\rm inf}$ as its current self-bound subhalo mass only if it was the central in the same halo in the previous output. Thus, if a satellite switches to a central and remains the central for multiple outputs, it has robustly established itself as the central subhalo, so it is assigned its current self-bound mass. However, if a central was a satellite (or a central in another smaller halo) in the previous output, it is assigned the sum of its parents' $M_{\rm inf}$, with the additional requirement that its $M_{\rm inf}$ cannot exceed its current self-bound mass.

A small fraction ($\sim 4\%$) of satellites composed of at least 50 particles are not easily identifiable with any progenitor subhalos and thus cannot be tracked to infall. On inspection, we find that these "orphaned" satellites are loosely self-bound portions of a central subhalo, remnants from a collision between a satellite and its central subhalo that soon re-merge with the central. Given their origins and fates, these orphans are not expected to host galaxies and are ignored.

Although we track subhalos down to 20 particles, we impose a much larger minimum infall mass to our sample to avoid selecting subhalos that artificially dissolve and merge with the central too early. This requires sufficient resolution of the radial density profile of a satellite subhalo at infall: if the satellite's core is smaller than a few times the force softening length, its profile will be artificially shallow and it will be stripped and disrupted prematurely. For calibration, we use the regime of overlap in mass between our two simulations of different mass resolution, requiring consistent subhalo mass functions, halo occupation distributions, and merger statistics for a minimum infall mass. For example, going too low in mass for the larger simulation resulted in more mergers and fewer satellites than for the same mass range in the smaller simulation. In the larger simulation, our consistency requirements led us to impose $M_{\rm inf} > 10^{12}\,h^{-1}\,{\rm M}_\odot$. For a fixed number of particles per subhalo, this scales down to $M_{\rm inf} > 10^{11}\,h^{-1}\,{\rm M}_\odot$ in the smaller, higher resolution simulation. Note that halos of mass

[8] There is some dependence on output time spacing in this definition: since a central subhalo typically continues to gain mass before it falls into a larger halo, shorter time steps (which catch it closer to infall) lead to a higher subsequent satellite $M_{\rm inf}$. Doubling the output spacing leads to satellites with $\sim 10\%$ lower infall mass.

[9] Though because of finite resolution, we find a weak systematic drop in $M_{\rm cen}/M_{\rm halo}$ with halo mass, varying from 93% to 87% for 10^{11} to $10^{14}\,h^{-1}\,{\rm M}_\odot$ in the higher resolution simulation.

10^{11} $(10^{12})\,h^{-1}\,\mathrm{M}_\odot$ cross below M_*, the characteristic mass of collapse, at $z = 1.5$ ($z = 0.8$), so we probe massive subhalos across most of our redshift range.

At $z = 2.6$, there are ~ 16000 subhalos with $M_{\rm inf} > 10^{11}\,h^{-1}\,\mathrm{M}_\odot$ in our $100\,h^{-1}\,\mathrm{Mpc}$ simulation and 9400 subhalos with $M_{\rm inf} > 10^{12}\,h^{-1}\,\mathrm{M}_\odot$ in our $250\,h^{-1}\,\mathrm{Mpc}$ simulation. At $z = 1$, there are ~ 29400 (2500) subhalos with $M_{\rm inf} > 10^{11}$ $(10^{12})\,h^{-1}\,\mathrm{M}_\odot$ in our $100\,h^{-1}\,\mathrm{Mpc}$ simulation.

6.2.4 Stellar Mass & Gas Content of Subhalo Galaxies

A galaxy's stellar mass is expected to be a non-linear, redshift-dependent function of its subhalo mass. An approximate relation based on abundance matching is given in Conroy & Wechsler (2008). At $z = 1$, they found that subhalos of infall mass 10^{11} $(10^{12})\,h^{-1}\,\mathrm{M}_\odot$ host galaxies of stellar mass $\sim 10^9$ $(10^{10.5})$ $\mathrm{M}_\odot$. At $z = 2.5$, subhalos at the above masses are expected to host lower mass galaxies, though quantitative relations at this redshift are less certain, and our subhalo and halo finders differ in detail from theirs. Our sample of $M_{\rm inf} > 10^{12}\,h^{-1}\,\mathrm{M}_\odot$ subhalos approximately corresponds to $L \gtrsim L_*$ galaxies at the redshifts we examine.

Although our simulations do not track the baryonic content of subhalos, most massive galaxies are gas-rich at high redshift. That is, at $z \approx 1$, 70% to 90% of $L \sim L_*$ galaxies are observed to be blue (Cooper et al. 2007; Gerke et al. 2007), possessing enough gas to be actively star forming. The fraction of gas-rich galaxies at higher redshift is more poorly constrained but is thought to be higher (Hopkins et al. 2008a). Thus, we anticipate that most, if not all, mergers we track have the capacity to drive galaxy activity such as starbursts and quasars.

6.2.5 Subhalo Mass & Circular Velocity

Figure 6.3 shows the radial density and circular velocity profiles for 8 satellite and 8 central subhalos with $V_{\rm c,max} \simeq 250\ \mathrm{km\,s^{-1}}$ $(M \sim 10^{12}\,h^{-1}\,\mathrm{M}_\odot)$ at $z = 2.6$ in the $100\,h^{-1}\,\mathrm{Mpc}$ simulation. Circular velocity is defined as $V_c \equiv \sqrt{GM(<r)/r}$, and since subhalos follow NFW density profiles, with a break in the power-law density profile at the scale radius, r_s, they have a maximum value in their circular velocity profiles, $V_{\rm c,max}$, at $r_{\rm max} = 2.2r_s$. The left panels show the radial profiles of all matter surrounding the subhalos, while the right panels show only that of matter assigned to the subhalos. Satellites and centrals have similar profiles at small radii, though the right top panel shows that satellites exhibit signs of tidal truncation at $\sim 50\,h^{-1}\,\mathrm{kpc}$. This is also visible in the circular velocity profile in the bottom left panel, where V_c for satellites rises sharply, exhibiting a transition to their host halos. For the centrals, the rise in V_c beyond $\sim 1\,h^{-1}\,\mathrm{Mpc}$ arises from neighboring structures.

Figure 6.4 shows the relation between subhalo infall mass, $M_{\rm inf}$, and infall maximum circular velocity, $V_{\rm c,inf}$, for subhalos at $z = 2.6$. We fit this relation to

$$V_{\rm c,inf}^{\gamma} = B(z) M_{\rm inf} \tag{6.3}$$

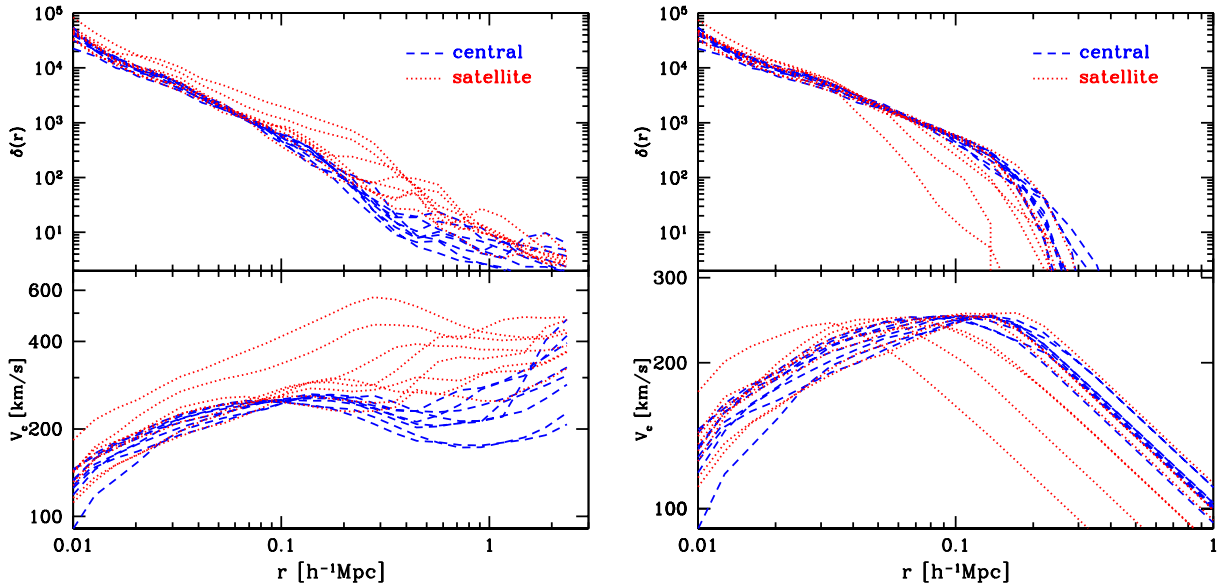

Figure 6.3: **Left**: Radial density profiles (top) and circular velocity profiles (bottom) of all matter around 8 satellite (dotted curves) and 8 central (dashed curves) subhalos with $V_{\rm c,max} \simeq 250$ km s^{-1} at $z = 2.6$. **Right**: Same, but only for matter assigned to the subhalos.

for all subhalos above $10^{11}\,h^{-1}\,{\rm M}_\odot$, finding $\gamma = 3$ holds to good approximation at all redshifts we examine, in agreement with the virial relation $V^2_{\rm c,max} \propto M/R \propto M/M^{1/3} \propto M^{2/3}$. The outliers with large $M_{\rm inf}$ relative to $V_{\rm c,inf}$ are satellites that experienced a major merger; under our prescription, a satellite child's $M_{\rm inf}$ is the sum of its parents' $M_{\rm inf}$, but a child's $V_{\rm c,inf}$ is that of its highest $V_{\rm c,inf}$ parent.

Fixing $\gamma = 3$, Fig. 6.5 shows the evolution of the amplitude $B(z) \equiv V^3_{\rm c,inf}/M_{\rm inf}$. A subhalo of a given mass has a higher maximum circular velocity at higher redshift, reflective of the increased density of the universe when the subhalo formed. As a subhalo subsequently accretes mass, its $V^3_{\rm c,max}$ grows more slowly than it mass (in cases of slow mass growth, we find $V^3_{\rm c,max}$ can remain constant). This is in agreement with Diemand et al. (2007), who found that halos undergoing mild mass growth (no major mergers) had less than 10% change in $V_{\rm c,max}$ and $r_{\rm max}$. We find that the evolution of $B(z)$ within the redshifts we probe can be well-approximated by

$$B(z) = 6.56 \times 10^{-6} e^{0.36z} ({\rm km/s})^3 h M_\odot^{-1}\,. \tag{6.4}$$

Thus, $M_{\rm inf} = 10^{11}$ $(10^{12})\,h^{-1}\,{\rm M}_\odot$ subhalos correspond to $V_{\rm c,inf} \simeq 120$ (250) km s^{-1} at $z = 2.6$ and $V_{\rm c,inf} \simeq 100$ (200) km s^{-1} at $z = 1$. Conversely, for fixed $V_{\rm c,inf}$, a subhalo is about half as massive at $z = 2.6$ than at $z = 1$.

Since we fit relations of satellite subhalo properties at infall, our results above are applicable equally to satellite and central subhalos. In addition, our results change by only a few percent if we instead consider host halos.

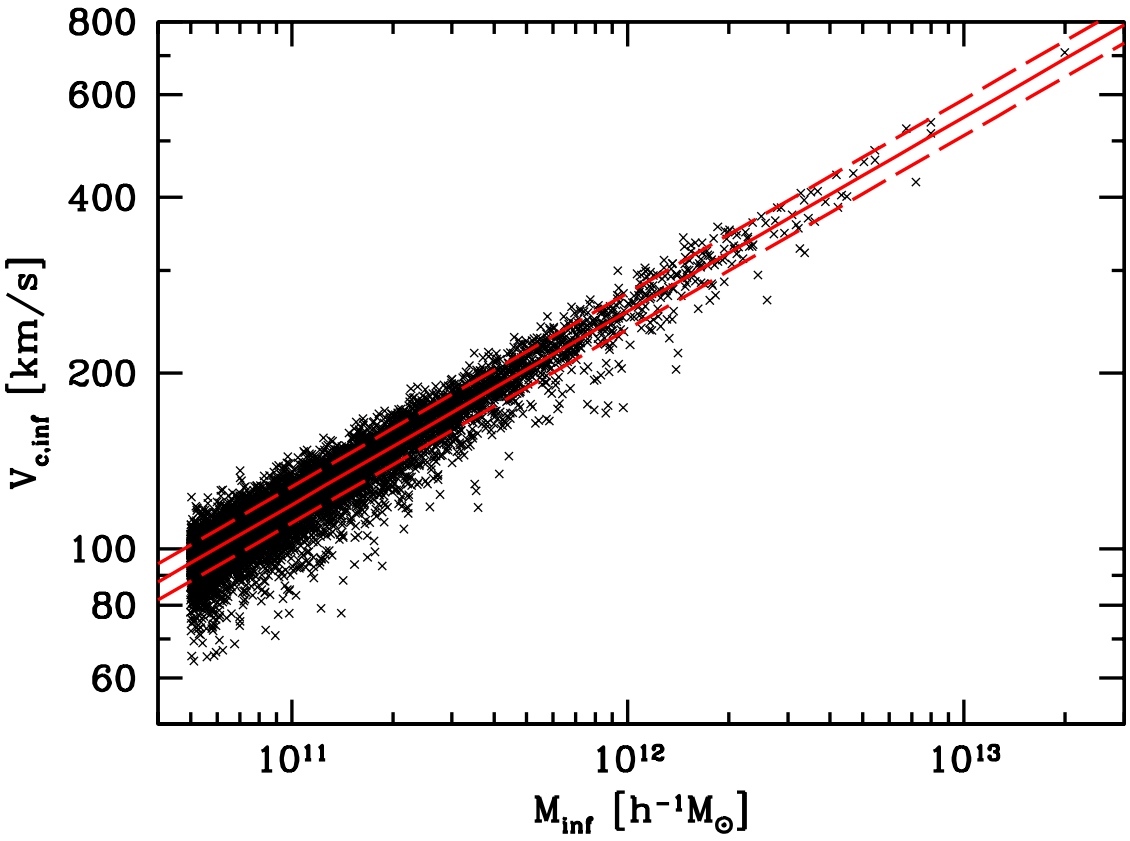

Figure 6.4: Relation between subhalo infall maximum circular velocity, $V_{\rm c,inf}$, and subhalo infall mass, $M_{\rm inf}$, at $z = 2.6$. Black points show a 25% sub-sample of all subhalos as a measure of scatter, solid red line shows the least squares fit to Eq. 6.3, and dashed red lines show the 1σ scatter, for subhalos with $M_{\rm inf} > 10^{11}\,h^{-1}\,{\rm M}_{\odot}$.

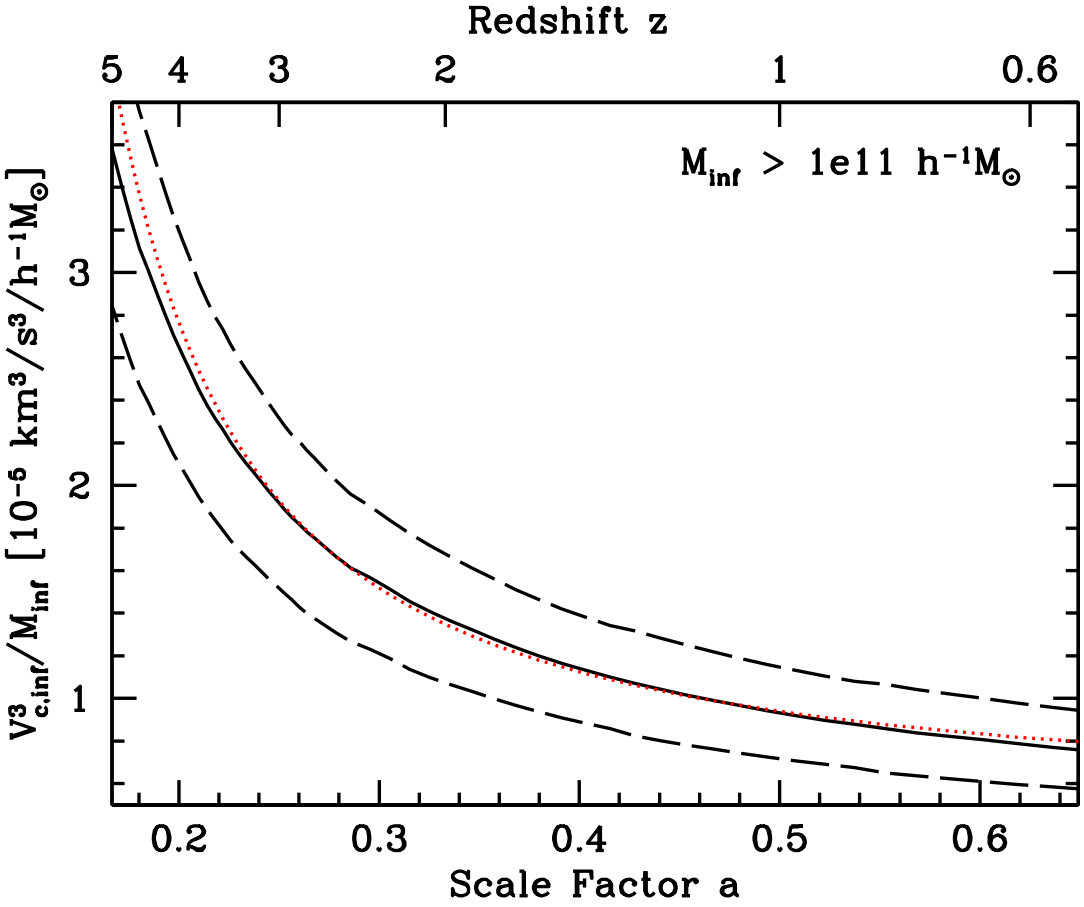

Figure 6.5: Evolution of the ratio of subhalo infall maximum circular velocity to infall mass, $B(z) = V^3_{\rm c,inf}/M_{\rm inf}$ (solid curve), and 1σ scatter (dashed curves) for subhalos with $M_{\rm inf} > 10^{11}\,h^{-1}\,{\rm M}_\odot$. Dotted curve shows fit to $B(z)$ of Eq. 6.4.

6.2.6 Satellite Subhalo Mass Function

Figure 6.6 shows the satellite subhalo mass function, scaled to host halo mass, for various host halo mass bins at $z = 1$. Thick curves show satellite masses selected on $M_{\rm inf}$, while thin curves show satellite masses selected on instantaneous bound mass. The rollover in the $M_{\rm inf}$ curves at low satellite mass indicates where satellites become numerically disrupted by resolution effects. Numerical disruption occurs at higher satellite $M_{\rm inf}$ for more massive halos, indicating that satellites of a fixed $M_{\rm inf}$ experience more pronounced tidal stripping in higher mass halos, where dynamical friction timescales and central densities are higher. The rollover in the highest halo mass bin occurs at $M_{\rm sat,inf} \approx 10^{11}\,h^{-1}\,{\rm M}_{\odot}$, which sets our minimum subhalo mass for robust tracking.

We find that the instantaneous bound mass function exhibits little-to-no systematic dependence on halo mass, in agreement with Angulo et al. (2008). This is in contrast to the infall mass function, which shows more satellites at a given mass ratio for more massive halos. This difference is driven by subhalo mass stripping. Averaged over the entire satellite population at this redshift, the satellite instantaneous bound mass is $\sim 30\%$ that of $M_{\rm inf}$, as can be seen by the x-axis offset of the solid and dashed curves. However, satellites exhibit less average mass loss in low-mass halos than high-mass halos, the instantaneous to infall mass ratios being 40% and 25%, respectively. This is considerably higher than the $5\% - 10\%$ at $z = 1$ found in the semi-analytic model of van den Bosch et al. (2005a). Additionally, van den Bosch et al. (2005a) and Giocoli et al. (2008) found the opposite trend with halo mass, that the average mass loss of satellites is higher for lower mass halos. They found that this arises because lower mass halos form (and accrete their subhalos) earlier, when the dynamical timescale is shorter. Thus, the satellites of lower mass halo are stripped both more rapidly and over a longer time period (see also Zentner et al. 2005). Finally, Giocoli et al. (2008) found that the scaled mass functions of subhalos at infall does not depend on halo mass, in seeming contrast with Fig. 6.6.

These discrepancies likely arises because we examine the masses of extant subhalos in our simulation, while van den Bosch et al. (2005a) and Giocoli et al. (2008) track subhalo mass loss much longer than our simulation does. Their semi-analytical model of subhalo mass loss has no prescription for central-satellite mergers, which preferentially serve to reduce highly stripped satellites from our sample.[10] Since satellites of a given infall mass to halo mass ratio have lower mass in lower mass halos, they are closer to our minimum subhalo finding mass threshold. Thus, a fixed amount of stripping will cause lower mass halos to have a reduced population of satellites of a given infall mass to halo mass ratio. It is unclear at what level of subhalo mass stripping we should expect the galaxies they host to become disrupted as well.

Various studies using high-resolution simulations have explored in detail the slope of the subhalo mass function (De Lucia et al. 2004; Gao et al. 2004a; Diemand et al. 2007; Madau et al. 2008; Angulo et al. 2008), finding that the (instantaneous) mass function of subhalos

[10]See Taylor & Babul (2005) and Zentner et al. (2005) for detailed comparisons of simulated subhalos with analytic models.

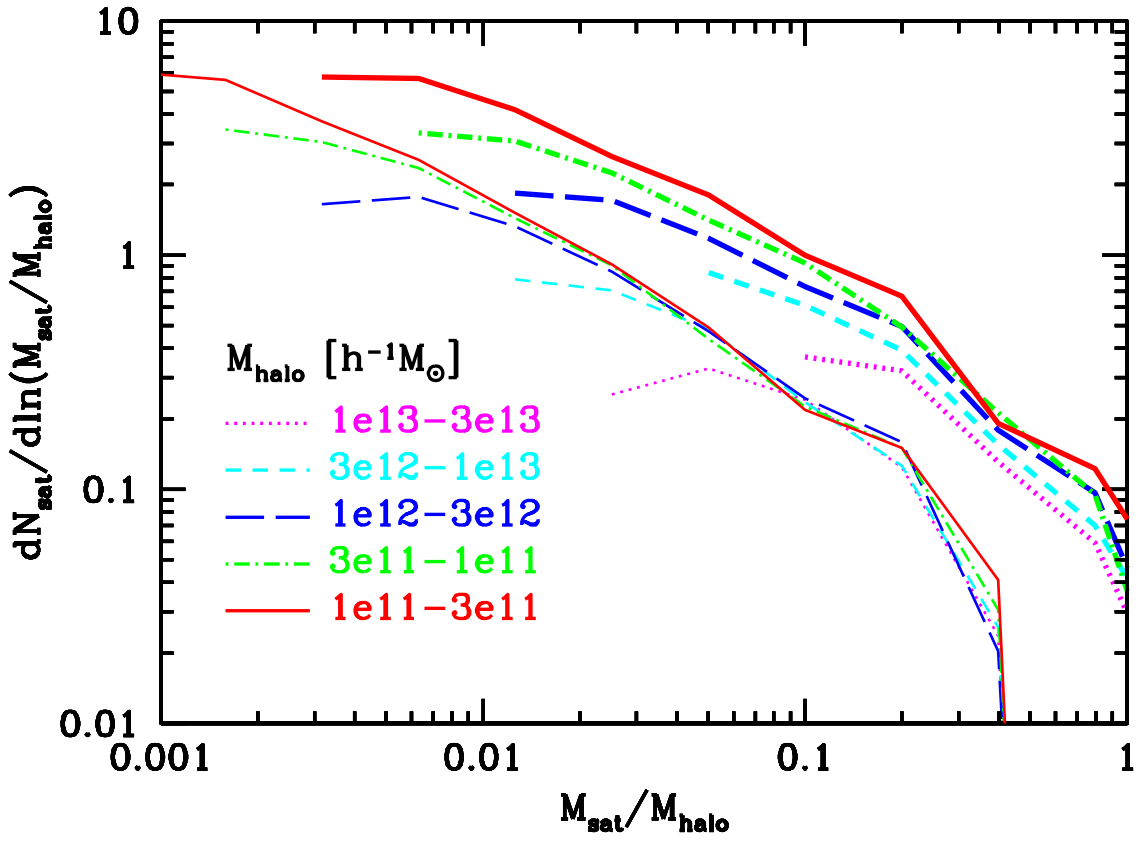

Figure 6.6: Satellite subhalo mass function, scaled to host halo mass, for various host halo mass bins, at $z = 1$. Thick curves show satellite mass selected on $M_{\rm inf}$, while thin curves show satellite mass selected on instantaneous bound mass. While the instantaneous bound mass function exhibits no dependence on halo mass, the infall mass function has a higher amplitude for more massive halos. An appreciable number of satellites exists at $M_{\rm sat,inf}/M_{\rm halo} \approx 1$ because of switches. Below the rollover at high satellite mass, both mass functions scale as $\frac{dN_{\rm sat}}{d\ln(M_{\rm sat}/M_{\rm halo})} \propto M_{\rm sat}^{-0.9}$ in agreement with instantaneous satellite subhalo bound mass functions found by numerous authors (see text).

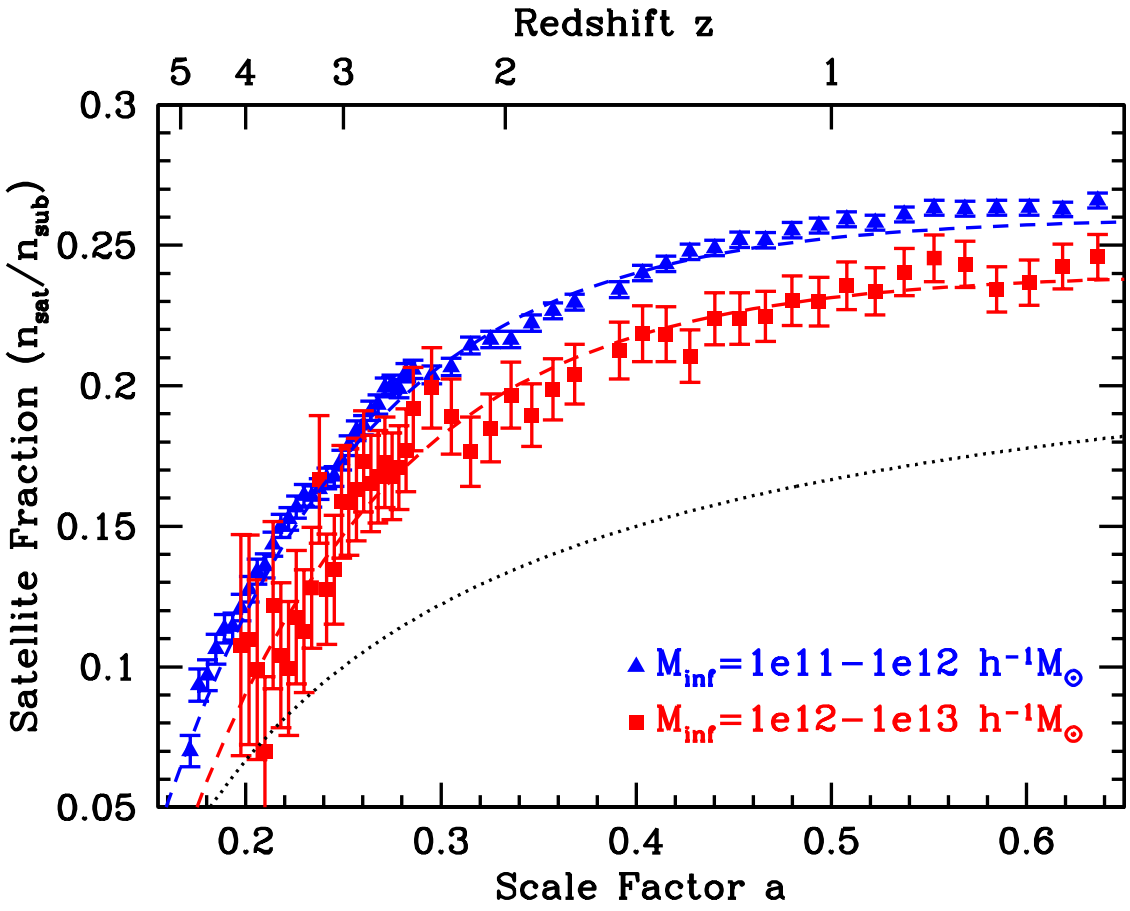

Figure 6.7: Evolution of the fraction of all subhalos that are satellites for $M_{\rm inf} = 10^{11} - 10^{12}\,h^{-1}\,{\rm M}_\odot$ (triangles) and $M_{\rm inf} = 10^{12} - 10^{13}\,h^{-1}\,{\rm M}_\odot$ (squares). Dashed curves show fits to Eq. 6.5. Dotted curve shows fit to Eq. 6.6 from Conroy & Wechsler (2008).

goes as $N_{\rm sat}(> M_{\rm sat}) \propto (M_{\rm halo}/M_{\rm sat})^{\alpha}$, with $\alpha = 0.9 - 1$.[11] We note, though, that these fits are based on cuts on instantaneous subhalo mass or circular velocity, not those at infall. However, we find that, between the rollover in $M_{\rm inf}$ at low and high satellite mass, the slopes of the mass functions selected on infall and instantaneous bound mass are the same within error, and $\alpha = 0.9$ fits our mass function selected on either mass. The similarity of the two slopes also implies that the mass loss rate of satellites does not depend strongly on satellite mass, in agreement with Giocoli et al. (2008).

6.2.7 Satellite Fraction

To frame our ensuing discussion of mergers, and the relative importance of satellite and central subhalos, Fig. 6.7 shows the evolution of the satellite fraction, $n_{\rm satellite}/n_{\rm subhalo}$, for subhalos of a fixed mass[12], which grows monotonically with time from $z = 5 - 0.6$, as

$$\frac{n_{\rm satellite}}{n_{\rm subhalo}} = C - e^{-\frac{\beta}{1+z}} \tag{6.5}$$

with $\beta = 9.7$ valid across all subhalo masses and $C = 0.26$ (0.24) for lower (higher) mass. The satellite fraction decreases with increasing subhalo mass since more massive subhalos are more likely to be centrals, and for a fixed subhalo mass the satellite fraction increases with time as the number of high mass halos hosting massive satellites increases. The increase in the satellite fraction is slowed at late times because the number of massive satellites in halos of a fixed mass decreases with time as the satellites coalesce with the central subhalo (see §6.6).

Note that Eq. 6.5 predicts a much higher satellite fraction than that of Conroy & Wechsler (2008), who found

$$\frac{n_{\rm satellite}}{n_{\rm subhalo}} = 0.2 - \frac{0.1}{3}z\,. \tag{6.6}$$

It is unlikely that the difference is driven by numerical effects, since both their and our simulations are of similar mass resolution and volume, and both analyses are based on similar subhalo infall mass cuts (we see similar satellite fractions selecting instead on fixed $V_{\rm c,inf}$). One likely factor is that, as noted above, our smaller output spacing yields higher infall mass for satellite subhalos, since we catch halos closer to infall when their mass is higher. In addition, they use a different halo and subhalo finding algorithm (Klypin et al. 1999; Kravtsov et al. 2004a), and their higher σ_8 (0.9 rather than our 0.8) would give a lower merger rate and thus fewer satellites (one expects satellite survival timescales not to change). If normalized to the same satellite fraction at a given epoch, the redshift evolution of Eqs. 6.5 and 6.6 are in rough agreement.

6.3 Merger Criteria & Rates

6.3.1 Merger Criteria

For two parents with $M_{\rm inf,2} \leq M_{\rm inf,1}$ sharing the same child subhalo at the next output they appear, a child is flagged as a (major) merger if $\frac{M_{\rm inf,2}}{M_{\rm inf,1}} > \frac{1}{3}$. If a child has more than two parents, we count multiple mergers if any other parents also exceed the above mass ratio with respect to the most massive parent.

[11] $N_{\rm sat}(> M_{\rm sat})$ has the same power law dependence on subhalo mass as $\frac{dN_{\rm sat}}{d\ln(M_{\rm sat}/M_{\rm halo}))}$.

[12] We show the satellite fraction for two mass bins, but since the mass function falls exponentially at these masses and redshifts, almost all objects are at the low end of the mass bin. Using instead a minimum mass cut changes our results by only a few percent.

Our mass ratio represents a trade-off between strong mergers (to maximize signal) and frequent merging (for statistical power). Galaxy mergers with stellar mass ratios closer than 3:1 are expected to drive interesting activity, such as quasars and starbursts, as mentioned above.[13]

For generality, the distribution of merger (infall) mass ratios, R:1, for both halos and subhalos in the mass and redshift regimes we consider can be approximated by

$$f(R) \propto R^{-1.1} \tag{6.7}$$

in reasonable agreement with the $R^{-1.2}$ distribution of galaxy mass ratios at $z < 0.5$ found in hydrodynamic simulations by Maller et al. (2006).[14] Thus, the counts and rates of mergers with (infall) mass ratio closer than R:1 can be approximately scaled from our results through the relation

$$N(< R) = 8.6\,(R^{0.1} - 1)N(< 3)\,. \tag{6.8}$$

Sometimes merger criteria are based on instantaneous subhalo mass gain (e.g., Thacker et al. 2006). However, as exemplified in Fig. 6.2, subhalos can gain significant mass without coalescence. We find that most cases of significant subhalo mass gain are not a two-body coalescence, and so we do not use this to select mergers. See Chapter 7 and related results in Maulbetsch et al. (2007) for more detail.

Sufficient output time resolution is necessary to properly resolve the merger population. Unless otherwise stated, we use the shortest simulation output spacing to define the subhalo merger time interval, corresponding to 50 Myr ($\sim$ 100 Myr) for $M_{\rm inf} > 10^{11}$ $(10^{12})\,h^{-1}\,{\rm M}_\odot$ at $z > 2.5$, and $\sim$ 200 Myr for all masses at $z < 1.6$. By tracking parent and child subhalo assignments across multiple output spacings, we found that longer output time spacings result in a lower subhalo merger rate, arising from a combination of effects. As stated above, shorter time steps catch halos closer to their infall, resulting in satellites with higher $M_{\rm inf}$, and hence more major satellite-central mergers. In addition, satellite-satellite mergers can be missed if their child merges into the central subhalo before the next time step. However, smaller output spacings are also more susceptible to switches, which can yield satellites with higher mass.

For halos, very short time steps can artificially enhance the merger rate, catching transient behavior as halos intersect, pass through each other, and re-merge. While we use FoF(0.168) instead of FoF(0.2) halos to help minimize artificial bridging effects, for a 50 Myr time spacing halo re-mergers still constitute a significant fraction of halo mergers. Thus we calculate all our halo mergers using $>$ 100 Myr output spacings, for which halo re-mergers constitute only a few percent of all mergers.

[13]Since galaxy stellar mass is a non-linear function of subhalo mass, a subhalo mass ratio of 3:1 may correspond to a galaxy merger of a more or less discrepant mass ratio. However, since the $M_{\rm stellar} - M_{\rm subhalo}$ relation is expected to peak for $M_{\rm subhalo} \sim 10^{12}\,h^{-1}\,{\rm M}_\odot$ (Conroy & Wechsler 2008), we do not expect this effect to strongly bias our results.

[14]The distribution of merger mass ratios also agrees well with the fit for halos at $z = 0$ provided by Wetzel et al. (2008).

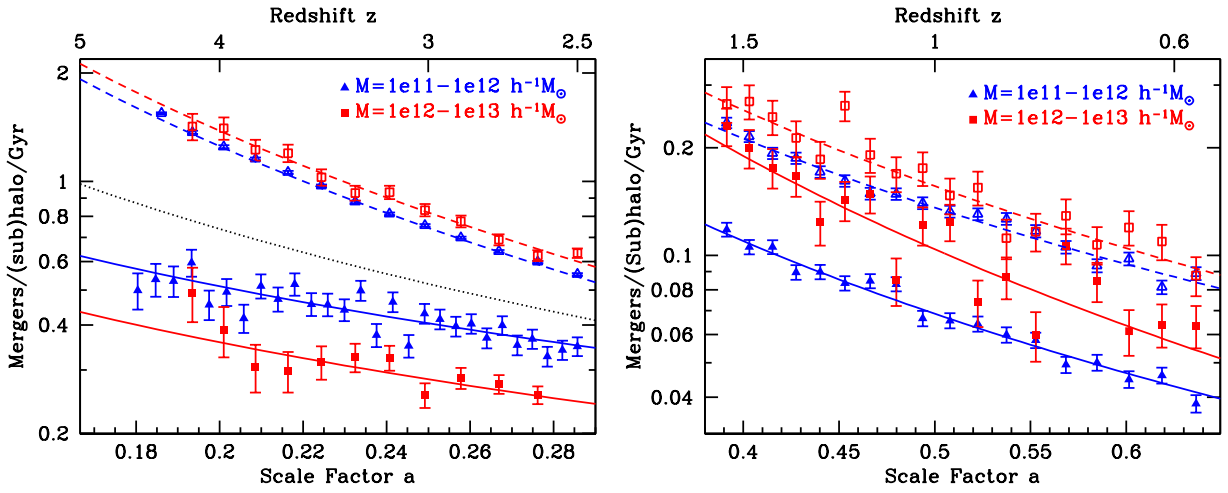

Figure 6.8: **Left**: Merger rate per object of subhalos (solid points) and halos (open points) as a function of the scale factor, for $M_{\rm inf} = 10^{11} - 10^{12}\,h^{-1}\,{\rm M}_\odot$ (triangles) and $M_{\rm inf} = 10^{12} - 10^{13}\,h^{-1}\,{\rm M}_\odot$ (squares) at $z = 5 - 2.5$. Solid (dashed) curves show fits of subhalo (halo) merger rates to Eq. 6.9, with fit parameters given in Table 6.1. **Right**: Same, but at $z = 1.6 - 0.6$. Also shown at left is the fit to the halo merger rate for halos with a central subhalo of $M_{\rm inf} = 10^{11} - 10^{12}\,h^{-1}\,{\rm M}_\odot$ (dotted curves).

Given our simulation volumes we are unable to probe statistically significant subhalo merger counts in halos more massive than $4\times10^{13}\,h^{-1}\,{\rm M}_\odot$ at $z > 2.5$ and $M \sim 10^{14}\,h^{-1}\,{\rm M}_\odot$ at $z < 1.6$. However, the majority of recently merged subhalos are centrals (discussed below), and selecting on higher mass host halos for a fixed subhalo mass restricts increasingly to recently merged satellites, of which there are comparatively fewer. Furthermore, nearly all subhalo mergers at a given mass occur in halos at most $5 - 10\times$ times more massive.

6.3.2 Fits to Simulation

Figure 6.8 shows the evolution of the merger rate per object—defined as the number of mergers per time per object—for both subhalos and halos of the same (infall) mass.[15] We fit the merger rate per object as

$$\frac{n_{\rm merge}}{n_{\rm obj} dt} = A(1+z)^\alpha \tag{6.9}$$

where $n_{\rm merge}$ is the number of (sub)halos whose parents match our mass ratio selection, $n_{\rm obj}$ is the total number of (sub)halos within the same mass range at the same output, and dt is the time interval between consecutive outputs. The best-fit values in each redshift regime

[15]Merger fraction errors are calculated using binomial statistics. Given M mergers out of N objects, the mostly likely fraction is $f = M/N$ with variance $\sigma_f^2 = \frac{M(N-M)+1+N}{(N+2)^2(N+3)}$.

Redshift		$z = 5 - 2.5$		$z = 1.6 - 0.6$	
Mass $[h^{-1}\ \mathrm{M}_\odot]$		$10^{11} - 10^{12}$	$10^{12} - 10^{13}$	$10^{11} - 10^{12}$	$10^{12} - 10^{13}$
Halos	A	0.029	0.032	0.034	0.034
	α	2.3	2.3	2.0	2.2
Subhalos	A	0.093	0.065	0.016	0.016
	α	1.1	1.1	2.1	2.6

Table 6.1: Amplitude, A, and power law index, α, for halo and subhalo merger rates fit to Eq. 6.9.

are shown in Table 6.1. Note that the merger rate we examine is the number of mergers per time *per object*, different from another common definition, the number of mergers per time *per volume*.[16]

The relation of subhalo mergers to halo mergers is nontrivial. Although subhalo mergers are the eventual result of halo mergers, the former are governed by dynamics within a halo and the latter by large-scale gravitational fields. For halos, both the slope and the amplitude of the merger rate exhibit little dependence on mass or redshift. Similarly, Fakhouri & Ma (2008) found $\alpha = 2 - 2.3$ for all halo masses at $z < 6$, and weak halo mass dependence of the amplitude. In contrast, the subhalo merger rate amplitude has strong dependence on mass and its slope depends strongly on redshift. Relative to the halo merger rate, the subhalo merger rate is lower in amplitude than that of halos of the same (infall) mass, and, most notably at $z > 2.5$, the rate of subhalo mergers falls off significantly more slowly that that of halos. This is consistent with earlier work: De Lucia et al. (2004) found a higher merger fraction for halos than subhalos, and Guo & White (2008) found strong mass dependence of the galaxy merger rate amplitude and that the slope becomes much shallower at $z > 2$ (see also Mateus 2008). Note that our halos are FoF(0.168) halos and so our merger rates can differ from those for FoF(0.2) halos; merging occurs sooner for a finder with a larger linking length.

We now focus on the relation between halo and subhalo merger rates to understand these trends with time.

6.3.3 Subhalo vs. Halo Merger Rates

A simple analytic argument based on dynamical infall time, that subhalo mergers are simply a delayed version halo mergers, leads one to expect that subhalo merger rates simply

[16]The former is simply the latter divided by the number density of objects of the same mass, but the merger rate per volume has qualitatively different behavior because the (comoving) number density of objects at a fixed mass increases with time in a redshift-dependent manner. Specifically, at high redshift where the mass function rapidly increases with time, the merger rate per volume for both halos and subhalos *increases* with time, reaching a peak at $z \sim 2.5$. Below this redshift, it decreases with time in a power law manner as in Fig. 6.8, though with a shallower slope of $\alpha \approx 1.5$.

track those of halos: they have the same time evolution, with the subhalo merger rate having a higher amplitude. In this argument, when two halos merge, the new satellite galaxy collides with the other central galaxy within a dynamical friction timescale, approximated by

$$t_{\rm merge} \approx C_o \frac{M_{\rm halo}/M_{\rm sat}}{\ln(1+M_{\rm halo}/M_{\rm sat})} t_{\rm dyn} \tag{6.10}$$

where $t_{\rm dyn} = 0.1 t_{\rm Hubble}$, $t_{\rm Hubble} = \frac{1}{H(z)}$, and $C_o \approx 1$ accounts for the ensemble averaged satellite orbital parameters (Conroy et al. 2007a; Binney & Tremaine 2008; Boylan-Kolchin et al. 2008; Jiang et al. 2008). Thus, for a fixed mass ratio, letting $m_o = M_{\rm halo}/M_{\rm sat}/\ln(1 + M_{\rm halo}/M_{\rm sat})$,

$$t_{\rm sat,merge} \approx 0.1\, C_o m_o t_{\rm Hubble} \approx 0.1\, C_o m_o t\,. \tag{6.11}$$

The evolution of the halo merger rate per object during matter-domination (valid at the high redshifts we examine), where $a \propto t^{2/3}$, is approximately

$$\frac{n_{\rm merge}}{n_{\rm halo} dt} = A(1+z)^\alpha = \left(\frac{t}{t_*}\right)^{-\frac{2}{3}\alpha} \tag{6.12}$$

with t_* some proportionality constant. Assuming all halo mergers lead to satellite-central subhalo mergers on a dynamical friction timescale, the subhalo merger rate per object would evolve with time as

$$\frac{n_{\rm merge}}{n_{\rm subhalo} dt} = \left(\frac{t - t_{\rm sat,merge}}{t_*}\right)^{-\frac{2}{3}\alpha} \tag{6.13}$$

$$= (1 - 0.1\, C_o m_o)^{-\frac{2}{3}\alpha} \left(\frac{t}{t_*}\right)^{-\frac{2}{3}\alpha} \tag{6.14}$$

and so the subhalo merger rate would simply track that of halos of the same mass, but with higher amplitude.

6.3.4 Resolving the Discrepancy

As Fig. 6.8 shows, however, this tracking does not occur, particularly at high redshift where the slope of the subhalo merger rates is much shallower than that of halos. One reason for this is that we compute the merger rate per object, in which we divide by the number of objects at the given mass, $n_{\rm obj}(m)$. Since halo masses are added instantaneously during halo mergers, a recently merged halo will instantly jump to a higher mass regime (with smaller $n_{\rm obj}$ in Eq. 6.9). In contrast, the central subhalo of the resultant halo will remain at a smaller mass for some time until its mass grows from stripping of the new satellite subhalo. So recently merged halos have lower than average $M_{\rm inf,cen}/M_{\rm halo}$), and the central's $n_{\rm obj}$ is higher.

In Fig. 6.8 (left) the dotted black curve fits the halo merger rate for halos selected with the same mass cut on their central subhalo infall mass. The amplitude is significantly

smaller, and the slope is also shallower ($\alpha = 1.6$) than for halos selected on full halo mass, showing that the above effect is stronger at earlier times. By the argument above, the ratio of amplitudes of the merger rate per object of halos to subhalos is $n_{\rm halo}/n_{\rm cen}$. A fixed (sub)halo mass cut probes lower $M/M_*(t)$ at later times, and the mass function drops exponentially with increasing $M/M_*(t)$ at these masses. Thus, a fixed $M_{\rm inf,cen}/M_{\rm halo}$ after a halo merger means $n_{\rm halo}/n_{\rm cen}$ becomes closer to unity at later times, leading to the shallower slope.

The measured subhalo mergers have an even lower amplitude and shallower slope than the dotted curve in Fig. 6.8, driven by two additional effects. First, a halo major merger might not lead to a subhalo major merger since the satellite-central merger mass ratio can be smaller than the mass ratios of their source halos. This is because $M_{\rm inf}$ naturally grows for a central but only grows for a satellite if it has a merger before coalescing with the central (see Wang & Kauffmann 2008, for a detailed analysis of this effect in terms of assigning baryons to subhalos). Since halos grow in mass more quickly at higher redshift, this effect is stronger at earlier times, further flattening the subhalo merger rate slope. Second, there is a significant contribution of recently merged satellites to the merger population. We find that satellites are twice as likely to have had a recent merger as centrals of the same mass, regardless of mass cut and redshift (see §6.4 for more detail). This enhances the merger rate, with a stronger enhancement at later times since the satellite fraction grows with time as in Fig. 6.7.

At lower redshift, Fig. 6.8 (right) shows that the amplitude of the subhalo merger rate remains lower than that of halos, but the slopes become similar, indicating the effects examined above become less time-dependent. Since the masses we probe are crossing $M_*(t)$ as these redshifts, the reduced amplitude from subhalo vs. halo mass cut becomes less sensitive to time. Similarly, our mass range crossing $M_*(t)$ means that halo mass growth slows, so the fraction of halo major mergers that leads to subhalo major mergers remains roughly constant with time. Finally, as shown in Fig. 6.7, the satellite fraction growth asymptotes at lower redshift, which means that the enhancement from recently merged satellites remains roughly constant.

6.4 Satellite vs. Central Mergers

The stereotypical galaxy merger is a satellite coalescing with the central in its halo and producing a central merger remnant. These mergers do dominate the merger population, both in parent types (central-satellite) and child type (central). However, while satellites form the minority of the subhalo population at all epochs (see Fig. 6.7), satellites are twice as likely to have had a recent merger as centrals of the same mass, regardless of mass and redshift.

Since the identities of satellite vs. central subhalos at this mass and redshift regime are not clear-cut (from switches), we characterize mergers both in terms of their parent types (central or satellite) and resulting child types. For mergers resulting in centrals, this ambiguity is not important: 97% arise from satellite-central parents, while the other 3%

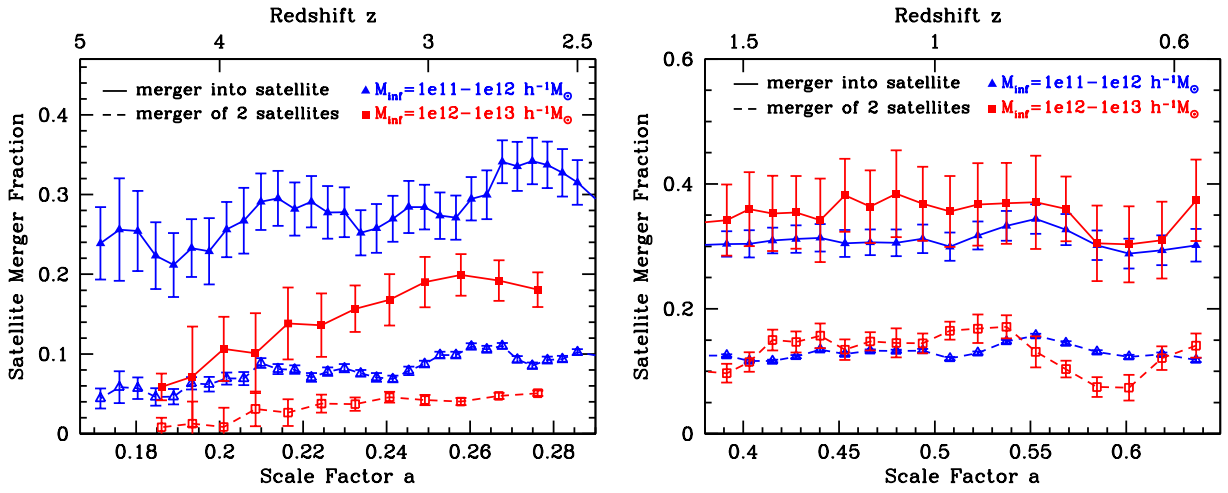

Figure 6.9: Satellite merger fraction at $z = 5 - 2.5$ (left) and $z = 1.6 - 0.6$ (right) for $M_{\rm inf} = 10^{11} - 10^{12}\,h^{-1}\,{\rm M}_\odot$ (triangles) and $M_{\rm inf} = 10^{11} - 10^{12}\,h^{-1}\,{\rm M}_\odot$ (squares). Closed points (solid curves) indicate the fraction of all subhalo mergers that result in a satellite, while open points (dashed curves) indicated the fraction of all subhalo mergers that arise from satellite-satellite parents.

arise from satellite-satellite parents during switches.[17]

Recently merged satellites are a more varied population. Figure 6.9 shows the contributions of satellite mergers to the overall merger populations as a function of the scale factor.[18] The fraction of all subhalo mergers that result in a satellite is $\sim 30\%$ for $M_{\rm inf} = 10^{11} - 10^{12}\,h^{-1}\,{\rm M}_\odot$, with little dependence on redshift. For $M_{\rm inf} = 10^{12} - 10^{13}\,h^{-1}\,{\rm M}_\odot$ it is $15 - 20\%$ at $z \sim 2.5$ and rises to $\sim 35\%$ at $z < 1.6$. Thus, at lower redshift ($z < 1.6$) where the satellite fraction asymptotes to $\sim 25\%$, the fraction of mergers that result in a satellite roughly reflects the satellite fraction as a whole.

Of these recently merged satellites, $20\% - 35\%$ come from satellite-satellite parents within a single halo, while $\sim 7\%$ arise when a central-satellite merger occurs in a halo as it falls into a larger halo, becoming a satellite. The rest arise from switches, when a satellite merges with a central and the resulting subhalo no longer is the most massive subhalo, thus becoming a satellite. These switches occur primarily in halos only a few times more massive than the satellite, typically for satellites in close proximity to their central. At higher halo masses, recently merged satellites are dominated by satellite-satellite parents. These satellite-satellite mergers preferentially occur in the outer regions of a halo and are comparatively less

[17] A few percent arise from central-central parents, when the central regions of two halos coalesce so quickly that they are not seen as satellite-central subhalos given finite time resolution. We include these as satellite-central parents.

[18] Satellite merger fractions are boxcar-averaged across three consecutive outputs to reduce noise from small number statistics.

common in the central regions. We examine in more detail the environmental dependence of subhalo mergers in Chapter 7.

Considering instead only parent types, Fig. 6.9 shows that $5-10\%$ of all mergers come from satellite-satellite parents at $z \sim 2.5$, a fraction which increases to $10-15\%$ at $z = 1.6$ and remains flat thereafter. Approximately 80% of all satellite-satellite mergers lead to a satellite child, while the rest lead to a central during a switch.

6.5 Galaxy & Halo Merger Counts

6.5.1 Counts of Recent Mergers

The distribution of the number of mergers per object within a fixed time interval gives the fraction of objects at a given epoch that might exhibit merger-related activity or morphological disturbance.[19] Multiple mergers as well might contribute to specific properties, for example, the formation and mass growth of elliptical galaxies (e.g., Boylan-Kolchin et al. 2005; Robertson et al. 2006; Naab et al. 2006; Conroy et al. 2007a).

Figure 6.10 shows the fraction of subhalos at $z = 2.6$ and $z = 1$ with a given number of mergers in the last 1 Gyr. At $z = 2.6$, 30% of subhalos have suffered at least one major merger. Interestingly, this fraction is nearly constant across the mass regimes we probe. In contrast, the fraction of halos with at least one major merger within 1 Gyr is about twice as large, with stronger mass dependence: higher mass halos experience more mergers. At high redshift, halos are also significantly more likely to have undergone multiple mergers than subhalos, which builds up the satellite population.

At $z = 1$, recent mergers of subhalos and halos become less common, with only 8% of subhalos having suffered at least one major merger in the last 1 Gyr. Objects which have had 1 or 2 mergers are still more common for halos than subhalos, though high mass subhalos exhibit a much higher fraction of 3 or more mergers than halos of the same (infall) mass. Note that subhalos that have undergone 1 merger can be either satellites or centrals, those that have undergone 2 or more mergers are almost entirely centrals. The build-up of the satellite population at higher redshift has allowed massive centrals to experience multiple mergers at lower redshift. This effect is stronger for more massive subhalos since they are more likely to be centrals, and they reside in higher mass halos with more massive satellites.

6.5.2 Fraction "On"

The fraction of halos that host recent mergers, $f_{\rm on}$, is of particular interest for quasar or starburst evolution models, and their feedback effects such as heating of the Intra-Cluster Medium (ICM). We select mergers up to 200 Myr after coalescence, motivated by the expected time interval during which quasars or starbursts remain observable (e.g., Hopkins

[19] This differs from the merger rates of §6.3, since we are tracking the histories of individual objects selected at a given redshift.

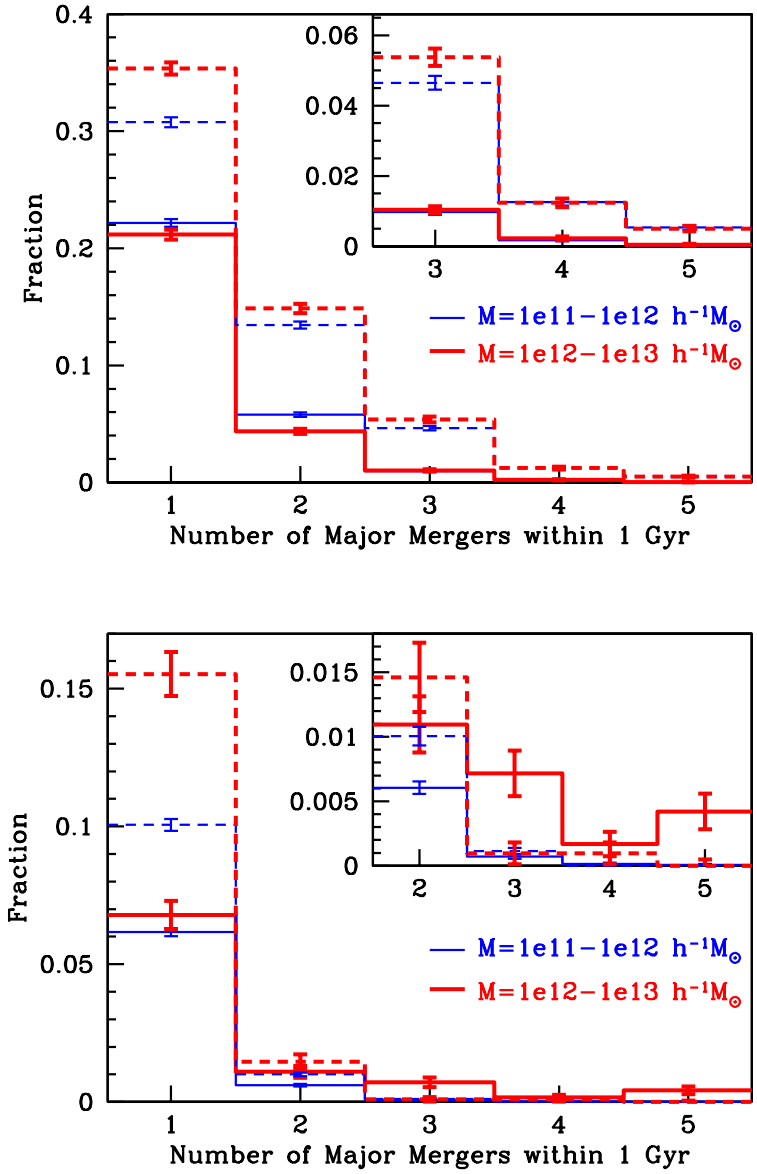

Figure 6.10: **Top**: Fraction of subhalos at $z = 2.6$ that have had a given number of mergers in the last 1 Gyr, for $M_{\rm inf} = 10^{11} - 10^{12}\,h^{-1}\,{\rm M}_\odot$ (thin lines) and $M_{\rm inf} = 10^{12} - 10^{13}\,h^{-1}\,{\rm M}_\odot$ (thick lines). Dashed lines show the same, but for host halos. 30% of subhalos have had at least one merger (independent of mass), while for halos this fraction is 50% (lower mass) and 57% (higher mass). Inset shows detail for > 2 mergers. **Bottom**: Same, but at $z = 1$. 8% of subhalos have had at least one merger (independent of mass), while for halos this fraction is 11% (lower mass) and 17% (higher mass). High mass subhalos show a much larger fraction of multiple mergers. Inset shows detail for > 1 merger.

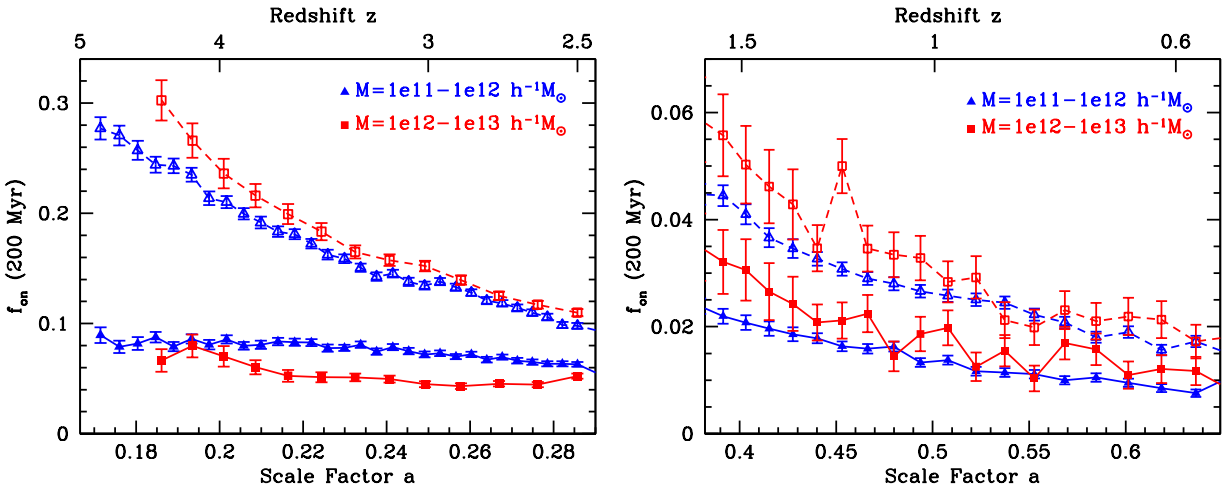

Figure 6.11: **Left**: Fraction of halos that host a subhalo-subhalo merger within the last 200 Myr (closed points, solid curves) at $z = 5 - 2.5$ for $M_{\rm inf} = 10^{11} - 10^{12}\,h^{-1}\,{\rm M}_\odot$ (triangles) and $M_{\rm inf} = 10^{12} - 10^{13}\,h^{-1}\,{\rm M}_\odot$ (squares). Open points (dashed curves) show the fraction of halos of the same mass that have suffered a major halo-halo merger in the same time interval. **Right**: Same, but at $z = 1.6 - 0.6$.

et al. 2005). This time interval is only illustrative, though, as one expects relevant lifetimes to depend strongly upon galaxy mass and merger ratio. Observables might depend upon dynamical time as well, although many quasar triggering effects might be related to microphysics—small scale interactions close to the merger—that do not evolve with time.[20]

Figure 6.11 shows the evolution of $f_{\rm on}$ for halos hosting subhalo mergers within the last 200 Myr. The same quantity is shown for halos with recent mergers themselves. At high redshift, $f_{\rm on}$ for halo mergers shows a steep decline from the decreasing halo merger rate. However, $f_{\rm on}$ for subhalo-subhalo mergers is flat from $z = 2.5 - 5$, because the subhalo merger rate per object decreases while the number of massive satellites in a given mass halo rises, causing the number of massive subhalo mergers within the halo to remain constant. At low redshift, where the satellite population grows more slowly, the evolution of this fraction for subhalo mergers more closely parallels that of halo mergers.

6.6 Evolution of the Satellite Halo Occupation

The redshift evolution of the satellite galaxy populations of dark matter halos is shaped by halo vs. galaxy mergers: halo mergers create satellites while galaxy mergers remove

[20] If we scale our $f_{\rm on}$ time interval by the dynamical time, the slope of $f_{\rm on}$ becomes slightly shallower, but the qualitative results do not change.

them.[21] If the infall rate of satellites onto a halo is different than the satellite destruction rate, the satellite halo occupation will evolve with time.

As shown in Fig. 6.8, at $z > 2.5$, the merger rate of subhalos is significantly lower and shallower in slope than that of halos, implying that subhalos are being created faster than they are destroyed, at a rate decreasing with time. Conversely, at $z < 1.6$ the merger rates of halos and subhalos exhibit approximately the same redshift dependence, and their amplitudes are similar (also recall from §6.3 that not all halo major merger lead to subhalo major mergers). Thus, for halos of a fixed mass, we expect a rapid rise in the satellite halo occupation prior to $z \sim 2$ and a levelling-off with more gradual evolution at lower redshift.

6.6.1 Satellite Halo Occupation in Simulation

The above trends are seen in Fig. 6.12, which shows the evolution of the satellite occupation per halo, for satellites with $M_{\rm inf} > 10^{11}\,h^{-1}\,{\rm M}_\odot$ in the $100\,h^{-1}\,$Mpc simulation. Satellite occupation counts are normalized using the last output at $z = 0.6$. More massive satellites ($M_{\rm inf} > 10^{12}\,h^{-1}\,{\rm M}_\odot$) have similar evolution, with a peak in the satellite halo occupation at $z \approx 2.5$. For a fixed satellite infall mass, less massive halos exhibit stronger satellite occupation evolution with redshift, leading to a more prominent peak.

6.6.2 Analytic Estimate of Satellite Halo Occupation

The rate of change of the satellite subhalo population per halo, for a fixed satellite $M_{\rm inf}$, is given by the rate at which satellites fall into a halo (the halo merger rate) minus the rate at which satellites coalesce with the central subhalo

$$\frac{dN_{\rm sat}}{dt} = \frac{dN_{\rm halo,merge}}{dt} - \frac{dN_{\rm sat-cen,merge}}{dt}\,. \tag{6.15}$$

The halo merger rate at all epochs is given by (§6.3)

$$\frac{dN_{\rm halo,merge}}{dt} = A(1+z)^\alpha = Aa^{-\alpha}\,. \tag{6.16}$$

The timescale for the satellite to coalesce with its central subhalo after infall is given to good approximation by

$$t_{\rm sat-cen,merge} \approx \frac{C_o}{10}\frac{M_{\rm halo}/M_{\rm sat}}{\ln(1+M_{\rm halo}/M_{\rm sat})}t_{\rm Hubble} \tag{6.17}$$

where C_o is a constant of order unity that accounts for the ensemble averaged satellite orbital parameters, and we leave it as our sole free parameter. The rate of satellite destruction (coalescence) is thus

$$\frac{dN_{\rm sat-cen,merge}}{dt} = \frac{10}{C_o}\frac{\ln(1+M_{\rm halo}/M_{\rm sat})}{M_{\rm halo}/M_{\rm sat}}H(z)\,. \tag{6.18}$$

[21] Though if one applies a mass threshold to a population, this is not strictly true since mergers also scatter lower mass objects into the population.

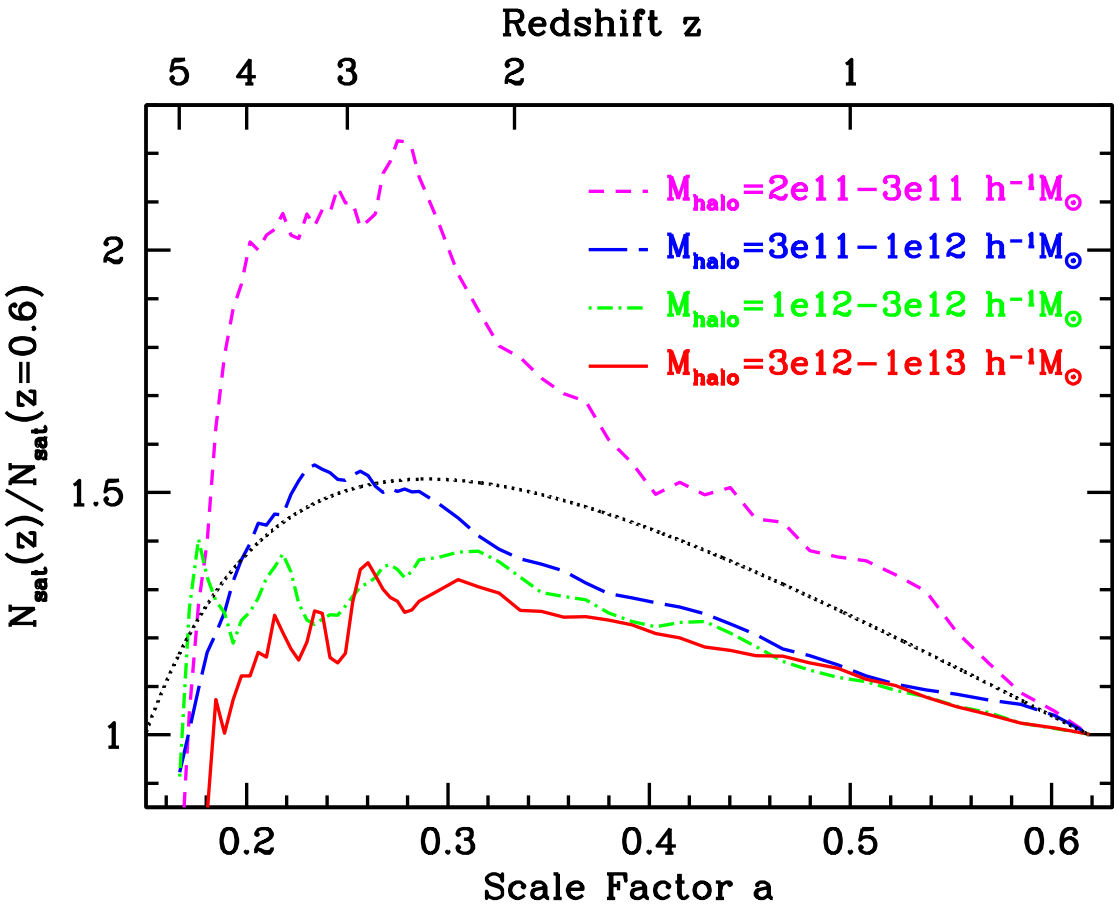

Figure 6.12: Evolution of the average number of satellite subhalos per halo for satellites with $M_{\rm inf} > 10^{11}\,h^{-1}\,{\rm M}_\odot$ and several halo mass bins. Satellite counts are normalized to those at $z = 0.6$ (the final output) and boxcar averaged across 3 outputs to reduce the small number statistics noise at early times. Dotted black curve shows fit of Eq. 6.21 for 3:1 mass ratio mergers using halo merger rate parameters from Table 6.1. All halos masses have a peak in satellite occupation at $z \sim 2.5$, and similar trends persist for higher mass satellites. Less massive halos exhibit stronger evolution with redshift, leading to a more prominent peak.

Combining Eqs. 6.16 and 6.18 into Eq. 6.15 one gets

$$\frac{dN_{\rm sat}}{dt} = Aa^{-\alpha} - \frac{10}{C_o}\frac{\ln(1+M_{\rm halo}/M_{\rm sat})}{M_{\rm halo}/M_{\rm sat}}H(z)\,. \tag{6.19}$$

At high redshift, $H(z) \approx H_o(\Omega_{\rm m,o}a^{-3})^{\frac{1}{2}}$, where $H_o \simeq 0.1h$ Gyr^{-1}, which implies

$$\frac{dN_{\rm sat}}{dt} \approx Aa^{-\alpha} - \frac{1}{C_o}\frac{\ln(1+M_{\rm halo}/M_{\rm sat})}{M_{\rm halo}/M_{\rm sat}}\Omega_{\rm m,o}^{\frac{1}{2}}a^{-\frac{3}{2}}\,. \tag{6.20}$$

Across all mass and redshift regimes, the power law index for halo mergers is $\alpha = 2 - 2.3$ (§6.3), and we find no additional dependence on merger mass ratio, suggesting a universal power law index.[22] Thus, the creation and destruction terms in Eq. 6.20 have differing dependencies on the scale factor, which implies they become equal at some redshift, where the satellite occupation per halo reaches a maximum.

Using the exact evolution of the Hubble parameter (in our cosmology) of $H(z) = H_o(\Omega_{\rm m,o}a^{-3} + \Omega_\Lambda)^{1/2}$ in Eq. 6.19, and integrating over a, the full evolution of the satellite occupation per halo is

$$\begin{aligned} N_{\rm sat}(a) = &\frac{A}{H_o}\int da\frac{a^{-(\alpha+1)}}{H(z)} \\ &- \frac{10}{C_o}\frac{M_{\rm sat}}{M_{\rm halo}}\ln\left(1+\frac{M_{\rm halo}}{M_{\rm sat}}\right)\ln(a) + K \end{aligned} \tag{6.21}$$

where the constant K accounts for initial (or final) conditions. Figure 6.12 shows the resultant $N_{\rm sat}(a)$, normalized to the satellite occupation per halo at final output, using typical values for the halo merger rate from Table 6.1 ($A = 0.032$ and $\alpha = 2.3$). These values correspond to 3:1 mass ratio mergers, for satellites with $M_{\rm inf} = 10^{11}\,h^{-1}\,{\rm M}_\odot$ this gives $M_{\rm halo} = 3\times10^{11}\,h^{-1}\,{\rm M}_\odot$. While the fit of this model to the simulation results is not exact, it nicely reproduces the general trends, especially given the simplicity of the model, which ignores halo (central) mass growth, satellite-satellite mergers, and switches. For instance, it correctly produces a lower peak in satellite occupation for halos with satellites of more discrepant mass ratios (more massive halos for a fixed satellite mass, or less massive satellites for a fixed halo mass), relative to the amplitude at low redshift. This is because the decreased infall times for smaller satellite-halo mass ratios cause a more dramatic fall (after the peak) in the satellite population for lower mass halos.

Agreement of this model with our simulations also requires $C_o \approx 2$, which can be compared with other work. Zentner et al. (2005) and Jiang et al. (2008) found that the ensemble averaged satellite orbital circularity distribution is given by $\langle\epsilon\rangle = 0.5 \pm 0.2$, with no strong dependence on redshift or satellite-halo mass ratio (though more recently, Wetzel (2010) found redshift dependence, see Chapter 5). When applied to detailed dynamical friction timescale fits from simulation, this yields $C_o \approx 0.6$ (Boylan-Kolchin et al. 2008) and

[22] Though merger rates for more discrepant mass ratios have higher amplitudes, as given by Eq. 6.7.

$C_o \approx 1.4$ (Jiang et al. 2008).[23] Taken at face value, our even higher value of C_o means that our satellites are taking longer to merge, suggesting that the discrepancy does not arise from artificial over-merging in our simulations. However, exact comparisons are difficult given the simple nature of our analytic model, and because both of these analyses used different halo and subhalo finding algorithms. Jiang et al. (2008), who used a simulation of roughly similar volume and mass resolution to ours, also incorporated hydrodynamics, which is likely to shorten the merger timescale since it introduces further dissipational effects to the subhalo orbits and reduces mass loss. Compared with Boylan-Kolchin et al. (2008), who performed much higher resolution simulations of isolated halo mergers, it is possible that our satellite subhalos experience more severe mass stripping upon infall, decreasing their mass and thus extending their subsequent infall time (see Eq. 6.10). A more detailed investigation of satellite infall timescales in a cosmological setting is needed, studies now in progress are targeting in particular the role of hydrodynamic effects (Dolag et al. 2009; Saro et al. 2008; Simha et al. 2009).

6.6.3 Comparison to Other Work on Satellite Occupation Evolution

Figure 6.12 shows a peak in the number of satellites per halo at $z \sim 2.5$. Fundamentally, the reason for this peak is that we select subhalos of *fixed* minimum *infall* mass in halos of *fixed* mass across time. If instead we examine the satellite occupation for halos above a minimum mass cut, the growth of massive halos (hosting more satellites) at late time would overwhelm the drop in the satellite population at a fixed halo mass, so the satellite halo occupation would grow monotonically and appear much like the satellite fraction in Fig. 6.7, which ignores halo mass.[24]

These results agree with the interpretation that more massive halos have later formation times and longer satellite infall times, and thus host more substructure at a given epoch (van den Bosch et al. 2005a; Zentner et al. 2005). Similarly, for a fixed satellite infall mass, the satellite halo occupation evolves more rapidly for less massive halos, as Zentner et al. (2005) and Diemand et al. (2007) found, though their results were based upon subhalo instantaneous mass and maximum circular velocity.

However, the peak in satellite halo occupation in Fig. 6.12 does not appear in Halo Occupation Distribution (HOD) evolution studies by Zentner et al. (2005) because they use a fixed cut on instantaneous maximum circular velocity across time. As was shown in Fig. 6.4, a fixed $V_{\rm c,max}$ probes lower mass at higher redshift, and this evolution in satellite mass overwhelms the satellite evolution of Fig. 6.12, leading to a monotonic rise in the satellite halo occupation with redshift. Similarly, Conroy et al. (2006) noted that the HOD

[23] The C_o values of these two fits agree only in extreme cases: maximally circular orbits for Boylan-Kolchin et al. (2008) or maximally eccentric orbits for Jiang et al. (2008).

[24] Though the satellite halo occupation would have a higher amplitude since it measures $n_{\rm sat}/n_{\rm central}$ while the satellite fraction measures $n_{\rm sat}/n_{\rm subhalo} = n_{\rm sat}/(n_{\rm central} + n_{\rm sat})$.

shoulder (the halo mass where a halo hosts only a central galaxy) becomes shorter at higher redshift as an increasing fraction of low-mass halos host more than one galaxy, finding a monotonically increasing satellite population with redshift. However, they compare fixed satellite number density (not mass) across redshift, which corresponds to a lower subhalo mass at higher redshift. Again, this overwhelms the evolution of Fig. 6.12, leading to a monotonic rise in the satellite population per halo with redshift.

In their semi-analytic model matched to simulation, van den Bosch et al. (2005a) found that the average subhalo mass fraction of a halo always decreases with time, and they claim that, as a result, the timescale for subhalo mass loss (approximately the dynamical infall time) is always smaller than the timescale of halo mass accretion (mergers). This implies that the satellite infall rate is always higher than the halo merger rate, and so the satellite HOD always decreases with time. However, this result refers to the total subhalo instantaneous mass per halo, not galaxy counts based on infall mass. If instead we examine the evolution of the satellite occupation per halo as in Fig. 6.12 selecting the satellites based on *instantaneous* subhalo mass instead of infall mass, we find a monotonic increase in the satellite occupation with no peak, in agreement with other authors above.

These examples all illustrate how the evolution of the HOD is dependent both on satellite mass assignment and selection of fixed mass vs. circular velocity vs. number density across time.

6.7 Summary & Discussion

Using high-resolution dark matter simulations in cosmological volumes, we have measured the rates, counts, and types of subhalo (galaxy) major mergers at redshift $z = 0.6 - 5$, describing their populations in terms of centrals vs. satellites and contrasting their merger properties with those of halos of the same (infall) mass. We assign subhalos their mass at infall (with the capacity for mass growth during satellite-satellite mergers), motivated by an expected correlation with galaxy stellar mass, but include no further semi-analytic galaxy modelling. We select mergers requiring 3:1 or closer infall mass ratios, motivated by the expectation that these can trigger activity such as quasars and starbursts related to Lyman break galaxies, sub-millimeter galaxies, and ULIRGs. We highlight our main results as follows:

- The merger rate per object of subhalos is always lower than that of halos of the same (infall) mass. Galaxies exhibit stronger mass dependence on the amplitude of their merger rate than halos, with more massive galaxies undergoing more mergers. While the slope of the halo merger rate per object is essentially redshift independent, the slope of the galaxy merger rate is much shallower than that of halos at $z > 2.5$ and parallels that of halos at $z < 1.6$.

- These differences in halos and subhalo merger rates arise because (1) halo mergers add mass to halos instantly, while central subhalo mass grows more gradually after a halo

merger; (2) halo major mergers do not necessarily lead to subhalo major mergers, since central subhalos experience mass growth while a satellite subhalo's infall mass typically remains constant as it orbits; and (3) the satellite subhalo fraction grows with time, and satellites are twice as likely to be recent mergers as centrals of the same infall mass.

- $15\% - 35\%$ of all recently merged subhalos are satellites, though a significant fraction of these arise from satellite-central parents during switches. $5\% - 15\%$ of galaxy mergers arise from satellite-satellite parents, with a higher fraction at lower redshift.

- At $z = 2.6$ ($z = 1$), 30% (8%) of galaxies have experience at least one major merger in the last 1 Gyr, regardless of mass. Halos are more likely to have experience multiple mergers in their recent history.

- The likelihood of a halo to host a recently merged galaxy, $f_{\rm on}$, does not evolve with time at $z > 2.5$ and falls with time at $z < 1.6$.

- Comparing galaxy and halo merger rates allows one to understand the evolution of the satellite halo occupation, and we approximated this behavior analytically including fits to our simulations. Selecting subhalos on fixed infall mass, the satellite halo occupation for halos of a fixed mass increases with time at high redshift, peaks at $z \sim 2.5$, and falls with time after that. This implies similar evolution for the satellite galaxy component of the HOD.

Our results, based entirely on the dynamics of dark matter, represent an important but preliminary step towards quantifying the nature of galaxy mergers in hierarchical structure formation. To compare to many observables we would need to include baryonic effects, and indeed such effects can provide corrections to the merger rates themselves (Dolag et al. 2009; Jiang et al. 2009; Saro et al. 2008). The merger rates here also do not include the extent to which the subhalos are gas-rich (required for some observables), though at the high redshifts we examine, we expect almost all massive galaxies to be gas-rich. While satellites can be stripped of much of their gas before merging with their central (e.g., Dolag et al. 2009; Saro et al. 2008), we have considered primarily massive satellites (relative to their host halos), which have short infall times and thus experience less gas stripping.

Timescales between observables and our measured merger event also play a role. In simulations, a quasar can appear up to ~ 1 Gyr after galaxy coalescence, though starbursts may occur more quickly (e.g., Hopkins et al. 2005; Springel et al. 2005a; Cox et al. 2008). However, morphological disturbance is clearest during first passage and final coalescence (Lotz et al. 2008b). The time scales for each signature to commence and/or persist also have a large scatter, ranging from 0.2 to 1.2 Gyr after the merger. Finally, specific observations will also have specific selection functions. The quantitative measurements provided here provide starting points for these analyses in addition to helping to understand the properties of galaxies and their mergers in general.

Unfortunately, our predictions are not easily compared to observations which estimate merger rates at $z \lesssim 1$ using close galaxy pairs or disturbed morphologies (most recently, Bell et al. 2006; Kampczyk et al. 2007; Kartaltepe et al. 2007; Lin et al. 2008; Lotz et al. 2008a; McIntosh et al. 2008; Patton & Atfield 2008) since they have found that the close pair fraction evolves as $(1 + z)^{\alpha}$ with a diverse range of exponents from $\alpha = 0$ to 4. Furthermore, translating these observations into galaxy or halo merger rates requires including more physical effects, such as time dependent galaxy coalescence timescales (Kitzbichler & White 2008; Mateus 2008) or inclusion of changes in numbers of host halos with redshift (Berrier et al. 2006).

Chapter 7

The Clustering & Host Halos of Galaxy Mergers at High Redshift

Abstract

High-resolution simulations of cosmological structure formation indicate that dark matter substructure in dense environments, such as groups and clusters, may survive for a long time. These dark matter subhalos are the likely hosts of galaxies. We examine the small-scale spatial clustering of subhalo major mergers at high redshift using high-resolution N-body simulations of cosmological volumes. Recently merged, massive subhalos exhibit enhanced clustering on scales $\sim 100 - 300\,h^{-1}\,\mathrm{kpc}$, relative to all subhalos of the same infall mass, for a short time after a major merger (< 500 Myr). The small-scale clustering enhancement is smaller for lower mass subhalos, which also show a deficit on scales just beyond the excess. Halos hosting recent subhalo mergers tend to have more subhalos; for massive subhalos the excess is stronger and it tends to increase for the most massive host halos. The subhalo merger fraction is independent of halo mass for the scales we probe. In terms of satellite and central subhalos, the merger increase in small-scale clustering for massive subhalos arises from recently merged massive central subhalos having an enhanced satellite population. Our mergers are defined via their parent infall mass ratios. Subhalos experiencing major mass gains also exhibit a small-scale clustering enhancement, but these correspond to two-body interactions leading to two final subhalos, rather than subhalo coalescence.

7.1 Introduction

A wealth of high redshift galaxy data is now accumulating, and many members in the resultant galaxy zoo are thought arise from galaxy mergers: quasars (Carlberg 1990), Lyman Break Galaxies (LBG; see Giavalisco 2002, for review), Sub-Millimeter Galaxies (SMG; see Blain et al. 2002, for review), Ultra-Luminous Infrared Galaxies (ULIRG; see Sanders &

Mirabel 1996, for review) and all starburst and starburst remnant galaxies (e.g., Barnes & Hernquist 1991; Noguchi 1991). Observational samples of these objects at $z \gtrsim 1$ are growing large enough to produce statistical measurements of clustering (e.g., Giavalisco et al. 1998; Blain et al. 2004; Croom et al. 2005; Ouchi et al. 2005; Cooray & Ouchi 2006; Hennawi et al. 2006; Kashikawa et al. 2006; Lee et al. 2006; Scott et al. 2006; Coil et al. 2007; Gawiser et al. 2007; Shen et al. 2007; Francke et al. 2008; Myers et al. 2008; Yamauchi et al. 2008; Yan et al. 2008; Yoshida et al. 2008) which can be compared to candidates in numerical simulations.

In high-resolution dark matter simulations, overdense, self-bound, dark matter substructures within host halos can survive for a long time (Tormen 1997; Tormen et al. 1998; Ghigna et al. 1998; Klypin et al. 1999; Moore et al. 1999). These "subhalos" are thought to be the hosts of galaxies, and indeed the identification of galaxies with subhalos reproduces many galaxy properties (e.g., Springel et al. 2001, 2005b; Zentner et al. 2005; Bower et al. 2006; Conroy et al. 2006; Vale & Ostriker 2006; Wang et al. 2006; Wetzel & White 2010). The complex dynamics of subhalos may thus be a good proxy for those of galaxies themselves, suggesting that galaxy mergers can be identified with subhalo mergers within simulations. We will use the terms galaxy and subhalo interchangeably hereon. Measurements of subhalo mergers can provide a quantitative reference for the identification of merger-related objects in observations and can aid in the correct interpretation of their clustering measurements.

One question of particular interest is whether small-scale clustering can probe merger activity. There has been much recent discussion of a "small-scale clustering enhancement" of galaxy subpopulations in simulations and observations, but several differing definitions of "enhancement" exist, mostly stemming from different choices of reference. For instance, small-scale enhancement has been used to describe clustering stronger than a power law extrapolated from larger scales, or clustering stronger than that of dark matter at small scales. However both of these behaviors are seen in non-merging samples. Luminous Red Galaxies in SDSS are not thought to be associated with (recent) mergers, yet their correlation function is much steeper than the dark matter on scales of several hundred kpc (Masjedi et al. 2006). One expects objects which populate halos more massive than $M_\star$ (the characteristic non-linear mass) will have an upturn in their correlation function on scales below the virial radius of the $M_\star$ halos since at this scale the clustering is dominated by pairs of objects within the same halo and the mass function is very steep (e.g., Seljak 2000; Peacock & Smith 2000). Quasars (thought to be associated with mergers) do exhibit a sharp upturn in clustering on very small scales ($25 - 50\,h^{-1}\,\mathrm{kpc}$) at $z \approx 1 - 3$ (Hennawi et al. 2006; Myers et al. 2008), but a comparison with galaxy clustering measurements at these scales and redshifts is lacking.[1] On slightly larger scales, low z quasar clustering observations show no excess above a power law (e.g. Padmanabhan et al. 2008, and discussion therein).

On the other hand, merger-related clustering effects are not unexpected. Recently, various authors have shown that the large-scale clustering of dark matter halos depends on their formation histories (known as "assembly bias"; e.g., Sheth & Tormen 2004; Gao et al.

[1]It is not clear how to interpret a galaxy clustering measurement on scales smaller than the galactic radius.

2005; Wechsler et al. 2006; Wetzel et al. 2007), and in particular, on recent halo merger activity ("merger bias"; Scannapieco & Thacker 2003; Wetzel et al. 2007, 2008).[2] Any such history or merger dependent clustering breaks the usually assumed direct link between large-scale clustering amplitude and halo mass. Analytical modeling of the small-scale clustering of quasars has been compared to observations, assuming that quasars are mergers and that mergers occur in denser environments (Hopkins et al. 2008b).

In this chapter, we focus on the small-scale clustering of subhalo mergers and its relation to their host halos. We use dark matter simulations to compare the small-scale clustering of recently merged subhalos at high redshifts to the clustering of the general subhalo population of the same infall mass. To interpret our results, we relate the merged subhalos to their host dark matter halos using the formalism of the halo model (Seljak 2000; Peacock & Smith 2000; Cooray & Sheth 2002), examining the dependence of subhalo mergers both on their host halo masses and their halo radial distribution profiles.

7.2 Numerical Techniques & Merger Definitions

7.2.1 Simulations & Subhalo Tracking

Our simulation and subhalo finding and tracking details are discussed extensively in Chapter 6, and we use the same dataset in this chapter. We select subhalos with $M_{\rm inf} > 10^{12}\,h^{-1}\,{\rm M}_{\odot}$ in the larger simulation and scale down to $M_{\rm inf} > 10^{11}\,h^{-1}\,{\rm M}_{\odot}$ in the smaller, higher resolution simulation, by requiring consistency between the two simulations in their overlap regime.[3] Halos of mass 10^{11} $(10^{12})\,h^{-1}\,{\rm M}_{\odot}$ cross below $M_{*}(z)$, the characteristic mass of collapse, at $z = 1.5$ ($z = 0.8$), so we probe $M > M_{*}(z)$ subhalos for much of the redshift range we consider. We also expect our sample of $M_{\rm inf} > 10^{12}\,h^{-1}\,{\rm M}_{\odot}$ subhalos to approximately correspond to $L \gtrsim L_{*}$ galaxies at the redshifts we examine (see, e.g., Conroy & Wechsler 2008, for halo-galaxy mass relation based on abundance matching). Additionally, most massive galaxies are gas-rich (blue) at $z \gtrsim 1$ (Cooper et al. 2007; Gerke et al. 2007; Hopkins et al. 2008a), possessing enough gas to be actively star forming. Thus, we anticipate that most, if not all, mergers we track have the capacity to drive galaxy activity such as starbursts and quasars.

[2] See also Furlanetto & Kamionkowski (2006) for analytic estimates, Percival et al. (2003) for a simulation limit on the effect, Croton et al. (2007); Tinker et al. (2008b) for halo assembly bias applied to galaxy clustering.

[3] Using the Millennium simulation (Springel et al. 2005b), Kitzbichler & White (2008) require an analytic model for satellite infall times after subhalo disruption to match small-scale galaxy clustering at $z \sim 0$. We do not expect this numerical disruption to significantly bias our results since our $100\,h^{-1}\,{\rm Mpc}$ simulation has higher mass and temporal resolution.

7.2.2 Merger Criteria

We select a subhalo as a major merger (henceforth merger) if its two most massive parents, with $M_{\rm inf,2} \leq M_{\rm inf,1}$, satisfy $M_{\rm inf,2}/M_{\rm inf,1} > 1/3$. As mentioned above, galaxy mergers with stellar mass ratios closer than 3:1 are expected to drive interesting activity, such as quasars and starbursts. Unless otherwise stated, we use the shortest simulation output spacing to define the merger time interval, corresponding to 50 Myr (~ 100 Myr) for $M_{\rm inf} > 10^{11}$ (10^{12}) $h^{-1}\,{\rm M}_\odot$ at $z > 2.5$, and ~ 200 Myr for all masses at $z < 1.6$.[4]

Other definitions of mergers produce significantly different merger samples. In related work, which inspired our investigation, Thacker et al. (2006) used a dark matter plus hydrodynamic simulation to measure the small-scale clustering of subhalos with recent large mass gains, finding that these subhalos have enhanced small-scale clustering relative to a population with the same large-scale ($\gtrsim 1\,h^{-1}\,{\rm Mpc}$) clustering. Mass gain is convenient in that it does not require histories beyond the previous time step, and mass gain is unambiguously defined for all subhalos. However, using our simulations and subhalo finder, the resulting sample is almost entirely different from the one defined above.[5] Specifically, using a mass gain merger definition in our simulations led to "mergers" where the two contributing galaxies almost always remained as distinct entities after the merger event. The most common instance of major mass gain is a satellite subhalo gaining mass during its movement within its host halo, particularly as it moves away from the halo center (see Fig. 2 in Chapter 6 and Diemand et al. (2007) for examples). A subhalo can also gain mass by stripping material from the outskirts of a nearby subhalo. In 75% of the cases of major mass gain, one of the progenitors contributed less than 10% of its mass to the resulting "merged" child. The most bound particles (where we expect the stellar component of a galaxy) were unaffected. We did find significantly increased small-scale clustering for these mass gain subhalos, attributable to the remaining nearby subhalo which just "merged" with it. Similar issues in using mass gain to define mergers were noted in Maulbetsch et al. (2007).

7.3 Small-Scale Spatial Clustering

When examining the effects of recent mergers on spatial clustering it is important to define an appropriate comparison sample. We have chosen all subhalos above the same given infall mass cut as the mergers, with a matched $M_{\rm inf}$ distribution. We match $M_{\rm inf}$ to remove any possible artificial biasing from mergers preferentially occurring for subhalos of higher mass. Using only a mass cut without matching the mass distribution leads to a similar, but weaker, effect. If infall mass is a good proxy for stellar mass, our merger and comparison samples correspond to populations matched in stellar mass.

[4] This gives 280 (490) mergers at $z = 2.6$ ($z = 1$) above the lower mass cut in our smaller, higher resolution simulation.

[5] For $M_{\rm inf} > 10^{11}\,h^{-1}\,{\rm M}_\odot$ subhalos at $z = 2.6$, 492 have $M_{\rm cont,2}/M_{\rm cont,1} > 1/3$, compared to the 260 for our infall mass ratio definition, with only 7 overlapping the two sets.

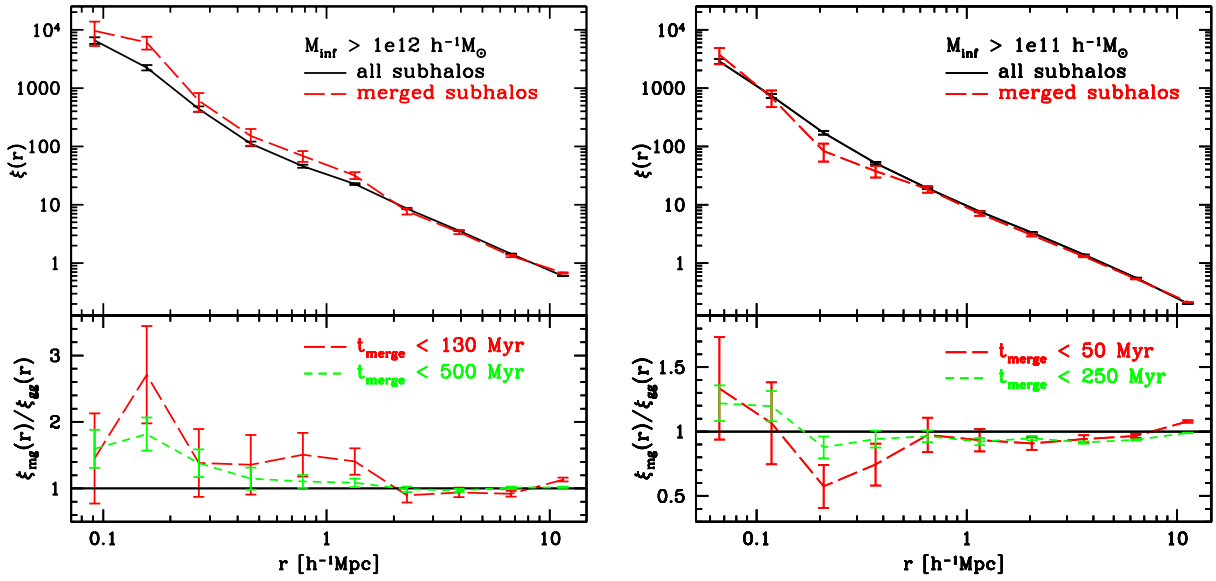

Figure 7.1: Cross-correlation of recently merged subhalos with all subhalos, $\xi_{mg}(r)$, and the auto-correlation of all subhalos, $\xi_{gg}(r)$, at $z = 2.6$, for $M_{\rm inf} > 10^{12}\,h^{-1}\,{\rm M}_\odot$ (left) and $M_{\rm inf} > 10^{11}\,h^{-1}\,{\rm M}_\odot$ (right). Infall mass, $M_{\rm inf}$, is matched between the merged and full subhalo samples. **Top Left**: $\xi_{mg}(r)$ for subhalos merging within the last 130 Myr (long-dashed curve) and $\xi_{gg}(r)$ for all subhalos (solid curve). **Bottom Left**: Ratio of the cross- and auto-correlations above, for mergers within the last 130 Myr (long-dashed curve) and 500 Myr (short-dashed curve). **Top Right**: $\xi_{mg}(r)$ for subhalos merging within the last 50 Myr (long-dashed curve) and $\xi_{gg}(r)$ for all subhalos (solid curve). **Bottom Right**: Ratio of the cross- and auto-correlations above, for mergers within the last 50 Myr (long-dashed curve) and 250 Myr (short-dashed curve). Higher mass subhalos show stronger enhanced clustering from mergers, but at both masses no signal persists for subhalos > 500 Myr after merging. Errors are given by $\sqrt{N_{\rm pair}}$ and do not include sample variance.

To measure the small-scale ($\sim 100-1000\,h^{-1}\,\mathrm{kpc}$) clustering of subhalo mergers relative to the clustering of the general subhalo population, we measure the cross-correlation function[6] of the merged and general population, ξ_{mg}, and the auto-correlation function of the general population, ξ_{gg}. Our limited volume unfortunately does not allow us to sub-divide our simulation to measure the sample variance error. We show $\sqrt{N_{\rm pair}}$ errors on the correlation function points, but we caution that this may underestimate the error by up to a factor of 2. Our clustering measurements are limited on small scales by the force resolution and on large scales by the simulation volume. We present results on scales where these effects are minor, and we further discuss the effects of finite simulation volumes and the statistics of massive halos in §7.4.3.

Figure 7.1 shows the spatial clustering of recently merged subhalos and the general subhalo population at $z = 2.6$, for two mass regimes and several merger time intervals. These results are representative of our results at other redshifts. Over the smallest time intervals, both high and low mass subhalos have a rise and a decline relative to the general population, with the rise being most prominent for higher mass subhalos and the decline most prominent for lower mass subhalos. For $M_{\rm inf} > 10^{11}\,h^{-1}\,\mathrm{M}_{\odot}$, we find an upper limit of 1.8× enhancement at $70\,h^{-1}\,\mathrm{kpc}$, increasing to 3× that of the general population at $\sim 150\,h^{-1}\,\mathrm{kpc}$ for $M_{\rm inf} > 10^{12}\,h^{-1}\,\mathrm{M}_{\odot}$. In addition, lower mass subhalos exhibit a deficit at $100 - 300\,h^{-1}\,\mathrm{kpc}$. The enhancement (or deficit) declines rapidly with the time since the merger, and we see no signal > 500 Myr after the merger. As time progresses central mergers will become satellites in larger halos and satellite mergers will move within their host halos (and perhaps merge with the central), washing out the correlation between the merger and its halo properties that we see at the time of the merger.

7.4 Halo Occupation Distribution & Radial Profile

The halo model (Peacock & Smith 2000; Seljak 2000; Cooray & Sheth 2002) can provide insight into the observed clustering signals of the merged subhalo population in Fig. 7.1. In this framework, galaxies populate dark matter halos such that their large-scale spatial clustering is determined primarily by the clustering of their host dark matter halos ("2-halo term"), while their small-scale spatial clustering arises from galaxies in the same host halo ("1-halo term"). The objects occupy dark matter halos according to a Halo Occupation Distribution (HOD) and have some radial profile within these halos. Since the clustering of recently merged galaxies differs from that of all galaxies, we expect mergers to differ from the general galaxy population in their HOD and/or profile.

[6]Not only is the cross-correlation of the mergers with the general population interesting in itself, but it also provides better statistics.

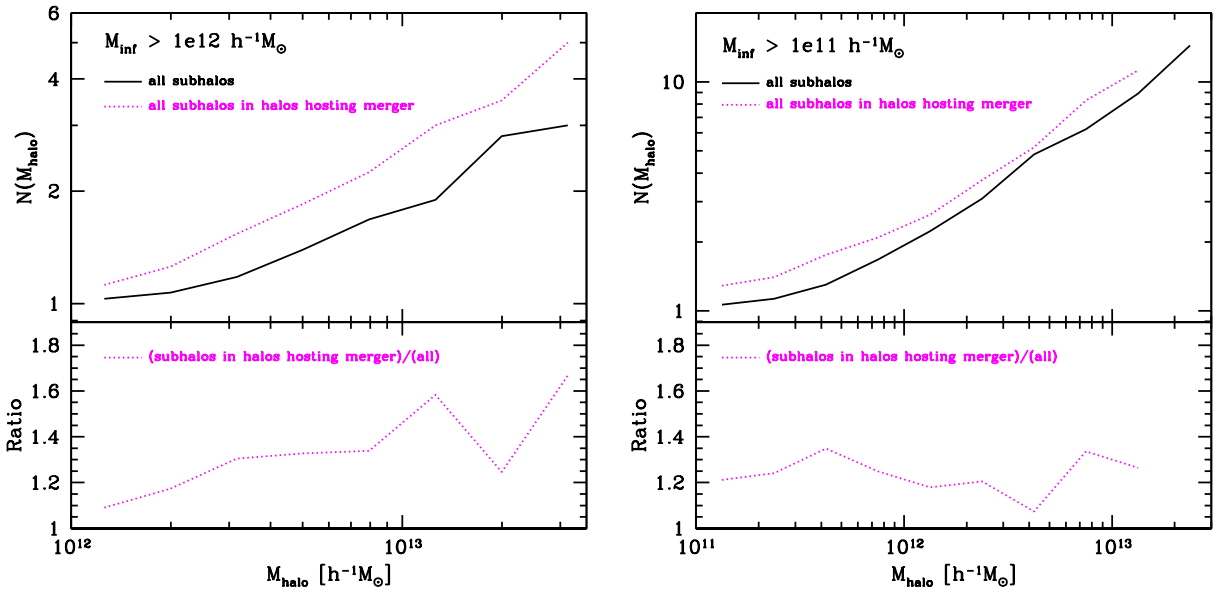

Figure 7.2: **Top Panels**: Halo Occupation Distribution (HOD) at $z = 2.6$ for all subhalos (solid curves) and subhalos in a halo hosting a recently merged subhalo (dotted curves). Shown are subhalos with $M_{\rm inf} > 10^{12}\,h^{-1}\,{\rm M}_\odot$ and mergers occurring within 130 Myr (left), and $M_{\rm inf} > 10^{11}\,h^{-1}\,{\rm M}_\odot$ and mergers occurring within 50 Myr (right). **Bottom Panels**: Ratio of the above HOD's of subhalos in a halo hosting a merger to that for all subhalos. There are more subhalos in halos with recently merged subhalos, and the effect is stronger for more massive subhalos. For recently merged massive subhalos, which show a strong increase in small-scale clustering, the relative subhalo excess in halos with mergers tends to increase with halo mass. Similar trends persist at all redshifts we probe.

7.4.1 HOD of Subhalos

Figure 7.2 shows the HOD of subhalos (central and satellite) at $z = 2.6$ (corresponding to the populations in Fig. 7.1) for all subhalos and for all subhalos within a halo hosting a recently merged subhalo. Clearly, halos hosting subhalo mergers tend to have more subhalos. This increase occurs for both our high and low mass samples and for all redshifts we probe. For massive subhalo mergers the increase is larger and tends to rise to larger halo mass, which enhances the cross-correlation for mergers. Although lower mass subhalo mergers also have more subhalos per halo, the relative number does not change strongly with increasing halo mass — host halo mass does not significantly influence merger statistics.

Note that we expect some increase in the number of subhalos above a given mass threshold from mergers of subhalos just below the mass threshold, while mergers between subhalos above the threshold decrease the number of subhalos. Which effect wins out requires detailed simulations such as ours.

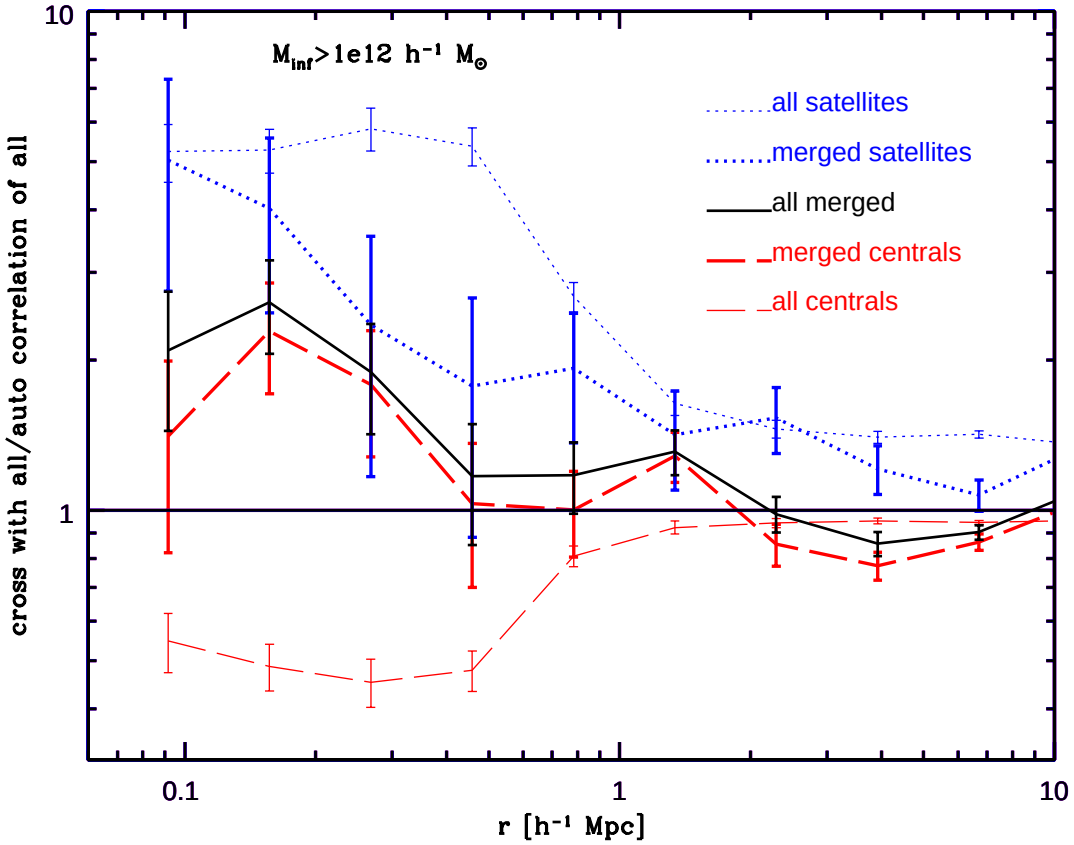

Figure 7.3: Cross-correlation of the component populations (merged and all satellites, merged and all centrals) with all subhalos (the latter with $M_{\rm inf}$ matched distribution), at $z = 2.6$ for $M_{\rm inf} > 10^{12}\,h^{-1}\,{\rm M}_\odot$, corresponding to the left hand panel of Fig. 7.1. Top to bottom at far left are $\xi_{\rm sat-all}/\xi_{\rm all}$, $\xi_{\rm sat,merged-all}/\xi_{\rm all}$, $\xi_{\rm all,merged-all}/\xi_{\rm all}$, $\xi_{\rm cen,merged-all}/\xi_{\rm all}$, $\xi_{\rm all-all}/\xi_{\rm all}$, $\xi_{\rm cen-all}/\xi_{\rm all}$.

7.4.2 Central & Satellite Cross-Correlation

We now distinguish between contributions from satellite and central subhalos to the correlation function and HOD of mergers and the general population. There are inherent subtleties in this breakdown; as mentioned earlier, the identification of satellite vs. central subhalos is not entirely clear-cut at these masses and redshifts. In particular, one type can switch to another, and often does for mergers. Also, other tracking schemes might alter the relation between central and satellite assignments we use. If switched satellite mergers are assigned as centrals, this will of course not change the observed clustering signal but would alter where the contribution from our switches shows up in the breakdown of central and satellite effects.

Figure 7.3 shows the ratios of the cross-correlations for central mergers and satellite

mergers to the auto-correlation of the full sample (the left hand side of Fig. 7.1 above), for $M_{\rm inf} > 10^{12}\,h^{-1}\,{\rm M}_{\odot}$ subhalos at $z = 2.6$. The ratios of the cross-correlations of the full central and satellite populations to the full subhalo population are also shown. As before, the full population is matched in $M_{\rm inf}$ to the merged population. In general, satellites have a larger cross-correlation with all subhalos compared to centrals because the minimum host halo mass for a subhalo of a given mass is larger for a satellite than a central subhalo (increasing the large-scale clustering), and a satellite will always have a central in its halo but not vice versa (increasing the small-scale clustering). The satellite and central cross-correlations must be summed, weighted by their population's fraction of the full population to get the full cross-correlation.

The merged central and merged satellite contributions to the cross-correlation differ from their counterparts in the full population. Generally, the merged satellites have decreased small-scale clustering, relative to all satellites, while merged centrals have enhancement relative to all centrals. In addition, satellites comprise a $\sim 1.5 - 2\times$ larger fraction of the merger population than of the full subhalo population ($N_{\rm sat,merged}/N_{\rm cen,merged} \neq N_{\rm sat}/N_{\rm cen}$), changing the relative weights satellite and central contributions in the full cross-correlation.[7] These three trends persist at all redshifts and subhalo masses, but their relative strengths vary to give the different behavior seen in Fig. 7.1 for different subhalo mass cuts.

7.4.3 Central & Satellite HOD

We can employ this central vs. satellite split for the HODs as well. Figure 7.4 shows the HODs for two mass ranges and two redshifts: at left is the HOD for high-mass subhalo mergers at $z = 2.6$, corresponding to Fig. 7.1 (left), and at right is the HOD corresponding to the less massive subhalos at $z = 1$, for a longer (230 Myr) merger time interval. The cross- to auto-correlation ratio for this latter sample is similar to that shown in Fig. 7.1 (right), but we show the results at lower redshift to illustrate the trends we see over a larger host halo mass range.

Figure 7.4 (left) shows that *high-mass* recently merged central subhalos occupy halos with an excess of satellites (relative to the average) at most host halo masses (dotted curve). The physical extent of the enhancement, $\sim 300\,h^{-1}\,{\rm kpc}$, coincides with the virial radius of the most massive halos ($\sim 4 \times 10^{13}\,h^{-1}\,{\rm M}_{\odot}$) in our simulations at $z \sim 2.6$. The enhancement of the satellite population in halos hosting recent central mergers is not as large for lower mass subhalos (the curve for this quantity is almost indistinguishable from that of the full satellite population, thus it is not shown in Fig. 7.4 right). This corresponds to the weakened enhancement, and decrement, in Fig. 7.1. In terms of the central vs. satellite subhalo breakdown, the increased satellite number for recently merged central subhalos has the strongest correspondence with increased small-scale clustering.

The other trends that we see appear across our redshift and mass regimes. For a fixed

[7] Since satellites preferentially reside in higher mass halos, if the recently merged population is comprised of a higher fraction of satellites, it will also exhibit enhanced large-scale clustering.

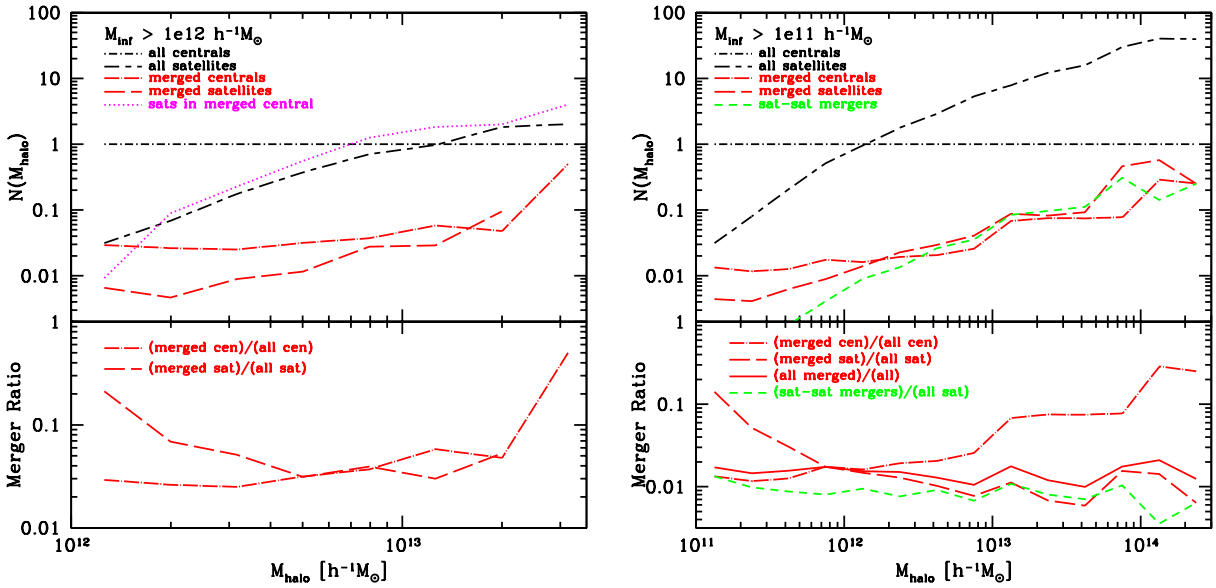

Figure 7.4: Halo Occupation Distribution (HOD), broken down in terms of merger types: centrals, satellites, recently merged centrals, and recently merged satellites. **Top Left**: Subhalos with $M_{\rm inf} > 10^{12}\,h^{-1}\,{\rm M}_\odot$ at $z = 2.6$, corresponding to the left hand side of Fig. 7.1 and the component contributions in Fig. 7.3. The merger time interval is 130 Myr. Also shown is the HOD for satellites in halos with a recently merged central. **Bottom Left**: Ratio of HOD's of recently merged centrals to all centrals and of recently merged satellites to all satellites. **Top Right**: Subhalos with $M_{\rm inf} > 10^{11}\,h^{-1}\,{\rm M}_\odot$ at $z = 1$ and mergers occurring within 230 Myr, with cross-correlation similar to the 250 Myr interval in Fig. 7.1 right at $z = 2.6$. The HOD is also shown for satellite-satellite mergers. No strong excess is seen for satellites in halos with a recently merged central (not shown). **Bottom Right**: Ratio of HOD's of recently merged centrals to all centrals, recently merged satellites to all satellites, and satellite-satellite mergers to all satellites. Also shown is the ratio of HOD's of subhalo mergers to all subhalos (regardless of type). Satellite-satellite mergers, and subhalo mergers (regardless of type), show no strong dependence on halo mass, though our statistics are not sufficient to rule out a cutoff at the highest mass.

subhalo mass cut, the fraction of centrals that have experienced a recent merger increases with halo mass. This causes an enhancement of the central merger cross-correlation with the full population, since the rise in central merger fraction with halo mass gives the overall recently merged central population proportionally more satellites when all halo masses are summed.

It is worth noting two points about the relative increase of central mergers in higher mass halos. The increase itself might be surprising, as both the number of satellites and the dynamical friction timescale increase approximately linearly with halo mass. One expects that the increase of possible satellites and the slowdown of their approach to the center would then cancel, rather than producing increased numbers of central mergers. Looking instead at merger parent types, we found that the central-satellite merger HOD does not increase as steeply as the merged central HOD. Central mergers in the highest mass halos are often satellite-satellite mergers whose child is a central (switches), rather than central-satellite mergers. While this is a small fraction (3%) of all central mergers, it is a larger fraction of those in high-mass halos.

Secondly, the increase of central mergers to higher mass halos suggests a possible error from neglecting high mass halos which are too rare to occur in the simulation volume. Their effect can be estimated analytically by extrapolating the central merger fraction as a function of halo mass, using the halo model to find the relative contribution of merged and all centrals to the cross-correlation at some given radius, and seeing how this changes as larger masses are included. We find that, on average, neglecting halos more massive than those found in our simulations only causes a small change in the cross-correlation of centrals with the full population. However, our largest halos are quite rare, and so the merger fraction in them does not always tend to the average. The rise in central merger fraction with halo mass is largest for our $M_{\rm inf} > 10^{11}\,h^{-1}\,{\rm M}_\odot$ subhalos and thus of most concern. As a check, we averaged our cross-correlation for the smaller simulation over several outputs to confirm the trends we see in Fig. 7.1 (right). The output to output variation does average to this trend, but individual outputs can show different sign effects, albeit with significant error bars. This is especially true at lower redshift, where our imperfect sampling of high mass halos plays a larger role. It might be counter-intuitive that $300\,h^{-1}\,$kpc clustering is not very well measured in a $100\,h^{-1}\,$Mpc cube, but the peak of the power spectrum is at large scales in a ΛCDM model and the scatter in the cross-correlation is driven by the contribution from rare, massive halos which host many satellites.

We now turn to the satellite HOD. Figure 7.4 (bottom) shows that the fraction of merged satellites to all satellites decreases with increasing host halo mass (long-dashed curve). However, a significant fraction of merged satellites are satellite-central switches, which dominate in low-mass halos where a central and satellite are more likely to be comparable in mass and thus able to switch. Additionally, some merged satellites are central-satellite mergers which then fell into the host halo. Examining instead merger parent type, satellite-satellite mergers are essentially a constant fraction of satellite subhalos across all halo masses (short-dashed line). We see a slight increase for massive host halos at $z = 2.6$ and no increase at $z = 1$. Additionally, we see weak evidence for a cutoff in the satellite-satellite merger HOD for the

most massive halos, consistent with the idea that increasing relative velocities of satellites in the most massive halos cuts off satellite-satellite mergers (Makino & Hut 1997). However, the high-mass halo statistics are poor in our modest simulation volumes.

A simple argument can be made which reproduces the observed scaling of the number of satellite-satellite mergers with the overall satellite population, based upon the HOD scaling with increasing halo mass and volume. For satellites with random orbital parameters in a halo of a fixed mass, the satellite-satellite merger probability will scale as number density squared ($n_{\rm sat}^2$), so the fraction of satellites undergoing satellite-satellite mergers scales as $n_{\rm sat}$. For halos above a few times the mass of a given satellite population, the number of satellites scales with the halo mass (e.g., Kravtsov et al. 2004a), which scales approximately with the halo volume, so $N_{\rm sat} \propto M_{\rm halo} \propto V_{\rm halo}$. Thus, $n_{\rm sat} \approx$ constant, so the satellite-satellite merger fraction remains roughly constant.

Finally, the lower right panel of Fig. 7.4 shows that when we do not split by type, the subhalo merger fraction is essentially independent of halo mass. Again, this contradicts the frequently expressed intuition that mergers are less frequent in higher mass halos, though we caution that our statistics are poor for cluster-mass halos, and we are working at high redshift.

7.4.4 Radial Distribution Profile

Figure 7.5 shows the other ingredient required to predict clustering: the (stacked) satellite radial distribution profile, for subhalos with $M_{\rm inf} > 10^{11}\,h^{-1}\,{\rm M}_\odot$ at $z = 2.6$ and a merger time interval of 50 Myr. We choose this mass regime and redshift because the high temporal resolution allows us to accurately identify the locations of mergers, though the behavior across all our mass and redshift regimes is consistent with these results. Shown are the profiles for all satellites, recently merged satellites, recently merged satellites from satellite-satellite parents (because of switches), and the NFW (Navarro et al. 1996) halo density profile. We normalize the density distributions to the average value within $2r_{200c}$.[8] We use $2r_{200c}$ because an appreciable fraction of satellite mergers occur just outside r_{200c} given the highly aspherical geometry of halos at this mass and redshift regime. The satellite subhalo profile well-traces the NFW profile from r_{200c} down to $0.2r_{200c}$, and shows no dependence on subhalo mass, consistent with the distribution of subhalos selected on infall mass at $z = 0$ of Nagai & Kravtsov (2005).[9] The deficit below $0.2\,r_{200c}$ is a result of finite spatial resolution, tidal disruption of subhalos near the halo center, and subhalos temporarily disappearing from the sample during a fly-by (see Fig. 1 of Chapter 6).

As Fig. 7.5 shows, the radial distribution profile of satellite mergers approximately

[8]We calculate the halo virial radius, r_{200c}, the radius within which the average density is 200× the critical density, from the FoF($b = 0.168$) mass by first converting to M_{200c} assuming a spherical NFW density profile, and then taking $M_{200c} = 200\frac{4\pi}{3}\rho_c r_{200c}^3$.

[9]When selecting subhalos on instantaneous bound mass, more massive halos are preferentially biased to the outer regions of a halo, since mass stripping leaves few massive subhalos in the inner region of a halo (see Nagai & Kravtsov 2005).

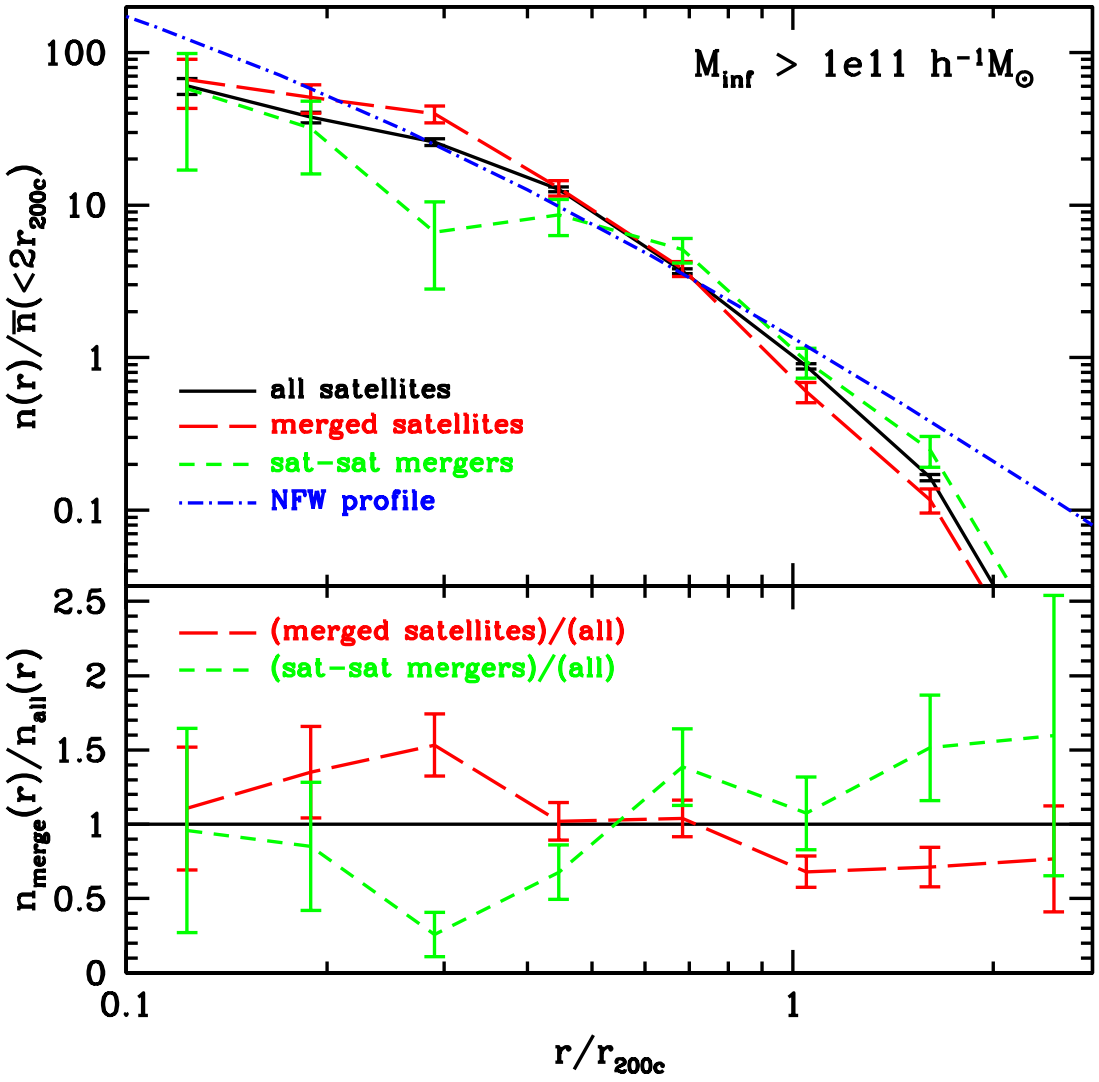

Figure 7.5: **Top**: Halo radial distribution profile of satellites with $M_{\rm inf} > 10^{11}\,h^{-1}\,{\rm M}_\odot$ at $z = 2.6$, for all satellites (solid curve), recent mergers (long-dashed curve), and mergers from satellite-satellite parents (short-dashed curve). The merger time interval is 50 Myr. Also shown is the halo NFW density profile (dot-dashed curve), using an NFW concentration of $c = 4$, typical for halos at this mass and redshift. Density distributions are normalized to the average density of the population within $2r_{200c}$. **Bottom**: Ratio of the recently merged satellite normalized density to that of all satellites (long-dashed curve) and the same for recent mergers from satellite-satellite parents (short-dashed curve). We find no dependence of these results on satellite infall mass or redshift.

follows that of the entire satellite population. The profile can be thought of as a measure of how satellite mergers correlate with centrals, bearing in mind that the distances are scaled by the halo virial radius. Relative to the density distribution of all satellites, recently merged satellites have a slightly more concentrated profile, with enhanced probability of being at $20\% - 40\%$ of the virial radius (long-dashed curve). This produces a relative deficit in clustering of recently merged satellites out to the halo virial radius. Considering instead recently merged centrals, we find that the profile of satellites in halos with a recently merged central traces the general satellite population without significant deviation (not shown).

While recently merged satellites exhibit a more concentrated profile, mergers between satellite-satellite subhalos preferentially occur in halo outskirts and are comparatively less common in the central regions (short-dashed curve). Thus, the enhanced probability of finding recent satellite mergers at small scales is driven by switches (when a satellite merges with a central and results in a satellite).

7.5 Merger Pairs

While we have focused on measuring merger clustering via the cross-correlation of mergers with the general population, we can also measure directly the statistics of our limited number of merger pairs and distinguish the different origins for the pair members. We focus on pairs of subhalos within $250\,h^{-1}\,\mathrm{kpc}$ which have both undergone a merger within the last ~ 250 Myr. In all such cases of close merger pairs, both subhalos inhabit the same halo. These pairs are quite rare: at $z = 2.6$, there are 24 (2) per $(100\,h^{-1}\,\mathrm{Mpc})^3$ for $M_{\rm inf} > 10^{11}(10^{12})\,h^{-1}\,\mathrm{M}_\odot$, while at $z = 1$ there are 2 per $(100\,h^{-1}\,\mathrm{Mpc})^3$ for $M_{\rm inf} > 10^{11}\,h^{-1}\,\mathrm{M}_\odot$ and none at the higher mass.

For two subhalos within the same halo, the two types of possible pairings are satellite-central and satellite-satellite. For $M_{\rm inf} > 10^{12}\,h^{-1}\,\mathrm{M}_\odot$, all pairs are composed of satellite-central subhalos, while for $M_{\rm inf} > 10^{11}\,h^{-1}\,\mathrm{M}_\odot$, 25% of close merger pairs are satellite-satellite subhalos. In all cases, the central-satellite pairs arise when a satellite-central merger occurs simultaneously with a satellite-satellite merger in a single halo. For the rarer cases of satellite-satellite merger pairs, two-thirds of the recently merged satellites arise from satellite-satellite parents within a halo, and one third arise from a satellite-central merger (a switch).

7.6 Summary & Discussion

Using high-resolution dark matter simulations in cosmological volumes, we have measured the small-scale spatial clustering for massive subhalo mergers at high redshift and compared against the clustering of the general subhalo population of the same mass. We have described the merger populations in terms of their HOD and radial profile, including the contributions of centrals vs. satellites. We assign subhalos their mass at infall, as a proxy for galaxy stellar mass, but make no further attempt to model the baryonic component. We

consider mergers with < 3:1 infall mass ratios, motivated by the expectation that these can trigger activity such as quasars or starbursts. Our main results are:

- At $z = 2.6$, recently merged, massive ($M_{\rm inf} > 10^{12}\,h^{-1}\,{\rm M}_\odot$) subhalos exhibit enhanced small-scale clustering compared to random subhalos with the same infall mass distribution. This excess peaks at $100 - 300\,h^{-1}\,{\rm kpc}$, while the clustering exhibits a dip at slightly larger scales. Lower mass subhalos ($M_{\rm inf} > 10^{11}\,h^{-1}\,{\rm M}_\odot$) exhibit signs of a small rise in clustering at $< 100\,h^{-1}\,{\rm kpc}$, with a deficit at slightly larger scales, though our results are noisy in this regime. We find similar behavior at $z = 1$. The merger signal weakens rapidly with time, vanishing for time intervals longer than 500 Myr after the merger.

- Considering their HOD, halos hosting recently merged subhalos tend to have more subhalos. This enhancement is stronger for more massive subhalos and exhibited growth with halo mass.

- Breaking the contributions to the cross-correlation into those from satellite and central subhalos, the recently merged massive centrals, which show the largest enhancement of small-scale clustering, preferentially occupy halos with more satellites. More generally, recently merged centrals occupy higher mass halos and recently merged satellites occupy lower mass halos with fewer (perhaps no other) satellites. The resulting increase for the central cross-correlation, decrease for the satellite cross-correlation, and change in the ratio of their contributions combine to produce the cross clustering enhancement or decrement.

- For the range of halo masses we probe, the (type-independent) subhalo merger fraction is independent of host halo mass. We find similar behavior for the halo mass dependence of satellite-satellite mergers, that the fraction of satellites that experience a merger with another satellite does not depend on halo mass, except perhaps in our poorly sampled largest mass halos ($\sim 10^{14}\,h^{-1}\,{\rm M}_\odot$).

- The radial profile of recently merged satellites roughly follows that of the entire satellite population, which also follows the halo density profile out to the virial radius. Satellite-satellite mergers preferentially occur in the outer regions of a halo.

- Mergers defined via major mass gain exhibit a strong small-scale clustering enhancement because significant mass gain is caused by interactions with a neighboring subhalo. However, in these cases the neighbor exists both before and after the "merger" (there is no coalescence), and the major mass gain criterion does not correspond to dynamically disturbed subhalos. Thus, we do not expect these objects to correlate with active galaxies.

Our measured subhalo merger enhancement suggests that, for populations with the same stellar mass at high redshifts, recent galaxy mergers should exhibit excess clustering

at small radius, with a possible decrement in clustering at slightly larger scales. This effect will persist for only a short period of time after the merger, with a stronger excess signal for galaxies of higher stellar mass. Measuring this small-scale cross-correlation (against a general population) requires a surprisingly large volume ($\gtrsim 100\,h^{-1}\,\mathrm{Mpc}$) because massive (satellite rich) halos contribute significant signal to the cross-correlation. Thus, a fair sample of rich halos is necessary for robust conclusions.

A comparison of the clustering of our mergers to observational phenomena is a nontrivial future step, since many merger observables depend on complex gas physics. Our results do not include whether the subhalos are gas-rich or not, though at the high redshifts we examine, we expect almost all galaxies to be gas-rich. Satellites can be stripped of much of their gas during infall (e.g., Dolag et al. 2009; Saro et al. 2008), though we have considered relatively massive satellites which have short infall times and thus experience less gas stripping.

Time scales for observables after a merger also have large uncertainty and scatter. For example, an optical quasar might appear only $\sim$ 1 Gyr after the merger (e.g., Hopkins et al. 2008b; Springel et al. 2005a), by which time the enhanced clustering that we see has disappeared. X-ray signals might appear sooner.[10] Starbursts (SMG, LBG, ULIRG) might also commence more rapidly after a merger (e.g., Cox et al. 2008) and thus appear a more promising analog to the effects we find here.

[10]We thank F. Shankar for suggesting this.

Chapter 8

What determines satellite galaxy disruption?

Abstract

In hierarchical structure formation, dark matter halos that merge with larger halos can persist as subhalos. These subhalos are likely hosts of visible galaxies. While the dense halo environment rapidly strips subhalos of their dark mass, the compact luminous material can remain intact for some time, making the correspondence of galaxies with severely stripped subhalos unclear. Many galaxy evolution models assume that satellite galaxies eventually merge with their central galaxy, but this ignores the possibility of satellite tidal disruption. We use a high-resolution N-body simulation of cosmological volume to explore satellite galaxy merging and disruption criteria based on dark matter subhalo dynamics. We explore the impact that satellite merging and disruption has on the Halo Occupation Distribution and radial profile of the remnants. Using abundance matching to assign stellar mass to subhalos, we compare with observed galaxy clustering, satellite fractions, and cluster satellite luminosity functions, finding that subhalos reproduce well these observables. Our results imply that satellite subhalos corresponding to $> 0.2\,L_*$ galaxies must be well-resolved down to $1 - 3\%$ of their mass at infall to robustly trace the galaxy population. We also explore a simple analytic model based on dynamical friction for satellite galaxy infall, finding good agreement with our subhalo catalog and observations.

8.1 Introduction

In the standard picture of galaxy formation, galaxies form at the centers of dark matter halos as baryons cool and contract toward the minimum of a halo's potential well (White & Rees 1978; Blumenthal et al. 1986; Dubinski 1994; Mo et al. 1998). But halos are not isolated objects: they merge over time, and smaller halos can survive as substructure halos

(subhalos) of larger halos after infall (Ghigna et al. 1998; Tormen et al. 1998; Moore et al. 1999; Klypin et al. 1999). Thus, while galaxies form within distinct host halos at high redshift, as the Universe evolves galaxies then correspond directly to dark matter subhalos (and since galaxies can be centrals or satellites, in our terminology a "subhalo" refers to a satellite substructure or the central halo).

The evolution of subhalos involves more complicated dynamics than the formation of halos themselves. Satellite subhalos experience severe mass stripping as they orbit, and dynamical friction causes their obits to sink toward halo center (Ostriker & Tremaine 1975). The evolution of galaxies is even more complex, involving gas dynamics, star formation, and various forms of feedback. Thus, the precise evolutionary relation between galaxies and subhalos remains uncertain. In particular, what is the relation between galaxy stellar mass and subhalo dark mass? Do satellite galaxies experience appreciable star formation after infall? How long after infall does a satellite galaxy survive, and what defines its final fate? How much of its stellar mass is funneled into the central galaxy in a merger, as opposed to tidally disrupting into Intra-Cluster Light (ICL)?

Various prescriptions exist to map galaxies onto dark matter subhalos. The simplest is based on subhalo abundance matching (SHAM), which assumes a monotonic relation between subhalo mass or circular velocity and galaxy stellar mass, populating subhalos such that one reproduces the observed stellar mass function (SMF; Vale & Ostriker 2006; Conroy et al. 2006; Shankar et al. 2006). Alternately, semi-analytic models track the star formation histories of subhalos across time with empirically motivated analytic prescriptions (see Baugh 2006, for a recent review). These methods all involve assumptions regarding satellite galaxy star formation after infall, the correspondence of galaxies with subhalos in the case of severe mass stripping, and the eventual fates of satellite galaxies.

Most models assume that all satellite galaxies eventually merge with their central galaxy. Indeed, infalling satellites have long been thought to affect the mass and morphological evolution of central galaxies (Hausman & Ostriker 1978). However, galaxy clusters are observed to contain an appreciable amount of stellar material in the form of ICL, though given its low surface brightness, constraints on the ICL vary considerably, from $5-50\%$ of the total cluster light (Lin & Mohr 2004; Zibetti et al. 2005; Gonzalez et al. 2007; Krick & Bernstein 2007). Additionally, ICL has been observed to contain significant structure, including tidal streams (Mihos et al. 2005). Thus, some satellite galaxies are at least partially, or perhaps entirely, disrupted into the ICL.

In simulations, the criteria for subhalo merging and disruption are influenced by mass and force resolution. Insufficiently resolved subhalos will disrupt artificially quickly, leading to the problem of "over-merging" (Klypin et al. 1999). A number of authors have examined in detail mass stripping from satellite subhalos over time (e.g., Maciejewski et al. 2009), however, using a fixed mass resolution limit for all subhalos, regardless of their infall mass, leads to lower mass subhalos becoming (artificially) disrupted more quickly. Cosmological N-body simulations are now attaining sufficient mass resolution to track subhalos through many orbits and extreme mass stripping, in some cases to masses much smaller than the luminous mass of the galaxies they would host. At infall, the dark mass of a subhalo is

an order of magnitude higher than its stellar mass, so tidal stripping of mass from subhalos cannot correspond directly to stellar mass stripping of its galaxy. Thus, in using dark matter subhalos to track galaxies, one must be careful both to treat subhalo merging and disruption in a self-consistent manner not dependent merely on numerical resolution, and to calibrate the point at which the galaxies they host become merged or disrupted.

A variety of schemes have been used to define satellite galaxy merging and disruption via subhalos in simulations. Under the assumption that a galaxies survives as long as its subhalo does, Wetzel et al. (2009a,b) use an absolute mass threshold for all subhalos, corresponding to their resolution limit, similar to Kravtsov et al. (2004a), whose model also implies that subhalos coalesce if their centers come within $50\,h^{-1}\,\mathrm{kpc}$. Several analyses assume that a satellite galaxy survives the disruption of its subhalo and eventually merges with its central galaxy by imposing an analytic infall timescale to a galaxy after subhalo disruption (Springel et al. 2001; Kitzbichler & White 2008; Saro et al. 2008; Moster et al. 2009). Alternately, Stewart et al. (2009) allow a satellite galaxy to merge before its subhalo is disrupted. They assume that a galaxy's baryonic mass is coupled to the 10% most bound mass of its subhalo and define satellite merging when a satellite subhalo has lost more than 90% of its mass at infall. Yang et al. (2009) consider a model where the survival probability of a satellite subhalo is a (decreasing) function of its infall mass to host halo mass ratio.

Other criteria have been used in purely semi-analytical models for the evolution of subhalos. Zentner et al. (2005) and Taylor & Babul (2004) consider a satellite subhalo to be tidally disrupted when the mass of the subhalo has been stripped to a value less than the mass within $a_{\rm dis}r_s$, where r_s is the subhalo's NFW (Navarro et al. 1996) scale radius at infall, with $a_{\rm dis} = 1$ (Zentner et al. 2005) or $a_{\rm dis} = 0.1$ (Taylor & Babul 2004). Assuming a typical halo concentration of $c = 10$, this implies that satellite subhalos will disrupt at 13% or 0.3% of their infall mass in the models, respectively – an order of magnitude difference. As an alternative to tidally disrupting, Zentner et al. (2005) consider the satellite subhalo merged with the center of its halo if it comes within 5 kpc. Applying the model of Zentner et al. (2005) to the build-up of the ICL, (Purcell et al. 2007) allow satellite disruption to begin at $\sim 20\%$ of infall mass (see also Monaco et al. 2006; Conroy et al. 2007b, for models of tidal disruption into the ICL).

Finally, mass loss criteria have also been applied to modelling dwarf-spheroidal galaxies in N-body simulations. Peñarrubia et al. (2008) find that dwarf satellites start to lose stellar mass to tidal stripping after 90% dark mass loss, but full disruption occurs only after $> 99\%$ dark mass loss. Macciò et al. (2009) find good agreement between their semi-analytic model and the Milky Way satellite luminosity function using $a_{\rm dis} = 0.5-1$, corresponding to $5-13\%$ of the infall mass remaining.

Given the wide range in criteria for satellite merging and disruption, it is informative to explore the implications of various criteria and to test empirically which match well to the observed galaxy population. Thus, in this chapter we examine the extent to which galaxies can be mapped onto simulated dark matter subhalos throughout their evolution. We assign galaxy stellar masses and luminosities to subhalos by matching their number densities to observed galaxy samples. We examine the effects that different criteria for

merging and disruption have on the satellite populations, including the HOD and radial distribution profile. By comparing spatial clustering, satellite fractions, and cluster satellite luminosity functions to observations, we test the correspondence of galaxies to subhalos, and we constrain the criteria for satellite galaxy merging and disruption.

Before continuing, we clarify the possible fates of satellite galaxies. The methods by which galaxies become removed from the satellite population are to (1) coalesce with the central galaxy, (2) coalesce with another satellite galaxy, (3) orbit outside their host halo, or (4) tidally disrupt into the ICL. As noted above, many galaxy evolution models assume only (1). As we describe below, our method for tracking subhalos in simulations intrinsically incorporates (2) and (3). Thus, this chapter focuses on methods for removing satellite galaxies via (1) and (4). Since our tracking of dark matter subhalos does not unambiguously differentiate between these (and since both can occur simultaneously), we will use the term "removal" of satellite galaxies to indicate any mechanism that causes (1) or (4), which we refer to as "merging" and "disruption", respectively.

8.2 Numerical Methods

8.2.1 Simulations & Subhalo Tracking

To find and track halos and their subhalos, we use dark matter-only N-body simulations using the TreePM code of White (2002). To track subhalos with high resolution, we use a simulation of 1500^3 particles in a periodic cube with side lengths $200\,h^{-1}\,\mathrm{Mpc}$. For our ΛCDM cosmology ($\Omega_m = 0.25$, $\Omega_\Lambda = 0.75$, $h = 0.72$, $n = 0.97$ and $\sigma_8 = 0.8$), in agreement with a wide array of observations (Smoot et al. 1992; Tegmark et al. 2006; Reichardt et al. 2009; Dunkley et al. 2009), this results in particle masses of $1.64\times10^8\,h^{-1}\,\mathrm{M}_\odot$ and a Plummer equivalent smoothing of $3kpc$. Initial conditions were generated by displacing particles from a regular grid using 2LPT at $z = 250$ where the RMS is 20% of the mean inter-particle spacing. We stored 45 outputs evenly in $\ln(a)$ from $z = 10$ to 0, with an output time spacing of $\sim 600\,\mathrm{Myr}$ at $z = 0.1$, the main redshift of interest in this chapter. Given the limited volume of this simulation, and its implications for spatial clustering, we also use a separate simulation of 1500^3 particles of size $720\,h^{-1}\,\mathrm{Mpc}$ and a particle mass of $7.67\times10^9\,h^{-1}\,\mathrm{M}_\odot$ with the same cosmology and halo finder, though independent initial conditions. We use this larger simulation to populate our subhalo catalog onto a more accurate halo mass function with more accurate large-scale clustering. To examine the influence of cosmological parameters, we also populate our subhalo catalog into a simulation of 1024^3 particles of size $500\,h^{-1}\,\mathrm{Mpc}$ with $n = 1.0$ and $\sigma_8 = 0.9$. We explore the influence of simulation size and cosmology in §8.6.

Our subhalo finding and tracking details are discussed extensively in Chapter 6[1] , though we have implemented a number of improvements for better performance, as described below.

[1]While of similar mass resolution, the simulation here has larger volume and better force resolution than in Chapter 6.

We find subhalos by first generating a catalog of halos using the Friends-of-Friends (FoF) algorithm (Davis et al. 1985) with a linking length of $b = 0.168$ times the mean inter-particle spacing.[2] We keep all groups that have more than 50 particles, and halo masses quoted below are these FoF masses. Within these "(host) halos" we then identify "subhalos" as gravitationally self-bound aggregations of at least 50 particles bounded by a density saddle point, using a new implementation of the *Subfind* algorithm (Springel et al. 2001), where densities are smoothed over 32 nearest neighbors. The "central" subhalo is defined as the most massive subhalo within its host halo, and it includes all halo matter not assigned to "satellite" subhalos, which is typically $\sim 90\%$ of the mass of the host halo. Thus, every sufficiently bound halo hosts one central subhalo and can host multiple satellite subhalos. A subhalo position is that of its most bound particle, and we define the halo center as that of its central subhalo.

Each subhalo is given a unique child at a later time, based on its 20 most bound particles. We track subhalo histories across four consecutive outputs at a time since subhalos can briefly disappear during close passage with or through another subhalo. In an improvement to the tracking method of Chapter 6, we now interpolate positions, velocities, and bound masses of these temporarily disappearing subhalos so that our tracking scheme does not artificially underestimate the satellite population.

Also, as discussed in Chapter 6, subhalo histories often include cases of "switches": if a satellite becomes more massive than the central, it becomes the central while the central becomes a satellite. In these cases, there is typically not a well-defined single peak that represents the center of the halo profile, and the nominal center can switch back and forth across output times. To avoid ambiguity in assigning subhalo bound and infall mass, our tracking method now eliminates switches by requiring that once a subhalo is a central, it remains so until falling into a more massive halo. This history-based approach assigns as central the oldest subhalo in the host halo, which would typically correspond to the most massive and evolved galaxy, better mapping to how central galaxies are defined observationally. However, since this criterion is based on subhalo history, while *Subfind* only uses the instantaneous density field to define the central (most massive) subhalo, the two definitions of subhalo centrality are in conflict in a small fraction cases. In these cases, we defer to the history-based approach, and we swap the subhalo bound masses of the history-based central and *Subfind*-based central, such that the history-based central is always the most massive subhalo, and by extension the most massive galaxy. We find this produces more stable subhalo catalogs, in terms of individual mass histories and the resultant subhalo mass function.

[2]The longer linking length of $b = 0.2$ is often used, but it is more susceptible to joining together distinct, unbound structures and assigning a halo that transiently passes by another as a subhalo.

8.2.2 The Stellar Mass of Subhalos

Since our goal is to test the correspondence between subhalos and galaxies, a critical issue is how to relate stellar mass to a subhalo. The simplest prescription assigns stellar mass to a subhalo based on its instantaneous bound dark mass or maximum circular velocity. However, this method leads to satellite subhalos with significantly less concentrated radial distributions than seen for satellite galaxies around the Milky Way (Kravtsov et al. 2004b) or galaxy clusters (Diemand et al. 2004). Better agreement with observations has been found using semi-analytic models of star formation applied to subhalo catalogs (Springel et al. 2001; Diaferio et al. 2001), which correlate stellar mass to a subhalo's mass at the time the stellar component was assembled (before infall), thus indicating that it necessary to use subhalo mass histories to accurately assign stellar mass (Gao et al. 2004a).

The motivation for this approach comes from the following physical model. As a halo falls into a larger one and becomes a subhalo, tidal stripping quickly removes bound mass from the outer regions of the subhalo, giving rise to significant mass loss shortly after accretion. This behavior has been explored both in simulations (e.g., Diemand et al. 2007; Limousin et al. 2009; Peñarrubia et al. 2008; Wetzel et al. 2009a) and observationally through galaxy-galaxy lensing (Limousin et al. 2007; Natarajan et al. 2007, 2009). However, the galaxy, being more compact and at the center of the subhalo, remains intact longer. Thus, dark mass stripping does not directly correspond to stellar mass stripping. The subhalo's gaseous component – being more diffuse and readily affected by ram-pressure stripping, tidal shocks, and adiabatic heating in the hot group environment – quickly becomes stripped after infall, halting subsequent star formation in the satellite galaxy. Thus, galaxy stellar mass is expected to correlate with the subhalo's mass immediately before infall (Nagai & Kravtsov 2005).

Observationally, there are a variety of claims for the star formation efficiency of satellite galaxies, with significant systematic dependence on group definition or HOD parametrization, criteria for blue (star forming) vs. red (quenched) split, and inclination effects (see Skibba 2009, for a comparison of HOD color models). The HOD analysis of the Sloan Digital Sky Survey (SDSS) of Zehavi et al. (2005) implies few faint blue satellites, and that at higher luminosity blue satellites are $3-5$ times less common than red satellites in groups. Examining group catalogs from SDSS, Weinmann et al. (2009) find an appreciable fraction ($>20\%$) of satellites in groups are blue, and fit a simple fading model where star formation in satellites quenches ~ 2 Gyr after infall (see also Kang & van den Bosch 2008). Using a subhalo catalog with an analytic prescription for star formation and quenching, Wang et al. (2007b) find an exponential decay time for satellite star formation after infall of ~ 2.3 Gyr. At $z \sim 1$, the clustering results of Coil et al. (2008) imply that immediate star formation quenching at infall is likely too restrictive at higher redshift.

Hydrodynamic simulations also indicate short yet finite timescales for halting star formation. High-resolution SPH simulations at $z \sim 0$ indicate that satellite star formation can continue for up to 1 Gyr after infall (Simha et al. 2009). While the assumption that satellite gas accretion rates are significantly lower than those of central galaxies may break down

at $z > 1$ (Kereš et al. 2009), the significantly more recent infall times of satellites at high redshift mediates this concern. Promisingly, Nagai & Kravtsov (2005) find good agreement in comparing the radial profiles of subhalos in dark matter-only simulations selected on infall mass with galaxies selected on stellar mass in dark matter plus hydrodynamic simulations.

Despite the above uncertainties, attempts to use subhalo infall mass (or infall maximum circular velocity) to assign stellar mass have been successful at reproducing various observed galaxy properties at a range of redshifts (Berrier et al. 2006; Conroy et al. 2006; Vale & Ostriker 2006; Wang et al. 2006; Yang et al. 2009), and so this is the approach we use here. The success of this method may be a derivative of its implicit allowance for some star formation after infall, as we describe below. Furthermore, our analysis is restricted to $z < 1$, where the approximation of rapid quenching of star formation is most valid.

8.2.3 Assigning Infall Mass & Stellar Mass

Motivated by its expected correlation with stellar mass, our scheme for assigning subhalo infall mass, $M_{\rm inf}$, is as follows. Centrals subhalos are assigned $M_{\rm inf}$ as their current bound mass. This mass represents halo mass not bound to any satellite subhalos and so it should track the gas mass available to accrete onto the central galaxy. We assign to a satellite subhalo its mass when it fell into its current host halo (its subhalo mass when it was last a central subhalo). With the expectation that a subhalo merger corresponds to a galaxy merger, if two satellite subhalos merge, their satellite child is given the sum of their infall masses. Thus, our tracking scheme inherently incorporates stellar mass growth though satellite-satellite mergers, an often-ignored but non-trivial contribution to galaxy evolution (Wetzel et al. 2009a,b; Seek Kim et al. 2009). If a satellite subhalo's orbit brings it outside its host halo, thus becoming its own distinct smaller halo, the subhalo is assigned its satellite parent's infall mass during the output immediately following ejection, but is assigned its current bound mass for subsequent outputs if it remains a separate central subhalo.

We assign stellar mass to our subhalo catalog by using subhalo abundance matching (SHAM) such that by construction we recover the observed stellar mass function. We rank order our subhalo catalog by infall mass, and assign stellar mass such that $n(> M_{\rm inf}) = n(> M_{\rm star})$, using the observed stellar mass function of Cole et al. (2001). Figure 8.1 shows the $M_{\rm star} - M_{\rm inf}$ relation, for our full satellite subhalo catalog (no removal threshold) and for the maximal threshold for satellite removal we consider. Since the satellite fraction increases at lower mass, the discrepancy is strongest there, though the offset is comparable to the error in the observed stellar mass function (Cole et al. 2001). The star formation efficiencies in Fig. 8.1 are in good agreement with the constrains from weak lensing of Mandelbaum et al. (2006) and also agree with the Milky Way, which has stellar mass of 5×10^{10} $M_\odot$ and a dark halo mass of about 2×10^{12} $M_\odot$ (Binney & Tremaine 2008), making $M_{\rm star}/M_{\rm halo} \approx 3\%$. See Moster et al. (2009) for a detailed comparison of derived $M_{\rm star} - M_{\rm subhalo}$ relations in the literature.

Despite the seeming requirement for rapid satellite quenching after infall, SHAM does implicitly allow for satellite star formation. This is because we match stellar mass to satel-

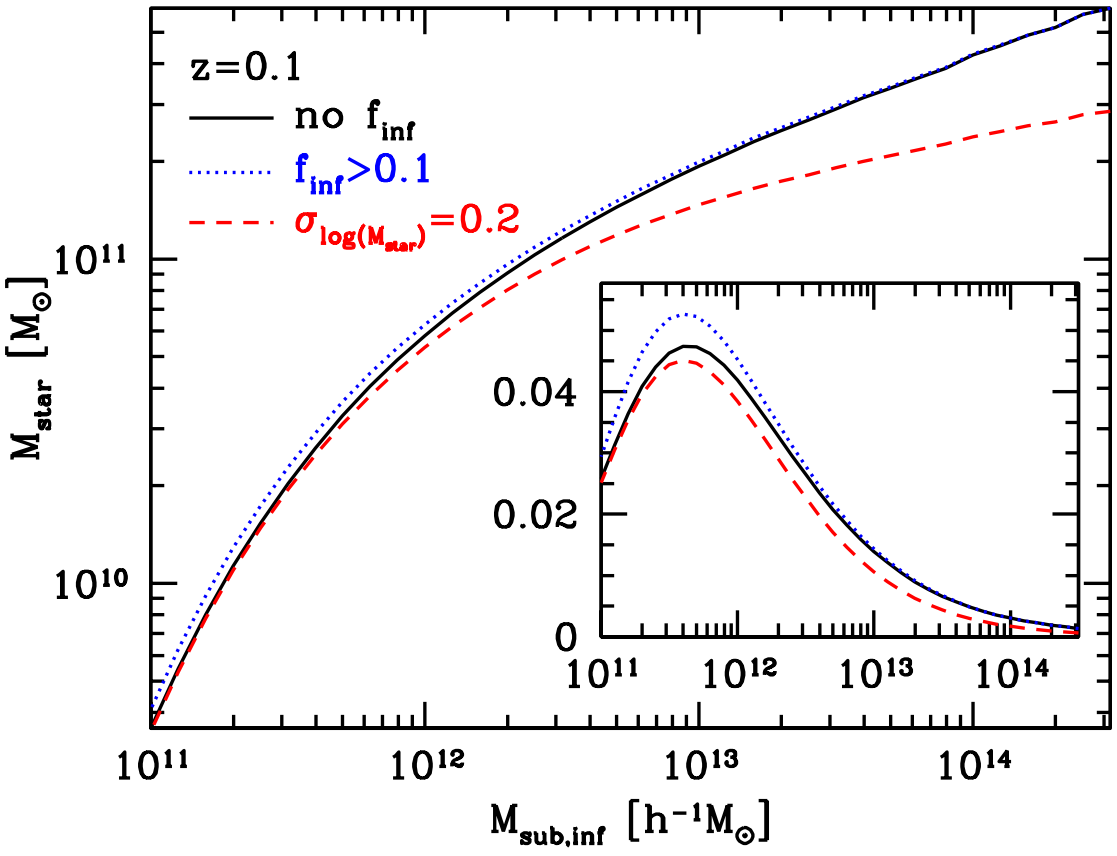

Figure 8.1: Relation between stellar mass, $M_{\rm star}$, and subhalo infall mass, $M_{\rm sub,inf}$, using subhalo abundance matching against the observed stellar mass function of Cole et al. (2001). Solid curve shows relation to our full subhalo catalog (no removal threshold), dotted curve shows the relation under our maximal threshold for satellite removal, and dashed curve shows the mean relation when using a log-normal 0.2 dex scatter in $M_{\rm star}$ at a fixed $M_{\rm sub,inf}$. Inset shows ratio $M_{\rm star}/M_{\rm sub,inf}$.

lites' infall mass at an observational epoch, not at the time of infall. At $z < 1$, satellite times since infall are typically several Gyr, and during that time satellite $M_{\rm inf}$ remains fixed. Thus, if there is appreciable evolution (growth) in the global $M_{\rm star} - M_{\rm inf}$ relation during that time, this will manifest itself as stellar mass growth for satellites. We have explored additional satellite star formation after infall by increasing all satellite infall masses by a fixed fraction, but we find that this is simply degenerate with increasing our satellite removal threshold given in the next section.

While the SHAM technique assumes a one-to-one correspondence between $M_{\rm inf}$ and $M_{\rm star}$, there may be considerable scatter in the relation. Fits to the spatial clustering of luminosity or stellar mass limited galaxies samples frequently require a "soft" turn on in the central galaxy occupation least they overpredict the large-scale clustering, which would naturally arise from scatter in observable at fixed (sub)halo mass. For example, Zheng et al. (2007), applying Halo Occupation Distribution (HOD) modeling to galaxies at $z \sim 0$ and ~ 1, find log-normal scatter in luminosity at fixed halo mass of $0.15-0.3$ dex, decreasing with increasing halo mass, consistent with the scatter of ~ 0.15 dex found in the group catalogs of Yang et al. (2008) at $z \sim 0$. Similarly, van den Bosch et al. (2007) find a lower limit of 0.2 dex scatter in halo mass at fixed luminosity from conditional luminosity function modeling, consistent with the results of More et al. (2009) from satellite kinematics. Tasitsiomi et al. (2004b) find good agreement in spatial clustering when matching subhalos to galaxies if they imposed significant scatter (0.6 dex) in luminosity at fixed subhalo maximum circular velocity.

To examine the importance of this scatter when comparing against observed galaxy samples, we also produce a stellar mass catalog by imposing a fixed 0.2 dex (log-normal) scatter in stellar mass at fixed subhalo infall mass such that we recover the observed SMF. The mean $M_{\rm star}$ at a fixed $M_{\rm inf}$ is shown as the dashed curve of Fig. 8.1. Since the mass function steeply falls with mass, introducing scatter biases $M_{\rm star}$ to a lower value at a fixed $M_{\rm inf}$. Higher scatter also causes a stellar mass threshold to correspond to a lower effective subhalo $M_{\rm inf}$ threshold.[3] This effect is particularly strong above $M_{\rm inf} \approx 10^{12}\,h^{-1}\,{\rm M}_\odot$, where the subhalo mass function starts to fall exponentially with mass.

We follow a similar approach to SHAM when we compare to observations of magnitude limited samples (§8.4), matching the number densities as $n(> M_{\rm inf}) = n(> L)$. The two assumptions – that stellar mass and luminosity are set by infall mass – are not fully consistent since luminosity may evolve even if stellar mass does not. However, it is not unnatural to assume the rank ordering is preserved in a population sense.

[3]This is not immediately apparent in Fig. 8.1, where it might appear that introducing scatter causes *increased* effective $M_{\rm inf}$ at fixed $M_{\rm star}$. This is because we show the mean $M_{\rm star}$ at a given $M_{\rm inf}$, which is qualitatively different than the mean $M_{\rm inf}$ at a given $M_{\rm star}$.

8.3 Impact of Satellite Removal

As a subhalo orbits in its host halo, dynamical friction removes energy from its orbit, bringing it closer to the central galaxy, while tidal forces strip its mass. While the satellite galaxy is expected to retain its stellar mass throughout most of the subhalo's mass stripping, eventually (though possibly in longer than a Hubble time) the galaxy will become removed from the satellite population, either from merging with the central galaxy or becoming disrupted into the diffuse ICL (or both). We now examine the impact different removal criteria have on the satellite population. We first focus on physically informative properties in the context of the halo model (Seljak 2000; Peacock & Smith 2000; Berlind & Weinberg 2002; Cooray & Sheth 2002), including the HOD and radial profile. However, since these are not direct observables, we reserve detailed comparisons with observations, via spatial clustering and satellite fractions, to the next section.

As described in the introduction, various prescriptions for satellite subhalo removal have been used. We focus primarily on the one used most often in previous work, which is also the most straightforward given our tracking: remove subhalos where the instantaneous bound mass to infall mass ratio, $f_{\rm inf} = M_{\rm bound}/M_{\rm inf}$, falls below some threshold. While dark matter-only simulations do not incorporate the complex hydrodynamics involved in galaxy evolution, if a satellite galaxy's gas is stripped before its stellar component, then it is conceivable that a simple criterion on subhalo dark matter stripping yields a good approximation for galaxy stellar mass removal since both experience purely gravitational interactions. We examine a range in threshold $f_{\rm inf}$ from $0.01-0.1$, which as we show in §8.4 brackets the observations, and even subhalos stripped to $f_{\rm inf} = 0.01$ remain well-resolved in the mass ranges we consider below. We refer to our subhalo catalog with no removal threshold as the "full" tracking model. Based on convergence tests, our subhalo catalog at $z = 0.1$ is robust to artificial disruption down to $\sim 10^{11.5}\,h^{-1}\,{\rm M}_\odot$, so the full tracking model serves as an upper limit to the satellite population. We explore different removal criteria in §8.7.

8.3.1 Halo Occupation Distribution

Figure 8.2 (top) shows the Halo Occupation Distribution (HOD) for our full tracking model ("no $f_{\rm inf}$") and for different minimum $f_{\rm inf} = M_{\rm bound}/M_{\rm inf}$ thresholds. We fit the HOD to

$$N_{\rm sat} = \left(\frac{M_{\rm halo}}{M_1}\right)^{\gamma} e^{-M_{\rm cut}/M_{\rm halo}} \tag{8.1}$$

with M_1, $M_{\rm cut}$ and γ as free parameters. The slope, γ, is given in Fig. 8.2 for each value of $f_{\rm inf}$. Raising the threshold for satellite removal, $f_{\rm inf}$, affects satellites more in higher mass halos, leading to a shallower slope. As the threshold increases, the HOD shoulder also becomes broader, meaning that more halos host only one galaxy. This indicates that satellite subhalos of a given $M_{\rm inf}$ are stripped more in higher mass halos, because of the stronger tidal fields and longer dwell times. This implies that the details of modeling satellite galaxy removal are more critical in cluster-mass halos than in lower mass groups.

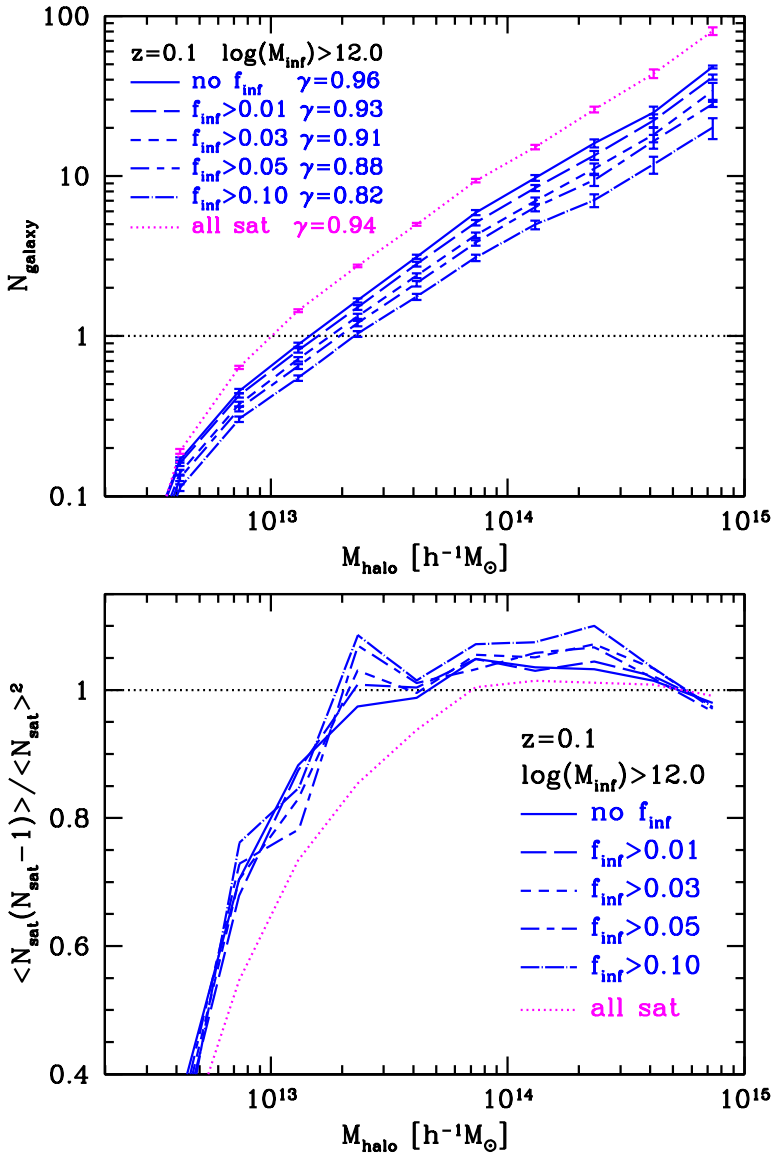

Figure 8.2: **Top**: Halo Occupation Distribution (HOD) for satellite subhalos with $M_{\rm inf} > 10^{12}\,h^{-1}\,{\rm M}_\odot$ ($M_{\rm star} > 10^{10.8}$ ${\rm M}_\odot$, $L > 0.6\,L_*$), for different minimum removal thresholds, $f_{\rm inf} = M_{\rm bound}/M_{\rm inf}$. Solid curve shows all resolved satellites, regardless of mass stripping ("no $f_{\rm inf}$"), while dotted curve shows all satellites ever accreted, even if they fall below the resolution limit (a model in which satellites never merge or disrupt). γ indicates best-fit slope to Eq. 8.1. Errors are standard deviation of the mean HOD at fixed halo mass. **Bottom**: Normalized second moment of satellite HOD.

The dotted curve also shows the HOD if satellites are never removed by disruption or merging with the central galaxy, in other words, every infalling galaxy survives until $z = 0.1$ (which we measure by analytically retaining every infalling halo). This provides a strict upper limit to the HOD, contingent only upon the accuracy of the halo merger trees and not on subhalo tracking and resolution. As we explore in §8.4, this scenario is highly disfavored.

In the halo model, the spatial clustering on large scales is dominated by galaxy pairs in separate halos ("2-halo" term), which depends on the first moment of the HOD, $\langle N \rangle(M_{\rm halo})$, where $N = N_{\rm sat} + 1$. However, the clustering on small scales is dominated by pairs within a halo ("1-halo" term), which depends on the second moment, $\langle N(N-1) \rangle(M_{\rm halo})$. Figure 8.2 (bottom) shows the normalized second moment of the satellite HOD, defined as $\langle N_{\rm sat}(N_{\rm sat} - 1) \rangle / \langle N_{\rm sat} \rangle^2$. The normalized second moment asymptotes to ≈ 1 at high halo mass, reflecting a nearly Poisson distribution, and it approaches zero at low halo mass where the probability of hosting one satellite remains finite while the probability of hosting two satellites goes to zero. Figure 8.2 shows some dependence on removal threshold, particularly at high halo mass where raising the threshold increases the second moment. This is driven by correlated infall, such as multiple satellites infalling as a group, and thus correlated amounts of mass stripping. This is supported by the fact that the "no removal" scenario (dotted curve), which represents all satellites ever accreted and is insensitive to mass stripping, is closer to Poisson.

8.3.2 Satellite Radial Density Profile

In addition to the number of satellites in a halo, we also explore how removal thresholds affect their locations. Figure 8.3 (top) shows the satellite radial density profile, obtained from stacking all halos hosting the given satellite subhalos. Radii are defined by the distance of a satellite to its central galaxy and are scaled to the host halo's virial radius, $R_{\rm vir}$, obtained from the halo FoF mass and concentration assuming a spherical NFW density profile ($R_{\rm vir} \approx R_{200c}$ at $z \approx 0$). Since halos are triaxial, particularly for those with significant substructure (recent mergers), the assumption of spherical symmetry is highly approximate (see e.g., White 2002, Fig. 2). Additionally, subhalos preferentially lie in a plane defined by their host halo's major axis (e.g., Kroupa et al. 2005; Faltenbacher et al. 2008; Libeskind et al. 2009), behavior also found for galaxies in SDSS (Brainerd 2005) and dwarf satellites around the Milky Way (Metz et al. 2009). This implies that the assumption of spherical symmetry is even less valid for subhalo populations, and that a spherical overdensity halo finder will miss satellites aligned along the halo major axis. Because of these effects, we find that selecting satellites out to $R_{\rm vir}$ only captures 70% of the entire satellite population, while going out to $2\,R_{\rm vir}$ captures 95%. Hence, number densities are normalized by the counts (using no removal threshold) within $2\,R_{\rm vir}$.

The full subhalo tracking model (no removal threshold) shows satellite subhalos tracing the NFW profile to good approximation down to $0.01\,R_{\rm vir}$, though this may represent over-resolution. Since stripping is more prominent in the halo's dense central region, raising the threshold preferentially removes satellites from the halo center, leading to a less concentrated profile. Figure 8.3 (bottom) shows the ratios of the profiles using various $f_{\rm inf}$ values to that

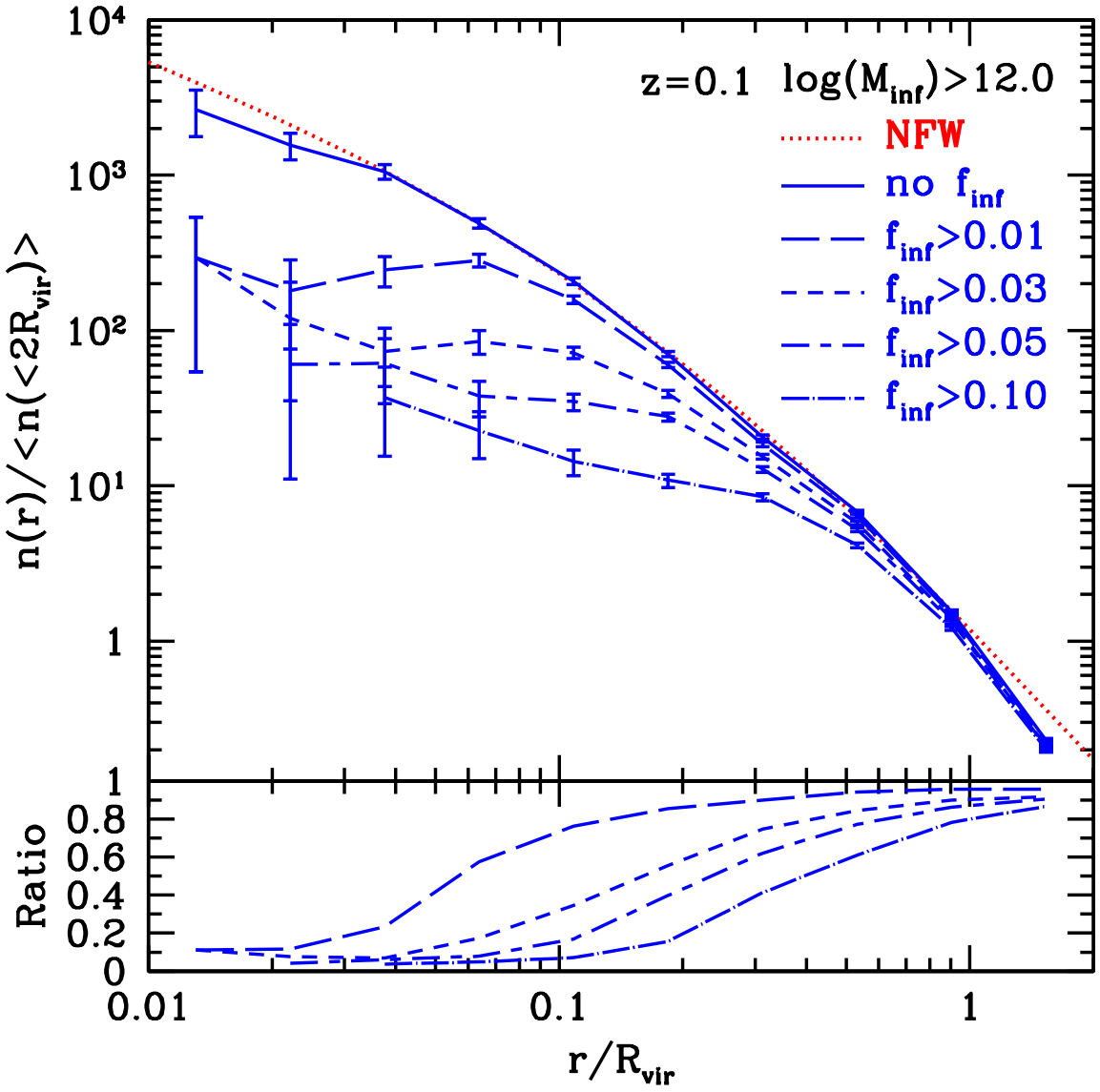

Figure 8.3: **Top**: Satellite radial density profile for satellites with $M_{\rm inf} > 10^{12}\,h^{-1}\,{\rm M}_\odot$ ($M_{\rm star} > 10^{10.8}$ M$_\odot$, $L > 0.6\,L_*$). Solid curve shows all resolved satellites (no removal threshold), while subsequent curves show different minimum removal thresholds. Radii are defined by distance to central galaxy and are scaled to the host halo virial radius, $R_{\rm vir}$. Densities are normalized to the number within $2\,R_{\rm vir}$ using no threshold. Errors bars indicate Poisson error in each radial bin. **Bottom**: Ratio of profile using a given $f_{\rm inf}$ threshold to that of using no removal threshold.

of the full tracking model. In all cases, significant suppression occurs below $0.4\,R_{\rm vir}$. Interestingly, for no $f_{\rm inf}$ threshold does the profile asymptote to unity, implying that mass stripping affects satellites even at large radii. The asymptotic value has no significant dependence on $M_{\rm inf}$ or on time since infall, indicating that this effect is not driven by satellites that have passed through the halo center, but instead by subhalos being significantly stripped during or soon after infall.

These profiles can be compared with observationally measured satellite surface density profiles in galaxy groups, a method typically based on stacking the profiles of galaxies from several groups. Some work indicates that satellite galaxies trace well their host halo's NFW profile. Using a compilation of local galaxy clusters, Diemand et al. (2004) find that the surface density profiles of their member galaxies match that cluster-mass halo particles in simulations within 20% scatter and no systematic offset down to $0.05\,R_{\rm vir}$. Similarly, van den Bosch et al. (2005b) examine satellite galaxies in Two Degree Field Galaxy Redshift Survey (2dFGRS), finding that they are consistent with following their host halo's density profile, though they were not able to discriminate distributions in halo cores.

Other work indicates that, while satellite density profiles can be fit by an NFW profile, they require a lower concentration parameter than the dark matter. Using clusters of mass $> 3 \times 10^{13}\,h^{-1}\,{\rm M}_\odot$, Lin et al. (2004b) find that galaxy profiles down to $0.02\,R_{\rm vir}$ require an NFW concentration parameter of $c = 2.9 \pm 0.2$. A similar analysis by Muzzin et al. (2007) finds that galaxies trace NFW with $c = 4.1 \pm 0.6$ down to $0.5\,R_{\rm vir}$. Examining lower mass ($< 10^{14}\,h^{-1}\,{\rm M}_\odot$) galaxy groups clusters in SDSS, Hansen et al. (2005) find that satellite profiles down to $0.1\,R_{\rm vir}$ can be well-fit with NFW profiles using $c < 3$, with similar results from the 2dFGRS and SDSS group catalogs of (Yang et al. 2005).

Concentrations of $c = 3-4$ are lower than the average halo concentration of $c = 5-6$ for cluster-mass halos in our simulations. Interestingly, an NFW profile with $c = 3$ is consistent with the satellite distribution in our simulation down to $0.06\,R_{\rm vir}$ using $f_{\rm inf} = 0.01$. However, differences in halo virial radii estimates, density normalizations, cluster centering, and galaxy luminosity thresholds make a detailed comparison difficult, as highlighted by the diversity in concentrations derived observationally.

One strong systematic uncertainty in measuring the profiles is how one chooses the halo center. Two common methods of defining a cluster center are the location of the Brightest Cluster Galaxy (BCG) and the peak of X-ray temperature profile. However, these are often offset by several 10's of kpc. For example, for rich clusters in the SDSS MaxBCG catalog, the median offset between the BCG and X-ray center is 58 kpc (Koester et al. 2007b). To estimate how such uncertainties propagate, we examine the degree to which centering changes the measured density at $0.1\,R_{\rm vir}$ by giving the central subhalo an arbitrary offset. We find that an offset of 10, 25, or $50\,h^{-1}\,{\rm kpc}$ leads to a change of +1%, +4% and −4% in the measured density, the error growing rapidly with offset amplitude. Requiring less than a 10% reduction in measured density at $0.1\,R_{\rm vir}$ for clusters requires an offset of less than $60\,h^{-1}\,{\rm kpc}$ in the central subhalo. Such offset may be minimized by selecting BCGs based on their color profiles (Bildfell et al. 2008).

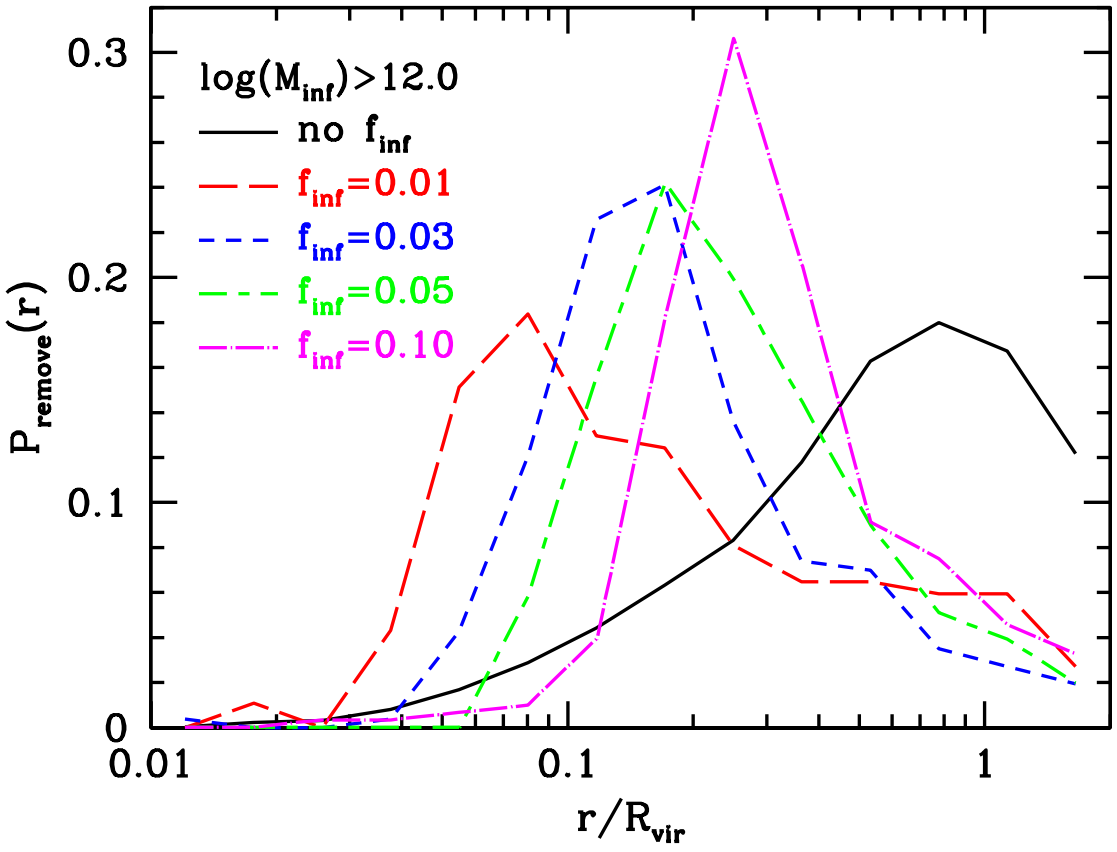

Figure 8.4: Satellite radial distribution probability (not divided by volume) at the time of crossing below a given removal threshold, $f_{\rm inf}$, for satellites with $M_{\rm inf} > 10^{12}\,h^{-1}\,{\rm M}_\odot$ ($M_{\rm star} > 10^{10.8}$ M$_\odot$, $L > 0.6\,L_*$). For reference, solid curve shows radial distribution of all resolved satellites at $z = 0.1$.

8.3.3 Radius at Removal: Merger vs. Disruption

While Fig. 8.3 shows the profile of extant satellites, it does not indicate the location of satellites when they became removed and where their central particles, associated with a stellar population, end up. This would provide a measure of whether satellite galaxies merge with the central galaxy or disrupt into the ICL. One route to examine this would be to track central "star" particles in subhalos after they become removed and examine their overall distribution at $z \sim 0$ (Murante et al. 2004; Willman et al. 2004; Sommer-Larsen et al. 2005; Rudick et al. 2006). We take a different approach and examine galaxy radial distribution at the time of removal. While Fig. 8.3 shows satellites *above* a threshold $f_{\rm inf}$, we now examine satellites *as* they fall below the threshold by selecting those within 25% of a given $f_{\rm inf}$ value.

Figure 8.4 shows the probability distribution that a satellite is at a given scaled radius for a given $f_{\rm inf}$ value. For reference, the solid curve shows the radial distribution of all resolved

satellites at $z = 0.1$, regardless of stripping. These are obtained from stacking all halos hosting the given satellites, though the results do not change significantly if we look only at cluster-mass halos. Satellites fall below a lower $f_{\rm inf}$ threshold at a smaller radius. This is expected in a model where subhalos are stripped of mass as dynamical friction brings their orbits to smaller radii. All thresholds display a broad distribution with radius, since stripping will also depend on satellite orbital parameters and time since infall (Boylan-Kolchin & Ma 2007). However, the distribution is more peaked for higher $f_{\rm inf}$ thresholds. This likely arises because significantly stripped subhalos are closer to halo centers, where their velocities are both higher and more radial. Indeed, as the removal threshold is raised from $f_{\rm inf} = 0.01$ to 0.1, the average (absolute) ratio of radial to tangential velocities for the satellites drops from 1.5 to 1.1. The average for the entire satellite population is between these at 1.4.

To understand their fates, one must know the direction in which satellites are moving as they are removed. If a satellite disrupts at large radius but is moving toward halo center on a highly radial orbit, its stellar mass may still funnel to the central galaxy. As a measure of this, we examine the fraction of satellites that are moving net inward towards halo center as they cross below $f_{\rm inf}$. We find only mild dependence on $f_{\rm inf}$: as the removal threshold is raised from $f_{\rm inf} = 0.01$ to 0.1, the fraction of satellites moving inward falls from 58% to 52%. Both are lower than the average for the entire satellite population of 62%.

The above results imply that more highly stripped satellites are more likely moving inward and their orbits are more radial. However, both of these trends with mass stripping are mild. Fig. 8.4 shows that, even in our most conservative case of $f_{\rm inf} = 0.01$, the (broad) peak of the radial probability distribution occurs at $\sim 50\,h^{-1}\,{\rm kpc}$. This, coupled with the fact that almost half of satellites at removal are moving outward and have significant tangential velocity components, implies that a significant fraction of satellite galaxies disrupt into the ICL, and do not immediately merge with the central galaxy (see also Monaco et al. 2006; Conroy et al. 2007b; Purcell et al. 2007; White et al. 2007).

8.3.4 Analytical Model for Satellite Removal

As an alternative to numerically tracking satellite subhalos, we can assign infalling halos a removal time at accretion and examine what impact different timescales have on the HOD. While individual merging or disruption times depend on satellite orbital parameters (Binney & Tremaine 2008; Boylan-Kolchin et al. 2008; Jiang et al. 2008), we use a simpler parametrization of satellite removal time which depends only on the halos' mass ratio at infall, assumed to hold for an ensemble average of satellites. Here, an infalling satellite halo with mass $M_{\rm sat,inf}$ merges with the central galaxy or becomes disrupted on a timescale

$$t_{\rm dyn} = C_{\rm dyn}\,\frac{M_{\rm halo}/M_{\rm sat,inf}}{\ln(1 + M_{\rm halo}/M_{\rm sat,inf})}\,t_{\rm Hubble} \tag{8.2}$$

where $t_{\rm Hubble} = H^{-1}(z)$, $M_{\rm halo}$ is the larger halo mass, and we leave $C_{\rm dyn}$ as a free parameter to match to different satellite removal thresholds.

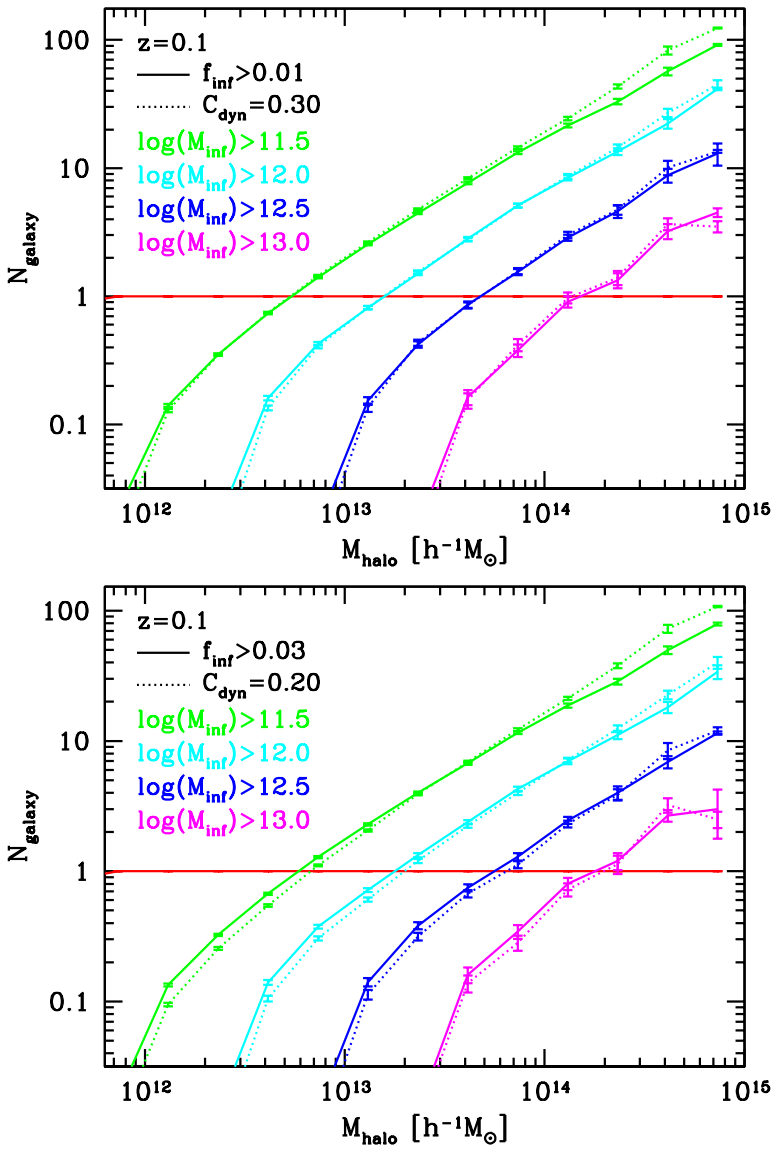

Figure 8.5: Halo Occupation Distributions (HOD) for multiple $M_{\rm inf}$-limited samples, using removal thresholds $f_{\rm inf} > 0.01$ (top) and $f_{\rm inf} > 0.03$ (bottom). $M_{\rm inf} = 10^{11.5}, 10^{12.0}, 10^{12.5}, 10^{13.0}\,h^{-1}\,{\rm M}_\odot$ corresponds to $M_{\rm star} = 10^{10.3}, 10^{10.8}, 10^{11.1}, 10^{11.3}$ ($L = 0.2, 0.6, 1.3, 2.1\,L_*$). Also shown are HODs for different values of $C_{\rm dyn}$ for dynamical friction infall time, chosen to match the subhalo catalog.

Figure 8.5 shows the HOD for multiple $M_{\rm inf}$-limited samples and two removal thresholds, $f_{\rm inf}$. Also plotted are the HODs using different values of $C_{\rm dyn}$ for dynamical friction. In each case, the $C_{\rm dyn}$ value is chosen to best match the subhalo catalog using the given $f_{\rm inf}$ value. Impressively, this sole free parameter can match well the subhalo catalogs across a broad range of subhalo and halo masses, and for multiple removal thresholds. Additionally, since satellite removal times depend on their orbital parameters the relative robustness of $C_{\rm dyn}$ across a wide halo and subhalo mass range indicates that satellite orbits do not vary significantly with mass, though Fig. 8.5 shows some hint of shorter infall times (more radial orbits) for satellites in more massive halos. As we shall see in §8.5, using Eq. 8.2 with the same value of $C_{\rm dyn}$ for the given $f_{\rm inf}$ also works well at higher redshift.

8.4 Comparisons with Observations

Having examined trends in subhalo properties with varying removal threshold, we now seek to constrain this freedom by comparing with observations. While the HOD and radial profile of the above sections are physically informative, they are not direct observables. The most direct comparison with data is via spatial clustering, which provides a scale-dependent test of our subhalo catalog at various masses. In addition, we compare to observed satellite fractions and cluster satellite luminosity functions, though these measures are less robust since they are derived from HOD modeling of spatial clustering or from constructing group catalogs, both of which are subject to systematic uncertainties in halo mass definition, HOD parametrization, and assumed cosmology.

We again use subhalo abundance matching, as outlined §8.2.3, but while we matched to the 2dF stellar mass function in §8.2.3, in this section we match to the number densities of r-band luminosity threshold samples in SDSS in order to provide a robust comparison against observed clustering results. Thus, here the requirements on matching are less restrictive, in that we need only match to a single threshold at a time rather than reproduce the entire luminosity function.

8.4.1 Spatial Clustering

For spatial clustering measurements, we compare against the SDSS galaxy clustering results of Zehavi et al. (2005) at $z \approx 0.1$. To measure spatial clustering, we use the two-dimensional projected galaxy auto-correlation function

$$w_p(r_p) = \int_{-\pi_{\rm max}}^{\pi_{\rm max}} d\pi \, \xi(r_p, \pi) \tag{8.3}$$

which has the advantage of effectively integrating over redshift-space distortions, which we incorporate using subhalo velocities. We use $\pi_{\rm max} = 40\,h^{-1}\,{\rm Mpc}$ to match the measurements against which we compare. This value represents a good balance between integrating over

redshift-space distortions and minimizing correlated noise from large-scale power (Padmanabhan et al. 2007).

Both large- and small-scale clustering are sensitive to the satellite population. In the limit that all galaxies are centrals (a halo hosts only one galaxy), the galaxy correlation function is simply that of the mass-limited halo sample of the same number density. As the threshold for satellite removal decreases and the satellite population increases, high-mass halos will host multiple galaxies. This serves to raise the minimum halo mass of the sample (at fixed number density) while further weighting the clustering from high-mass halos which host more satellites. Satellites in a halo are also close spatially, to each other and to the central. Thus, satellites boost both the large- and small-scale clustering.

The small-scale clustering is also dependent on the radial profile of the satellites, though this sensitivity is mild. In the limit that central-satellite pairs dominate, the clustering on scale r_p comes from satellites at a large fraction of $r_{\rm vir}$ in small halos and satellites nearer the center of larger halos. Given the steepness of the mass function and the available halo volume, the first contribution dominates, weakening the sensitivity to the inner profile. Therefore, $w_p(r_p)$ is only mildly sensitive to the radial dependence of satellite removal, though in the extreme limit of no satellites it drops off rapidly on small scales because of halo exclusion.

Figure 8.6 shows $w_p(r_p)$ of luminosity-threshold samples from SDSS. These are compared against the $M_{\rm inf}$-threshold subhalo catalog for several removal thresholds, $f_{\rm inf}$, each matched to the threshold number density of the SDSS sample. The magnitude-limited samples of $M_r < -20.5$ and < -21.5 correspond to subhalo $M_{\rm inf}$-limited thresholds of $M_{\rm inf} \approx 10^{12}$ and $10^{13}\,h^{-1}\,{\rm M}_\odot$, spanning a range we are able to probe with robust resolution and good statistics. Impressively, the simple prescription for satellite removal of $f_{\rm inf} = 0.01 - 0.03$, combined with simple number density matching to assign luminosity, matches well at small and large scales, across over an order of magnitude in $M_{\rm inf}$. We find similar agreement with the $M_r < -20.0$ sample, corresponding to $M_{\rm inf} > 10^{11.75}\,h^{-1}\,{\rm M}_\odot$, if the "Sloan Great Wall" (Gott et al. 2005) is removed, but because of the involved uncertainty we do not include this sample to constrain $f_{\rm inf}$. The $M_r < -19.5$ sample, corresponding to $M_{\rm inf} > 10^{11.5}\,h^{-1}\,{\rm M}_\odot$, agrees as well but is on the edge of robust resolution, so it does not provide a robust constraint.

We also investigate the influence of luminosity-mass scatter. Because of the steepness in the subhalo mass function, adding scatter lowers the effective $M_{\rm inf}$ threshold at a fixed number density, and this effect is stronger at higher $M_{\rm inf}$ (see Fig. 8.1). Thus, Fig. 8.7 shows $w_p(r_p)$ for most luminous samples, assuming 0.2 dex scatter in luminosity at fixed $M_{\rm inf}$. As expected from the decreased effective mass threshold, adding scatter reduces the clustering amplitude, and the effect is stronger at larger scales. However, the goodness of agreement between observations and $f_{\rm inf} = 0.01 - 0.03$ is not significantly changed, except for the $M_r < -21.5$ sample where agreement is improved somewhat, suggesting necessary scatter at high mass.

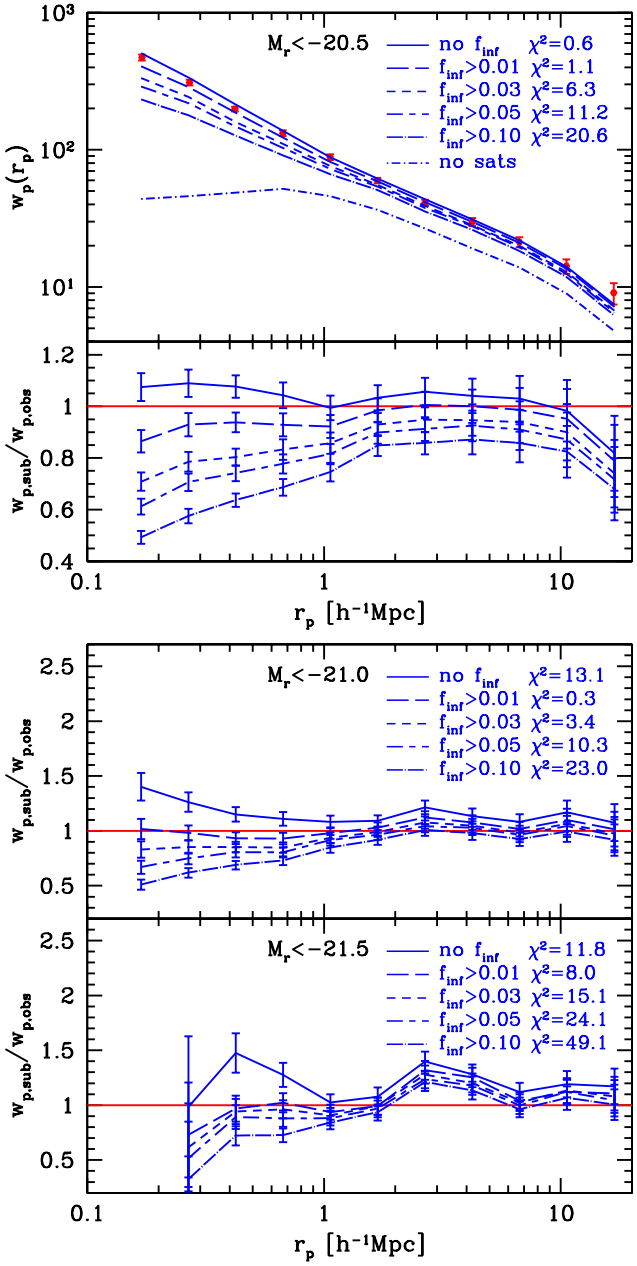

Figure 8.6: Projected auto-correlation function at $z = 0.1$ for several removal thresholds, $f_{\rm inf}$, (curves) each matched in number density to magnitude-limited samples in SDSS assuming no $L_r - M_{\rm inf}$ scatter and compared with measured $w_p(r_p)$ of Zehavi et al. (2005) (points). **Top**: $w_p(r_p)$ (top) and ratio of simulation to observed $w_p(r_p)$ (bottom) for $M_r < -20.5$ sample. **Bottom**: Ratio of simulation to observed $w_p(r_p)$ for $M_r < -21.0$ and < -21.5 samples. $M_r < -20.5$, -21.0, and -21.5 correspond to subhalo $M_{\rm inf} \gtrsim 10^{12}$, $10^{12.5}$, and $10^{13}\,h^{-1}\,{\rm M}_\odot$. Also shown is the reduced χ^2 of the fit to observation for each $f_{\rm inf}$.

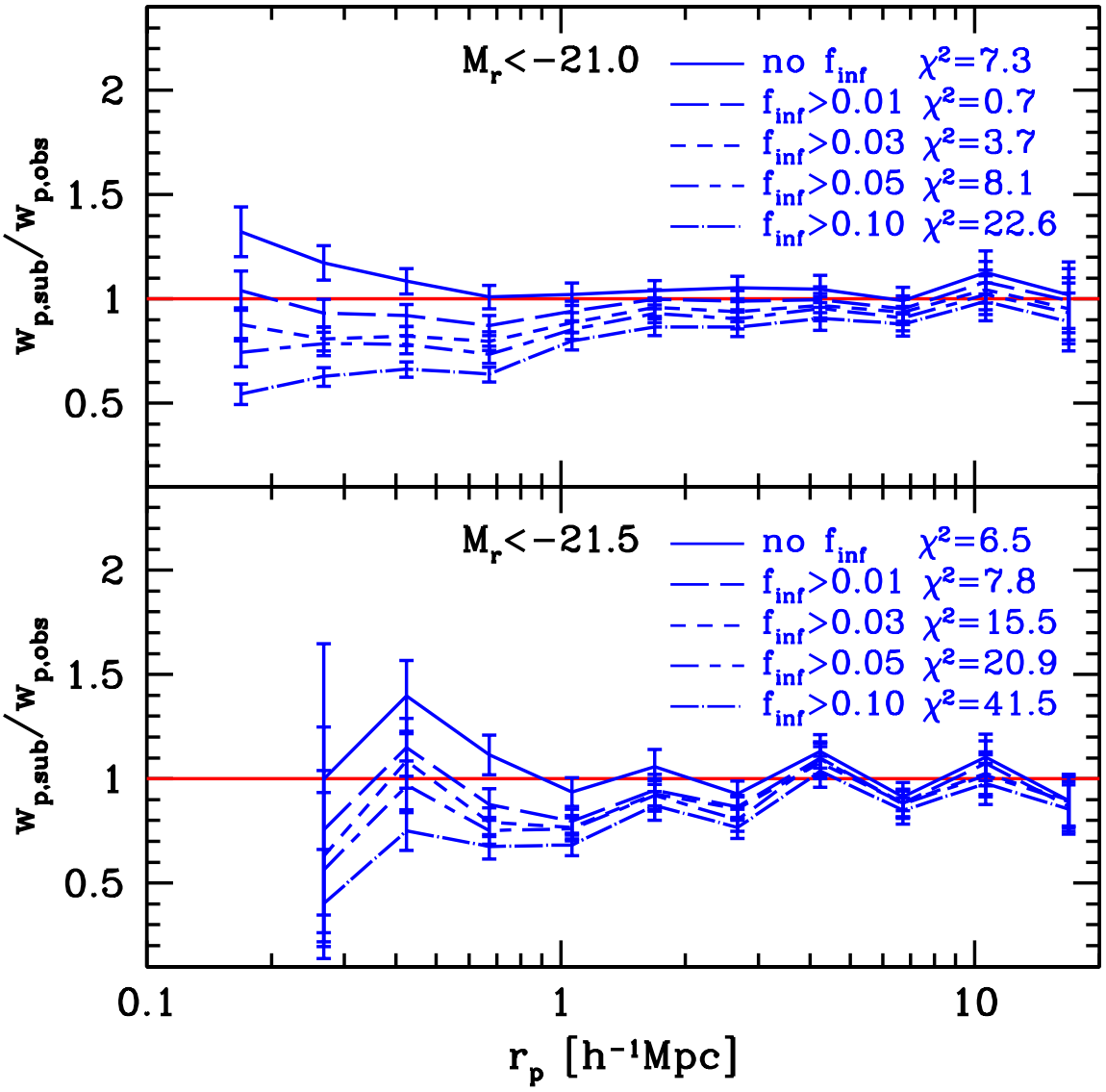

Figure 8.7: Same as Fig. 8.6 (bottom), but luminosity is matched to subhalos assuming 0.2 dex scatter in L_r at fixed $M_{\rm inf}$.

8.4.2 Satellite Fraction

We next compare against the observed satellite fraction: the fraction of galaxies above a given luminosity threshold that are satellites. Since the satellite fraction is an integral over the HOD, it integrates the effects of §8.3 into a single number as a function of $M_{\rm inf}$: as the threshold for removal is raised, the satellite fraction drops.

We compare against a variety of values derived from SDSS and 2dFGRS, all at a median $z = 0.05-0.1$. Again we stress that determining satellite fractions from observations requires significant modeling. Zehavi et al. (2005) and Zheng et al. (2007) satellite fractions were both derived from fitting HODs to the number density and spatial clustering of galaxy samples from SDSS, though they used different HOD parametrizations. Tinker et al. (2007) used a similar technique applied to 2dFGRS. Additionally, Yang et al. (2008) satellite fractions were obtained directly from the SDSS group catalogs of Yang et al. (2007).

Figure 8.8 (top) shows observed satellite fractions, abundance matched to our subhalo catalog and plotted as a function of $M_{\rm inf}$. The observationally-based analyses yield similar results, which also agree with values from galaxy-galaxy lensing (Mandelbaum et al. 2006), though there is considerable scatter. At the low mass end, the amplitude from Tinker et al. (2007) is anomalously low, which may be driven by the fact that the 2dFGRS is a blue-selected samples and thus could be missing a large population of satellites there, since satellites are preferentially redder than centrals (van den Bosch et al. 2008). Given the consistency of the three other samples at low mass, we consider their values more robust in that regime. At the high mass end, the satellite fractions from Zheng et al. (2007) show an upturn; since the satellite fraction is expected to decrease with mass and the amplitude of the highest two mass bins are considerably different than the other samples, we will not consider them as robust data points.

Also shown are satellite fractions from our subhalo catalog for various removal thresholds, $f_{\rm inf}$. Since the satellite fraction should rise with decreasing galaxy mass, the rollover at low mass clearly shows the limits of numerical resolution below $M_{\rm inf} = 10^{11.5}\,h^{-1}\,{\rm M}_\odot$. Above this mass, $f_{\rm inf} \approx 0.03$ works well across over two decades in $M_{\rm inf}$, consistent with results from spatial clustering.

Note that the satellite fraction remains non-zero up to $M_{\rm inf} \sim 10^{14}\,h^{-1}\,{\rm M}_\odot$, resulting from low redshift cluster-cluster mergers (e.g. Cohn & White 2005). This implies that $\sim 10\%$ of galaxy clusters should be expected to host a satellite BCG, as supported by observations which shown a number of clusters hosting BCG-BCG pairs (e.g., Liu et al. 2009). In a sample of rich clusters from the SDSS MaxBCG catalog, 15% host two BCGs (Koester et al. 2007a).

We can also use our analytic model for satellite removal as in §8.3.4 to examine how different $C_{\rm dyn}$ values for dynamical friction affect the satellite fraction, as shown in Fig. 8.8 (bottom). Discounting the results of Tinker et al. (2007) at low mass, which exhibit a flattening that is not seen in any of the other samples, our simple analytic model provides good agreement with observations using $C_{\rm dyn} = 0.2-0.3$. This provides a consistent picture, since using $C_{\rm dyn} = 0.2-0.3$ matches the subhalo HOD using $f_{\rm inf} = 0.01-0.03$ (Fig. 8.5), which is also the range of $f_{\rm inf}$ that best matches observed clustering. Additionally, this analytic model

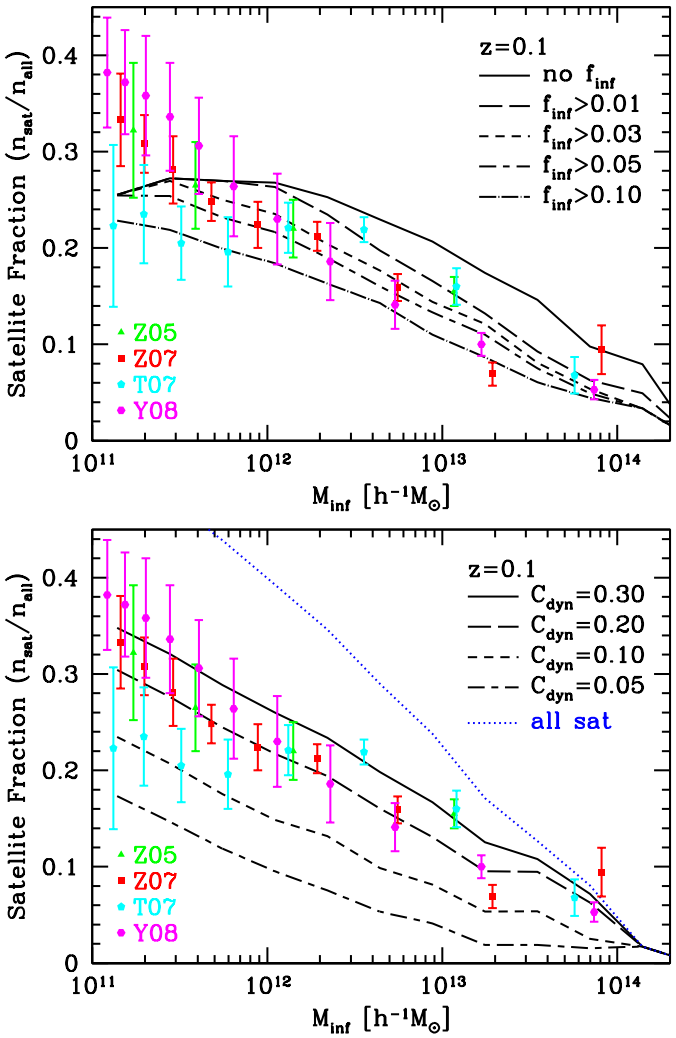

Figure 8.8: Satellite fraction vs. infall mass. **Top**: Using various removal thresholds, $f_{\rm inf}$, from the subhalo catalog. Points show observationally derived values, matched in number density to our subhalo catalog, from Zehavi et al. (2005) (Z05), Zheng et al. (2007) (Z07), Tinker et al. (2007) (T07), and Yang et al. (2008) (Y08). **Bottom**: Using the analytic model for satellite halo infall of Eq. 8.2 and various values of $C_{\rm dyn}$ for dynamical friction. Good agreement with observation (no rollover) continues at low mass since the analytic model depends only on resolving halos prior to infall. Dotted curve shows keeping all satellites ever accreted.

works well even below our mass threshold for reliably tracking satellite subhalos, showing no rollover at low mass since it depends only on resolving halos prior to infall.

The dotted curve in Fig. 8.8 (bottom) shows the satellite fraction if satellites are never removed (merge with central or tidally disrupt), which we measure by analytically retaining every infalling halo, as in Fig. 8.2. The slight deficit compared with the full subhalo catalog at high mass arises because satellites in this analytic model do not gain mass via merging with other satellites. While this "no removal" scenario provides a reasonable estimate at high mass, where halos have formed only recently and so their average times since infall are short, it grossly overpredicts the satellite fraction at lower mass. This demonstrates the clear failure of a scenario in which satellite galaxies never merge or disrupt.

Overall, we find that $C_{\rm dyn} \approx 0.25$ both matches well to the satellite removal criteria that agrees with spatial clustering, and it directly produces satellite fractions in agreement with observations. Conroy et al. (2007a) apply a similar dynamical infall model as ours to halo merger trees to examine the growth of the Luminous Red Galaxy (LRG) population. They find that $C_{\rm dyn} = 0.1$ fit observations well, though they were unable to put precise constraints on this value. Figure 8.8 (bottom) shows that such a value would underpredict the observed satellite fraction across a broad mass range.

$C_{\rm dyn} = 0.2$ also agrees well with a similar analysis by (Wetzel et al. 2009a), who match the evolution of satellite subhalos in simulations at $z \gtrsim 1$. They also pointed out that, given typical satellite orbital circularity distributions (Zentner et al. 2005; Jiang et al. 2008), the detailed fits to dynamical friction infall times of Boylan-Kolchin et al. (2008) and Jiang et al. (2008) predict $C_{\rm dyn} = 0.06$ and 0.14, respectively. The latter value, obtained from an analysis of a cosmological simulation not dissimilar from ours, is marginally consistent with our results. However, the former clearly is not. This can partially be attributed to the different mass dependence in the parametrization of Boylan-Kolchin et al. (2008): they used a fit similar to Eq. 8.2 but with $(M_{\rm halo}/M_{\rm sat,inf})^{1.3}$ in the numerator. Their added exponent factor doubles their merging and disruption time (with respect to ours) for a 10 : 1 mass ratio merger. While this does provide better agreement, it still leads to a 10 : 1 infall timescale that is half of ours. Given that their fit was obtained from an analysis of significantly higher resolution mergers of two isolated, spherical (Hernquist profile) halos, this highlights the importance of realistic cosmological settings for calibrating satellite merging and disruption timescales.

Finally, we note that the above analytic model of satellite removal is dependent on halo definition. In particular, if halos are defined to have a larger radius, then satellites will accrete sooner and hence the analytic removal time will be longer. As compared with the commonly used FoF($b = 0.2$), $r_{b=0.168} \approx 0.86\, r_{b=0.2}$. Thus, the best-match $C_{\rm dyn} \approx 0.25$ values represents a lower limit to that of satellites in halos using FoF($b = 0.2$).[4]

[4]In principle, changing halo definition can also change the mass ratio in Eq. 8.2 and hence the removal time, since halo concentration scales weakly with mass. However, the mass enhancement from FoF($b = 0.168$) to FoF($b = 0.2$) is nearly independent of concentration and redshift. The relation to spherical overdensity halos will depend on concentration and redshift (see White 2001, for more on halo conversion).

8.4.3 Cluster Satellite Luminosity Function

Since the correlation function and satellite fraction conflate satellites within a variety of host halo masses, we finally test our subhalo catalog by examining satellites specifically in the densest environments: galaxy clusters. We compare the luminosity function of satellites within galaxy clusters in our simulation with that determined from the SDSS MaxBCG catalog (Hansen et al. 2009). Here, we abundance match our subhalo catalog at $z = 0.25$ to the SDSS i-band galaxy luminosity function at that redshift (Sheldon et al. 2009), from which the cluster catalog in Hansen et al. (2009) is drawn. Additionally, we assume 0.15 dex scatter in luminosity at fixed subhalo mass. We then compute the luminosity function of satellites in clusters of a given richness, where we define richness as in Hansen et al. (2009) as the number of red sequence satellite galaxies with $L > 0.4L_*$ within the cluster virial radius. We use their fit to the red galaxy fraction vs. cluster richness (their Eq. 13) to scale our total satellite counts to those of red galaxies (this fraction is $65 - 80\%$ in the richness range we probe).

Figure 8.9 shows the results of our subhalo catalog, using a removal threshold of $f_{\rm inf} > 0.02$, as compared with Hansen et al. (2009). We find good agreement for both high and low bins of cluster richness. Since $M_i = -19$ corresponds to a subhalo infall mass of $10^{11.4}\,h^{-1}\,{\rm M}_\odot$, the agreement in Fig. 8.9 across a wide range of luminosities demonstrates that our subhalo catalog, with a model for merging and disruption, successfully traces the galaxy population in the densest environments down to our expected numerical resolution threshold. Figure 8.9 does exhibit some excess of very bright cluster satellites in our catalog, though the limited number of massive clusters in our simulation volume precludes a definitive test in that regime.

8.5 High Redshift

8.5.1 HOD & Analytic Removal

Examining the effects of removal thresholds on the HOD at higher redshift, we find little change in the fractional reduction in the satellite HOD as $f_{\rm inf}$ is increased. This supports a picture where satellite subhalo mass stripping is quite rapid after infall, such that the shorter average times since infall at higher redshift do not lead to a significantly less stripped satellite subhalo population.

We also examine our analytic model for satellite removal timescale (Eq. 8.2) at higher redshift. In particular, we test the validity of the scaling of $t_{\rm dyn}$ with $t_{\rm Hubble}$. Figure 8.10 shows the HOD at $z = 1$ and 2 for both the subhalo catalog and analytic model, using the same $f_{\rm inf}$ and $C_{\rm dyn}$ values as in Fig. 8.5 (bottom). The agreement at all host halo and satellite masses remains relatively robust given the simplicity of the model. This agreement is partially a result of the decreasing dependence of the analytical model on $C_{\rm dyn}$ at higher z, when halos of a given mass have formed and been accreted more recently, so allowing longer infall times does not significantly increase the number of satellites. This is demonstrated by decreasing difference in the HOD for $C_{\rm dyn} = 0.2$ (dashed curves) as opposed to the

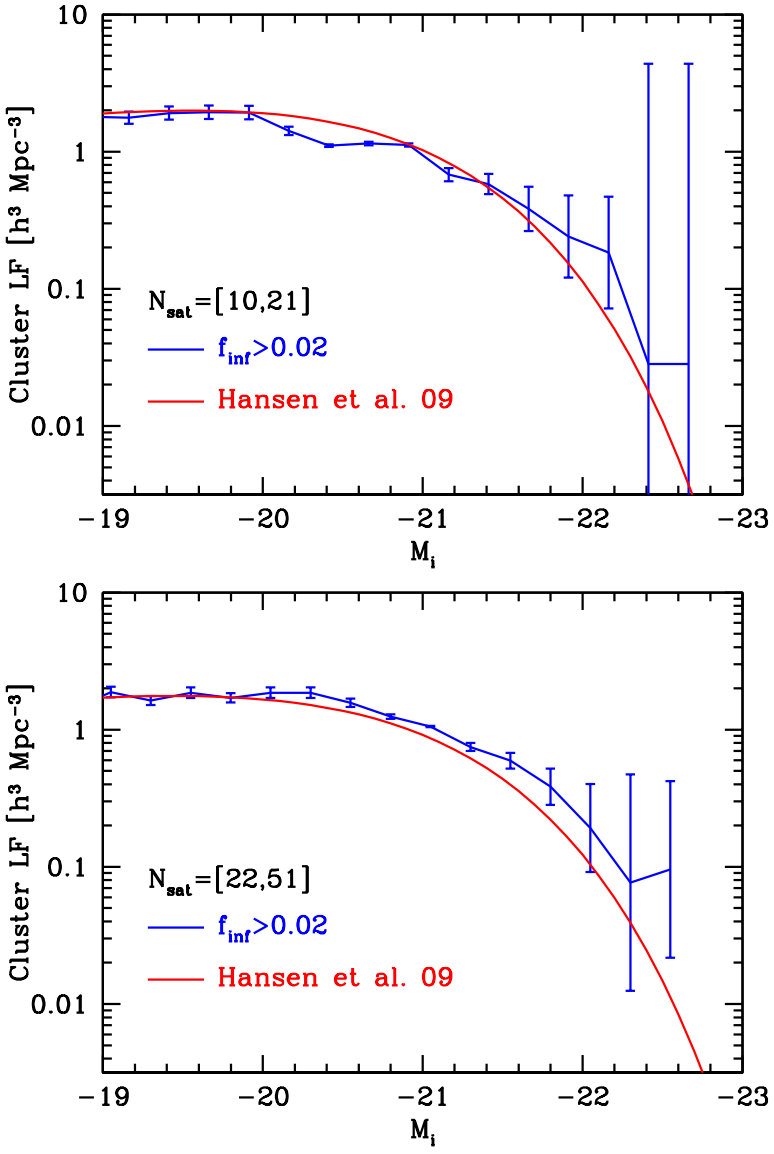

Figure 8.9: Luminosity function of satellites in galaxy clusters at $z = 0.25$, for lower (top) and higher (bottom) cluster richness bins. Subhalos are abundance matched to the SDSS i-band luminosity function (Sheldon et al. 2009), assuming 0.15 dex scatter in luminosity at fixed subhalo mass, and satellites retained if their $f_{\rm inf} > 0.02$. Solid curve shows fit to SDSS MaxBCG catalog from Hansen et al. (2009).

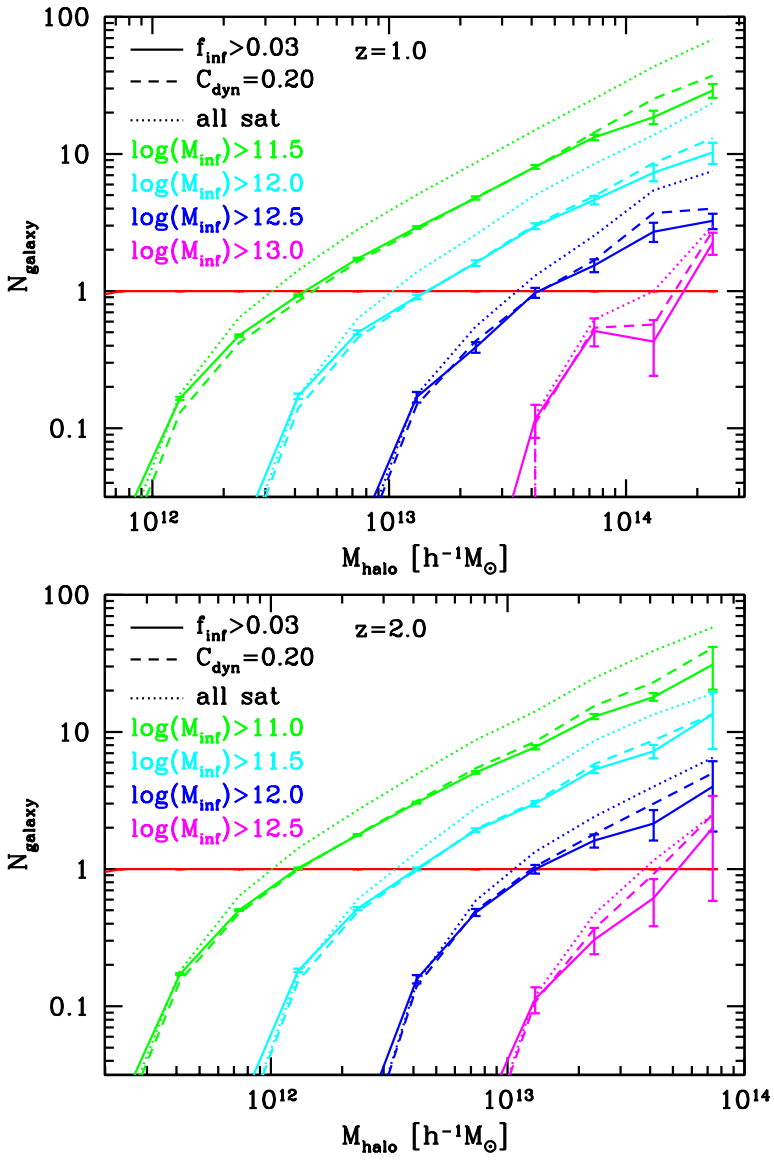

Figure 8.10: Same as Fig. 8.5, but at $z = 1$ (top) and $z = 2$ (bottom). A given $C_{\rm dyn}$ value maps nearly as well to a given removal threshold, $f_{\rm inf}$, at high z as at $z = 0.1$. Dotted curves show keeping all satellites ever accreted. At higher z, this case exhibits less excess with respect to the dynamical infall prescription.

"no removal" scenario (dotted curves). Moreover, using $C_{\rm dyn} \gtrsim 0.3$ produces no additional enhancement in the HOD at $z > 2$.

This result has clear implications for modelling galaxy evolution at high redshift. Since the details in modeling satellite galaxy infall matter less at higher redshift, nearly all uncertainty in understanding galaxy evolution at high redshift lies in the gas and radiation physics and not in the dynamics of dark matter.

8.5.2 Spatial Clustering at $z \sim 1$

We also examine whether our criteria for satellite removal hold at higher redshift by comparing with galaxy clustering results at $z \sim 1$ from the Deep Extragalactic Evolutionary Probe 2 (DEEP2) survey (Coil et al. 2006), as shown in Fig. 8.11. Here, we use abundance matching to match the number densities of B-band luminosity threshold galaxy samples in DEEP2. We find that using abundance matching with no scatter in the $L_B - M_{\rm inf}$ relation causes our subhalo catalog to exhibit significant excess in clustering as compared with DEEP2 for all but the lowest few r_p bins. We find improved agreement using significant (0.6 dex) scatter, as shown for two luminosity thresholds corresponding to subhalos above our robust resolution limit. Using even larger scatter improves the agreement on large scales, but it underpredicts clustering on smaller scales.

At $z \sim 1$, the small scale ($r_p < 1\,h^{-1}\,{\rm Mpc}$) clustering provides a consistent picture with the results at $z = 0.1$, favoring a removal threshold of $f_{\rm inf} = 0.01 - 0.05$. However, despite the large luminosity-mass scatter, our subhalo catalog overpredicts the clustering as compared with DEEP2 on large scales. Curiously, at face value, DEEP2 clustering at $r_p \sim 10\,h^{-1}\,{\rm Mpc}$ favors a model with *no* satellite galaxies.

There are a number of possible reasons for why DEEP2 suggests increased scatter and/or reduced clustering. DEEP2 selects on B-band luminosity, which is more susceptible to recent star formation, and since satellites at $z \sim 1$ are redder than centrals at a given stellar mass (Zheng et al. 2007; Tinker & Wetzel 2009), this could bias the clustering low since satellites preferentially live in more massive halos, which are more highly biased. As discussed in §8.2.2, it is possible that the $L - M_{\rm inf}$ relation has more scatter at higher redshift. However, large scatter alone is unable to match the clustering at all scales. Clustering in DEEP2 could be biased low because their selection criteria miss $\sim 10\%$ of red galaxies in their survey volume, although this effect is likely to be mild both because red galaxies form the minority of the population at all luminosity thresholds and because $w_p(r_p)$ is nearly the same for red and blue galaxies at $r_p \sim 10\,h^{-1}\,{\rm Mpc}$ (Coil et al. 2008). Alternately, if DEEP2 is missing an appreciable number of galaxies in their survey volume (regardless of color), our abundance matching method will correlate to the observed galaxies artificially high subhalo masses, leading to enhanced clustering. Or the disagreement could be a statistical fluctuation. The DEEP2 survey volume of $\sim (100\,h^{-1}\,{\rm Mpc})^3$ is susceptible to sampling variance, and the clustering at different scales are highly correlated, so the discrepancy may not be statistically significant. Since we do not have a covariance matrix for the observations, we are unable to determine the goodness-of-fit.

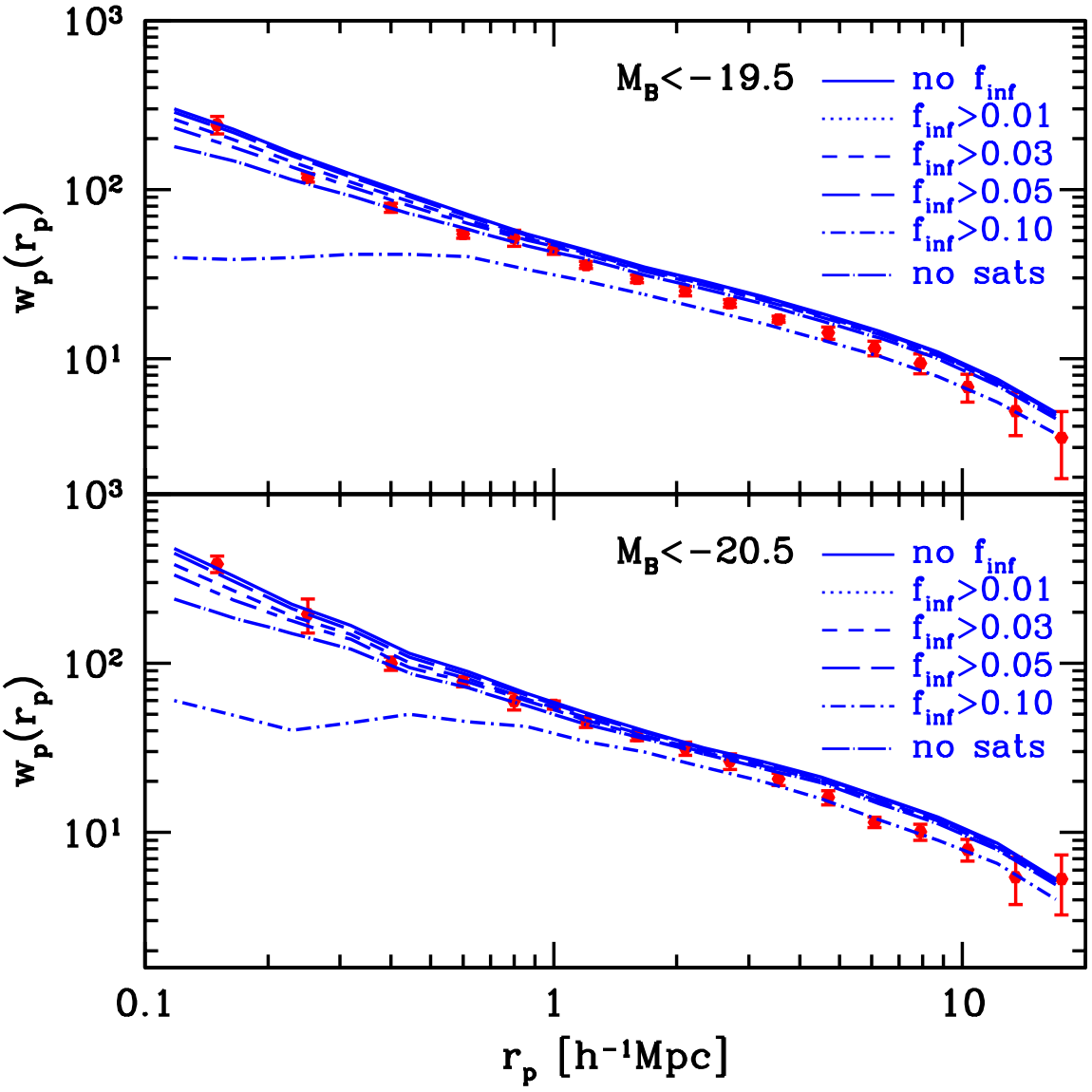

Figure 8.11: Projected auto-correlation function for several removal thresholds, $f_{\rm inf}$, as compared with the observed clustering at $z \sim 1$ of Coil et al. (2006). $M_B < -19.5, -20.5$ samples correspond to subhalo $M_{\rm inf} \gtrsim 10^{11.5}$, $10^{12.0}\,h^{-1}\,{\rm M}_\odot$. Abundance matching here assumes 0.6 dex scatter in L_B at fixed $M_{\rm inf}$.

Interestingly, Conroy et al. (2006) find good agreement with DEEP2 clustering using similar method based on abundance matching against subhalo catalogs. Their better agreement (lower clustering) may stem from their different assumed cosmology ($\sigma_8 = 0.9$), and/or their simulation sizes (80 and $120\,h^{-1}\,$Mpc), significantly smaller than the one used here. Suggestively, a recent HOD analysis using color information finds a similar clustering trend as ours, namely, good agreement at small scales but excess clustering at $r_p \gtrsim 1\,h^{-1}\,$Mpc (Tinker & Wetzel 2009).

Thus, while our satellite removal criteria are consistent with clustering at $z \sim 1$ in DEEP2 at $r_p < 1\,h^{-1}\,$Mpc given $L_B - M_{\rm inf}$ scatter, the above uncertainties and lack of agreement in large-scale clustering do not allow us to obtain strong constraints from these higher redshift data.

8.5.3 Evolution of the Satellite Fraction

Finally, we explore how the satellite fraction evolves with redshift. Figure 8.12 (top) shows the satellite fraction as a function of $M_{\rm inf}$ at various redshifts, using $f_{\rm inf} = 0.02$. At a fixed infall mass, the satellite fraction monotonically increases with time, arising from the decreasing dynamical friction infall time with respect to the typical halo merger timescale (Wetzel et al. 2009a). The evolution of the rollover at low mass, arising from numerical disruption, indicates that the resolution limit decreases with higher redshift, when satellites have been accreted more recently.

Since the $M_{\rm star} - M_{\rm inf}$ relation evolves with time, Fig. 8.12 (bottom) shows the satellite fraction instead as a function of $M_{\rm star}$, obtained by abundance matching against the SMF of Cole et al. (2001) at $z = 0.1$ and Marchesini et al. (2009) at higher redshift. Points show the satellite fraction at fixed $M_{\rm inf}$ values. At high mass, the $M_{\rm star} - M_{\rm inf}$ relation exhibits only mild evolution, but at lower mass, subhalos at a fixed $M_{\rm inf}$ grow rapidly in $M_{\rm star}$.

This result has two important implications. First, in examining a galaxy population of fixed stellar mass, simulation resolution becomes even less of a limitation at higher redshift than Fig. 8.12 (top) would indicate, since at the low mass end galaxies of a fixed $M_{\rm star}$ move to a higher $M_{\rm star}$ with redshift. This is evidenced by the lack of rollover in the stellar mass satellite fraction at higher redshift.

Second, the growth of $M_{\rm star}$ at fixed $M_{\rm inf}$ for $M_{\rm star} < 10^{11}$ M$_\odot$ demonstrates how SHAM implicitly allows for satellite star formation. For example, if a satellite were accreted at $z = 1$ with $M_{\rm star} = 4 \times 10^{10}$ M$_\odot$, following the points of fixed $M_{\rm inf}$ in Fig. 8.12 (bottom) shows that SHAM-assigned stellar mass would increase by $\sim 20\%$ by $z = 0.1$.

8.6 Impact of Simulation Size & Cosmology

Given finite computational capacity, there is always a trade-off between simulation resolution and volume. While our high-resolution $200\,h^{-1}\,$Mpc simulation is able to track halo substructure with high fidelity, its limited volume poses problems for accurately recovering

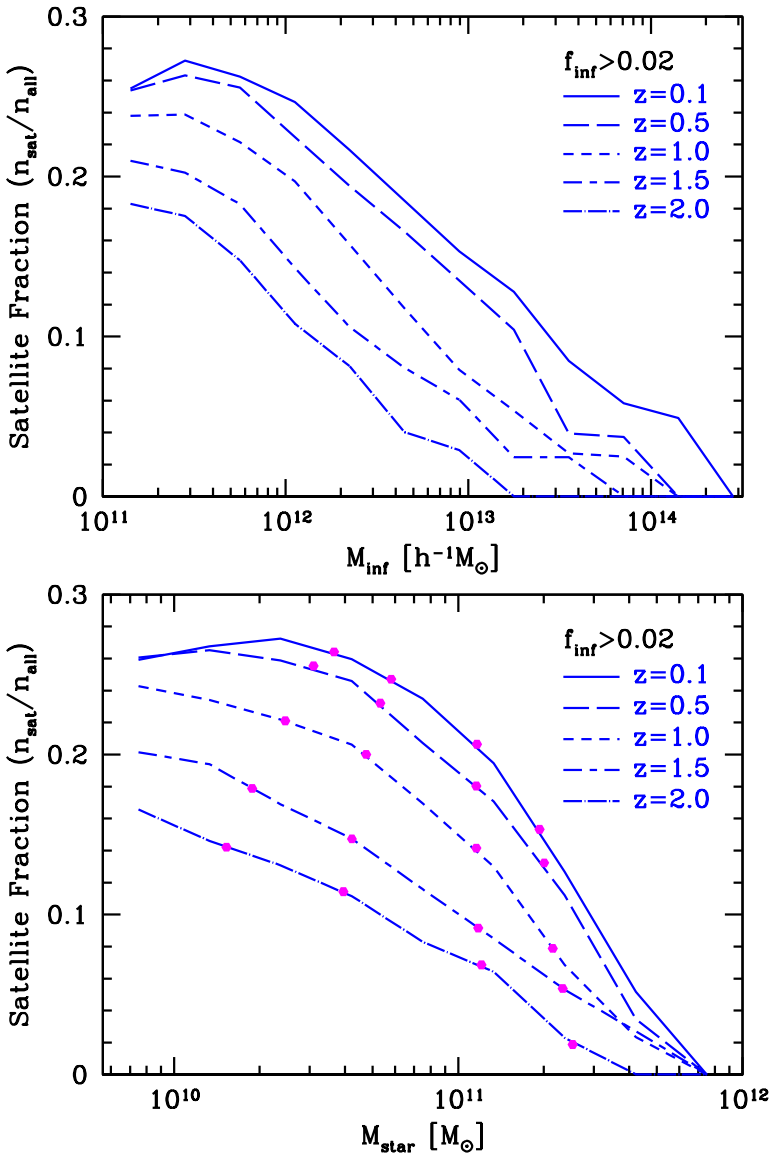

Figure 8.12: Satellite fraction vs. mass at various redshifts, using a removal threshold of $f_{\rm inf} = 0.02$. **Top**: Subhalos binned in $M_{\rm inf}$. The turnover in satellite fraction occurs at lower $M_{\rm inf}$ at higher z, indicating that resolution effects less critical at higher z. **Bottom**: Subhalos binned in $M_{\rm star}$, based on abundance matching. Points indicate values at fixed $M_{\rm inf}$ of $10^{11.75}, 10^{12.0}, 10^{12.5}, 10^{13.0}\,h^{-1}\,{\rm M}_\odot$, highlight the evolving $M_{\rm star} - M_{\rm inf}$ relation.

the high mass end of the halo mass function and large-scale spatial clustering. This is not merely an issue of limited statistics and sample variance: by imposing mean density on a limited volume, we are not probing an entirely representative realization of the Universe, and the limited volume truncates power on scales larger than the simulation size.

Comparing the halo statistics of the $200\,h^{-1}\,\mathrm{Mpc}$ and $720\,h^{-1}\,\mathrm{Mpc}$ simulations (which have different resolution but the same cosmology and halo finder, as described in §8.2.1), we find that the halo mass function at $z = 0.1$ in the $200\,h^{-1}\,\mathrm{Mpc}$ simulation is 5% lower than that in the $720\,h^{-1}\,\mathrm{Mpc}$ simulation from $3 \times 10^{11}\,h^{-1}\,\mathrm{M}_\odot$ (the resolution limit of the larger simulation) to $3 \times 10^{14}\,h^{-1}\,\mathrm{M}_\odot$, with no dependence on mass in this interval. This implies that the deficit is driven not by resolution effects, but instead by truncated large-scale power and sample variance. Above $3 \times 10^{14}\,h^{-1}\,\mathrm{M}_\odot$, the $200\,h^{-1}\,\mathrm{Mpc}$ simulation exhibits a significant deficit in halo density ($\sim 20\%$), with its most massive halo being $8 \times 10^{14}\,h^{-1}\,\mathrm{M}_\odot$, as opposed to $2 \times 10^{15}\,h^{-1}\,\mathrm{M}_\odot$ in the larger simulation. Additionally, we find an error of several percent in the halo correlation function measured at $10\,h^{-1}\,\mathrm{Mpc}$ in the $200\,h^{-1}\,\mathrm{Mpc}$ simulation as compared with the larger one, and it is significantly truncated on scales $\gtrsim 0.1\,L_{\mathrm{box}}$.

To test these finite-volume issues on subhalo clustering, we create a second subhalo catalog by mapping our high-resolution subhalo catalog onto the halo catalog of the larger, less resolved simulation. Based on convergence tests from simulations of multiple sizes, the larger simulation accurately reproduces the spatial clustering on the scales of interest. We randomly match two halos of the same mass from the two simulations, and we take subhalos from the halo in the high-resolution simulation and paste them onto the halo in the larger simulation. We place the central subhalo at the potential minimum of the halo, and we place the satellite subhalos using a random overall orientation such that their positions with respect to all other subhalos in the host halo are retained. Since halos of $M > 8 \times 10^{14}\,h^{-1}\,\mathrm{M}_\odot$ do not have a counterpart in the high-resolution simulation, we use fits to the satellite HOD extrapolated to higher halo mass to populate these halos in the larger simulation, assigning the satellite radial distributions to follow their halo NFW profiles with a random phase. To examine the influence of cosmology, we also populate our subhalo catalog into our $500\,h^{-1}\,\mathrm{Mpc}$ simulation which uses $n = 1.0$ and $\sigma_8 = 0.9$.

Figure 8.13 shows the effects of both simulation size and cosmology on the correlation function of subhalos corresponding to $M_r < -21.0$. Subhalos in the larger simulation with the same cosmology exhibit somewhat enhanced $w_p(r_p)$ on the largest and smallest scales. The change on moderate to small scales arises primarily because our re-population method ignores any environmental effects on the satellites, like halo alignment. However, the large scale clustering amplitude is little affected. We thus conclude that the $200\,h^{-1}\,\mathrm{Mpc}$ simulation is not significantly affected by its size on these scales.

We emphasize, however, that the spatial clustering in smaller simulation sizes is significantly affected on these scales. We have performed the same comparisons with observations as in Fig. 8.13 with a simulation of the same mass resolution and subhalo finder as the $200\,h^{-1}\,\mathrm{Mpc}$ simulation, but was a smaller $125\,h^{-1}\,\mathrm{Mpc}$ cube.[5] We find a noticeable deficit

[5]The initial conditions for this simulation did have a some low modes at low k.

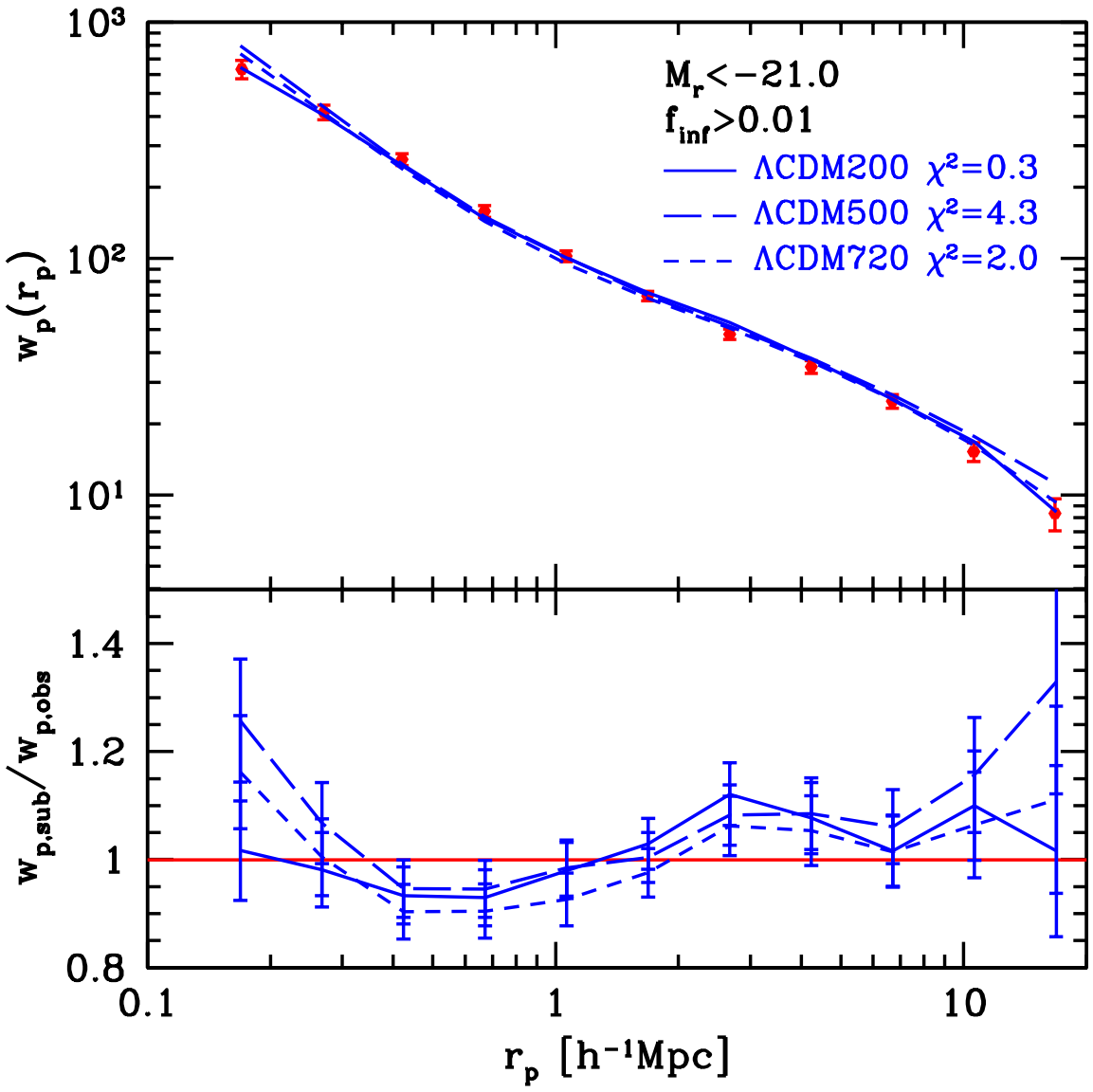

Figure 8.13: Same as Fig. 8.6, but using a fixed $f_{\rm inf} = 0.01$ for subhalos directly from the $200\,h^{-1}$ Mpc simulation, and for subhalos populated into host halos in the $720\,h^{-1}$ Mpc simulation (same cosmology) and $500\,h^{-1}$ Mpc simulation (different cosmology). $w_p(r_p)$ (top) and ratio of simulations to observed $w_p(r_p)$ (bottom). Also shown is the reduced χ^2 of the fit to observation for each simulation.

in $w_p(r_p)$ at all subhalo masses both on large *and* small scales as compared with observations and our $200\,h^{-1}\,\mathrm{Mpc}$ simulation. The former is readily expected, driven by mean density and a truncation of large-scale power. The latter effect is more subtle, arising from the truncation of the halo mass function at high mass, which strongly affects the overall satellite population since these halos host many satellites. Thus, we stress that in comparing the spatial clustering of subhalos in simulations to observed galaxies, both resolution and finite volume effects need be considered.

Figure 8.13 also shows that changing cosmology to $n = 1.0$ and $\sigma_8 = 0.9$ leads to a similar but stronger enhancement in $w_p(r_p)$ which is less consistent with observations. Thus, if σ_8 is considerably larger than our fiducial value of 0.8, our best-fit $f_{\rm inf}$ of 0.01 might be an underestimate.

8.7 Comparisons with Other Removal Criteria

As discussed in the introduction, various authors have used different criteria to define satellite galaxy removal via dark matter subhalos. Here, we examine how other criteria compare against our fiducial case, the subhalo bound mass to infall mass ratio, $f_{\rm inf}$.

As shown by our full tracking scheme (keeping subhalos to 50 particles), using a fixed mass criterion can reasonably match observations if the mass threshold corresponds to $1-5\%$ of the infall mass. As simulations increase in resolution, it thus becomes increasingly necessary to model for satellite removal before subhalos reach numerical disruption.

Models which remove a satellite subhalo after its mass has been stripped to a value less than the mass within a fixed fraction ($a_{\rm dis}$) of its NFW scale radius (e.g., Taylor & Babul 2004; Zentner et al. 2005; Macciò et al. 2009) are largely degenerate with our fiducial $f_{\rm inf}$ criterion, since subhalo concentration scales only weakly with mass. For a typical halo concentration of $c = 10$, our results suggest $a_{\rm dis} \approx 0.3$, within the range $0.1-1$ often assumed.

Given that total baryonic to dark mass ratio in a halo is nearly 10%, Stewart et al. (2009) assumed that a satellite merges with its central galaxy when it drops below 10% of infall mass. However, we find that $f_{\rm inf} = 0.1$ noticeably underpredicts the satellite population. A lower threshold is needed, likely both because the stellar to dark mass ratio is significantly lower ($\sim 4\%$), and because any baryonic mass will be more compact than the 10% most bound dark mass.

Since the $M_{\rm star}/M_{\rm inf}$ ratio varies with subhalo mass (Fig. 8.1), it is not obvious that our best-fit removal threshold, based on subhalos of $M_{\rm inf} > 10^{11.5}\,h^{-1}\,\mathrm{M}_\odot$ ($L > 0.2\,L_*$), can be simply extrapolated to modelling dwarf-spheroidal systems around the Milky Way. However, our results are consistent with allowed dark mass stripping fractions to match the Milky Way population (Peñarrubia et al. 2008; Macciò et al. 2009).

Instead of mass stripping-based criteria, we also examine criteria based on satellite tidal radius or distance from halo center (central galaxy). To obtain precise central-satellite separations, we linearly extrapolate satellite positions between subsequent outputs to find the minimum separation. For succinct comparison, we compare satellite fractions against

$f_{\rm inf} = 0.02$, the fiducial criterion which matches well to observations as shown above.

As was shown in Fig. 8.4, a correlation exists between a satellite's distance from its central galaxy and falling below a given $f_{\rm inf}$ value. Thus, Fig. 8.14 (top) shows satellites removed when coming within a fixed physical distance from the central galaxy. Despite the stripping-distance correlation, compared with our fiducial case this model underpredicts satellites at low mass and overpredicts at high mass. Combined with the results from our full tracking model (fixed mass threshold), this implies that any successful removal criteria must scale with the mass or radius of the satellite subhalo.

In this vein, the middle panel shows satellite removal if a satellite subhalo's tidal (Jacobi) radius falls below a given value, where

$$r_{\rm tid} = A \left[\frac{M_{\rm sat}}{3 M_{\rm halo}(< r)} \right]^{1/3} r \tag{8.4}$$

and where r is the physical separation from satellite to halo center, $M_{\rm sat}$ is the instantaneous bound satellite mass, $M_{\rm halo}(< r)$ is the halo mass within r, and A is a constant that accounts for the host halo's density profile (see Binney & Tremaine 2008, Eqs. 8.107 and 8.108). Assuming that a satellite disrupts when within its host halo's inner NFW profile lets us set $A = 1.4$, and we measure $M_{\rm sat}$ and $M_{\rm halo}(< r)$ directly from our simulation. As a simple analytic alternative, we have investigated modelling the halos at infall as isothermal spheres (as applied to Binney & Tremaine 2008, Eq. 9.86), which produces similar results. Figure 8.14 (middle) shows the satellite fraction for tidal radii motivated by typical galaxy sizes. Similar to using fixed satellite distance, this method predicts too shallow of a dependence on satellite infall mass, likely a manifestation of its weak (1/3 power) scaling with mass ratio.

Finally, we consider a removal criterion defined simply by a linear scaling relation between satellite halo – host halo mass and radius at infall. Specifically, removal occurs when

$$r < B \left(\frac{M_{\rm sat,inf}}{M_{\rm halo}} \right) R_{\rm halo,vir} \tag{8.5}$$

where B is some constant. Note that if satellite and host halos are isothermal spheres, such that $M(< r)/M_{\rm vir} = r/R_{\rm vir}$, and $B = 1$, the above criterion is met when the halo mass interior to r equals the satellite's infall mass. Figure 8.14 (bottom) shows the results using $B = 1$ and 0.5. This model provides good agreement with our fiducial case because of the strong (linear) scaling with mass ratio, with $B = 0.5$ well matching the overall amplitude. Thus, this method may provide a useful approximation for simple analytic models of satellite evolution.

Various works using semi-analytic models grafted onto subhalo populations use an analytic model to track satellite galaxies after subhalo disruption in order to match small-scale galaxy clustering at $z \sim 0$ (e.g., Springel et al. 2001; Kitzbichler & White 2008; Saro et al. 2008). While this method does provide a means to overcome limited mass resolution, its fundamental assumption, that all satellite galaxies eventually merge with the central galaxy, is not consistent with the dynamics of subhalos at removal that we find, or with observed ICL fractions.

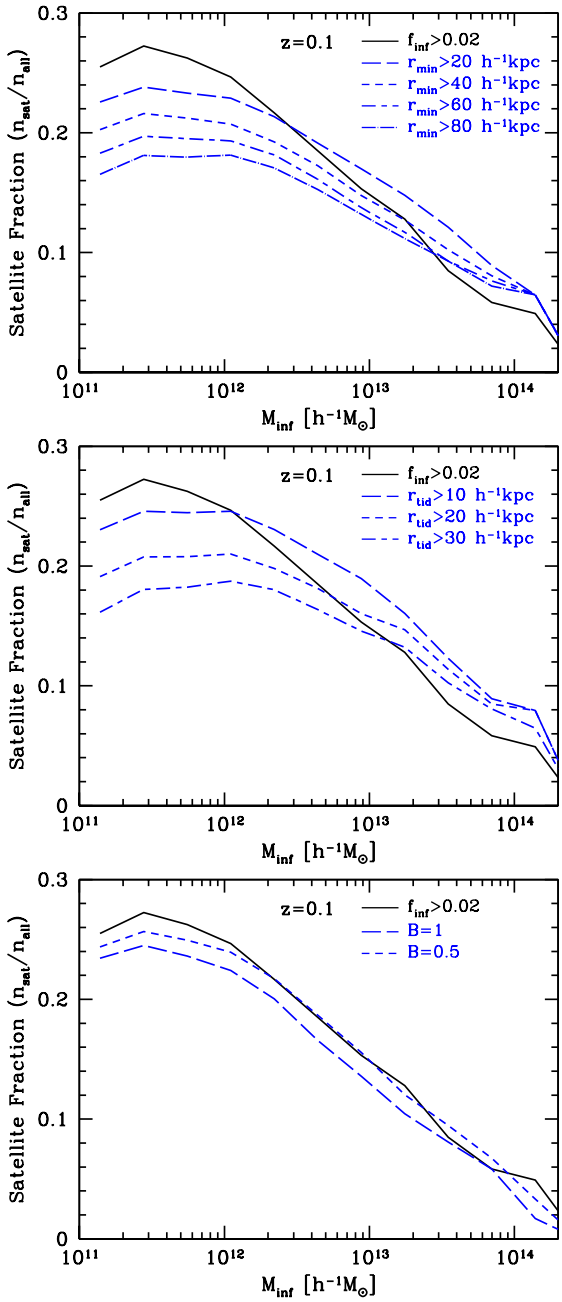

Figure 8.14: Satellite fraction vs. subhalo infall mass, using various removal criteria. **Top**: Satellite removed when it passes within a given physical distance of its central galaxy. **Middle**: Satellite removed when its tidal radius falls below the given value. **Bottom**: Satellite removed when it passes within radius at which both satellite subhalo and host halo have same interior mass (ignores satellite mass stripping), both using NFW profiles from simulation and approximating halos as isothermal spheres.

As an alternative, Henriques et al. (2008), using semi-analytic catalogs from the Millennium simulation, consider all satellite galaxies at $z = 0$ whose subhalo has fallen below numerical resolution as tidally disrupting into ICL (implying that central-satellite mergers do not occur). While this represents a highly simplified model, entirely contingent on a fixed numerical resolution mass, it does provide better agreement with the observed faint end of the galaxy luminosity function and allows for contribution to ICL consistent with observations. Seek Kim et al. (2009) use the same semi-analytic models and find better agreement with observed spatial clustering by assuming that satellite luminosity is instantly reduced at infall to roughly the ratio of satellite halo to host halo mass. This model implies nearly total stellar mass stripping of low mass satellites immediately upon infall, in disagreement with our method which tracks mass loss over time across all satellite masses self-similarly.

Interestingly, Moster et al. (2009) use SHAM applied to a simulation of similar mass and force resolution to ours, and they find that they need to analytically track satellite galaxies after subhalo disruption to match galaxy clustering, in opposition to our findings. This difference may arise because their simulation size is $100\,h^{-1}\,\mathrm{Mpc}$, and as we discuss in §8.6, simulation volumes smaller than $200\,h^{-1}\,\mathrm{Mpc}$ tend to underpredict subhalo spatial clustering on all scales.

8.8 Summary & Conclusion

We use a high-resolution dark matter-only N-body simulation of cosmological volume to track halos and their substructure, examining the fates of satellite galaxies. Under the assumption that galaxies reside at the centers of subhalos and that stellar mass is related to infall mass, we assign stellar masses to subhalos through abundance matching, such that we recover the observed stellar mass function. Our subhalo catalog intrinsically incorporates satellite-satellite mergers and satellite orbiting beyond their halo radius. Thus, we examine different criteria for satellite galaxy removal (tidal disruption or merging with the central galaxy), using only information from the dark matter density field, and focusing primarily on the criterion based on the subhalo bound mass to infall mass ratio, $f_{\mathrm{inf}} = M_{\mathrm{bound}}/M_{\mathrm{inf}}$. We highlight our main results as follows:

- Raising the threshold for removal, f_{inf}, causes a reduction in the satellite HOD at all masses, such that more halos host only one galaxy. Additionally, higher f_{inf} leads to a shallower HOD slope, implying that modelling satellite removal is more important in higher mass halos.

- Disrupted/merged satellites reside primarily in the inner halo regions, and raising the removal threshold leads to a less concentrated satellite density profile. A small fraction of satellites are disrupted out to the halo virial radius.

- Most satellites fall below the removal threshold at a halo radius of $40 - 100\,h^{-1}\,\mathrm{kpc}$, the distance increasing with f_{inf}. The orbits of these satellites are only mildly radial

and nearly half are directed outward from halo center, indicating that a substantial fraction of satellites are disrupted into the ICL as opposed to merging with the central galaxy.

- Our subhalo catalog matched in number density to observed galaxy samples at $z = 0.1$ reproduces well the projected correlation function at all scales and over a large range in subhalo masses using $f_{\rm inf} = 0.01 - 0.03$. Using reasonable (0.2 dex) luminosity-mass scatter does not change our results appreciably.

- Our subhalo catalog also agrees well with observed satellite fractions and cluster satellite luminosity functions for similar values of $f_{\rm inf}$. A scenario in which satellite galaxies never merge or disrupt is not feasible.

- Methods for satellite removal based on physical separation from central galaxy or tidal radii predict too shallow of a dependence on subhalo mass. Better agreement arises from methods that scale linearly with subhalo mass.

- A simple analytical model for satellite removal timescale, based only on the satellite-halo mass ratio at infall and scaling with the Hubble time, reproduces well both our subhalo catalog up to high redshift, and the observed satellite fraction at $z = 0.1$. The best-fit $C_{dyn} \approx 0.25$ implies a substantially longer removal time than that derived from other dynamical friction models.

We emphasize that our results are based on examining subhalo merging and disruption in dark matter-only simulations, and the best-fit criteria to observations may change somewhat for simulations incorporating hydrodynamics and accurate galaxy stellar profiles. For example, gas dynamics can affect orbits of the subhalos themselves, though this appears to be small (Jiang et al. 2009). More importantly, a realistic subhalo stellar component is likely to be more compact and immune to stripping than the dark matter. Recent works find some enhancement of satellite subhalo survivability in SPH simulations with star formation than in dark matter-only simulations, though the strength of this effect is unclear (Dolag et al. 2009; Weinberg et al. 2008).

The largest source of uncertainty in our method is the assignment of stellar luminosity to subhalos. While abundance matching to subhalo infall mass does allow for "passive" satellite star formation as the $M_{\rm star} - M_{\rm inf}$ relation evolves, it may underpredict the star formation in satellite galaxies, particularly at higher redshift. We have investigated how additional satellite star formation after infall influences our results by increasing all satellite infall masses by a fixed fraction. Because our removal criterion is based on mass stripping, this is largely degenerate with increasing removal threshold. Thus, to the extent that satellites experience significant star formation after infall (beyond what is implicitly in SHAM), our best-fit removal threshold may represent a slightly underestimate. A more detailed prescription for star formation quenching can be related to environmental dependence of galaxy color, though we save incorporating properties beyond stellar mass or luminosity to future work.

Despite these uncertainties, our best fit mass stripping criterion for removal provides a consistent picture with galaxy stellar mass to dark mass ratios. Abundance matching at $z = 0.1$ gives $M_{\rm star}/M_{\rm sub,inf} \approx 4\%$ for $M_{\rm inf} \sim 10^{12}\,h^{-1}\,{\rm M}_\odot$ (Fig. 8.1). This implies that all of the stellar mass is only slightly more compact than the most bound dark matter of the same mass. Thus, it is unlikely that galaxies within subhalos that fall below $f_{\rm inf} \sim 0.01$ can remain intact. If satellite galaxies have been stripped of most of their gas, then the gravitational dynamics of the stellar material will simply follow that of the dark matter, and since the dark mass fraction within a galaxy's radius is close to unity, dark mass stripping below $f_{\rm inf} \sim 0.01$ must correspond to some amount of baryonic stripping. While our binary model of merging and disruption is clearly an oversimplification, it does provides a good match to current observations.

Finally, our results imply strong constraints on simulations needed for robust subhalo populations, both in resolution and volume. Taking $f_{\rm inf} = 0.01$ as a conservative limit of our removal threshold and ~ 30 particles as minimum resolution for tracking subhalos in dense environments, this implies that at least ~ 3000 particles are needed at infall to robustly track satellites, which is consistent with our convergence tests on subhalo mass functions at $z = 0.1$. This resolution requirement is relaxed somewhat at high redshift ($z > 1$), where average satellite times since infall are shorter so satellite have experienced less stripping. Additionally, our tests on simulation volumes indicate that cube sizes $\lesssim 200\,h^{-1}\,{\rm Mpc}$ have considerable difficulty reproducing representative halo mass functions and spatial clustering. Taken together, these resolution and volume effects necessitate a wide dynamical range, using several billion particles, for simulations used to investigate galaxy evolution and galaxy large-scale structure in a cosmological context.

Bibliography

Abadi, M. G., Moore, B., & Bower, R. G. 1999, MNRAS, 308, 947
Allgood, B., Flores, R. A., Primack, J. R., Kravtsov, A. V., Wechsler, R. H., Faltenbacher, A., & Bullock, J. S. 2006, MNRAS, 367, 1781
Allgood, B. A. 2005, PhD thesis, University of California, Santa Cruz, United States – California
Angulo, R. E., Lacey, C. G., Baugh, C. M., & Frenk, C. S. 2008, ArXiv e-prints 0810.2177
Aubert, D., Pichon, C., & Colombi, S. 2004, MNRAS, 352, 376
Bardeen, J. M., Bond, J. R., Kaiser, N., & Szalay, A. S. 1986, ApJ, 304, 15
Barnes, J. E. & Hernquist, L. 1996, ApJ, 471, 115
Barnes, J. E. & Hernquist, L. E. 1991, ApJ, 370, L65
Baugh, C. M. 2006, Reports on Progress in Physics, 69, 3101
Beisbart, C. & Kerscher, M. 2000, ApJ, 545, 6
Beisbart, C., Kerscher, M., & Mecke, K. 2002, in Lecture Notes in Physics, Berlin Springer Verlag, Vol. 600, Morphology of Condensed Matter, ed. K. Mecke & D. Stoyan, 358–390
Bell, E. F., Phleps, S., Somerville, R. S., Wolf, C., Borch, A., & Meisenheimer, K. 2006, ApJ, 652, 270
Benson, A. J. 2005, MNRAS, 358, 551
Benson, A. J., Kamionkowski, M., & Hassani, S. H. 2005, MNRAS, 357, 847
Berlind, A. A., Kazin, E., Blanton, M. R., Pueblas, S., Scoccimarro, R., & Hogg, D. W. 2006, ArXiv Astrophysics e-prints 0610524
Berlind, A. A. & Weinberg, D. H. 2002, ApJ, 575, 587
Berrier, J. C., Bullock, J. S., Barton, E. J., Guenther, H. D., Zentner, A. R., & Wechsler, R. H. 2006, ApJ, 652, 56
Bezanson, R., van Dokkum, P. G., Tal, T., Marchesini, D., Kriek, M., Franx, M., & Coppi, P. 2009, ApJ, 697, 1290
Bildfell, C., Hoekstra, H., Babul, A., & Mahdavi, A. 2008, MNRAS, 389, 1637
Binney, J. & Tremaine, S. 2008, Galactic Dynamics: Second Edition (Princeton University Press, Princeton, NJ)
Biviano, A. & Poggianti, B. M. 2009, A&A, 501, 419
Blain, A. W., Chapman, S. C., Smail, I., & Ivison, R. 2004, ApJ, 611, 725
Blain, A. W., Smail, I., Ivison, R. J., Kneib, J.-P., & Frayer, D. T. 2002, Phys. Rep., 369, 111

Blumenthal, G. R., Faber, S. M., Flores, R., & Primack, J. R. 1986, ApJ, 301, 27
Bond, J. R., Cole, S., Efstathiou, G., & Kaiser, N. 1991, ApJ, 379, 440
Bond, J. R., Kofman, L., & Pogosyan, D. 1996, Nature, 380, 603
Borgani, S. 2006, ArXiv Astrophysics e-prints
Bower, R. G. 1991, MNRAS, 248, 332
Bower, R. G., Benson, A. J., Malbon, R., Helly, J. C., Frenk, C. S., Baugh, C. M., Cole, S., & Lacey, C. G. 2006, MNRAS, 370, 645
Boylan-Kolchin, M. & Ma, C.-P. 2007, MNRAS, 374, 1227
Boylan-Kolchin, M., Ma, C.-P., & Quataert, E. 2005, MNRAS, 362, 184
—. 2008, MNRAS, 383, 93
Brainerd, T. G. 2005, ApJ, 628, L101
Bullock, J. S., Kolatt, T. S., Sigad, Y., Somerville, R. S., Kravtsov, A. V., Klypin, A. A., Primack, J. R., & Dekel, A. 2001, MNRAS, 321, 559
Butcher, H. & Oemler, Jr., A. 1984, ApJ, 285, 426
Carlberg, R. G. 1990, ApJ, 350, 505
Cavaliere, A., Colafrancesco, S., & Menci, N. 1992, ApJ, 392, 41
Cohn, J. D., Bagla, J. S., & White, M. 2001, MNRAS, 325, 1053
Cohn, J. D. & White, M. 2005, Astroparticle Physics, 24, 316
—. 2008, MNRAS, 385, 2025
Coil, A. L., Hennawi, J. F., Newman, J. A., Cooper, M. C., & Davis, M. 2007, ApJ, 654, 115
Coil, A. L., Newman, J. A., Cooper, M. C., Davis, M., Faber, S. M., Koo, D. C., & Willmer, C. N. A. 2006, ApJ, 644, 671
Coil, A. L., Newman, J. A., Croton, D., Cooper, M. C., Davis, M., Faber, S. M., Gerke, B. F., Koo, D. C., Padmanabhan, N., Wechsler, R. H., & Weiner, B. J. 2008, ApJ, 672, 153
Colberg, J. M., White, S. D. M., Jenkins, A., & Pearce, F. R. 1999, MNRAS, 308, 593
Colberg, J. M., White, S. D. M., Yoshida, N., MacFarland, T. J., Jenkins, A., Frenk, C. S., Pearce, F. R., Evrard, A. E., Couchman, H. M. P., Efstathiou, G., Peacock, J. A., Thomas, P. A., & The Virgo Consortium. 2000, MNRAS, 319, 209
Cole, S. & Kaiser, N. 1989, MNRAS, 237, 1127
Cole, S., Norberg, P., Baugh, et al. 2001, MNRAS, 326, 255
Conroy, C., Ho, S., & White, M. 2007a, MNRAS, 379, 1491
Conroy, C. & Wechsler, R. H. 2008, arXiv: 0805.3346
Conroy, C., Wechsler, R. H., & Kravtsov, A. V. 2006, ApJ, 647, 201
—. 2007b, ApJ, 668, 826
Conselice, C. J. 2006, MNRAS, 373, 1389
Cooper, M. C., Newman, J. A., Coil, A. L., Croton, D. J., Gerke, B. F., Yan, R., Davis, M., Faber, S. M., Guhathakurta, P., Koo, D. C., Weiner, B. J., & Willmer, C. N. A. 2007, MNRAS, 376, 1445
Cooray, A. & Ouchi, M. 2006, MNRAS, 369, 1869
Cooray, A. & Sheth, R. 2002, Phys. Rep., 372, 1

Coppin, K., Chapin, E. L., Mortier, A. M. J., et al. 2006, MNRAS, 372, 1621
Cox, T. J., Dutta, S. N., Di Matteo, T., Hernquist, L., Hopkins, P. F., Robertson, B., & Springel, V. 2006, ApJ, 650, 791
Cox, T. J., Jonsson, P., Somerville, R. S., Primack, J. R., & Dekel, A. 2008, MNRAS, 384, 386
Croft, R. A. C., Dalton, G. B., Efstathiou, G., Sutherland, W. J., & Maddox, S. J. 1997, MNRAS, 291, 305
Croom, S. M., Boyle, B. J., Shanks, T., Smith, R. J., Miller, L., Outram, P. J., Loaring, N. S., Hoyle, F., & da Ângela, J. 2005, MNRAS, 356, 415
Croton, D. J., Gao, L., & White, S. D. M. 2007, MNRAS, 374, 1303
Davis, M., Efstathiou, G., Frenk, C. S., & White, S. D. M. 1985, ApJ, 292, 371
De Lucia, G., Kauffmann, G., Springel, V., White, S. D. M., Lanzoni, B., Stoehr, F., Tormen, G., & Yoshida, N. 2004, MNRAS, 348, 333
De Propris, R., Conselice, C. J., Liske, J., Driver, S. P., Patton, D. R., Graham, A. W., & Allen, P. D. 2007, ApJ, 666, 212
De Propris, R., Liske, J., Driver, S. P., Allen, P. D., & Cross, N. J. G. 2005, AJ, 130, 1516
Dekel, A. & Birnboim, Y. 2006, MNRAS, 368, 2
Dekel, A., Birnboim, Y., Engel, G., Freundlich, J., Goerdt, T., Mumcuoglu, M., Neistein, E., Pichon, C., Teyssier, R., & Zinger, E. 2009, Nature, 457, 451
Dekel, A., Devor, J., & Hetzroni, G. 2003, MNRAS, 341, 326
Diaferio, A., Kauffmann, G., Balogh, M. L., White, S. D. M., Schade, D., & Ellingson, E. 2001, MNRAS, 323, 999
Diemand, J., Kuhlen, M., & Madau, P. 2007, ApJ, 667, 859
Diemand, J., Moore, B., & Stadel, J. 2004, MNRAS, 352, 535
Dolag, K., Borgani, S., Murante, G., & Springel, V. 2009, MNRAS, 399, 497
D'Onghia, E., Besla, G., Cox, T. J., & Hernquist, L. 2009, Nature, 460, 605
D'Onghia, E., Springel, V., Hernquist, L., & Keres, D. 2010, ApJ, 709, 1138
Dubinski, J. 1994, ApJ, 431, 617
Dunkley, J., Komatsu, E., Nolta, M. R., Spergel, D. N., Larson, D., Hinshaw, G., Page, L., Bennett, C. L., Gold, B., Jarosik, N., Weiland, J. L., Halpern, M., Hill, R. S., Kogut, A., Limon, M., Meyer, S. S., Tucker, G. S., Wollack, E., & Wright, E. L. 2009, ApJS, 180, 306
Efstathiou, G., Frenk, C. S., White, S. D. M., & Davis, M. 1988, MNRAS, 235, 715
Eisenstein, D. J. & Loeb, A. 1995, ApJ, 439, 520
Evrard, A. E., Bialek, J., Busha, M., White, M., Habib, S., Heitmann, K., Warren, M., Rasia, E., Tormen, G., Moscardini, L., Power, C., Jenkins, A. R., Gao, L., Frenk, C. S., Springel, V., White, S. D. M., & Diemand, J. 2008, ApJ, 672, 122
Fakhouri, O. & Ma, C.-P. 2008, MNRAS, 386, 577
Faltenbacher, A. 2009, ArXiv e-prints
Faltenbacher, A., Allgood, B., Gottlöber, S., Yepes, G., & Hoffman, Y. 2005, MNRAS, 362, 1099
Faltenbacher, A., Jing, Y. P., Li, C., Mao, S., Mo, H. J., Pasquali, A., & van den Bosch, F. C. 2008, ApJ, 675, 146

Francke, H., Gawiser, E., Lira, P., Treister, E., Virani, S., Cardamone, C., Urry, C. M., van Dokkum, P., & Quadri, R. 2008, ApJ, 673, L13
Furlanetto, S. R. & Kamionkowski, M. 2006, MNRAS, 366, 529
Gao, L., De Lucia, G., White, S. D. M., & Jenkins, A. 2004a, MNRAS, 352, L1
Gao, L., Springel, V., & White, S. D. M. 2005, MNRAS, 363, L66
Gao, L. & White, S. D. M. 2007, MNRAS, 377, L5
Gao, L., White, S. D. M., Jenkins, A., Stoehr, F., & Springel, V. 2004b, MNRAS, 355, 819
Gawiser, E., Francke, H., Lai, et al. 2007, ApJ, 671, 278
Gerke, B. F., Newman, J. A., Faber, S. M., Cooper, M. C., Croton, D. J., Davis, M., Willmer, C. N. A., Yan, R., Coil, A. L., Guhathakurta, P. andKoo, D. C., & Weiner, B. J. 2007, MNRAS, 376, 1425
Ghigna, S., Moore, B., Governato, F., Lake, G., Quinn, T., & Stadel, J. 1998, MNRAS, 300, 146
—. 2000, ApJ, 544, 616
Giavalisco, M. 2002, ARA&A, 40, 579
Giavalisco, M., Steidel, C. C., Adelberger, K. L., Dickinson, M. E., Pettini, M., & Kellogg, M. 1998, ApJ, 503, 543
Gill, S. P. D., Knebe, A., & Gibson, B. K. 2005, MNRAS, 356, 1327
Gill, S. P. D., Knebe, A., Gibson, B. K., & Dopita, M. A. 2004, MNRAS, 351, 410
Giocoli, C., Tormen, G., & van den Bosch, F. C. 2008, MNRAS, 386, 2135
Gnedin, O. Y., Hernquist, L., & Ostriker, J. P. 1999, ApJ, 514, 109
Gnedin, O. Y. & Ostriker, J. P. 1997, ApJ, 474, 223
Gonzalez, A. H., Zaritsky, D., & Zabludoff, A. I. 2007, ApJ, 666, 147
Gott, J. R. I., Jurić, M., Schlegel, D., Hoyle, F., Vogeley, M., Tegmark, M., Bahcall, N., & Brinkmann, J. 2005, ApJ, 624, 463
Gottlöber, S., Kerscher, M., Kravtsov, A. V., Faltenbacher, A., Klypin, A., & Müller, V. 2002, A&A, 387, 778
Gottlöber, S., Klypin, A., & Kravtsov, A. V. 2001, ApJ, 546, 223
Gunn, J. E. & Gott, III, J. R. 1972, ApJ, 176, 1
Guo, Q. & White, S. D. M. 2008, MNRAS, 384, 2
Hahn, O., Porciani, C., Dekel, A., & Carollo, C. M. 2008, arXiv: 0803.4211
Hamana, T., Yoshida, N., Suto, Y., & Evrard, A. E. 2001, ApJ, 561, L143
Hansen, S. M., McKay, T. A., Wechsler, R. H., Annis, J., Sheldon, E. S., & Kimball, A. 2005, ApJ, 633, 122
Hansen, S. M., Sheldon, E. S., Wechsler, R. H., & Koester, B. P. 2009, ApJ, 699, 1333
Harker, G., Cole, S., Helly, J., Frenk, C., & Jenkins, A. 2006, MNRAS, 367, 1039
Hartley, W. G., Gazzola, L., Pearce, F. R., Kay, S. T., & Thomas, P. A. 2008, MNRAS, 386, 2015
Hausman, M. A. & Ostriker, J. P. 1978, ApJ, 224, 320
Heitmann, K., Lukić, Z., Fasel, P., Habib, S., Warren, M. S., White, M., Ahrens, J., Ankeny, L., Armstrong, R., O'Shea, B., Ricker, P. M., Springel, V., Stadel, J., & Trac, H. 2008, Computational Science and Discovery, 1, 015003

Hennawi, J. F., Strauss, M. A., Oguri, M., Inada, N., Richards, G. T., Pindor, B., Schneider, D. P., Becker, R. H., Gregg, M. D., Hall, P. B., Johnston, D. E., Fan, X., Burles, S., Schlegel, D. J., Gunn, J. E., Lupton, R. H., Bahcall, N. A., Brunner, R. J., & Brinkmann, J. 2006, AJ, 131, 1

Henriques, B. M., Bertone, S., & Thomas, P. A. 2008, MNRAS, 383, 1649

Herbert-Fort, S., Zaritsky, D., Jin Kim, Y., Bailin, J., & Taylor, J. E. 2008, MNRAS, 384, 803

Hopkins, A. M. & Beacom, J. F. 2006, ApJ, 651, 142

Hopkins, P. F., Cox, T. J., Kereš, D., & Hernquist, L. 2008a, ApJS, 175, 390

Hopkins, P. F., Hernquist, L., Cox, T. J., Di Matteo, T., Martini, P., Robertson, B., & Springel, V. 2005, ApJ, 630, 705

Hopkins, P. F., Hernquist, L., Cox, T. J., & Kereš, D. 2008b, ApJS, 175, 356

Hopkins, P. F., Hernquist, L., Cox, T. J., Younger, J. D., & Besla, G. 2008c, ApJ, 688, 757

Infante, L., Strauss, M. A., Bahcall, N. A., Knapp, G. R., Lupton, R. H., Kim, R. S. J., Vogeley, M. S., Brinkmann, J., Csabai, I., Fukugita, M., Hennessy, G., Ivezić, Ž., Lamb, D. Q., Lee, B. C., Pier, J. R., & York, D. G. 2002, ApJ, 567, 155

Jeltema, T. E., Hallman, E. J., Burns, J. O., & Motl, P. M. 2008, ApJ, 681, 167

Jenkins, A., Frenk, C. S., White, S. D. M., Colberg, J. M., Cole, S., Evrard, A. E., Couchman, H. M. P., & Yoshida, N. 2001, MNRAS, 321, 372

Jiang, C. Y., Jing, Y. P., Faltenbacher, A., Lin, W. P., & Li, C. 2008, ApJ, 675, 1095

Jiang, C. Y., Jing, Y. P., & Lin, W. P. 2009, ArXiv e-prints

Jing, Y. P., Suto, Y., & Mo, H. J. 2007, ApJ, 657, 664

Kaiser, N. 1984, ApJ, 284, L9

Kampczyk, P., Lilly, S. J., Carollo, C. M., Scarlata, C., Feldmann, R., Koekemoer, A., Leauthaud, A., Sargent, M. T., Taniguchi, Y., & Capak, P. 2007, ApJS, 172, 329

Kang, X. & van den Bosch, F. C. 2008, ApJ, 676, L101

Kartaltepe, J. S., Sanders, D. B., Scoville, N. Z., Calzetti, D., Capak, P., Koekemoer, A., Mobasher, B., Murayama, T., Salvato, M., Sasaki, S. S., & Taniguchi, Y. 2007, ApJS, 172, 320

Kashikawa, N., Yoshida, M., Shimasaku, K., et al. 2006, ApJ, 637, 631

Kauffmann, G. & Haehnelt, M. 2000, MNRAS, 311, 576

Kauffmann, G. & White, S. D. M. 1993, MNRAS, 261, 921

Kauffmann, G., White, S. D. M., & Guiderdoni, B. 1993, MNRAS, 264, 201

Kereš, D., Katz, N., Fardal, M., Davé, R., & Weinberg, D. H. 2009, MNRAS, 395, 160

Kereš, D., Katz, N., Weinberg, D. H., & Davé, R. 2005, MNRAS, 363, 2

Khochfar, S. & Burkert, A. 2006, A&A, 445, 403

Kitayama, T. & Suto, Y. 1996a, MNRAS, 280, 638

—. 1996b, ApJ, 469, 480

Kitzbichler, M. G. & White, S. D. M. 2008, MNRAS, 391, 1489

Klypin, A., Gottlöber, S., Kravtsov, A. V., & Khokhlov, A. M. 1999, ApJ, 516, 530

Koester, B. P., McKay, T. A., Annis, J., Wechsler, R. H., Evrard, A. E., Rozo, E., Bleem, L., Sheldon, E. S., & Johnston, D. 2007a, ApJ, 660, 221

Koester, B. P., McKay, T. A., Annis, J., et al. 2007b, ApJ, 660, 239
Kolatt, T. S., Bullock, J. S., Sigad, Y., Kravtsov, A. V., Klypin, A. A., Primack, J. R., & Dekel, A. 2000, ArXiv Astrophysics e-prints 0010222
Komatsu, E., Smith, K. M., Dunkley, J., Bennett, C. L., Gold, B., Hinshaw, G., Jarosik, N., Larson, D., Nolta, M. R., Page, L., Spergel, D. N., Halpern, M., Hill, R. S., Kogut, A., Limon, M., Meyer, S. S., Odegard, N., Tucker, G. S., Weiland, J. L., Wollack, E., & Wright, E. L. 2010, ArXiv e-prints
Kowalski, M., Rubin, D., Aldering, G., et al. 2008, ApJ, 686, 749
Kravtsov, A. V., Berlind, A. A., Wechsler, R. H., Klypin, A. A., Gottlöber, S., Allgood, B., & Primack, J. R. 2004a, ApJ, 609, 35
Kravtsov, A. V., Gnedin, O. Y., & Klypin, A. A. 2004b, ApJ, 609, 482
Krick, J. E. & Bernstein, R. A. 2007, AJ, 134, 466
Kroupa, P., Theis, C., & Boily, C. M. 2005, A&A, 431, 517
Lacey, C. & Cole, S. 1993, MNRAS, 262, 627
—. 1994, MNRAS, 271, 676
Landy, S. D. & Szalay, A. S. 1993, ApJ, 412, 64
Larson, D., Dunkley, J., Hinshaw, G., Komatsu, E., Nolta, M. R., Bennett, C. L., Gold, B., Halpern, M., Hill, R. S., Jarosik, N., Kogut, A., Limon, M., Meyer, S. S., Odegard, N., Page, L., Smith, K. M., Spergel, D. N., Tucker, G. S., Weiland, J. L., Wollack, E., & Wright, E. L. 2010, ArXiv e-prints
Lee, K.-S., Giavalisco, M., Gnedin, O. Y., Somerville, R. S., Ferguson, H. C., Dickinson, M., & Ouchi, M. 2006, ApJ, 642, 63
Lemson, G. & Kauffmann, G. 1999, MNRAS, 302, 111
Li, Y., Mo, H. J., van den Bosch, F. C., & Lin, W. P. 2007, MNRAS, 379, 689
Libeskind, N. I., Frenk, C. S., Cole, S., Jenkins, A., & Helly, J. C. 2009, MNRAS, 399, 550
Lilly, S. J., Le Fevre, O., Hammer, F., & Crampton, D. 1996, ApJ, 460, L1+
Limousin, M., Kneib, J. P., Bardeau, S., Natarajan, P., Czoske, O., Smail, I., Ebeling, H., & Smith, G. P. 2007, A&A, 461, 881
Limousin, M., Sommer-Larsen, J., Natarajan, P., & Milvang-Jensen, B. 2009, ApJ, 696, 1771
Lin, L., Koo, D. C., Willmer, C. N. A., Patton, D. R., Conselice, C. J., Yan, R., Coil, A. L., Cooper, M. C., Davis, M., Faber, S. M., Gerke, B. F., Guhathakurta, P., & Newman, J. A. 2004a, ApJ, 617, L9
Lin, L., Patton, D. R., Koo, D. C., Casteels, K., Conselice, C. J., Faber, S. M., Lotz, J., Willmer, C. N. A., Hsieh, B. C., Chiueh, T., Newman, J. A., Novak, G. S., Weiner, B. J., & Cooper, M. C. 2008, ApJ, 681, 232
Lin, Y.-T. & Mohr, J. J. 2004, ApJ, 617, 879
Lin, Y.-T., Mohr, J. J., & Stanford, S. A. 2004b, ApJ, 610, 745
Liu, F. S., Mao, S., Deng, Z. G., Xia, X. Y., & Wen, Z. L. 2009, MNRAS, 396, 2003
Lotz, J. M., Davis, M., Faber, S. M., et al. 2008a, ApJ, 672, 177
Lotz, J. M., Jonsson, P., Cox, T. J., & Primack, J. R. 2008b, MNRAS, 391, 1137
Ludlow, A. D., Navarro, J. F., Springel, V., Jenkins, A., Frenk, C. S., & Helmi, A. 2009, ApJ, 692, 931

Lupton, R. 1993, Statistics in theory and practice, ed. Lupton, R.
Macciò, A. V., Dutton, A. A., van den Bosch, F. C., Moore, B., Potter, D., & Stadel, J. 2007, MNRAS, 378, 55
Macciò, A. V., Kang, X., Fontanot, F., Somerville, R. S., Koposov, S., & Monaco, P. 2009, MNRAS, 1907
Maciejewski, M., Colombi, S., Springel, V., Alard, C., & Bouchet, F. R. 2009, MNRAS, 396, 1329
Madau, P., Diemand, J., & Kuhlen, M. 2008, ApJ, 679, 1260
Madau, P., Ferguson, H. C., Dickinson, M. E., Giavalisco, M., Steidel, C. C., & Fruchter, A. 1996, MNRAS, 283, 1388
Majumdar, S. & Mohr, J. J. 2003, ApJ, 585, 603
Makino, J. & Hut, P. 1997, ApJ, 481, 83
Maller, A. H., Katz, N., Kereš, D., Davé, R., & Weinberg, D. H. 2006, ApJ, 647, 763
Mandelbaum, R., Seljak, U., Kauffmann, G., Hirata, C. M., & Brinkmann, J. 2006, MNRAS, 368, 715
Marchesini, D., van Dokkum, P. G., Förster Schreiber, N. M., Franx, M., Labbé, I., & Wuyts, S. 2009, ApJ, 701, 1765
Masjedi, M., Hogg, D. W., Cool, R. J., Eisenstein, D. J., Blanton, M. R., Zehavi, I., Berlind, A. A., Bell, E. F., Schneider, D. P., Warren, M. S., & Brinkmann, J. 2006, ApJ, 644, 54
Mateus, A. 2008, arXiv: 0802.2720
Maulbetsch, C., Avila-Reese, V., Colín, P., Gottlöber, S., Khalatyan, A., & Steinmetz, M. 2007, ApJ, 654, 53
McBride, J., Fakhouri, O., & Ma, C. 2009, MNRAS, 398, 1858
McCarthy, I. G., Frenk, C. S., Font, A. S., Lacey, C. G., Bower, R. G., Mitchell, N. L., Balogh, M. L., & Theuns, T. 2008, MNRAS, 383, 593
McIntosh, D. H., Guo, Y., Hertzberg, J., Katz, N., Mo, H. J., van den Bosch, F. C., & Yang, X. 2008, MNRAS, 388, 1537
McLure, R. J., Cirasuolo, M., Dunlop, J. S., Foucaud, S., & Almaini, O. 2008, arXiv: 0805.1335
Metz, M., Kroupa, P., & Jerjen, H. 2009, MNRAS, 394, 2223
Mihos, J. C., Harding, P., Feldmeier, J., & Morrison, H. 2005, ApJ, 631, L41
Mihos, J. C. & Hernquist, L. 1996, ApJ, 464, 641
Miller, L., Percival, W. J., Croom, S. M., & Babić, A. 2006, A&A, 459, 43
Mo, H. J., Mao, S., & White, S. D. M. 1998, MNRAS, 295, 319
Mo, H. J. & White, S. D. M. 1996, MNRAS, 282, 347
Monaco, P., Murante, G., Borgani, S., & Fontanot, F. 2006, ApJ, 652, L89
Moore, B., Ghigna, S., Governato, F., Lake, G., Quinn, T., Stadel, J., & Tozzi, P. 1999, ApJ, 524, L19
Moore, B., Lake, G., & Katz, N. 1998, ApJ, 495, 139
More, S., van den Bosch, F. C., Cacciato, M., Mo, H. J., Yang, X., & Li, R. 2009, MNRAS, 392, 801
Moster, B. P., Somerville, R. S., Maulbetsch, C., van den Bosch, F. C., Maccio', A. V., Naab,

T., & Oser, L. 2009, ArXiv e-prints
Murali, C., Katz, N., Hernquist, L., Weinberg, D. H., & Davé, R. 2002, ApJ, 571, 1
Murante, G., Arnaboldi, M., Gerhard, O., Borgani, S., Cheng, L. M., Diaferio, A., Dolag, K., Moscardini, L., Tormen, G., Tornatore, L., & Tozzi, P. 2004, ApJ, 607, L83
Muzzin, A., Yee, H. K. C., Hall, P. B., Ellingson, E., & Lin, H. 2007, ApJ, 659, 1106
Myers, A. D., Richards, G. T., Brunner, R. J., Schneider, D. P., Strand, N. E., Hall, P. B., Blomquist, J. A., & York, D. G. 2008, ApJ, 678, 635
Naab, T., Khochfar, S., & Burkert, A. 2006, ApJ, 636, L81
Nagai, D. & Kravtsov, A. V. 2005, ApJ, 618, 557
Natarajan, P., De Lucia, G., & Springel, V. 2007, MNRAS, 376, 180
Natarajan, P., Kneib, J., Smail, I., Treu, T., Ellis, R., Moran, S., Limousin, M., & Czoske, O. 2009, ApJ, 693, 970
Navarro, J. F., Frenk, C. S., & White, S. D. M. 1996, ApJ, 462, 563
—. 1997, ApJ, 490, 493
Navarro, J. F., Ludlow, A., Springel, V., Wang, J., Vogelsberger, M., White, S. D. M., Jenkins, A., Frenk, C. S., & Helmi, A. 2010, MNRAS, 402, 21
Neto, A. F., Gao, L., Bett, P., Cole, S., Navarro, J. F., Frenk, C. S., White, S. D. M., Springel, V., & Jenkins, A. 2007, MNRAS, 381, 1450
Noguchi, M. 1991, MNRAS, 251, 360
Ostriker, J. P., Spitzer, Jr., L., & Chevalier, R. A. 1972, ApJ, 176, L51+
Ostriker, J. P. & Tremaine, S. D. 1975, ApJ, 202, L113
Ouchi, M., Hamana, T., Shimasaku, K., Yamada, T., Akiyama, M., Kashikawa, N., Yoshida, M., Aoki, K., Iye, M., Saito, T., Sasaki, T., Simpson, C., & Yoshida, M. 2005, ApJ, 635, L117
Ouchi, M., Shimasaku, K., Okamura, S., Furusawa, H., Kashikawa, N., Ota, K., Doi, M., Hamabe, M., Kimura, M., Komiyama, Y., Miyazaki, M., Miyazaki, S., Nakata, F., Sekiguchi, M., Yagi, M., & Yasuda, N. 2004, ApJ, 611, 660
Padmanabhan, N., White, M., & Eisenstein, D. J. 2007, MNRAS, 376, 1702
Padmanabhan, N., White, M., Norberg, P., & Porciani, C. 2008, arXiv: 0802.2105
Patton, D. R. & Atfield, J. E. 2008, ApJ, 685, 235
Patton, D. R., Carlberg, R. G., Marzke, R. O., Pritchet, C. J., da Costa, L. N., & Pellegrini, P. S. 2000, ApJ, 536, 153
Patton, D. R., Pritchet, C. J., Carlberg, R. G., Marzke, R. O., Yee, H. K. C., Hall, P. B., Lin, H., Morris, S. L., Sawicki, M., Shepherd, C. W., & Wirth, G. D. 2002, ApJ, 565, 208
Patton, D. R., Pritchet, C. J., Yee, H. K. C., Ellingson, E., & Carlberg, R. G. 1997, ApJ, 475, 29
Peñarrubia, J., Navarro, J. F., & McConnachie, A. W. 2008, ApJ, 673, 226
Peacock, J. A. 1999, Cosmological Physics (Cosmological Physics, by John A. Peacock, pp. 704. ISBN 052141072X. Cambridge, UK: Cambridge University Press, January 1999.)
Peacock, J. A. & Smith, R. E. 2000, MNRAS, 318, 1144
Percival, W. & Miller, L. 1999, MNRAS, 309, 823
Percival, W. J., Reid, B. A., Eisenstein, D. J., et al. 2009, ArXiv e-prints

Percival, W. J., Scott, D., Peacock, J. A., & Dunlop, J. S. 2003, MNRAS, 338, L31
Poole, G. B., Babul, A., McCarthy, I. G., Fardal, M. A., Bildfell, C. J., Quinn, T., & Mahdavi, A. 2007, MNRAS, 380, 437
Press, W. H. & Schechter, P. 1974, ApJ, 187, 425
Purcell, C. W., Bullock, J. S., & Zentner, A. R. 2007, ApJ, 666, 20
Reed, D., Governato, F., Quinn, T., Gardner, J., Stadel, J., & Lake, G. 2005, MNRAS, 359, 1537
Reichardt, C. L., Ade, P. A. R., Bock, J. J., Bond, J. R., Brevik, J. A., Contaldi, C. R., Daub, M. D., Dempsey, J. T., Goldstein, J. H., Holzapfel, W. L., Kuo, C. L., Lange, A. E., Lueker, M., Newcomb, M., Peterson, J. B., Ruhl, J., Runyan, M. C., & Staniszewski, Z. 2009, ApJ, 694, 1200
Robertson, B., Cox, T. J., Hernquist, L., Franx, M., Hopkins, P. F., Martini, P., & Springel, V. 2006, ApJ, 641, 21
Rowley, D. R., Thomas, P. A., & Kay, S. T. 2004, MNRAS, 352, 508
Rudick, C. S., Mihos, J. C., & McBride, C. 2006, ApJ, 648, 936
Sales, L. V., Navarro, J. F., Abadi, M. G., & Steinmetz, M. 2007, MNRAS, 379, 1464
Sanders, D. B. & Mirabel, I. F. 1996, ARA&A, 34, 749
Sandvik, H. B., Möller, O., Lee, J., & White, S. D. M. 2007, MNRAS, 377, 234
Sarazin, C. L. 2005, in X-Ray and Radio Connections (eds. L.O. Sjouwerman and K.K Dyer) Published electronically by NRAO, http://www.aoc.nrao.edu/events/xraydio Held 3-6 February 2004 in Santa Fe, New Mexico, USA, (E8.00) 3 pages, ed. L. O. Sjouwerman & K. K. Dyer
Saro, A., De Lucia, G., Dolag, K., & Borgani, S. 2008, MNRAS, 391, 565
Scannapieco, E. & Thacker, R. J. 2003, ApJ, 590, L69
Scott, S. E., Dunlop, J. S., & Serjeant, S. 2006, MNRAS, 370, 1057
Seek Kim, H., Baugh, C. M., Cole, S., Frenk, C. S., & Benson, A. J. 2009, ArXiv e-prints
Seljak, U. 2000, MNRAS, 318, 203
Seljak, U. & Warren, M. S. 2004, MNRAS, 355, 129
Shankar, F., Lapi, A., Salucci, P., De Zotti, G., & Danese, L. 2006, ApJ, 643, 14
Sheldon, E. S., Johnston, D. E., Masjedi, M., Mc Kay, T. A., Blanton, M. R., Scranton, R., Wechsler, R. H., Koester, B. P., Hansen, S. M., Frieman, J. A., & Annis, J. 2009, ApJ, 703, 2232
Shen, Y., Strauss, M. A., Oguri, M., Hennawi, J. F., Fan, X., Richards, G. T., Hall, P. B., Gunn, J. E., Schneider, D. P., Szalay, A. S., Thakar, A. R., Vanden Berk, D. E., Anderson, S. F., Bahcall, N. A., Connolly, A. J., & Knapp, G. R. 2007, AJ, 133, 2222
Sheth, R. K., Connolly, A. J., & Skibba, R. 2005, ArXiv Astrophysics e-prints 0511773
Sheth, R. K., Mo, H. J., & Tormen, G. 2001, MNRAS, 323, 1
Sheth, R. K. & Pitman, J. 1997, MNRAS, 289, 66
Sheth, R. K. & Tormen, G. 1999, MNRAS, 308, 119
—. 2004, MNRAS, 350, 1385
Silk, J. & White, S. D. 1978, ApJ, 223, L59
Simha, V., Weinberg, D. H., Davé, R., Gnedin, O. Y., Katz, N., & Kereš, D. 2009, MNRAS,

399, 650
Skibba, R. A. 2009, MNRAS, 392, 1467
Slosar, A., Hirata, C., Seljak, U., Ho, S., & Padmanabhan, N. 2008, Journal of Cosmology and Astro-Particle Physics, 8, 31
Smoot, G. F., Bennett, C. L., Kogut, A., Wright, E. L., et al. 1992, ApJ, 396, L1
Somerville, R. S., Lemson, G., Kolatt, T. S., & Dekel, A. 2000, MNRAS, 316, 479
Sommer-Larsen, J., Romeo, A. D., & Portinari, L. 2005, MNRAS, 357, 478
Springel, V., Di Matteo, T., & Hernquist, L. 2005a, MNRAS, 361, 776
Springel, V., White, S. D. M., Jenkins, A., Frenk, C. S., Yoshida, N., Gao, L., Navarro, J., Thacker, R., Croton, D., Helly, J., Peacock, J. A., Cole, S., Thomas, P., Couchman, H., Evrard, A., Colberg, J., & Pearce, F. 2005b, Nature, 435, 629
Springel, V., White, S. D. M., Tormen, G., & Kauffmann, G. 2001, MNRAS, 328, 726
Steidel, C. C., Adelberger, K. L., Shapley, A. E., Pettini, M., Dickinson, M., & Giavalisco, M. 2003, ApJ, 592, 728
Stephens, A. W., Schneider, D. P., Schmidt, M., Gunn, J. E., & Weinberg, D. H. 1997, AJ, 114, 41
Stewart, K. R., Bullock, J. S., Barton, E. J., & Wechsler, R. H. 2009, ApJ, 702, 1005
Stewart, K. R., Bullock, J. S., Wechsler, R. H., Maller, A. H., & Zentner, A. R. 2008, ApJ, 683, 597
Tacconi, L. J., Genzel, R., Smail, I., et al. 2008, ApJ, 680, 246
Tasitsiomi, A., Kravtsov, A. V., Gottlöber, S., & Klypin, A. A. 2004a, ApJ, 607, 125
Tasitsiomi, A., Kravtsov, A. V., Wechsler, R. H., & Primack, J. R. 2004b, ApJ, 614, 533
Taylor, J. E. & Babul, A. 2004, MNRAS, 348, 811
—. 2005, MNRAS, 364, 535
Tegmark, M., Eisenstein, D. J., Strauss, M. A., et al. 2006, Phys. Rev. D, 74, 123507
Thacker, R. J., Scannapieco, E., & Couchman, H. M. P. 2006, ApJ, 653, 86
Tinker, J., Kravtsov, A. V., Klypin, A., Abazajian, K., Warren, M., Yepes, G., Gottlöber, S., & Holz, D. E. 2008a, ApJ, 688, 709
Tinker, J. L., Conroy, C., Norberg, P., Patiri, S. G., Weinberg, D. H., & Warren, M. S. 2008b, ApJ, 686, 53
Tinker, J. L., Norberg, P., Weinberg, D. H., & Warren, M. S. 2007, ApJ, 659, 877
Tinker, J. L. & Wetzel, A. R. 2009, ArXiv e-prints
Toomre, A. & Toomre, J. 1972, ApJ, 178, 623
Tormen, G. 1997, MNRAS, 290, 411
—. 1998, MNRAS, 297, 648
Tormen, G., Diaferio, A., & Syer, D. 1998, MNRAS, 299, 728
Tormen, G., Moscardini, L., & Yoshida, N. 2004, MNRAS, 350, 1397
Vale, A. & Ostriker, J. P. 2006, MNRAS, 371, 1173
van den Bosch, F. C., Aquino, D., Yang, X., Mo, H. J., Pasquali, A., McIntosh, D. H., Weinmann, S. M., & Kang, X. 2008, MNRAS, 387, 79
van den Bosch, F. C., Tormen, G., & Giocoli, C. 2005a, MNRAS, 359, 1029
van den Bosch, F. C., Yang, X., Mo, H. J., & Norberg, P. 2005b, MNRAS, 356, 1233

van den Bosch, F. C., Yang, X., Mo, H. J., Weinmann, S. M., Macciò, A. V., More, S., Cacciato, M., Skibba, R., & Kang, X. 2007, MNRAS, 376, 841
Vikhlinin, A., Kravtsov, A. V., Burenin, R. A., Ebeling, H., Forman, W. R., Hornstrup, A., Jones, C., Murray, S. S., Nagai, D., Quintana, H., & Voevodkin, A. 2009, ApJ, 692, 1060
Vitvitska, M., Klypin, A. A., Kravtsov, A. V., Wechsler, R. H., Primack, J. R., & Bullock, J. S. 2002, ApJ, 581, 799
Wang, H., Mo, H. J., & Jing, Y. P. 2009, MNRAS, 396, 2249
Wang, H. Y., Jing, Y. P., Mao, S., & Kang, X. 2005, MNRAS, 364, 424
Wang, H. Y., Mo, H. J., & Jing, Y. P. 2007a, MNRAS, 375, 633
Wang, L. & Kauffmann, G. 2008, MNRAS, 391, 785
Wang, L., Li, C., Kauffmann, G., & De Lucia, G. 2006, MNRAS, 371, 537
—. 2007b, MNRAS, 377, 1419
Warren, M. & Salmon, J. 1993, Supercomputing '93, 12
Warren, M. S., Abazajian, K., Holz, D. E., & Teodoro, L. 2006, ApJ, 646, 881
Wechsler, R. H., Bullock, J. S., Primack, J. R., Kravtsov, A. V., & Dekel, A. 2002, ApJ, 568, 52
Wechsler, R. H., Zentner, A. R., Bullock, J. S., Kravtsov, A. V., & Allgood, B. 2006, ApJ, 652, 71
Weinberg, D. H., Colombi, S., Davé, R., & Katz, N. 2008, ApJ, 678, 6
Weinmann, S. M., Kauffmann, G., van den Bosch, F. C., Pasquali, A., McIntosh, D. H., Mo, H., Yang, X., & Guo, Y. 2009, MNRAS, 394, 1213
Wetzel, A. R. 2010, ArXiv e-prints
Wetzel, A. R., Cohn, J. D., & White, M. 2009a, MNRAS, 395, 1376
—. 2009b, MNRAS, 394, 2182
Wetzel, A. R., Cohn, J. D., White, M., Holz, D. E., & Warren, M. S. 2007, ApJ, 656, 139
Wetzel, A. R., Schulz, A. E., Holz, D. E., & Warren, M. S. 2008, ApJ, 683, 1
Wetzel, A. R. & White, M. 2010, MNRAS, 403, 1072
White, M. 2001, A&A, 367, 27
—. 2002, ApJS, 143, 241
White, M., Zheng, Z., Brown, M. J. I., Dey, A., & Jannuzi, B. T. 2007, ApJ, 655, L69
White, S. D. M. 1978, MNRAS, 184, 185
—. 1994, ArXiv Astrophysics e-prints
White, S. D. M. & Rees, M. J. 1978, MNRAS, 183, 341
Willman, B., Governato, F., Wadsley, J., & Quinn, T. 2004, MNRAS, 355, 159
Yamauchi, C., Yagi, M., & Goto, T. 2008, MNRAS, 390, 383
Yan, R., Newman, J. A., Faber, S. M., Coil, A. L., Cooper, M. C., Davis, M., Weiner, B. J., Gerke, B. F., & Koo, D. C. 2008, arXiv: 0805.0004
Yang, X., Mo, H. J., & van den Bosch, F. C. 2006, ApJ, 638, L55
—. 2008, ApJ, 676, 248
—. 2009, ApJ, 693, 830
Yang, X., Mo, H. J., van den Bosch, F. C., Pasquali, A., Li, C., & Barden, M. 2007, ApJ, 671, 153

Yang, X., Mo, H. J., van den Bosch, F. C., Weinmann, S. M., Li, C., & Jing, Y. P. 2005, MNRAS, 362, 711
Yoshida, M., Shimasaku, K., Kashikawa, N., et al. 2006, ApJ, 653, 988
Yoshida, M., Shimasaku, K., Ouchi, M., Sekiguchi, K., Furusawa, H., & Okamura, S. 2008, ApJ, 679, 269
Zehavi, I., Zheng, Z., Weinberg, D. H., et al. 2005, ApJ, 630, 1
Zel'Dovich, Y. B. 1970, A&A, 5, 84
Zentner, A. R., Berlind, A. A., Bullock, J. S., Kravtsov, A. V., & Wechsler, R. H. 2005, ApJ, 624, 505
Zhang, J., Ma, C.-P., & Fakhouri, O. 2008, MNRAS, 387, L13
Zhao, D. H., Jing, Y. P., Mo, H. J., & Börner, G. 2003a, ApJ, 597, L9
—. 2009, ApJ, 707, 354
Zhao, D. H., Mo, H. J., Jing, Y. P., & Börner, G. 2003b, MNRAS, 339, 12
Zheng, Z., Coil, A. L., & Zehavi, I. 2007, ApJ, 667, 760
Zibetti, S., White, S. D. M., Schneider, D. P., & Brinkmann, J. 2005, MNRAS, 358, 949